ESTIMATION OF SYSTEM DAMPING AT THE LOTUNG SITE BY APPLICATION OF SYSTEM IDENTIFICATION

Steven D. Glaser
Alena L. Leeds

Division of Engineering
Colorado School of Mines
Golden, CO 80401

A Report to:

ABSTRACT

Possibly the best set of data for earthquake excitation of soils exists for the test site operated by the Taiwan Power Company in conjunction with the Electric Power Research Institute (EPRI) at Lotung Taiwan. At this site, two locations are instrumented with three-component accelerometers at depths of 47 m, 17 m, 11 m, 6 m, and at the surface. One array is in the free-field, while the other is adjacent to a one-quarter scale nuclear containment vessel. The site is also well instrumented with piezometers at various depths and locations. The simplified soil profile consists of 30 m to 35 m of silty sand and sandy silt with some gravel, overlaying a thick clay and silt deposit. The water table is within half a meter of the ground surface. This area is seismically active, and strong shaking generated by many earthquakes exhibiting a wide range of magnitudes have been recorded since 1986.

For this study the modal frequencies and damping ratios were calculated for events 3, 4, 7, 8, 9, 10, 12 and 16 with local magnitudes ranging from 4.5 to 7.0. The modal frequencies and damping ratios calculated are examined for the effect of local energy intensity and soil structure interaction. Modal frequencies are seen to decrease with increasing intensity once a certain threshold of acceleration/intensity is reached. This result is consistent with the data obtained by other authors using different techniques. For the 0-6 m interval the decrease in frequency with event energy is less pronounced under a model containment structure than in the free field. This soil-structure effect is increasingly diminished with depth and absent by the 17-47m interval. Calculated damping values demonstrate an expected increase with input seismic energy. For the 0-6 m and 6-11 m intervals the damping values are higher under the model structure than in the free field. This distinction is completely missing in the 17-47 m results. The transition to non-linear behavior, while less pronounced with increasing depth, consistently occurs above a peak acceleration of 0.05 g or Arias Intensity of 100 m/sec.

The results clearly indicate a degree of non-linear response over the intervals studied. Evidence of a decrease in specific interval fundamental frequency and an accompanying general trend of increased damping with higher seismic energy are clear. Comparison of the results of this study with previous work considered with the inherent superiority of parametric modeling for transient and/or non-stationary time series such as earthquakes indicate that system identification is a more robust method for identifying fundamental frequencies and damping values for layers of earth materials when borehole information is available.

ACKNOWLEDGMENTS

TABLE OF CONTENTS

CHAPTER 1 - INTRODUCTION

1.1   Background

There are many unanswered questions of interest to the geotechnical community concerning the behavior of soils subjected to earthquake excitation. Foremost among them are questions concerning the strain-dependent non-linear behavior of soils, and soil-structure interaction. In an attempt to gain further rational understanding of these problems the Electric Power Research Institute (EPRI), the Colorado School of Mines (CSM), and the Structures Division of the National Institute of Standards and Technology (NIST) formed a cooperative research team to evaluate ground motion time histories recorded at the Lotung site, Taiwan.

Much of the necessary data was made available by EPRI from the Lotung site. The Lotung strong motion data set are an extremely unique set of data. The completeness of this input-output data set makes it ideal for analysis using system identification (SI) methods. Data from the Wildlife Site, Imperial Valley CA, and Treasure Island are freely available. This report lays out the work undertaken with funding provided by NIST under Award Number 60NANB500074.

1.2   Why Use System Identification?

An important goal for earthquake engineering is the ability to estimate soil properties without intruding into the soil mass. For the engineer interested in seismic behavior of soils, the dynamic properties of the soil are of interest, particularly large-strain properties. The archetypal large strain field excitation is earthquake strong motion. Ideally, both ground motions into the soil layer of interest and on the surface above the layer are recorded, as illustrated by the cartoon in Fig. 1.1. Given this known input propagating upward from depth, and the output at the top of the soil column, the behavior of the soil can be modeled by inverse theory. If a suitable model is chosen to represent the system of interest, the estimated model parameters will correspond to important mechanical parameters of the system, such as damping, natural frequency, and stiffness. This estimation of parameters is commonly known as system identification (SI).
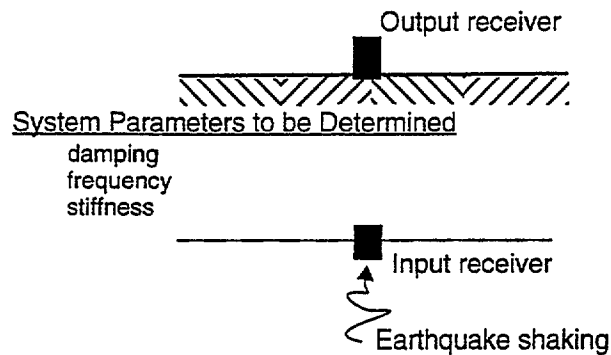
Fig. 1.1 - Configuration of the System Identification Method.

The traditional method of geotechnical analysis of dynamic soil motions is through the Fourier transform. However, serious problems arise when this method is applied to short data streams, and to signals changing through time — non-stationary signals. This study was undertaken to show the effectiveness of a different type of model, a parametric model commonly used in automatic control and geophysics, which avoids many of the limitations inherent with calculating the system transfer function by Fourier techniques. An important aspect of this particular parametric model is the theoretical link between the estimated system parameters and the mechanical parameters of a lumped-mass oscillator. The parametric model allows estimates of system dynamic properties to be made if an input-output data set is available.

1.3   Scope

This report presents detailed SI analyses of the full suite of seismic events at the Lotung site. Estimates of resonant frequencies and damping, and the dependence of these quantities on earthquake intensity will be presented. To this end the Lotung site itself will be introduced in Chapter 2 through geological, seismological, and geotechnical descriptions. The SI procedures will be discussed in detail in Chapter 3. Chapter 4 presents results of the system identification of the Lotung site data, with a discussion and conclusions given in Chapter 5. Appendix A describes the signal processing used on the raw data, with the integration procedure given in Appendix B. The pore water pres ire time histories are shown in Appendix C. A literature review of damping values measured by other researchers is compiled in Appendix D. Finally, comparisons of actual interval outputs and modeled outputs for all events and intervals is given in Appendix E.

CHAPTER 2 - THE LOTUNG SITE, TAIWAN

2.1 Introduction and Geography

With the growth of the use of nuclear-powered generating plants in the 1970's, many safety related questions about the seismic performance of these plants arose. In the early 1980's, EPRI and the Taiwan Power Co. constructed two scale models (1/4 and 1/12 scale) of a nuclear containment structure near Lotung, Taiwan. This is a very seismically active area in northeast Taiwan (see Fig. 2.1). The site and structures were elaborately instrumented so that soil and structural response, and soil-structure interaction, to earthquakes could be carefully studied (Tang et al., 1989; Liu and Yeh, 1985).

2.2 Instrumentation

The soil instrumentation includes a three-arm surface array, as shown in Fig. 2.2a. The arms radiate approximately 47 m from the 1/4 scale containment structure. In addition, there are two downhole arrays of accelerometers extending to a depth of 47 m, as shown in Fig. 2.2b. The surface accelerometers are triaxial force-balance units (Kinemetrics FBA-13) oriented in the N-S, E-W, and vertical directions. The downhole arrays (DHA and DHB) are modified Kinemetrics FBA-13H units oriented in the N-S, E-W, and vertical directions. DHA is located 3 m from the containment vessel and DHB is located 47 m from the structure, allowing identification of the effects of the structure on soil response. The downhole instruments are located at depths of 6 m, 11 m, 17 m, and 47 m. The simplified soil profile consists of 30-35 m of silty sand and sandy silt with some gravel, above clayey silt and silty clay. The water table is within half a meter of the ground surface, under artesian pressure.

2.3 Site Characterization

The basic geology of the Lotung site is summarized by Wen and Yeh (1984) and Tang (1987). The area consists of a recent alluvium layer 40 to 50 m thick overlying a Pleistocene formation that varies from 150 to 500 m in thickness. Underlying the Pleistocene material is a Miocene basement rock. Characteristic geological profiles also showing compressional wave velocities are shown in Fig. 2.3. Example soil profiles are shown on Fig. 2.4. The locations of the boreholes from which the profiles were constructed are shown on Fig. 2.5.

3
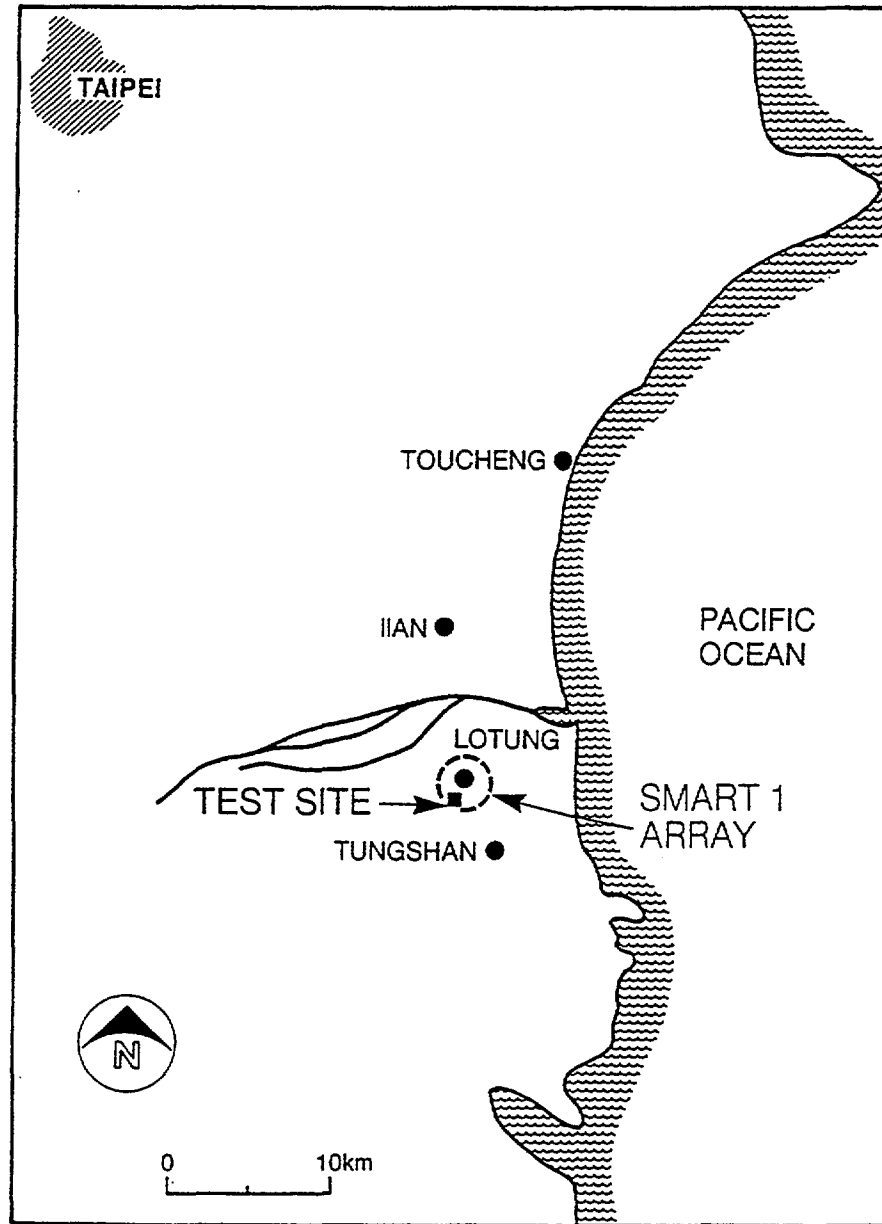
Fig. 2.1 Location of Lotung Large-Scale Seismic Test Site (LSST).

DHB

6m — DHB6
5m — DHB11
6m — DHB17

30m — DHB47

(B) Downhole Instrument Arrays
(After Tang, 1987)

45.7m

3.2m

DHA

6m
11m
17m

47m

1/4-scale model

10.52m

4.57m

FA1-5 DHB

Arm 1

DHA

N

Arm 2

30.48m

6.10m
6.10m
3.05m

1.5m

Arm 3

■ Triaxial accelerometers

(A) Surface Instrument Arrays
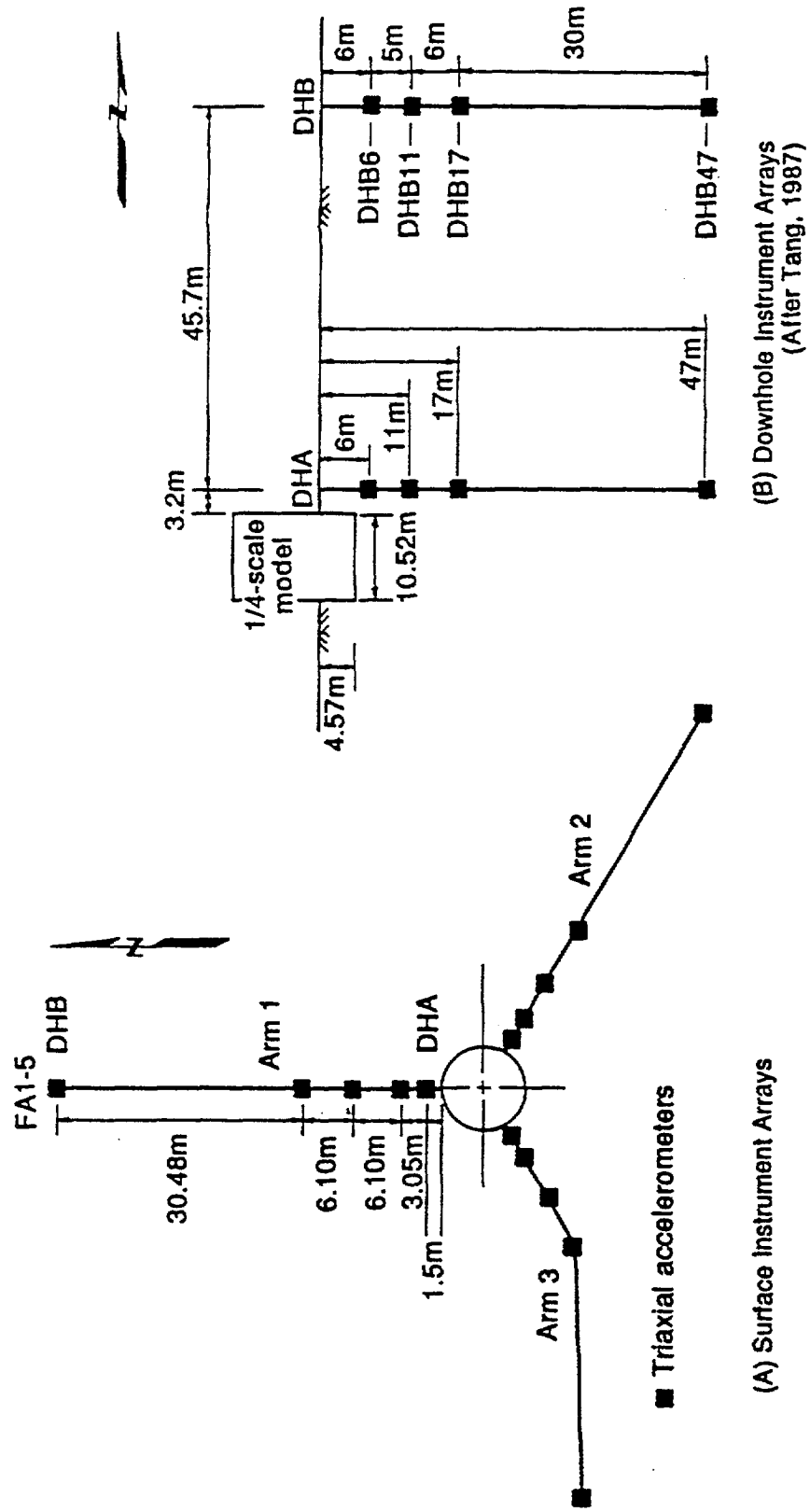
Fig. 2.2 Location of surface and downhole instrumentation at the Lotung site. (Chang et al., 1991b)

Five stages of laboratory testing programs were performed at the LSST during specific phases of the project to determine engineering properties of the soil. A summary of the tests performed is included here and the specific references for the test results are given below.

1. 1984 Jong Shing Boring Services (JSBS) Laboratory Testing Program

Index properties:
    Soil classification
    Grain size analyses
    Moisture contents
    Specific gravity
    Dry density and void ratio
    Atterberg limits
Engineering properties:
    Direct shear tests
    Triaxial shear tests
    Unconfined compression tests

2. 1987 National Taiwan University (NTU) Laboratory Testing Program

Index properties:
    Grain size analyses
    Moisture content
    Specific gravity
    Dry density
    Atterberg limits
Engineering properties:
    Uniaxial - load/unload and cyclic loading tests
    Triaxial - compression, extension and cyclic loading tests
    Resonant column
    Hydrostatic - load/unload and cyclic loading tests
    Compaction tests

3. 1987 University of California at Davis (UCD) Laboratory Testing Program

Engineering properties:
    Triaxial shear loading
    Cyclic triaxial liquefaction testing

The UCD phase of the laboratory testing was performed in conjunction with the installation of pore water pressure transducers at the site. Pore water pressures were measured in the samples during these dynamic laboratory tests.

4. 1989 NTU Laboratory Testing Program

Engineering properties:
    One dimensional rebound
    Resonant column
    Cyclic triaxial liquefaction
    Permeability
    Cyclic triaxial modulus

These additional tests were performed by NTU for the specific purpose of investigating the form of the shear modulus versus shearing strain and material damping versus shearing strain curves for undisturbed soil samples.

5. 1990 UCD Laboratory Testing Program

Engineering properties:
    Cyclic triaxial modulus
    Cyclic triaxial liquefaction
    Cyclic simple shear
    One dimensional rebound
    Permeability

These tests by UCD were independent of the 1989 NTU tests and were performed to investigate discrepancies in modulus and damping data found from analysis of 1987 results for the LSST site. In addition, it provided additional data on the cyclic strength and liquefaction properties of the soil. Blowcount results from the standard penetration test (SPT) are shown on Fig. 2.6 for 2 of the 3 drilling and sampling programs. The appearance of an occasional layer requiring an excess of 50 blows per foot indicates a gravelly soil zone that occurs in discrete lenses rather than as a consistent layer. Results of cone penetration test (CPT) soundings are shown in Fig. 2.7 and 2.8. Occasional spikes in tip resistance values confirm the presence of the gravelly lenses.

S   **N**

Recent Alluvium (430 - 760 m/s)

Alluvium (1400 - 1700 m/s)

Pleistocene Formation
(1800 - 2000 m/s)

Miocene Layer (3300 - 4000 m/s)

Depth (meters)

0   1 km
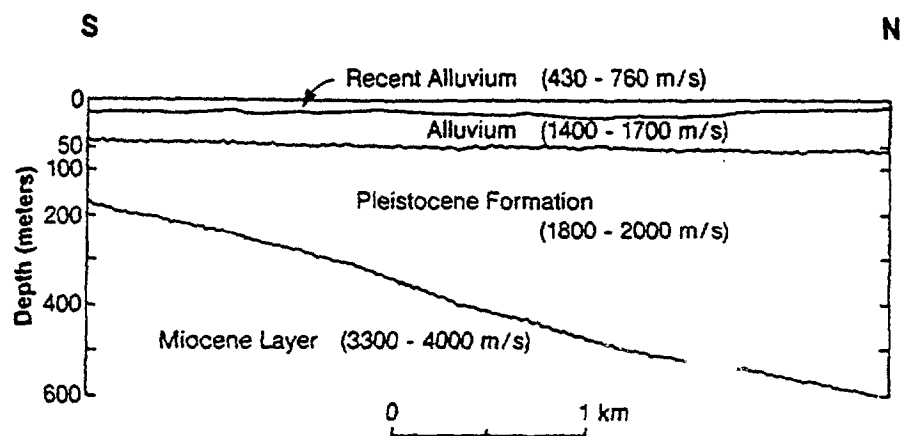
a) Geological Profile and Compressional Wave Velocity Along North-South Section

After Tang (1)

W   **E**

Recent Alluvium (430 - 760 m/s)

Alluvium (1400 - 1700 m/s)

Pleistocene Formation
(1800 - 2000 m/s)

Miocene Layer (3300 - 4000 m/s)

Depth (meters)

0   1 km
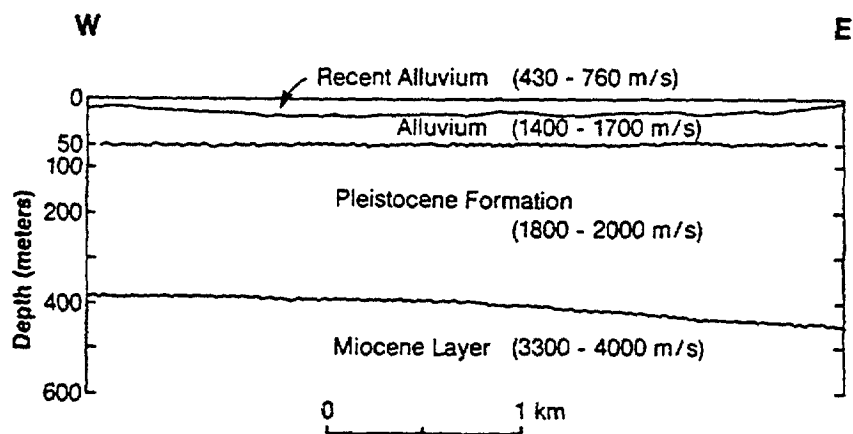
b) Geological Profile and Compressional Wave Velocity Along East-West Section

Fig. 2.3 Geological profiles for the Lotung site.

PROFILE I

L2 | L7 | L3 — Depth (meters)

- Silty Sand with Gravel and Rotten Wood
- Silty Sand with Gravel
- Silty Sand with Gravel
- Sandy Silt
- Sandy Silt & Silty Fine Sand
- Sandy Silt
- Silty Sand with Gravel
- Silty Clay
- Sandy Silt with Gravel
- Silty Fine Sand
- Silty Sand with Gravel
- Sandy Silt
- Silty Sand with Gravel
- Sand with Gravel
- Sandy Silt with Silty Sand and Gravel
- Silty Clay with Silty Sand
- Silty Fine Sand and Sandy Silt Interbedded
- Silty Fine Sand
- Clayey Silt
- Sand with Gravel
- Silty Sand with Gravel
- Sandy Silt with Silty Sand
- Sandy Silt & Clayey Silt
- Clayey Silt
- Silty Clay with Some Rotten Wood
- Silty Clay
- Sandy Silt & Clayey Silt
- Silty Sand with Gravel
- Clayey Silt
- Silty Clay

PROFILE I

PROFILE II

L1 | L3 | L4 — Depth (meters)

- Sandy Silt & Silty Fine Sand
- Silty Sand with Gravel
- Silty Sand with Gravel
- Silty Fine Sand & Sandy Silt
- Silty Fine Sand with Silt
- Sandy Silt
- Silty Sand with Gravel
- Silty Fine Sand & Sandy Silt
- Silty Sand with Gravel
- Sandy Silt with Gravel
- Silty Sand with Gravel
- Sandy Silt
- Sandy Silt
- Silty Sand with Gravel
- Silty Sand with Gravel
- Sandy Silt with Silty Sand & Gravel
- Silty Sand
- Clayey Silt
- Clayey Silt
- Silty Clay with Sandy Silt
- Sandy Silt with Gravel
- Silty Fine Sand
- Sandy Silt & Silty Fine Sand
- Silty Sand with Gravel
- Silty Sand with Gravel
- Sandy Silt & Clayey Silt
- Silty Clay
- Clayey Silt
- Silty Clay with Thin Layer of Sandy Silt and with Some Rotten Wood
- Sandy Silt & Clayey Silt
- Clayey Silt & Sandy Silt
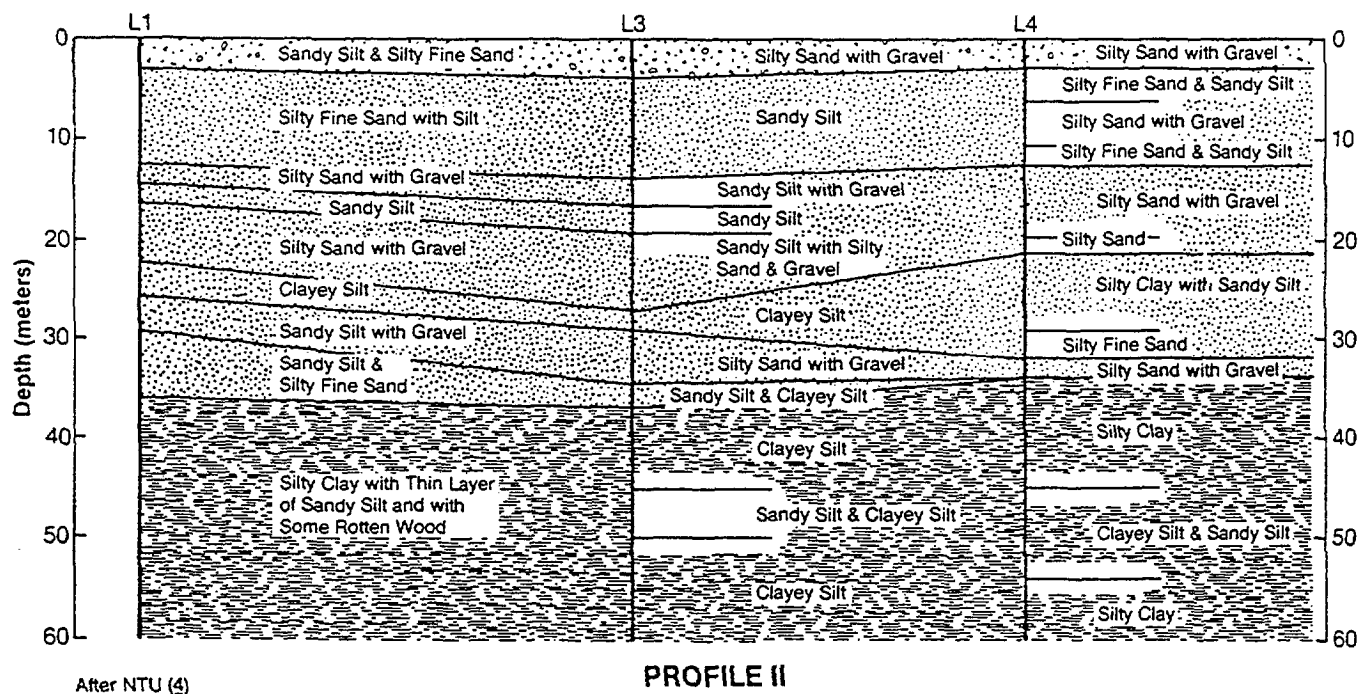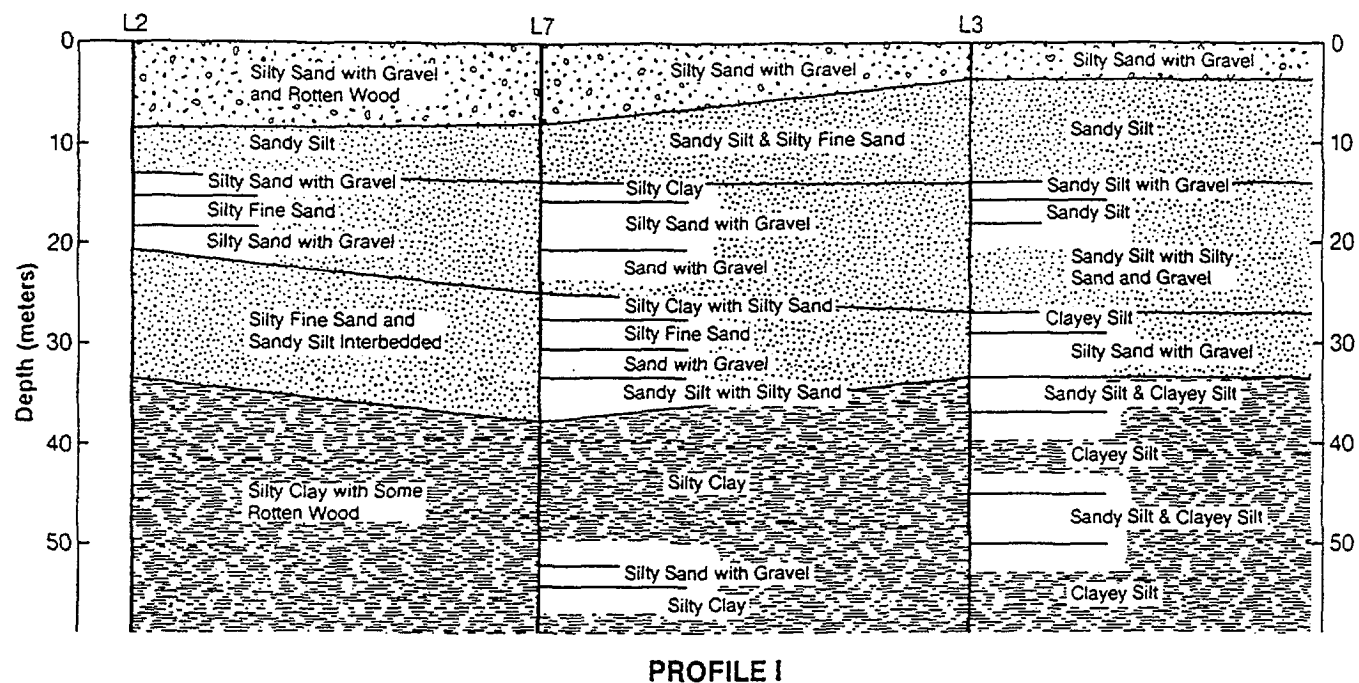- Clayey Silt
- Silty Clay

After NTU (4)

PROFILE II

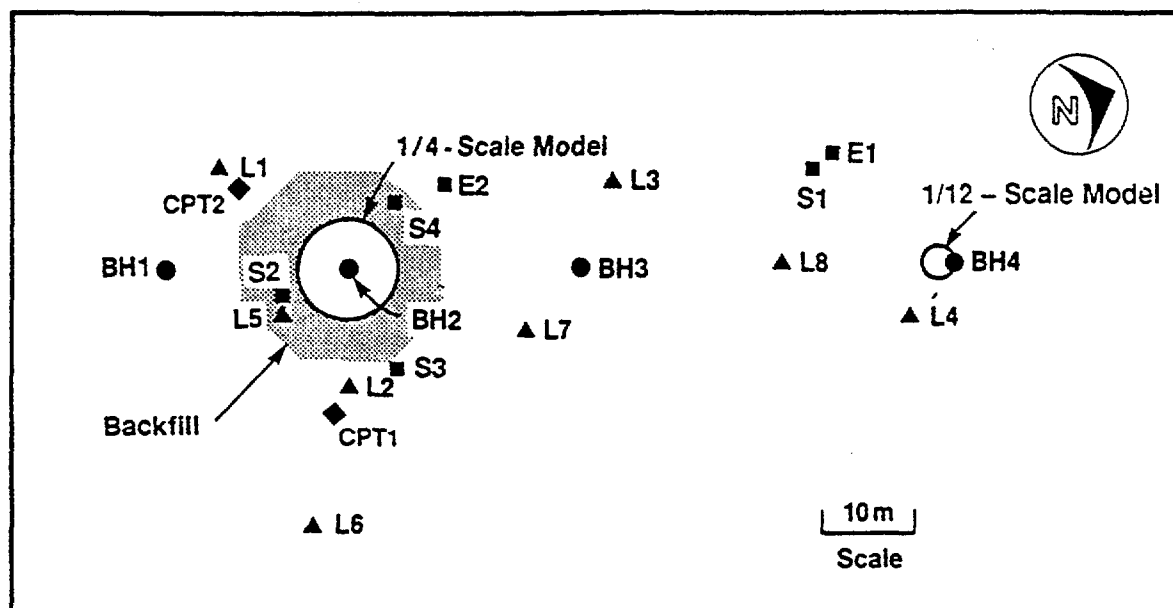Fig. 2.4 Detailed soil profiles developed during the NTU field program. (EPRI, 1989)

9

Symbols

●   Borehole Drilled During JSBS Program

▲   Borehole Drilled During WECC Program

■   Borehole Drilled During MAA Program

◆   CPT Sounding During UCD Program

Fig. 2.5 Location of boreholes and soundings at the Lotung site. (Anderson, 1993)
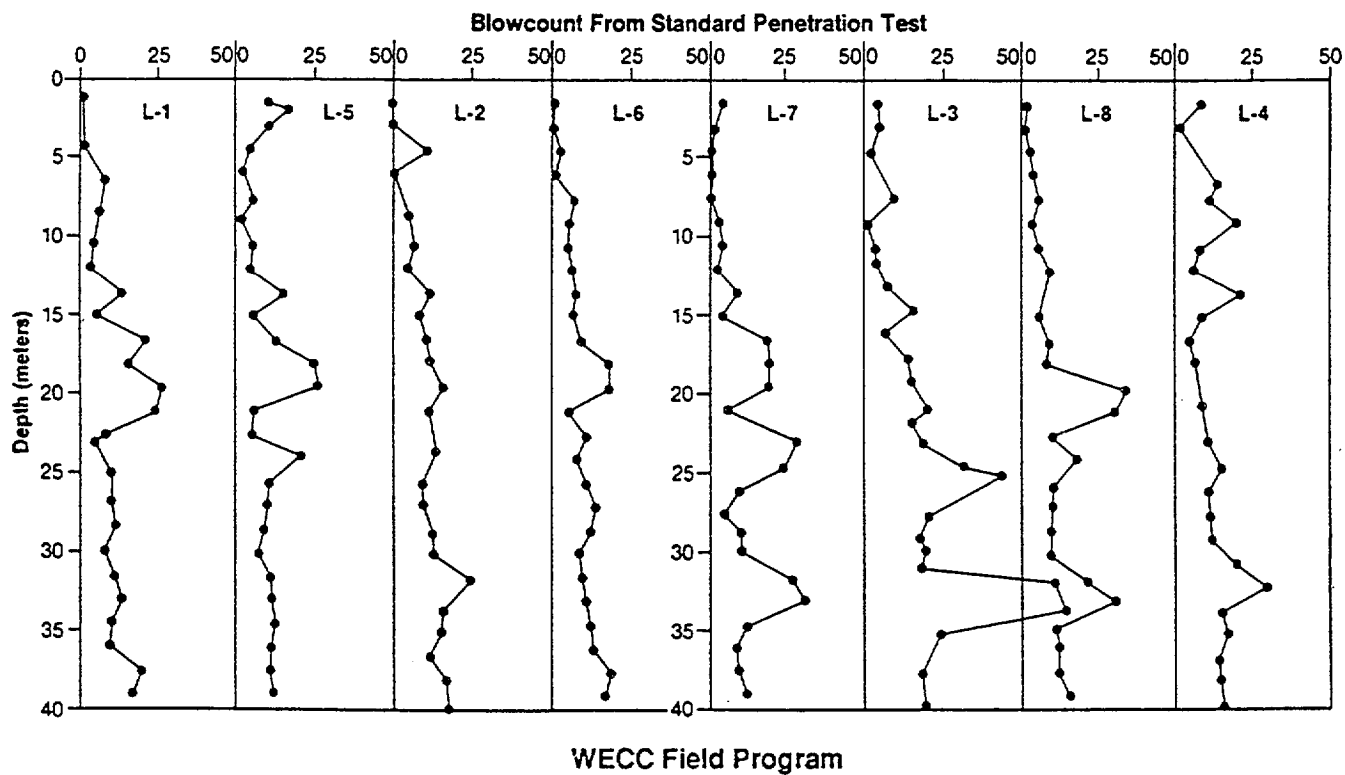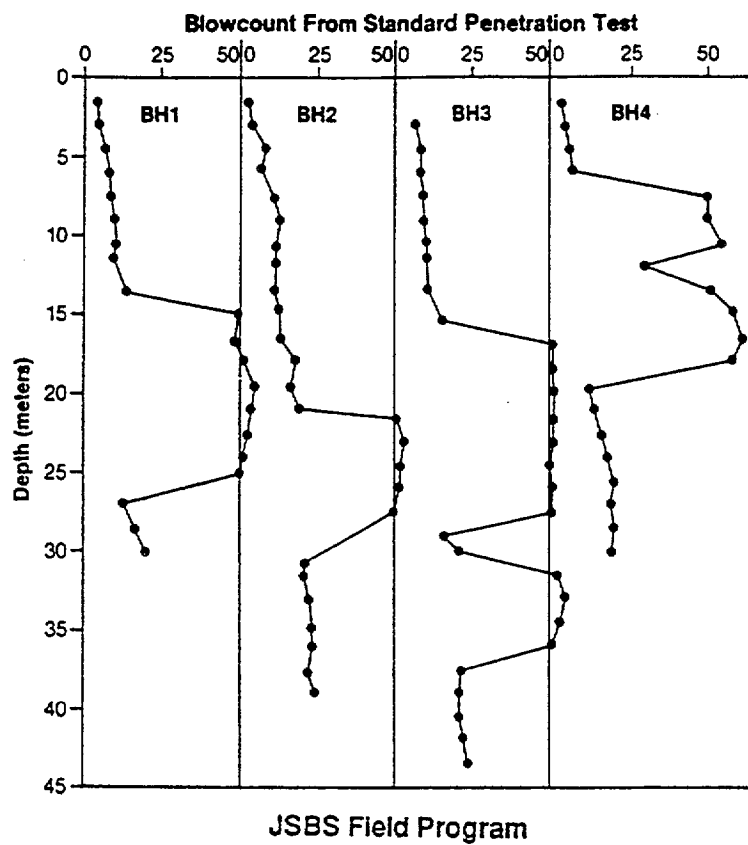
Fig. 2.6 SPT blowcounts recorded at Lotung test site. (Anderson, 1993)
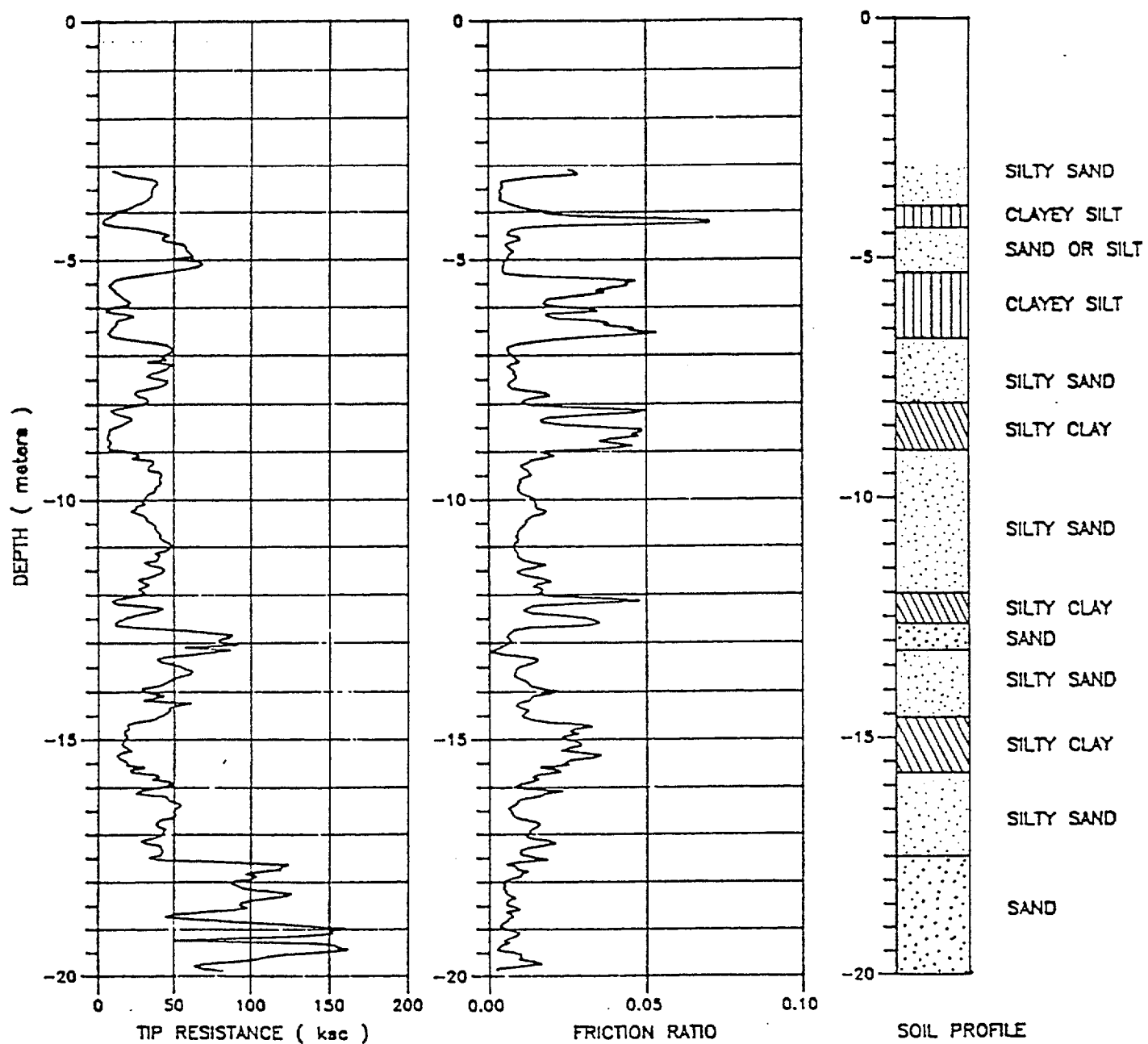
Fig. 2.7 Cone tip resistance, friction ratio and estimated soil profile, CPT1. (Anderson, 1993)

DEPTH (meters)

TIP RESISTANCE (ksc)

FRICTION RATIO

SOIL PROFILE

SILTY SAND
CLAYEY SILT
SILTY SAND
CLAYEY SILT
SILTY SAND
SILTY CLAY
SILTY SAND
SILTY CLAY
SAND
SILTY SAND
SILTY CLAY
SILTY SAND
SAND
SILT
SAND
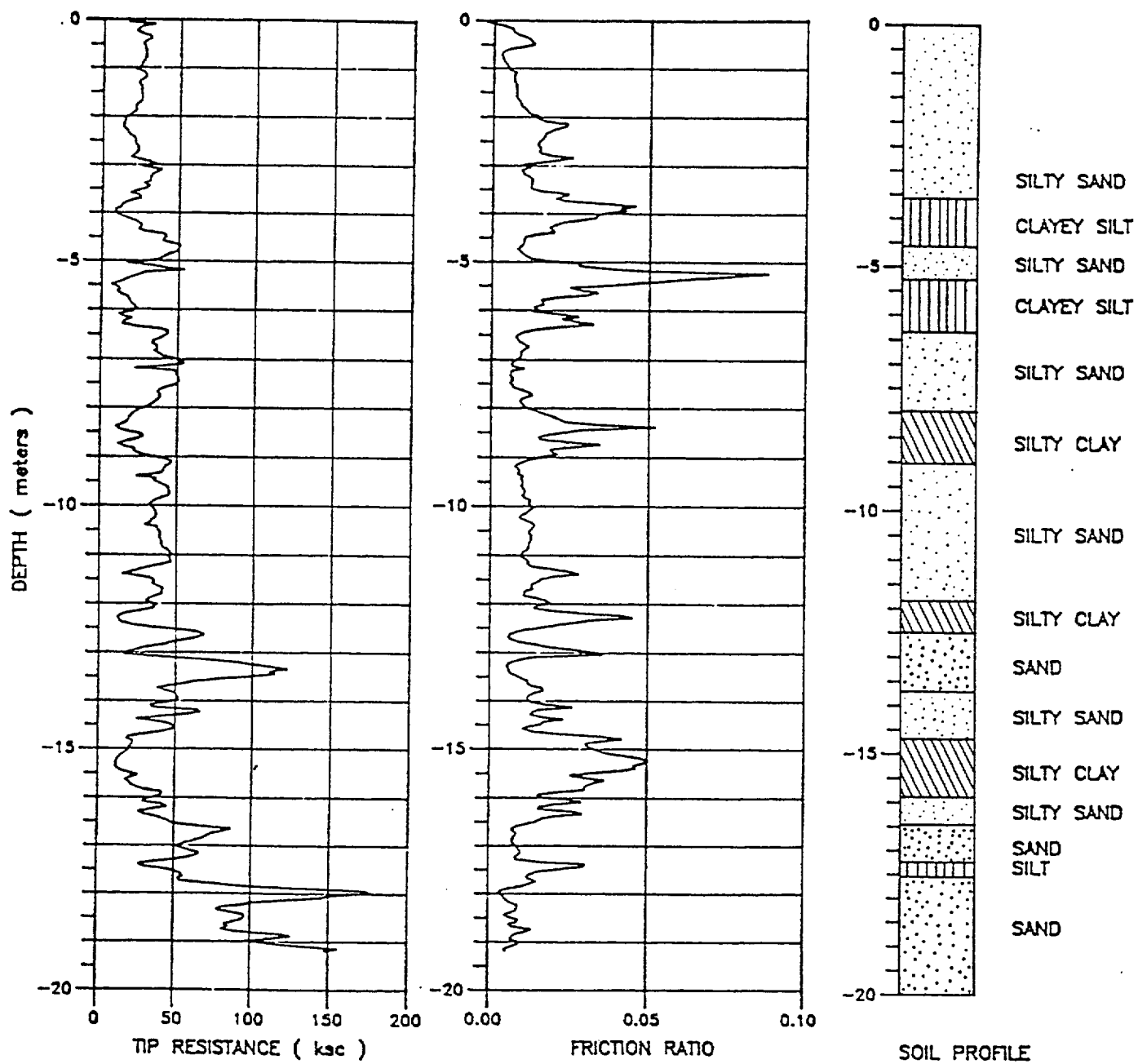
Fig. 2.8 Cone tip resistance, friction ratio and estimated soil profile, CPT2. (Anderson, 1993)

2.4   Seismology

A summary of the properties of measured temblors is given in Table 2.1.   The epicenters for these events is shown on the map presented in Fig. 2.9. Events 4, 12, and 16 will be considered "large" events, with peak accelerations over 0.17 g. Events 12 and 16 were major events and have been discussed in detail (e.g. EPRI, 1989; Chang et al., 1991a, b; Anderson, 1993). Of these four large events, temblors 7 and 16 were deep focus events, and event 12 was an event occurring nearby and near the surface. Event 8, although a low acceleration event, is of special interest as it was an immediate aftershock of event 7.

Examination of the Arias Intensity (Arias, 1970) for the events considered produces a different picture of the energy absorbed by the site for each earthquake. The Arias intensities for the Lotung temblors are given in Table 2.1, where it is seen that events 16, 12, 4, and 7 are the most energetic. The Arias Intensity, I_a, is defined as

$$I_a = \frac{\pi}{2g} \int_0^\infty [a(t)]^2 dt, \tag{2.1}$$

Where a is the acceleration time history. Whereas peak acceleration is simply the amplitude of the largest peak during the strong motion, Arias Intensity considers not only the amplitude of the acceleration but the duration and frequency content as well. Therefore Arias Intensity is a fuller measure of the disturbance at a given site.

A reasonable assumption is that dynamic soil behavior is a function of excitation energy. This assumption has recently been supported by many careful experimental studies (e.g. Figueroa et al., 1994). The Arias Intensity is directly proportional to the energy input into the soil during earthquake excitation. In an attempt to normalize results to locally specific conditions, Arias Intensity and peak input acceleration will be used as a measure of event energy.

2.5   Pore Pressure Generation

Over the history of the Lotung experiment, more than 30 pore water pressure transducers were installed at the site (Shen et al., 1987). The location of these sensors in relation to the three-

arm surface array is shown in Fig. 2.10. The soil conditions at several pertinent locations are given in Table 2.2. As reported by Shen et al. (1987), most of the sensors ailed due to mechanical problems. However, several remained in operating condition and were triggered by events 12, 16, and 17.

A typical pore pressure record is shown in Fig. 2.11 in relation to the acceleration time history. Information as to in situ pore pressure and increase for each sensor for events 12, 16, and 17 are given in Tables 2.4 and 2.5, with the time histories from events 12 and 16 are given in Appendix C.

Table 2.1 Properties of the recorded LSST series of earthquakes.

Event	Epicentral Distance (km)	Focal Depth (km)	Local Magnitude	Peak Acceleration	Arias Intensity (m/s)
2	-	-	5.3	0.03	-
3	-	-	5.5	0.01	74
4	-	-	6.5	0.49	1845
5	-	-	-	0.04	73
6	31.4	0.9	5.4	0.04	126
7	66.2	15.8	6.5	0.21	652
8	69.2	21.8	6.2	0.03	139
9	5.0	1.1	4.5	0.07	192
10	6.1	0.9	4.5	0.04	36
11	6.0	2.0	5.0	0.10	-
12	5.2	1.6	6.2	0.20	2710
13	-	-	6.2	0.05	161
14	-	-	4.9	0.05	124
15	-	-	-	0.05	386
16	77.9	6.9	7.0	0.17	3995
17	-	-	-	0.04	310
18	-	-	-	0.03	91
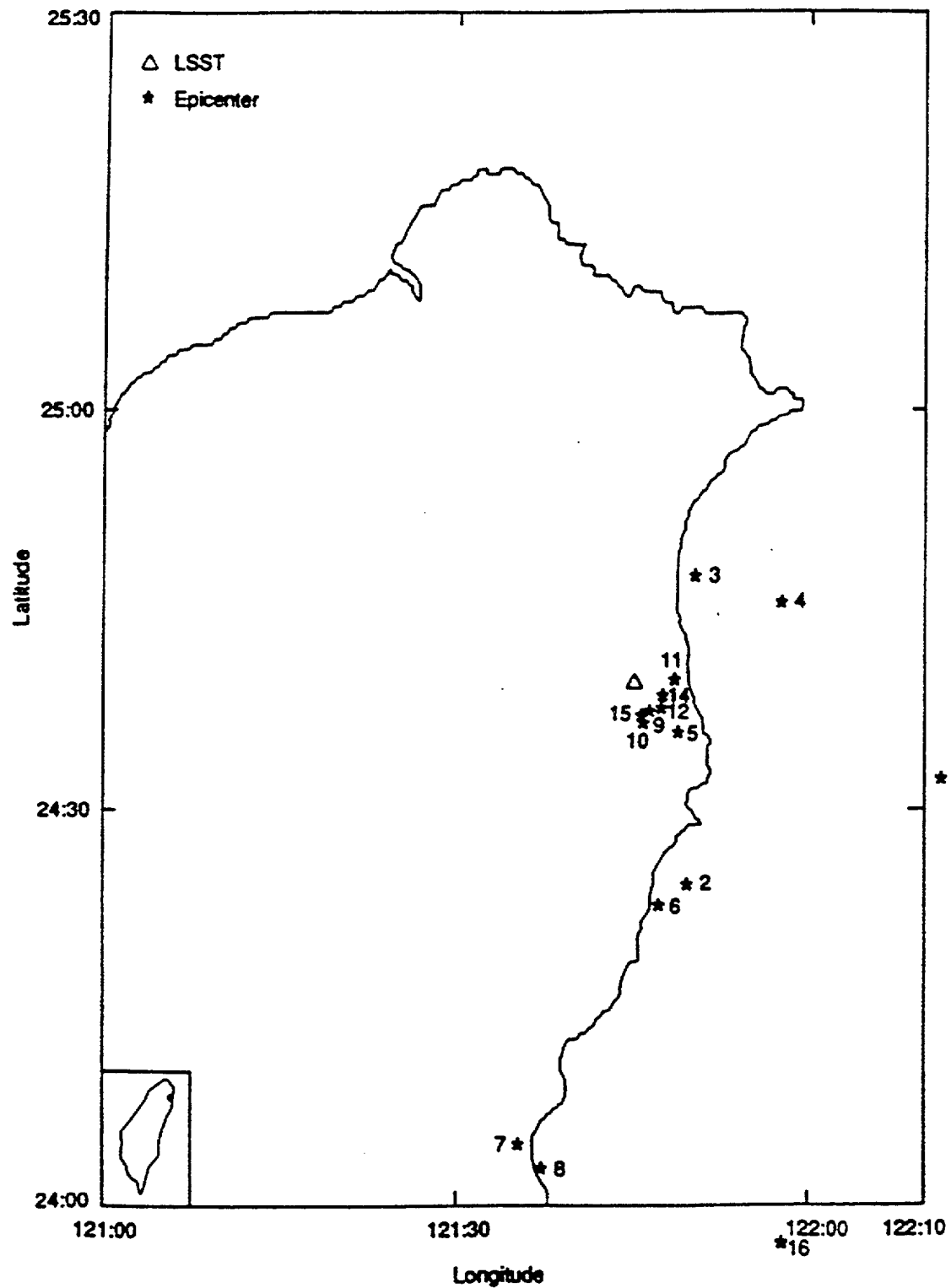
Note: The epicentral locations for Events LSST Nos. 13, 17 and 18 were not determined.

Fig. 2.9 Locations of the epicenters for Lotung seismic events 1 through 18. (Tang et al., 1992)
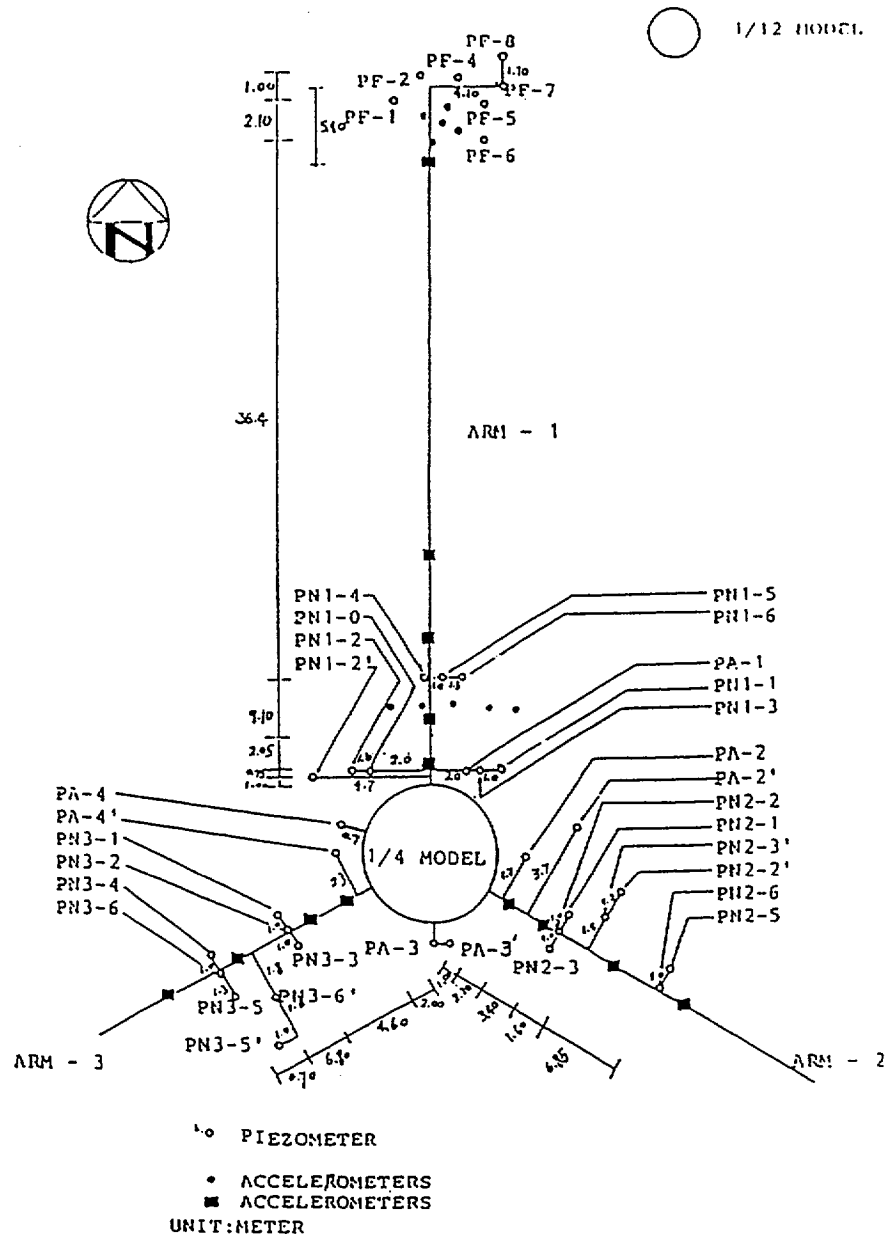
Fig. 2.10 Location of the pore water pressure sensors at the Lotung test site. (EPRI, 1989)

17

Table 2.2 Soil conditions at the locations of pore water pressure sensors. (EPRI, 1989)

PA-1	W(%)	PF-1	W(%)	PF-5	W(%)
F = 15.2 SM+G	7.8	F = 10.9 SM-SC	12.4	F = 92.7 SM	33.3
CH 1 D = 5.06M T = ML F =68.5% R = 9	37.8	CH 5 D = 3.25M T = ML F = 56.3% R = 18	40	CH 9 D = 12.0M T = ML F = 65.5% R = 3	31.6
F = 14.6 SM		F = 50.2 ML	27.0	F = 26.9 SM	21.9

PN1-0	W(%)	PN1-1	W(%)	PF-2	W(%)
F = 10.9 SM+G	12.4	F = 15.2 CL	7.8	F = 92.4 CL-ML	40
CH 11 D = 3.16M T = ML F = 92.4% R = 5.5	40	CH 12 D = 6.03M T = SM F = 43.8% R = 25.5	37.8	CH 6 D = 6.05M T = ML F = 50.2% R = 4	68
F = 50.2 ML-CL	27.0	F = 14.6 SM	24.3	F = 57.0 CL-ML	32.3

PN2-1	W(%)	PA-3'	W(%)	PN3-1	W(%)
F = 10.1 SM	15.9	F = 8.6 SM+G	7.2	F = 47.6 SM-SC	21.4
CH 18 D = 6.30M T = SM F = 19.5% R = 16.5 (23)	14.6	CH 21 D = 5.10M T = SM+G F = 32.0% R = 17 (20.4)	21.5	CH 24 D = 6.30M T = SM F = 39.9% R = 12 (12.4)	32.7
F = 42.7 SM	28.3			F = 64.9 ML	31.2

PN3-2	W(%)			PN2-2'	W(%)
F = 97.3 CL	34.3			F = 10.1 SM	15.9
CH 29 D = 11.0M T = ML F = 68.6% R = 3	31.2	W: water content F: fine-grained fraction R: Δu/u₀ (%) D: depth of sensor T: soil type		CH 23 D = 8.00M T = SM F = 19.5% R = 4.3	14.6
F = 31.7 SM	35.8			F = 42.7 SM	28.3

Legend:
- W: water content
- F: fine-grained fraction
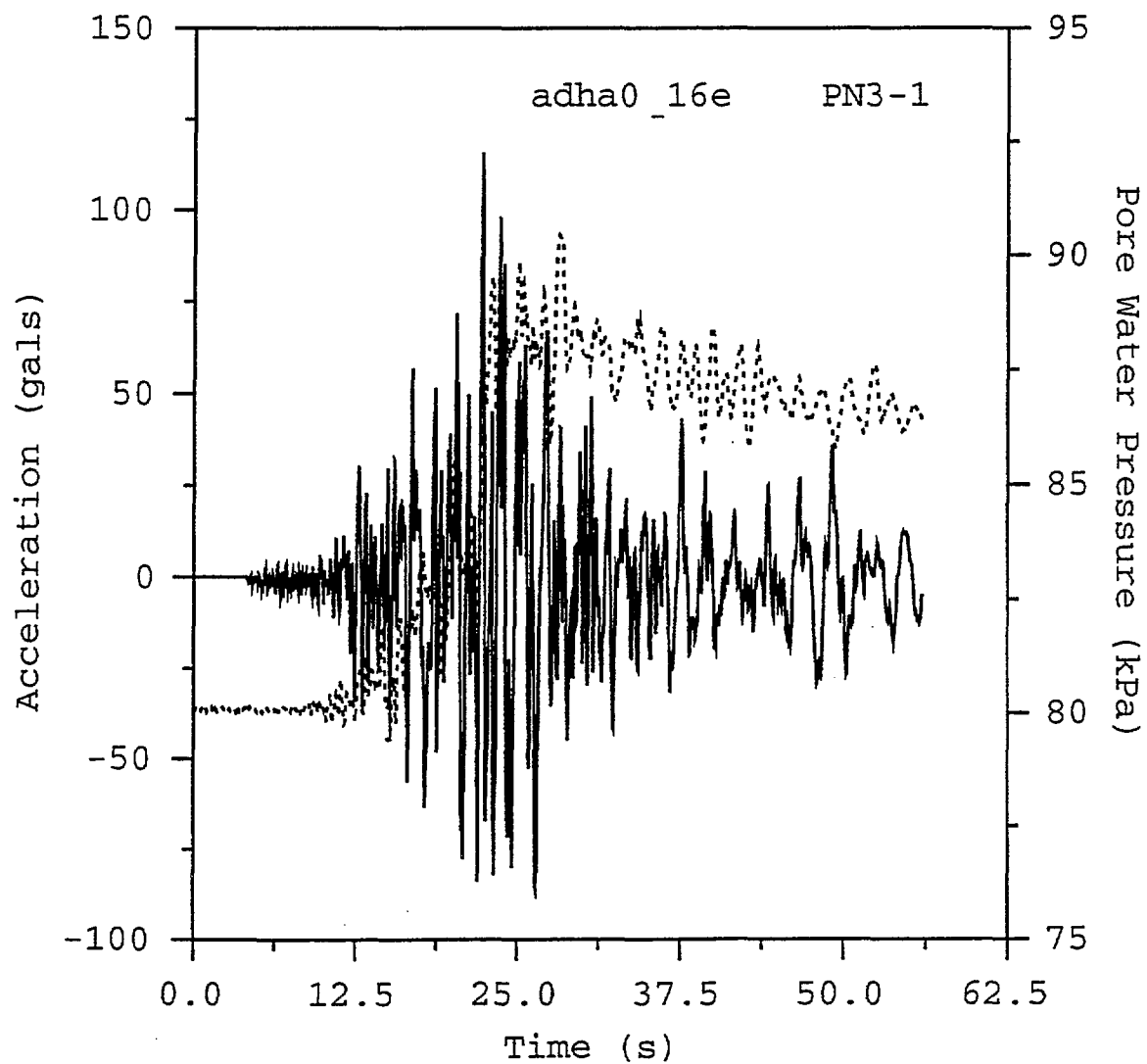- R: $\Delta u/u_0$ (%)
- D: depth of sensor
- T: soil type

Fig. 2.11 Typical pore pressure record from event 16, LSST. Depth = 6.38 m; initial hydrostatic pressure = 72.6 kPa; increase in pore water pressure = 8.68 kPa.

Table 2.3 Peak pore water pressures, event 12. (Tang et al., 1992)

Sensor No.	Channel No.	Depth, h (m)	Event LSST12			
			$u_o^{(2)}$ (kPa)	$u_p^{(3)}$ (kPa)	$\Delta u^{(4)}$ (kPa)	File Name
PA-1	1	5.06	54.60	59.90	5.30	E12C01.PWP
PF-1	5	3.25	32.80	38.97	6.17	E12C05.PWP
PF-2	6	6.05	55.70	57.67	1.97	E12C06.PWP
PF-5	9	12.00	121.85	.126.14	4.29	E12C09.PWP
PN1-0	11	3.16	39.72	42.12	2.40	E12C11.PWP
PN1-1	12	6.03	61.30	78.35	17.05	E12C12.PWP
PN1-4	15	5.53	62.34	65.53	3.19	E12C15.PWP
PN2-1	18	6.30	62.12	73.36	11.24	E12C18.PWP
PA-3'	21	5.10	56.15	69.88	13.73	E12C21.PWP
PN3-1	24	6.38	72.60	81.28	8.68	E12C24.PWP
PN3-2	29	11.00	116.60	123.41	6.81	E12C29.PWP

Notes: (1) This table was modified from reference (2).
(2) u_o - Hydrostatic pressure based on initial readings of the · recordings.
(3) u_p - Recorded peak pore water pressure.
(4) $\Delta u = u_p - u_o$ - Peak induced pore water pressure.

Table 2.4 Peak pore water pressures, event 16. (Tang et al., 1992)

Sensor No.	Channel No.	Depth, h (m)	Event LSST16			
			$u_o^{(2)}$ (kPa)	$u_p^{(3)}$ (kPa)	$\Delta u^{(4)}$ (kPa)	File Name
PF-8	17	15.00	114.60	135.35	20.75	E16C17.PWP
PN2-1	18	6.30	66.90	83.60	16.70	E16C18.PWP
PA-3'	21	5.10	56.30	68.74	12.44	E16C21.PWP
PN2-2'	23	8.00	97.20	106.61	9.41	E16C23.PWP
PN3-1	24	6.38	80.10	90.44	10.34	E16C24.PWP

Notes: (1) This table was modified from reference (2).
      (2) u_o - Hydrostatic pressure base on initial readings of the recordings.
      (3) u_p - Recorded peak pore water pressure.
      (4) Δu - u_p - u_o - Peak induced pore water pressure.

Table 2.5 Peak pore water pressures, event 17. (Tang et al., 1992)

Sensor No.	Channel No.	Depth, h (m)	Event LSST17			
			$u_o^{(2)}$ (kPa)	$u_p^{(3)}$ (kPa)	$\Delta u^{(4)}$ (kPa)	File Name
PF-8	17	15.00	114.60	128.73	14.13	E17C17.PWP
PN2-1	18	6.30	66.90	72.77	5.87	E17C18.PWP
PA-3'	21	5.10	56.30	61.08	4.78	E17C21.PWP
PN2-2'	23	8.00	97.20	101.92	4.72	E17C23.PWP
PN3-1	24	6.38	80.10	84.48	4.38	E17C24.PWP

Notes: (1) This table was modified from reference (2).
(2) u_o - Hydrostatic pressure based on initial readings of event LSST16 recordings.
(3) u_p - Recorded peak pore water pressure.
(4) $\Delta u = u_p - u_o$ - Peak induced pore water pressure.

2.6 Some Previous System Identification Studies of the Lotung Site.

2.6.1 Zeghal et al.

Zeghal et al., (1995) used cross-spectral analysis of the data set to calculate resonant frequencies up to the twelfth mode of vibration for the LSST site as a whole. The study showed consistent values for the six earthquakes used for the analysis. Elgamal et al. (1995) in a companion paper document a technique for evaluating the soil shear stress-strain histories directly from the downhole acceleration records using linear interpolation between downhole accelerometers. They use the results of the calculation to estimate the soil damping at different depths as a function of strain amplitude.

Zeghal et al. (1995) estimated shear moduli and modal damping for a full suite of events, the results of which are included in Appendix D. Shear moduli were estimated for low-energy events (e.g. Events 5, 10, 13) to be 46 MPa for the 6 m depth, 63 MPa for the 11 m depth, and 69 MPa for the 17 m depth.

Zeghal et al. (1995) found much more scatter in their estimates of damping than for shear modulus, as expected from theory (this will be discussed in detail in Chapter 3), especially for low strain ($< 3 \times 10^{-3}$%). Damping was also found to be at or above the commonly accepted values put forth by Seed and Idriss (1970). For Event 16, which generated an excess pore water pressure equal to about 25% of the effective overburden stress, the shear modulus reduction was about 14 to 17%.

2.6.2 Chang et al.

Chang et al. have undertaken a series of studies of Lotung using parameter identification to evaluate the non-linear response of soils due to strong motion (Chang et al., 1991b, 1990, 1989). The first phase of the work concentrated on calculating a transfer function for the soil at several different points of the excitation history. The strong motion record was divided in three sections: (1) initial motion before strain levels high enough to degrade the soil was reached, (2) peak motion,

and (3) the coda or ring-down. The transfer functions were estimated from the ratios of smoothed output Fourier spectra and input spectra from various depths.

The shear moduli showed a marked decrease from the initial low-level excitation to peak deformation. Depending on the depth used as input, the modulus reduction factor ranged from 0.60 to 0.14. These values are for a magnitude 6.5 earthquake exhibiting a peak horizontal acceleration of 0.21 g. As a check on reality, the S-wave amplitudes for the initial segment were in very good agreement with the actual measured values. A troublesome point is the large discrepancy in modulus reduction factor for the two horizontal components. The expectation is that they would be virtually identical, since soil degradation is usually thought of as a scalar quantity.

The results from the forward propagation non-linear DESRA-2 (Lee and Finn, 1985) analysis show good agreement between actual and calculated displacement for frequencies up to about 6 Hz. There was also good correlation for phase angle for frequencies up to about 3 Hz. The shape of the equivalent damping ratio curve back-calculated from the non-linear analysis is different from that normally expected. Rather than the expected hyperbolic curve, the field curve is S-shaped. This uncommon S-shaped curve is the same shape as that calculated by Abdel-Ghaffar and Scott (1979) from actual field data.

Further work on the shear modulus reduction curve based on actual large strain measurement is reported by Chang et al. (1991b), using shearing strains calculated by SHAKE. The results show that for small strains (surface acceleration < 0.03 g), the results from geophysical methods, resonant column, and system identification are in good agreement. For intermediate strains (5×10^{-3} to 2×10^{-2}) the back calculated values for modulus reduction are up to twenty percent lower than the resonant column measurements. For higher strains of 3×10^{-2} to 2×10^{-1}, the results from cyclic triaxial tests are in fair agreement with the field values for shear modulus, with moderated scatter for the laboratory data.

CHAPTER 3 - PROCEDURES FOR SYSTEM IDENTIFICATION

3.1   System Identification

3.1.1   Parametric Modeling

The goal of system identification is to model a system in a manner that provides needed mechanical information about that system. The most common techniques have evolved from electrical and mechanical engineering, and involve solving the inverse problem for the system transfer function. Each method has limitations; in the words of G. E. P. Box, "All models are incorrect, but some are more useful than others."

The process of inversion allows the estimation of the system response function (filter) if the input and output signals are known. A simple model for characterizing a system is as a parametric relationship between system input and output. Such a model, referred to as an autoregressive-moving average (ARMA) model, is based on discrete time series analysis:

$$y_t = a_1 y_{t-1} + a_2 y_{t-2} + \ldots + b_0 x_t + b_1 x_{t-1} + \ldots \equiv \left(\sum_{j=0}^{nb} b_j x_{t-j} + \sum_{k=1}^{na} a_k y_{t-k} \right) \quad (3.1)$$

where y_j is the actual output data sequence, x_j is the input sequence (assume white noise for simple spectral estimation), na and nb are the AR and MA orders, respectively, and the subscript is the time step counter. The output is seen as a combination of the input history acted upon by the "b" coefficients plus the past outputs acted upon by the "a" coefficients. The input series, involving the "b" coefficients, is a causal moving average (MA) process (convolutional). The series involving weighted past output values ("a" coefficients) is a noncausal autoregressive (AR) process. The lengths of the AR and MA processes (model order) must be explicitly chosen so that the model best represents the process.

Applying the shifting theorem to Eq. 3.1. yields the Fourier transform (Bracewell, 1978)

$$Y_\omega (1 + a_1 e^{i\omega} + a_2 e^{2i\omega} + \ldots) = X_\omega (b_0 + b_1 e^{i\omega} + b_2 e^{2i\omega} + \ldots) \quad (3.2)$$

where i is $\sqrt{-1}$ and ω is circular frequency. Applying the Z-transform (Bracewell, 1978), where $z^k = e^{ki\omega}$, and rearranging, yields the frequency domain transfer function H_ω

$$H_\omega = \frac{Y_\omega}{X_\omega} = \frac{b_o + b_1 z^1 + b_2 z^2 + \ldots}{1 - a_1 z^1 - a_2 z^2 + \ldots} \tag{3.3}$$

The ARMA model is very powerful in that it can easily model sharp drops, sharp peaks, and smooth spectral behavior. It is also the most parsimonious estimator (Robinson, 1982), describing a complex process with very few parameters calculated from a small length of data. Parametric modeling avoids many of the difficulties inherent in the traditional Fourier methods, discussions of which can be found in many books and journals (e.g., Glaser, 1993; Johansson, 1993; Pandit, 1991). Extensions of this model, e.g., ARMAX, ARX, Box-Jenkins, allow input, system, and output noise to be expressly modeled (Ljung, 1987). In particular, the ARX model includes the effect of uncertainties and noise as a white noise term.

The ARMA model has special significance since it can be derived directly from the differential equation of motion for an N-degree-of-freedom (DOF) system, with the damping ratio and resonant frequency as the model parameters (e.g., Gersch and Luo, 1970). A $2n$-$2n$ ARMA model is therefore a valid model for a layered soil system, or soil-structure interaction problem. The damping ratio and resonant frequency of the N-degree-of-freedom oscillators are contained in the $2n$ AR parameters. Phase relations are preserved in the MA parameters. The modal frequencies ξ_j, percent of critical damping ω_j, (Ghanem et al., 1991) and power participation factor p_j (Pandit, 1991; Safak, 1988) are calculated from the system poles and residues found from partial-fraction expansion of Eq. 3.3. The modal parameters are defined as

$$\omega_j = \frac{\sqrt{\lambda_j^2 + \delta_j^2}}{\Delta t} \tag{3.4}$$

$$\xi_j = \frac{\delta_j}{\sqrt{\lambda_j^2 + \delta_j^2}} \tag{3.5}$$

$$p_j = -r_j \operatorname{conj}(z_j) - z_j \operatorname{conj}(r_j) \tag{3.6}$$

where $\lambda = \text{Arg}(z_j)$, $d_j = -(0.5)\ln|z_j|^2$, z_j is the pole for mode j, r_j is the residue for mode j, and Δt is the digitization rate.

3.1.2 Adaptive (recursive) model estimation

Traditional methods of system estimation, both parametric and non-parametric, are strictly valid only for stationary data. A stationary signal is one whose statistics do not change with time. The commonly invoked, loose definition of stationarity requires that the variance of the signal be constant over any and all time windows. Inherent in the Fourier transformation of a time series to the frequency domain is the averaging of the signal components over the sampling period T. A piece of time is frozen over this period and the assumption made that all time before and after is the same, i.e. repeated forever. The energies present at each component frequency are integrated over the entire time period T.

The difficulty with non-stationary signals is that these energies are changing during this period. If the frequencies present are changing over this time window, the resulting estimation, regardless of method used, will be a smeared average as if all the frequencies with a given energy were active throughout the entire period. For weakly non-stationary processes, the effect over a small time period is unimportant. If needed, the signal can be cut into relatively stationary sections and spectra found using methods specially designed for short data segments, i.e. Burg's method.

The field of adaptive filtering was formed to model non-stationary processes. As the statistics of the signal change through time, the filter "adapts" to the changing variance with new parameters that reflect the structure of the system at that point. The predicted value for the next time step can be compared with the actual value, and the difference (referred to as innovations)

$$(y_t - \hat{y}_t)^2 \tag{3.7}$$

where y_t is actual output at time t, and $\hat{y}_t$ is the prediction of output at time t made at time $t\text{-}1$, will give a measure of how well the filter is doing its job. The term "innovations" is used because this information is new information that can not be predicted by the model at this particular step.

27

Autoregressive parameters can be sequentially estimated so that the parameters are adaptive to the changing nature of the process (Marple and Lawrence, 1987). The AR parameters are updated after each data point, tracking slowly non-stationary signals. A forgetting factor, commonly a damped negative exponential, is used so that older data carries less and less weight. A frequency domain estimation can be made at any time step by evaluating the AR parameters around the unit circle, giving the spectral representation of the behavior of the process at that time.

The most popular direct adaptive filter, or process model, is the so-called Kalman filter (Kalman, 1960; Kalman and Bucy, 1961). Sorenson (1970) points out that the Kalman approach is a direct descendant of Gauss's least squares, except now neither the signal nor the noise model must be stationary — the state may change from sample point to sample point. Nau and Oliver (1979) state that the Kalman filter is based on a dynamic AR model defined by "two concurrent random equations of motion":

$$x_t = H^T_{t-1}\Phi_t + a_t \tag{3.8}$$

the AR(p) equations of motion, and the "motions" of the parameters,

$$\Phi_t = \Phi_{t-1} + b_t \tag{3.9}$$

where p = number of prior observations utilized,
H_{t-1} = vector of p prior data observations $x_{t-1}, x_{t-2}, ..., x_{t-p}$,
Φ_t = vector of p AR parameters,
a_t = Gaussian white noise with 0 mean and variance σ^2
b_t = Gaussian white noise with 0 mean and covariance matrix Q.

Equation 9 estimates a value of Φ_t comprised of **p** previous parameters, through a random walk equation. The estimate uses the weighted **p** previous data points, and yields a new observation x_t when added to a new noise value. The least squares solution solves the equations so that the innovations (Eq. 3.7) — new, dynamic information that cannot be predicted — are minimized in a least squares sense each time step.

The theory behind the Kalman filter can be manipulated to yield the system parameters for the case where there is no *a priori* information about the noise, and even when there is no information about the input signal. The so-called extended Kalman filter has been very successfully applied to non-stationary (and non-linear) estimation problems (Ljung, 1979; Astrom and Eykhoff, 1971). The manner of application is actually straight-forward. The Kalman model is constantly updating its estimation of the dynamic process by examining the innovations. The dynamics can be due to a changing input or noise process, or it can be due to the system itself changing. The effect is a linearization between single time steps, but if the system is changing slowly compared to the time step used, the linearization is "invisible" and the non-linear behavior is well modeled.

3.2   Application of Parametric Models

Previous work sponsored by NIST (Glaser, 1995) demonstrated that the MATLAB software package (MathWorks, 1993) is ideally suited for manipulation, processing, and presentation of earthquake data. MATLAB is a matrix-based system which evolved from the LINPAC and EISPAC libraries commonly used for mainframe FORTRAN numerical analysis. Complex numerical problems can be speedily solved without programming in the traditional sense.

For this study, the standard routines contained in the MATLAB System Identification Toolbox (Ljung, 1993, 1987) allowed SI to be used as a tool accessible to the geotechnical engineer. Virtually every approach and algorithm encountered in the literature by the author could be duplicated rapidly and accurately. When run on an Silicon Graphics Indy workstation, all aspects of the analysis were quick enough to be interactive.

Analysis begins by determining if the event can be modeled as stationary segments. A recursive segmentation scheme, which attempted to break the data into segments with a chosen maximum variance (Ljung, 1987) is used. However, it is not possible to determine the "correct" variance a priori. In these cases a more direct method is used — the output simulated by the calculated system has to accurately model the actual measured output.

3.2.1 Choice of Model Order, and Validation

When possible the input-output data record is broken into segments based on a mechanistic understanding of the seismic event and soil behavior gained from study of the pore pressure behavior. Initially it is assumed that the various segments are basically stationary. If the stationary model can not accurately and parsimoniously simulate the segment output, a non-stationary recursive model is used. In addition, the appropriateness of the model is checked by insuring 99 percent confidence in both the whiteness of the residual autocorrelation function and the cross-correlation function between the input and output residuals (Bohlin, 1987).

The stationary SI algorithm uses a least squares estimation for the ARX model. It is necessary to estimate the number of parameters to be calculated, which is essentially estimating the degree of freedom of the soil system. There is no obvious answer to the degrees of freedom of the system, so several verification techniques are employed to insure that a proper model order is estimated. Model order is increased in $2n$-$2n$ steps corresponding to an additional degree of freedom each. The simulated output of the model is then compared with the actual output for congruence, and the fewest parameters needed to accurately characterize the system was chosen as the system model order. Examination of the pole and zero plot insures that excessive, overlapping parameters are not included (Ljung, 1987). If the segments proved non-stationary, they are analysed using a recursive Kalman filter technique that expressly accounts for non-stationarity (Ljung, 1987). The trade-off relative to the stationary ARMA algorithm is reduced certainty.

Each input/output pair was initially submitted to an overall algorithm that calculates the loss function (normalized sum of squared prediction errors, Eq. 3.7) versus model order for a suite of pre-selected model orders. A typical loss function plot is shown in Fig. 3.1, for Event 16, DHA 0-11 m. As is obvious from this plot, the waveforms only carry information from the first 3-4 modes (12-16 parameters) - there is very little improvement in estimation quality for more parameters. The results of the loss function calculation were compared with the model orders chosen by other criteria, in particular the Akaike information theoretic criterion (AIC) and Rissanen's minimum description length (MDL) tests, which gave the same results. The AIC looks for a model that minimizes the 'information distance' to the actual system. The MDL searches for

a model that minimizes the length of the description of the data, i.e. the most efficient model (Ljung,1987).

In most cases, the fits were excellent for a small number of parameters. An example is shown in Fig. 3.2 which shows the model and actual values of output for DHA Event 16, 0-11 m, NS component for a 2-DOF model (8 parameters). For this calculation, the rms error (unnormalized loss function) varied from 1.037 for the 2-DOF model to 1.018 for a 10-DOF model, indicating that no new information is presented by the more complicated models. In general, the match between actual and modeled outputs for all waveforms investigated were not fundamentally improved by using up to 40 parameters (10-DOF). Given that the data does not have an infinite signal-to-noise ratio, i.e. there is noise present from many sources including quantization, there is only a limited amount of information that can be taken from the data (e.g. Pierce, 1980; Shannon, 1949; Shannon and Weaver, 1949). Experience has shown that any estimate above the second mode is tenuous at best, although numerically we are only limited by computational power as to how many modes we want to calculate.

The decision-making process as to model choice will now be shown in detail. Figures 3.3 to 3.13 document the process of model selection for a rapidly converging choice. Figure 3.3 is a plot showing the input and output data set for DHA Event 12, 6 m to surface interval. From the similarity of the input and output time series we would expect that a relatively uncomplicated filter would describe the system. Figure 3.4 is the loss function plot for that interval. The steep drop in loss function between 4 and 8 parameters is another indication that a simple system description is expected. Figures 3.5, 3.6, and 3.7 show the comparison of model vs. actual output for 1-DOF, 3-DOF and 5-DOF systems, respectively. Examination of the curve fits for the various models indicates a slight improvement in fit between actual and estimated interval output with increasing model order, from 0.3459 to 0.3056. In fact, the change from the 3-DOF to the 5-DOF system only improves the match by 0.0055.

The residual analysis plots for the same models, shown in Figs. 3.8 - 3.10, also demonstrate that no additional statistically significant information is being extracted beyond the 3-DOF system. Comparison of Figures 3.11-12, the pole-zero plots for the 3-DOF and 5-DOF models, show that
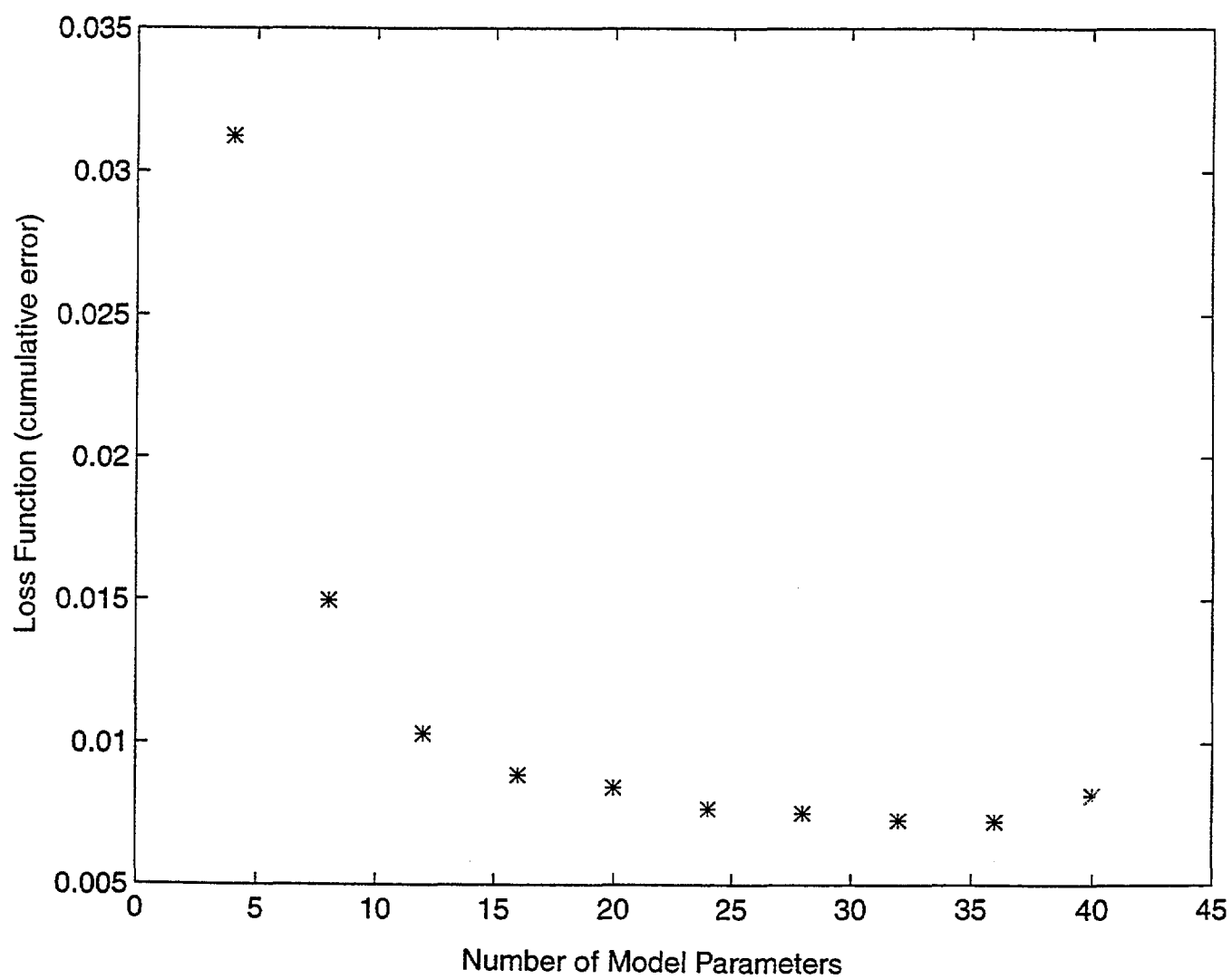
Figure 3.1   Loss function versus number of modal parameters used to model Event16 N-S, DHA,
0 - 11 meters depth interval.
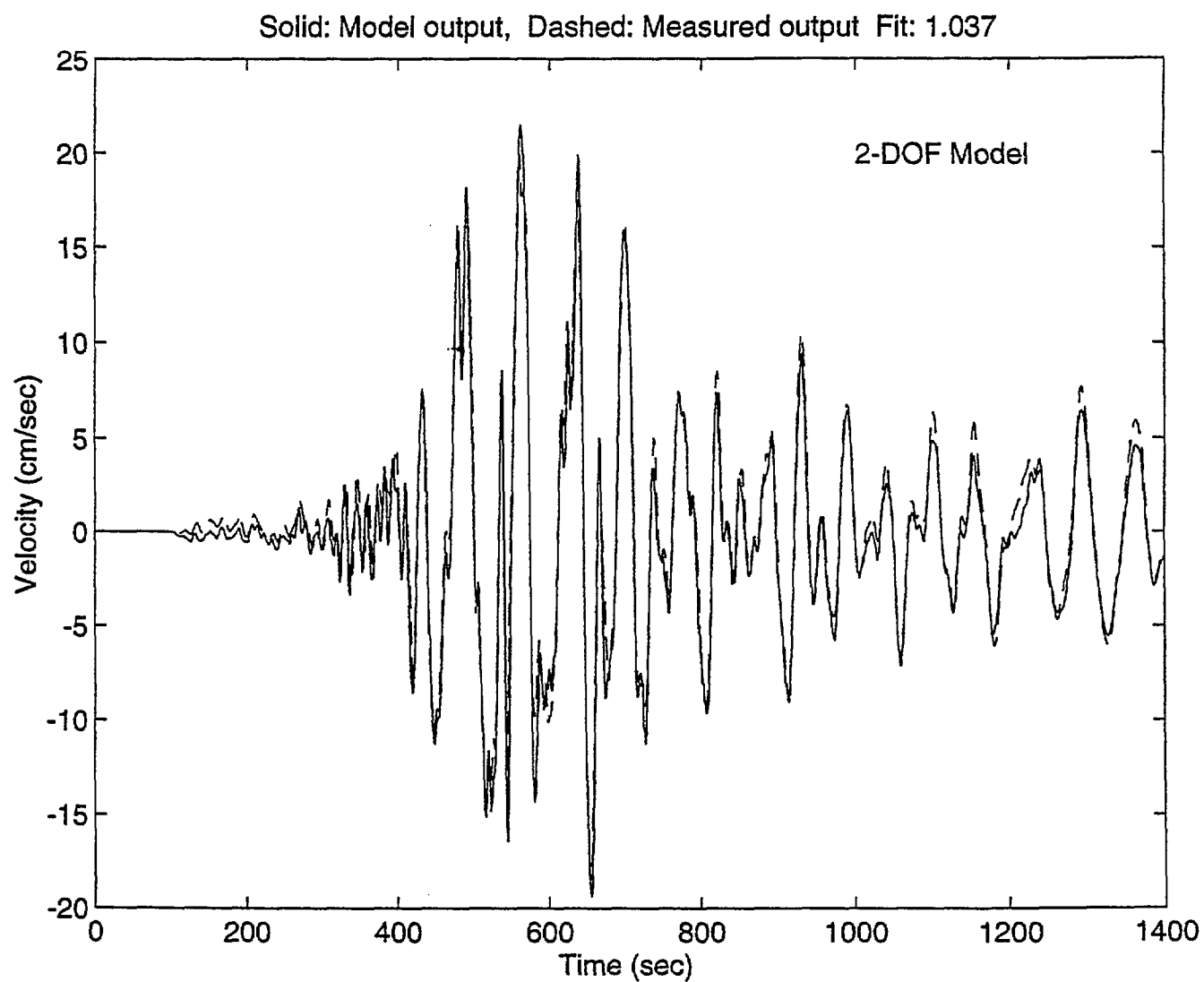
Figure 3.2 Comparison of actual and modeled output for Event16 N-S, DHA, 0 - 11 meters depth
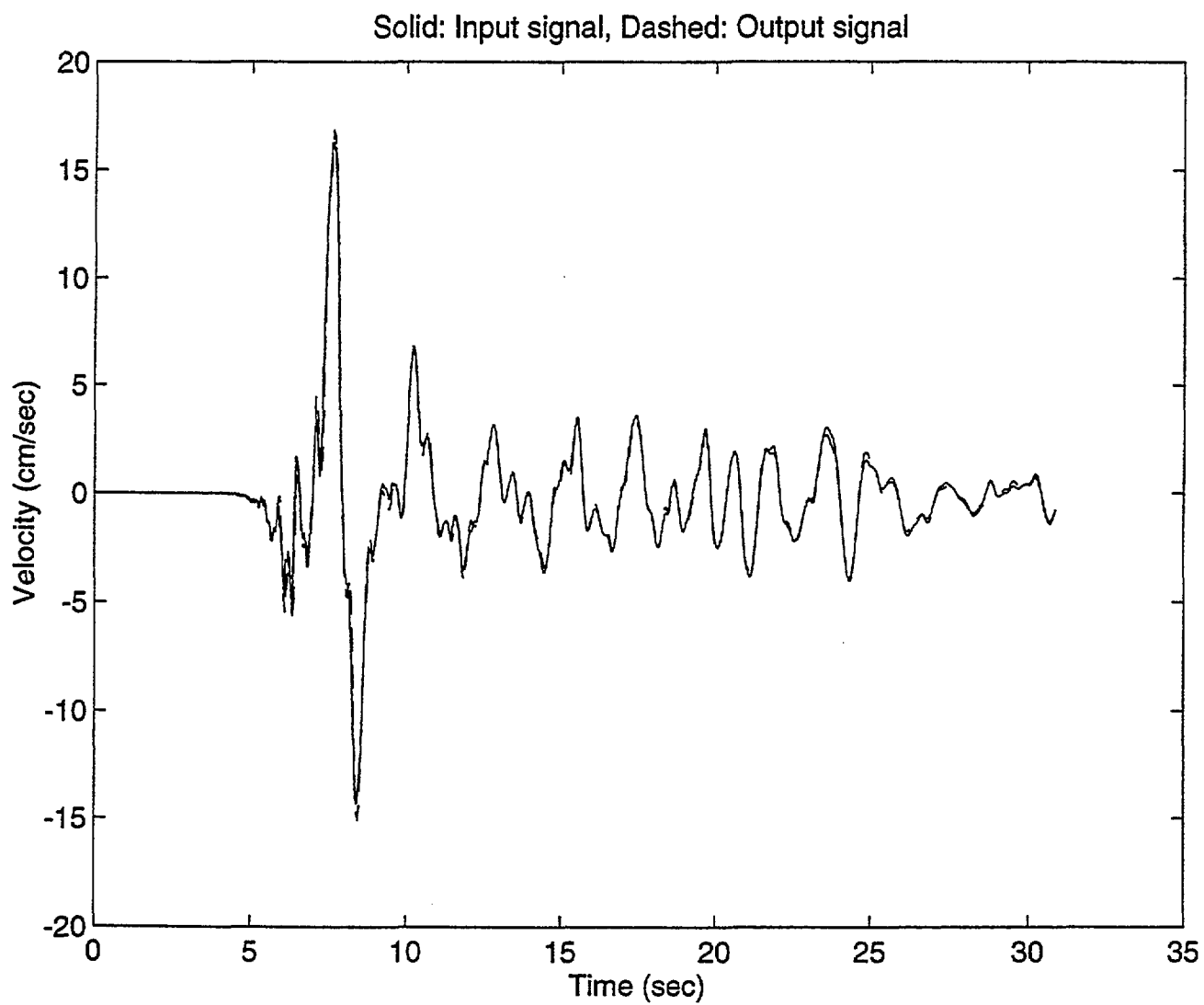   interval.

Figure 3.3 Comparison of actual signal input and output for Event16 N-S, DHA, 0 - 6 meters depth
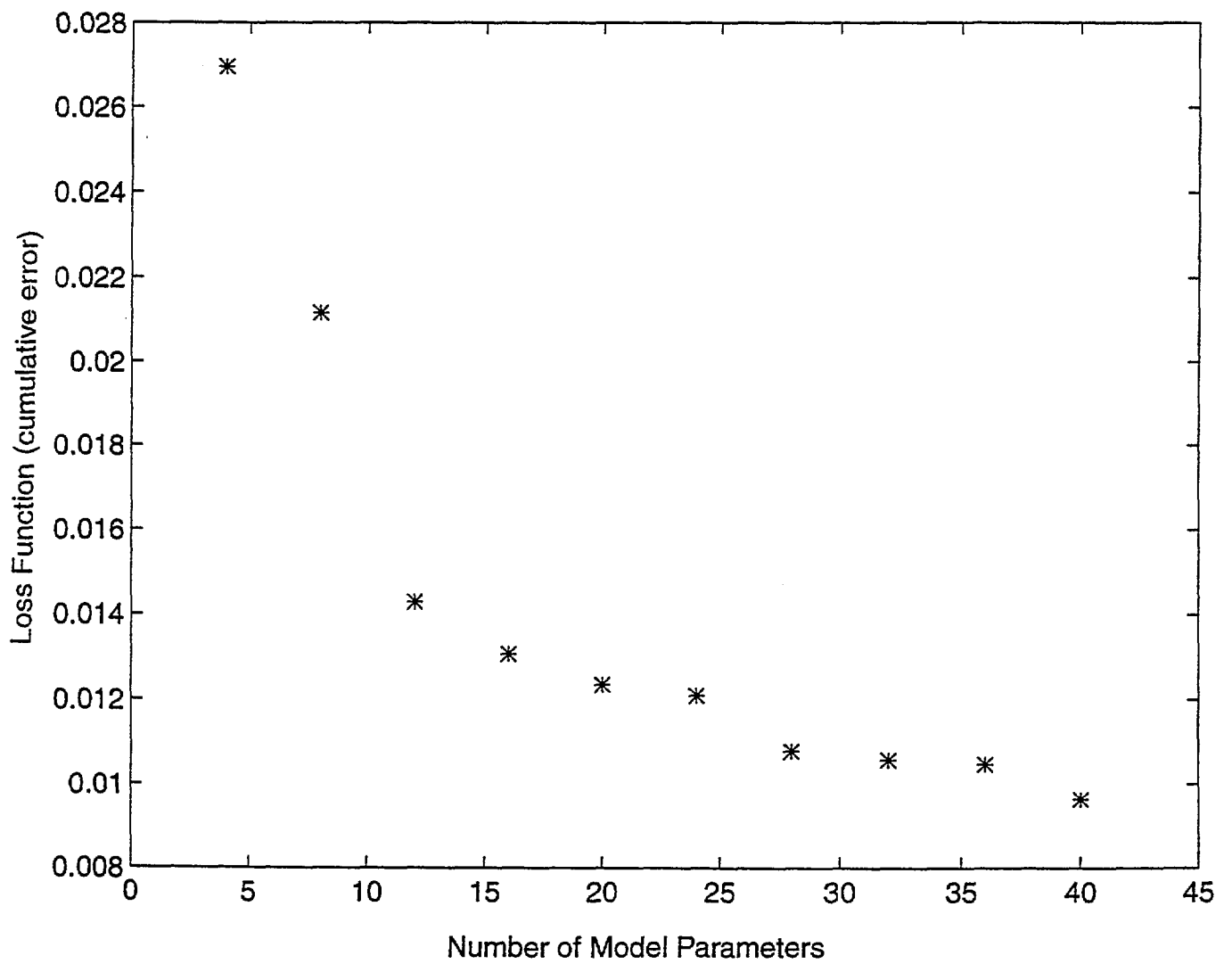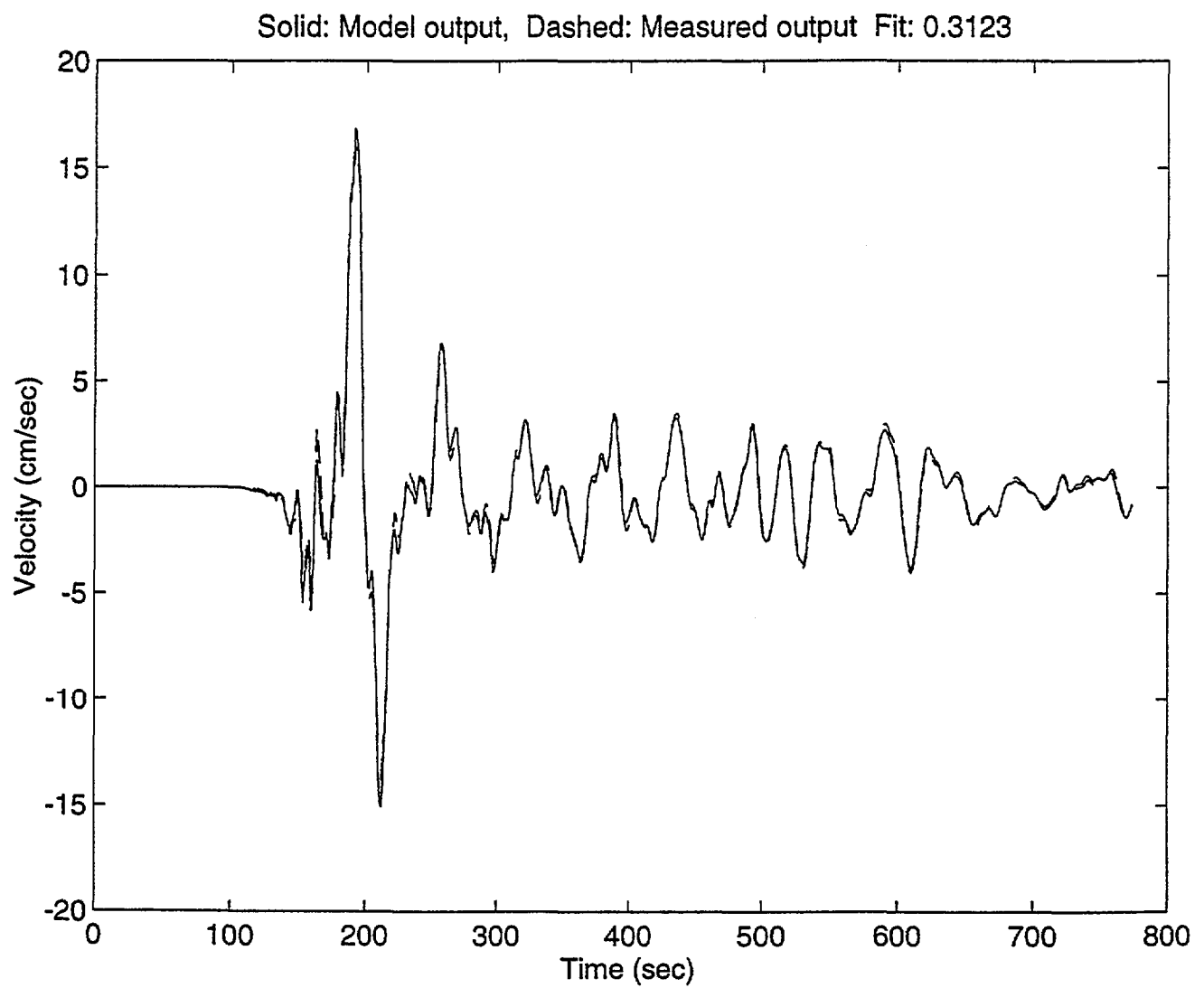interval.

Figure 3.4 Loss function versus number of modal parameters used to model Event12 N-S, DHA, 0 - 6 meters depth interval.

Figure 3.5   Actual versus 1 - DOF model output for Event12 N-S, DHA, 0 - 6 meters depth interval.

Solid: Model output, Dashed: Measured output Fit: 0.3367
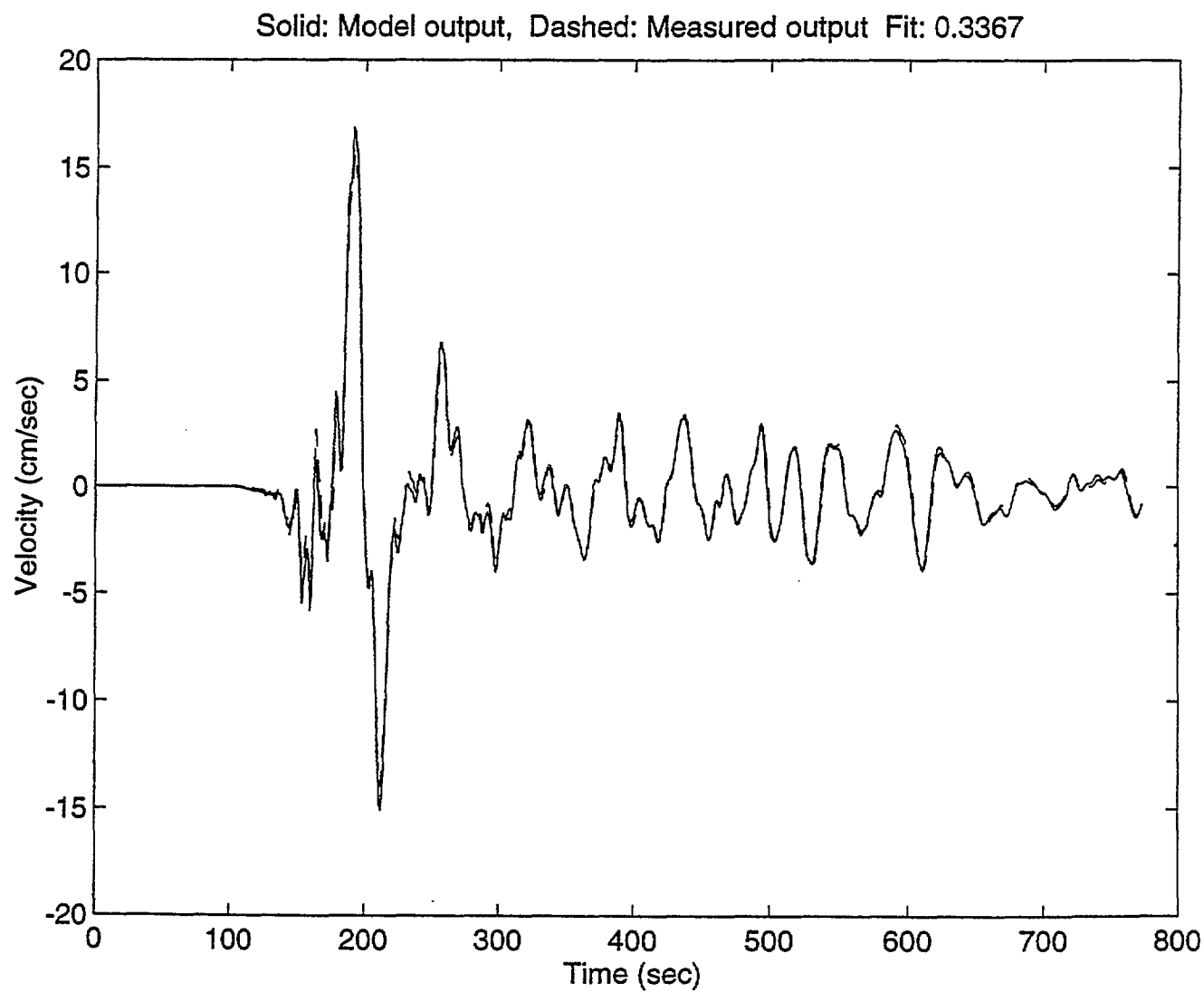
Figure 3.6   Actual versus 3 - DOF model output for Event12 N-S, DHA, 0 - 6 meters depth
interval.
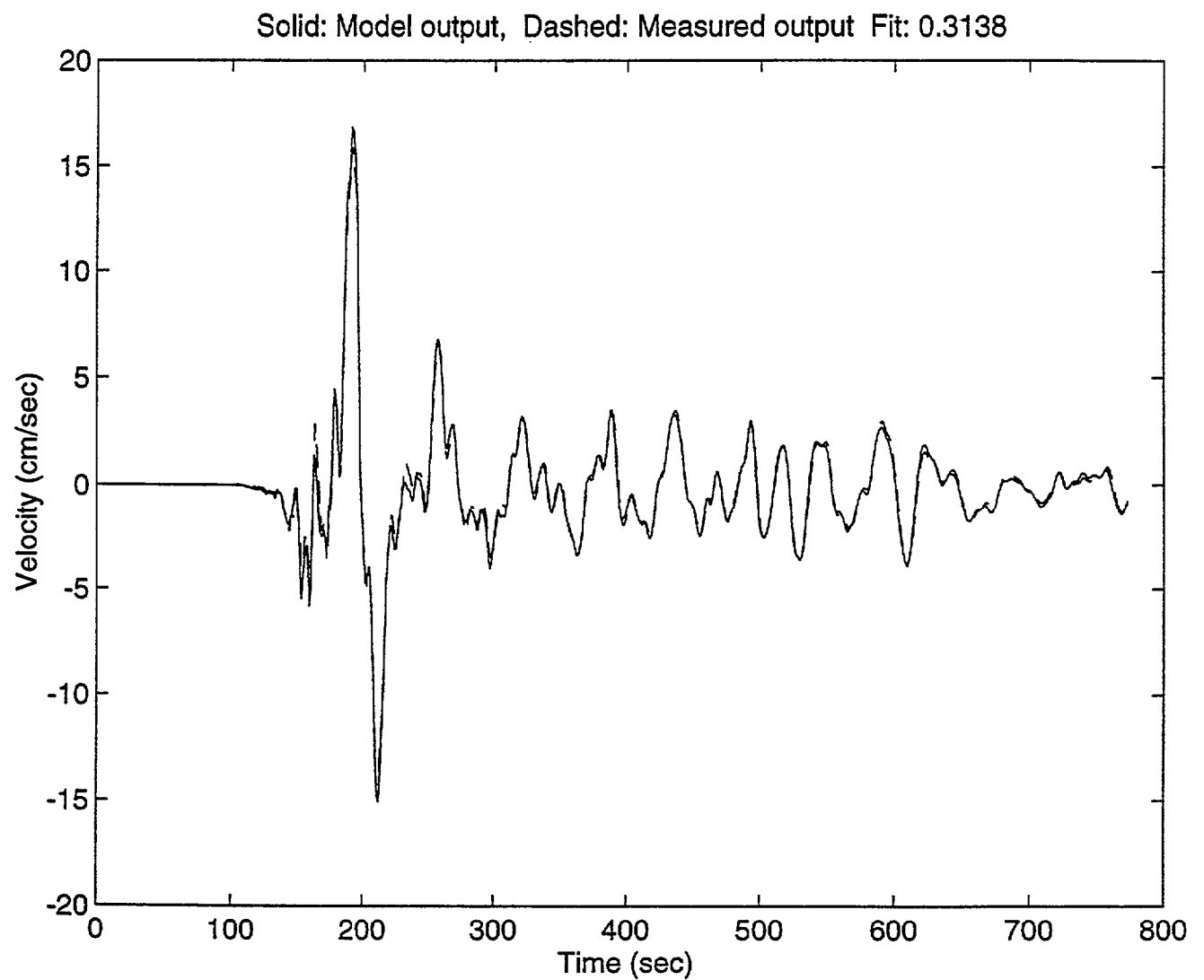
Figure 3.7   Actual versus 5 - DOF model output for Event12 N-S, DHA, 0 - 6 meters depth
interval.
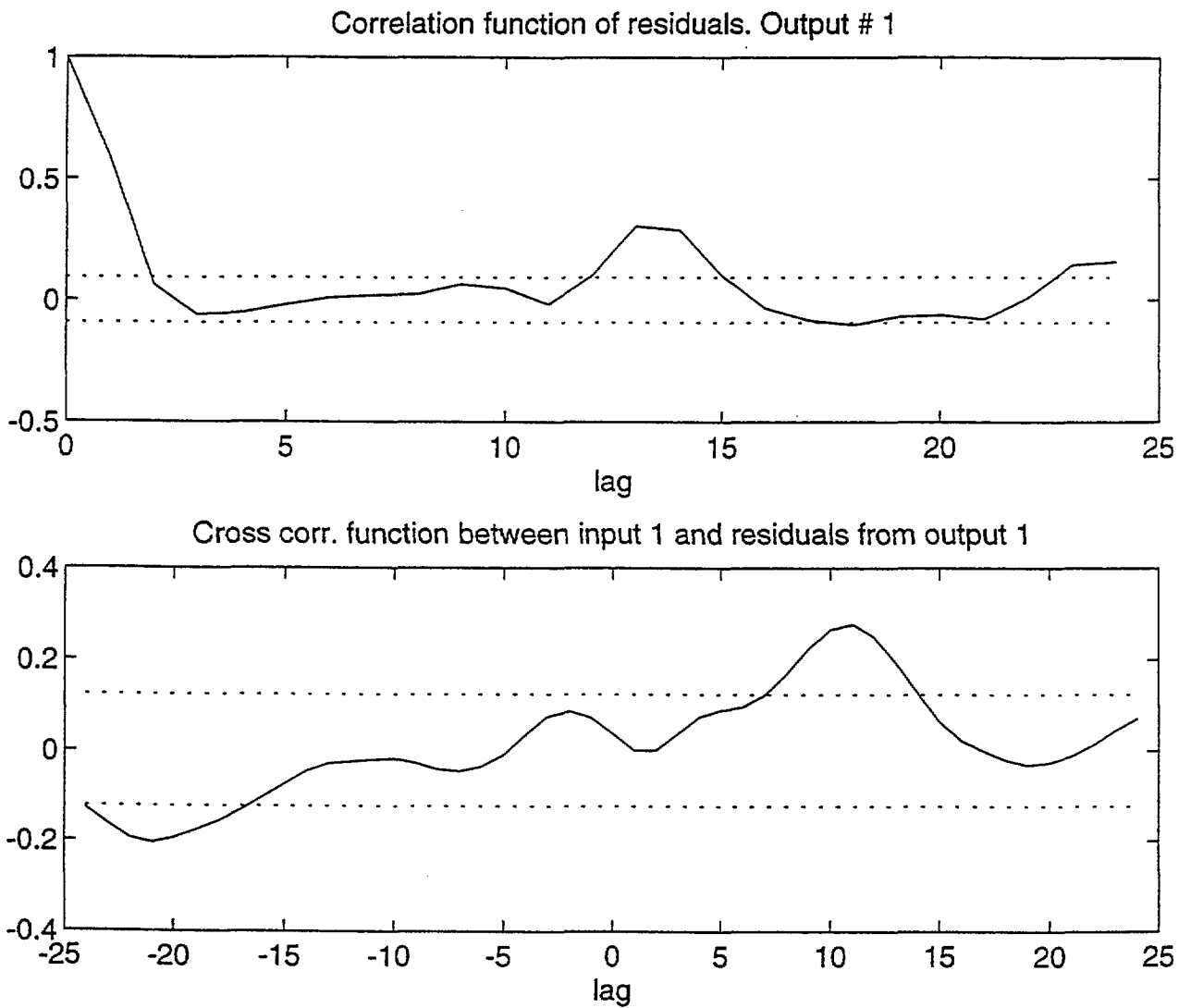
Figure 3.8 Residual analysis plot for 1-DOF model, DHA, event 12, 0-6m, n-s
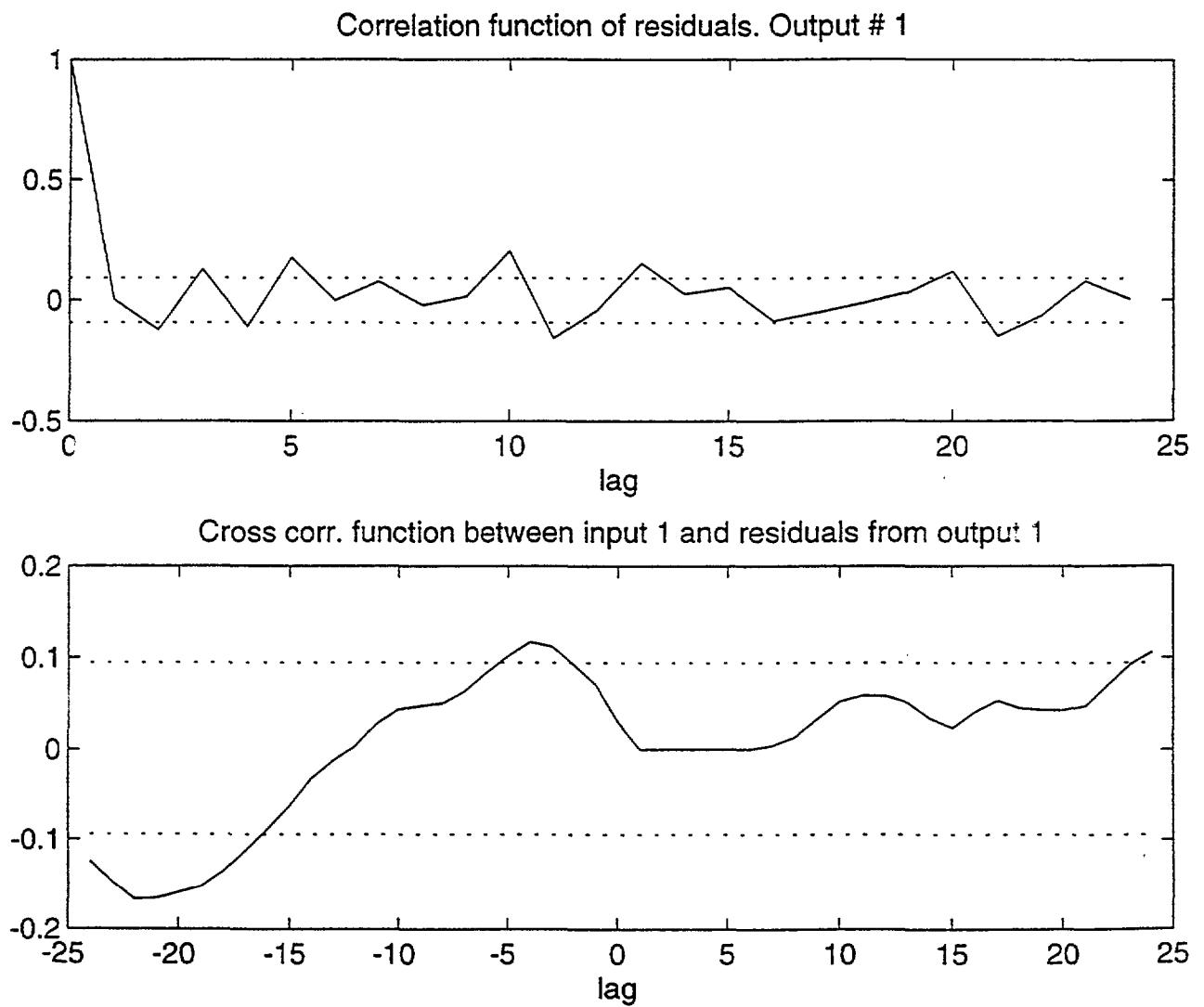
Figure 3.9 Residual analysis plot for 3-DOF model, DHA, event 12, 0-6m, n-s
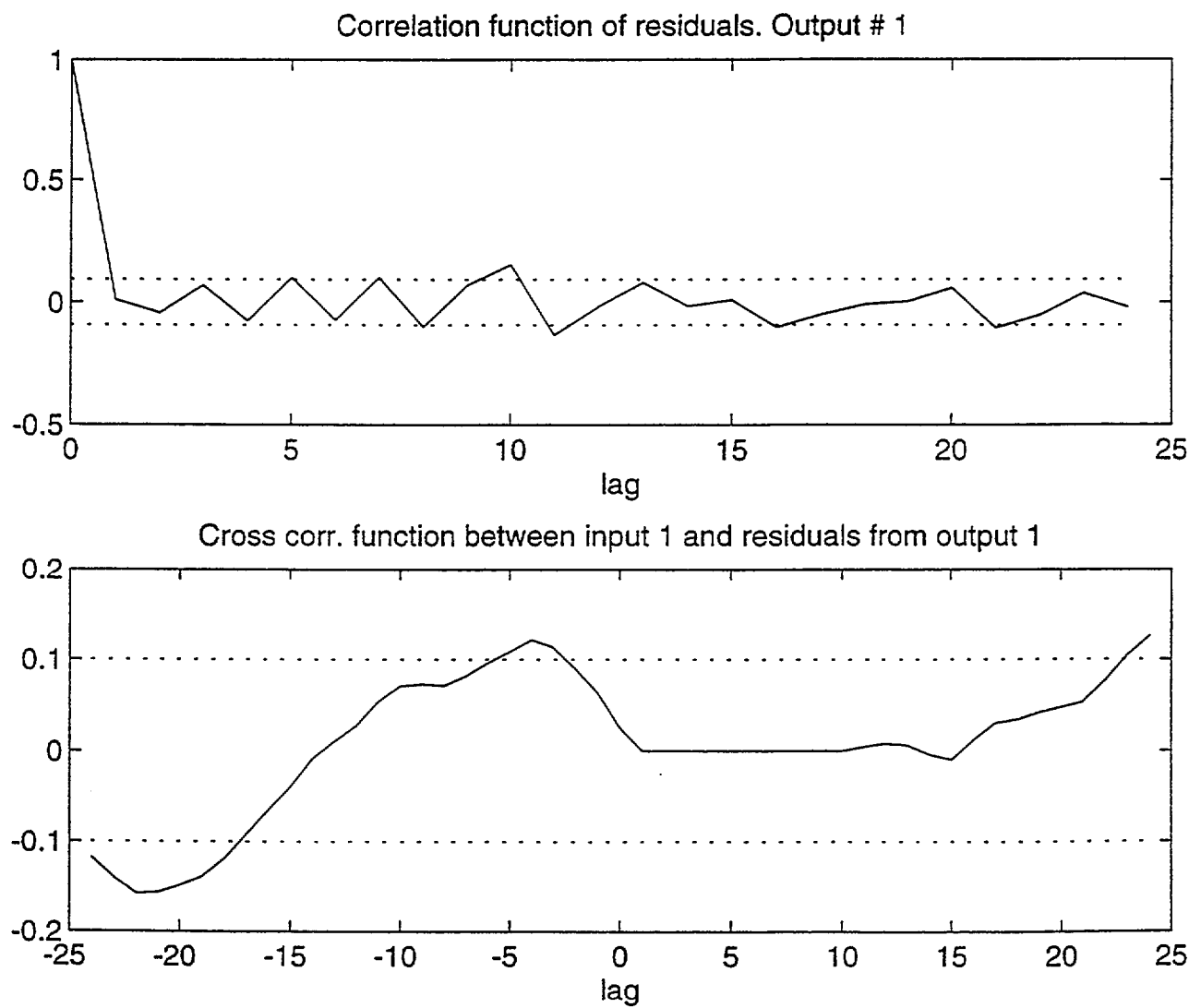
Figure 3.10 Residual analysis plot for 5-DOF model, DHA, event 12, 0-6m, n-s
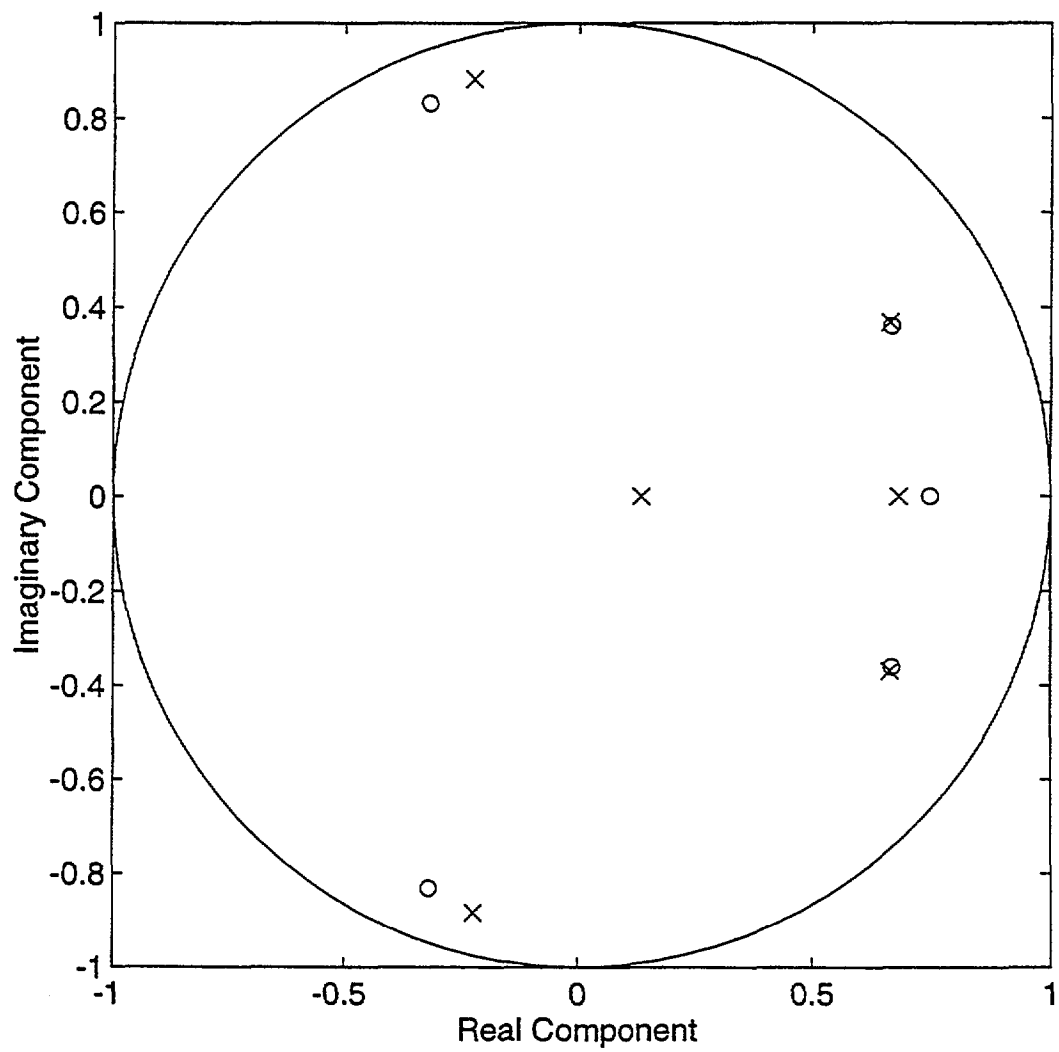
Figure 3.11   Pole - zero plot for 3 - DOF model of Event12 N-S, DHA, 0 - 6 meters depth interval.
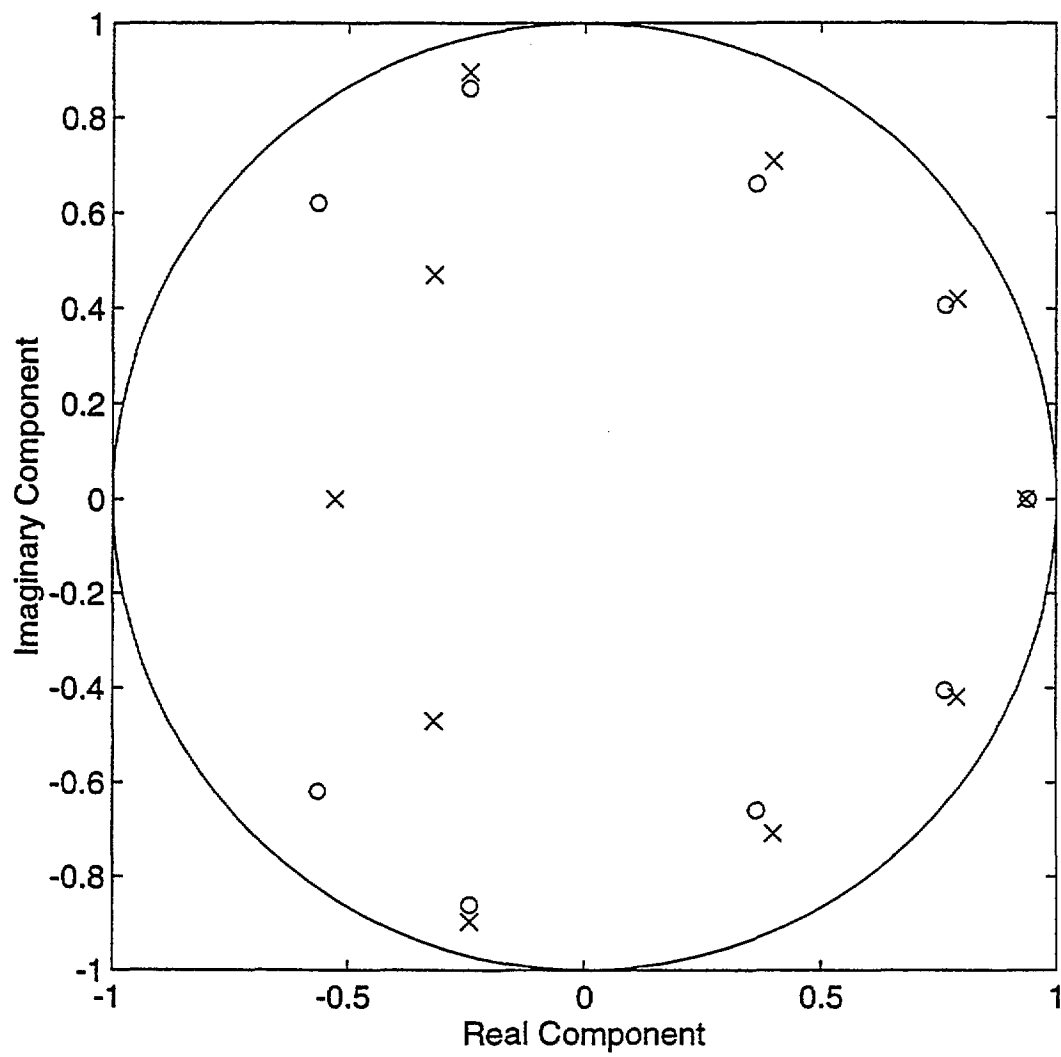
Figure 3.12   Pole - zero plot for 5 - DOF model of Event12 N-S, DHA, 0 - 6 meters depth interval.

the poles and zeros begin overlapping for the 5-DOF case, due to no "new information" available to be extracted, indicating the model order is too high or unnecessarily complicated for the interval being studied. Thus a 3-DOF model was the choice to represent this interval and event. Table 3.1 summarizes the calculated modal frequencies and damping ratios for the models examined in this analysis.

In some cases the models generated did not adequately represent the system for a very small model order. Figure 3.14 is the loss function plot for DHA, event 4, 6-11 m depth, east-west component showing a slower rate of convergence with increasing model order compared to the previous example. The fit for the 1-DOF model is 0.6347. The curve fits initially become poorer as the model order increases to a maximum of 0.702 for the 3-DOF system. From a 4-DOF to a 5-DOF model the fit improves again from 0.6852 to 0.6185. Figures 3.15-16 are the residual analysis plots for the 3-DOF and 5-DOF systems respec vely, and indicate an improvement in information extraction is occurring for the 5-DOF model over the 3-DOF model. A 6-DOF model, however, shows a decrease in the fit of the actual to predicted values to 0.6317 without additional information utilization. This can be demonstrated by comparing Figure 3.17, the residual analysis plot for the 6-DOF model, to Figure 3.16. For this interval a 5-DOF model was chosen to represent the system for this event.

Some intervals could not be well matched using a standard ARX model. These intervals were successfully fitted using either a recursive RARX model. Recursive techniques allow the system parameters to chang every time step if necessary to produce a suitable match of model to actual system output. These algorithms are thus ideal for non-stationary or difficult to match signals. Figure 3.18 is a plot showing the best fit of an ARX model to actual output for DHA, Event 4, 47-17 m depth. In this case the "best-fit" ARX model is a 1 DOF or 48 parameter model! Figure 3.19 shows the increased performance in fit for a recursive model, in this case an 3-DOF RARX model. Note that this implies that the system is changing - softening - through time.

Table 3.1 Calculated modal frequencies and damping ratios for models calculated for Event12 N-S, DHA, 0 - 6 meters depth interval.

System Degrees of Freedom	Mode	Frequency (Hz)	Damping (% of Critical)	Participation Factor
1	1st	2.49	83	0.90
2	1st	2.16	38	0.27
	2nd	5.13	61	0.69
3	1st	0.72	100	-0.06
	2nd	2.34	19	0.13
	3rd	6.64	16	0.16
4	1st	0.35	100	-0.02
	2nd	2.25	17	0.14
	3rd	5.32	20	0.21
	4th	8.34	13	-0.06
5	1st	0.40	100	-0.01
	2nd	2.37	18	0.15
	3rd	6.03	17	-0.02
	4th	6.13	53	0.91
	5th	9.16	10	-0.08
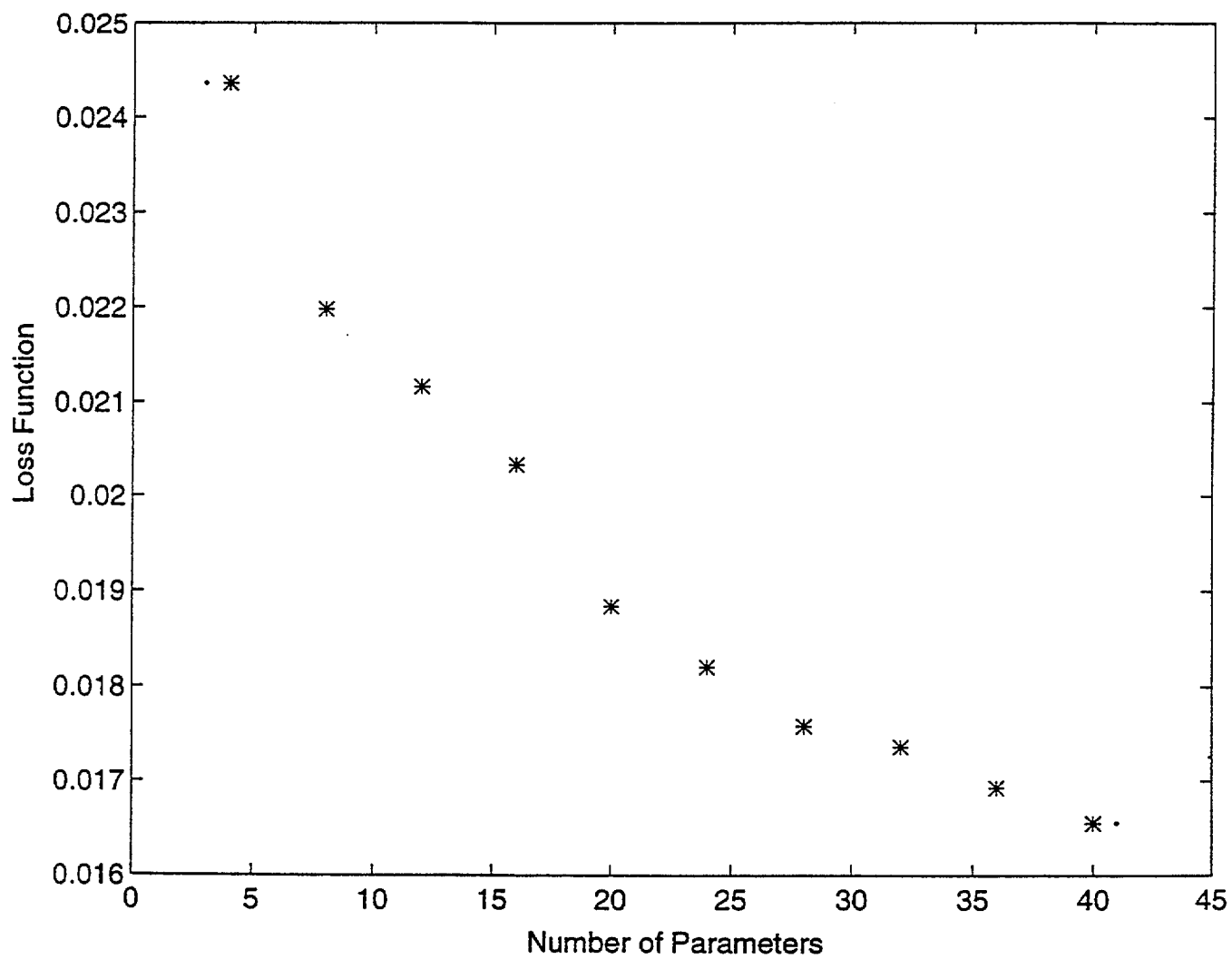
Figure 3.14 Loss function versus number of parameters, Event 4, DHA, E-W, 6 - 11 m depth.
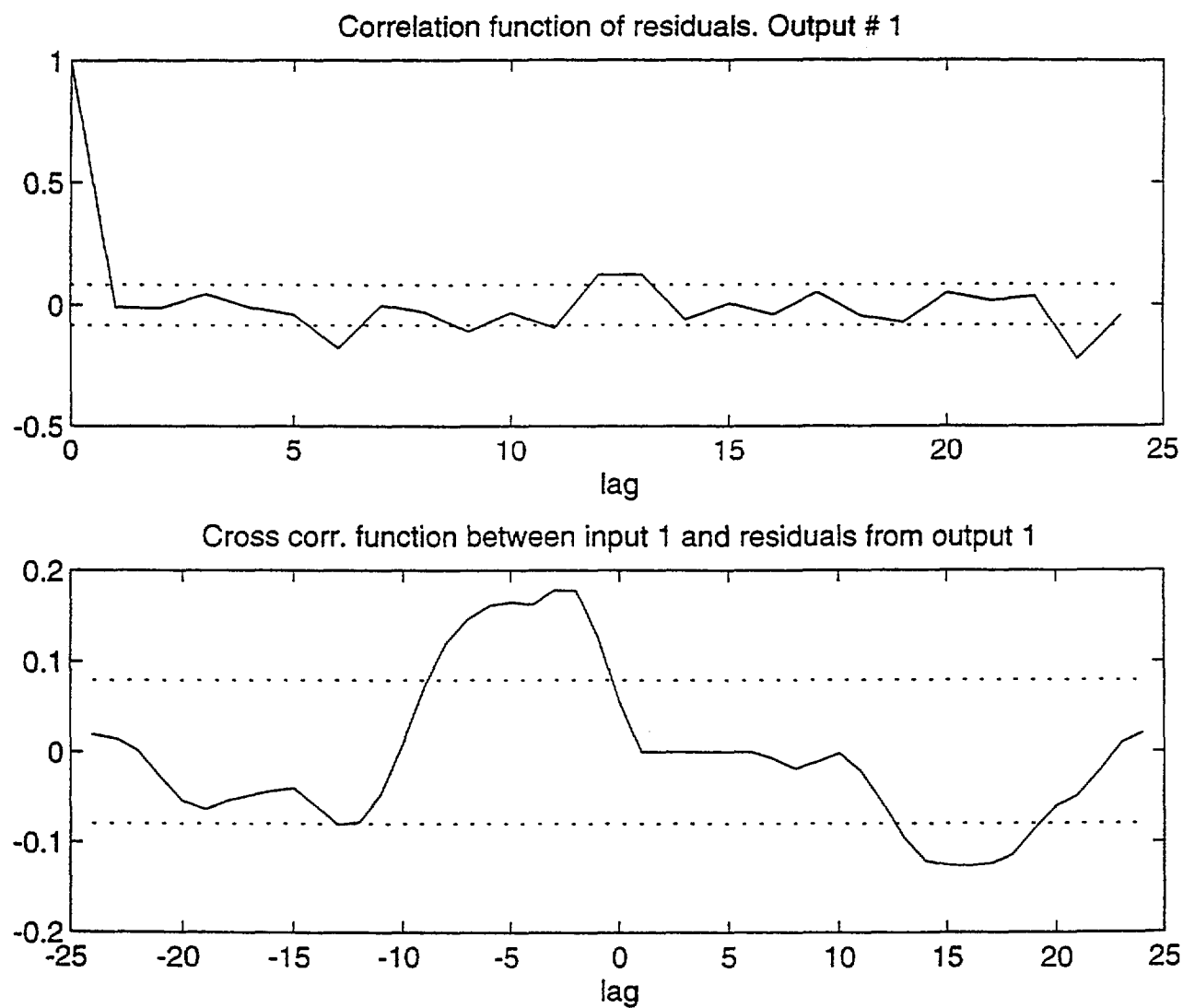
Figure 3.15 Residual analysis plot for 3-DOF model, Event 4, DHA, E-W, 6 - 11 m depth.
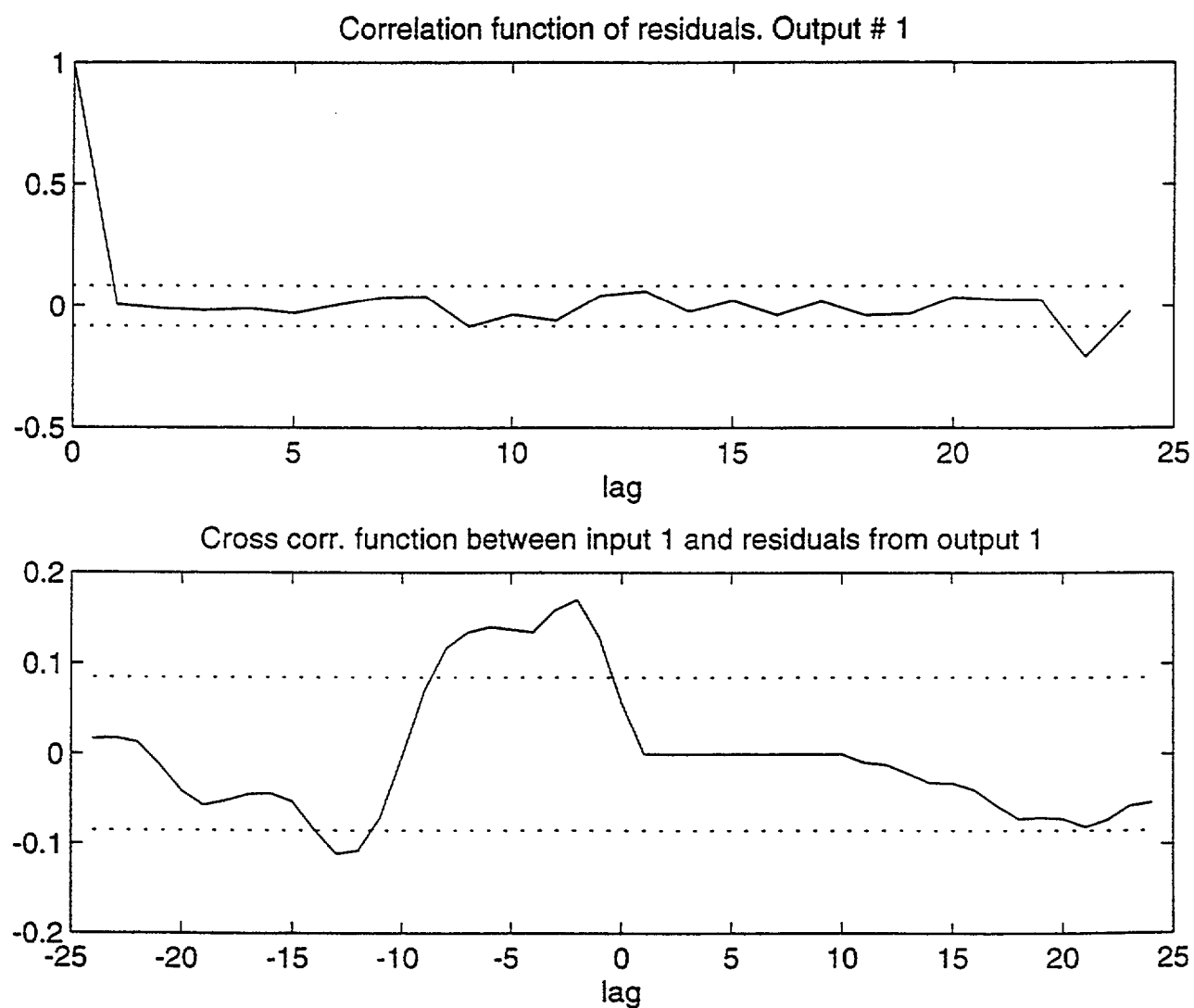
Figure 3.16 Residual analysis plot for 5-DOF model, Event 4, DHA, E-W, 6 - 11 m depth.
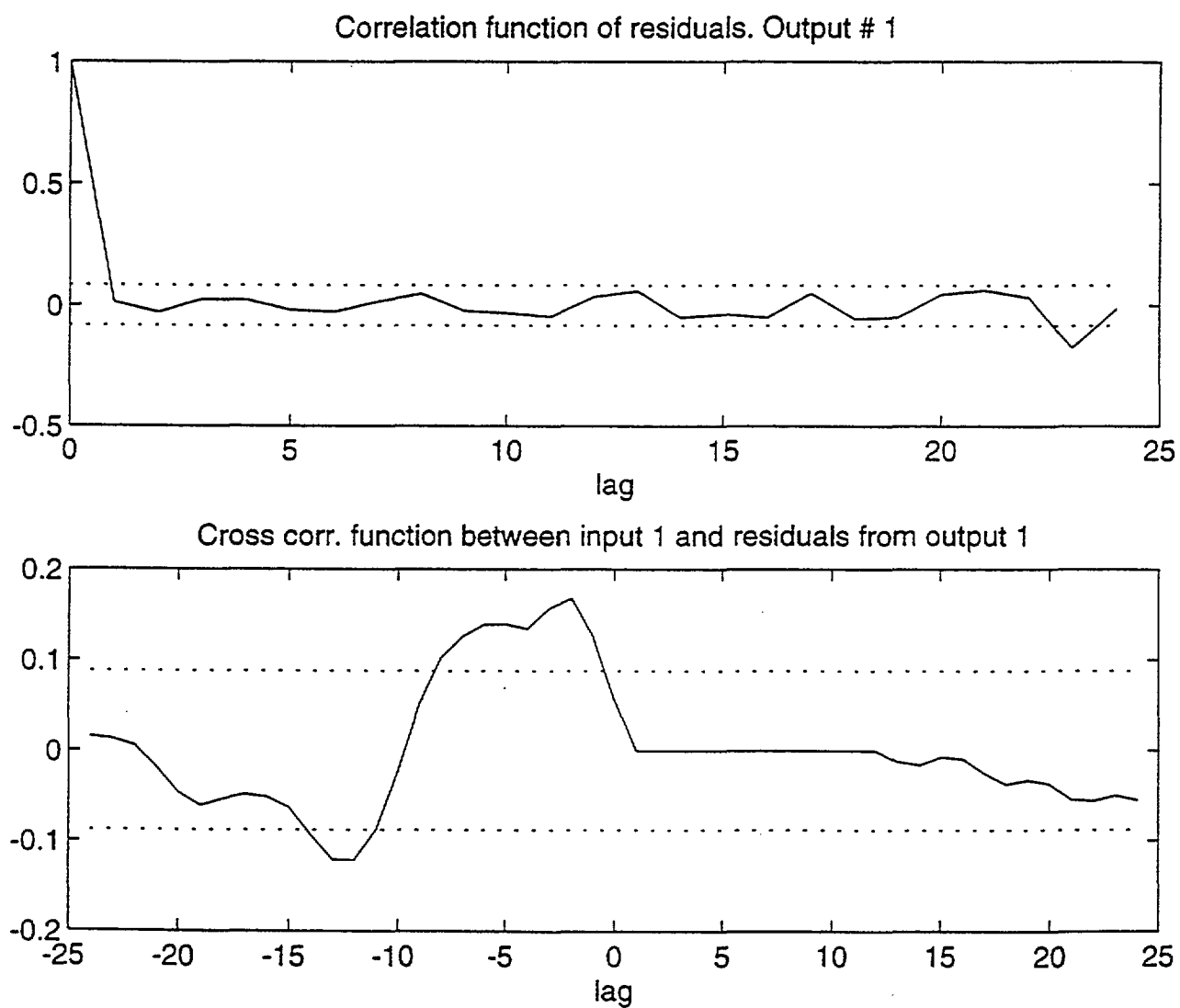
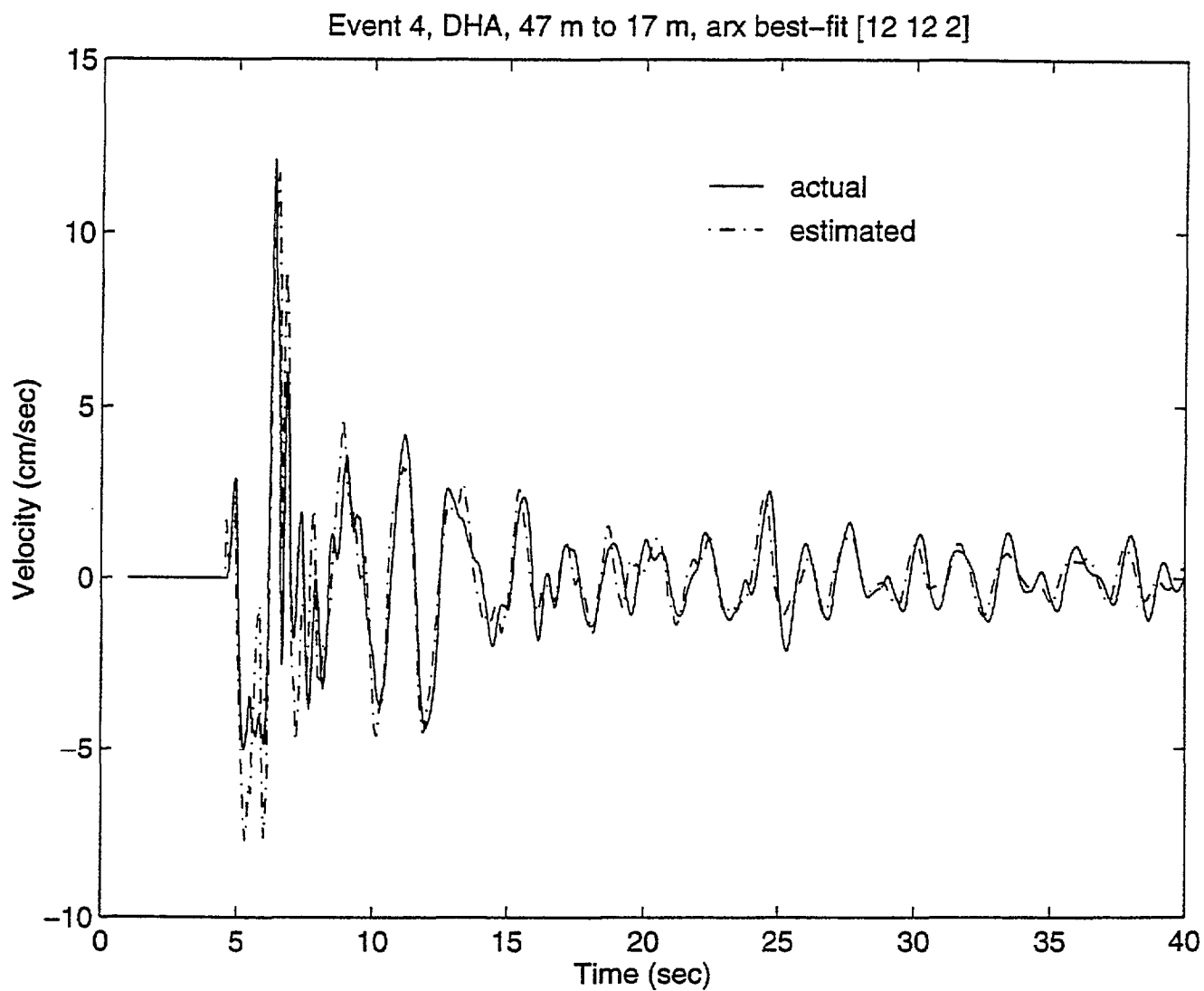Figure 3.17 Residual analysis plot for 6-DOF model, Event 4, DHA, E-W, 6 - 11 m depth.

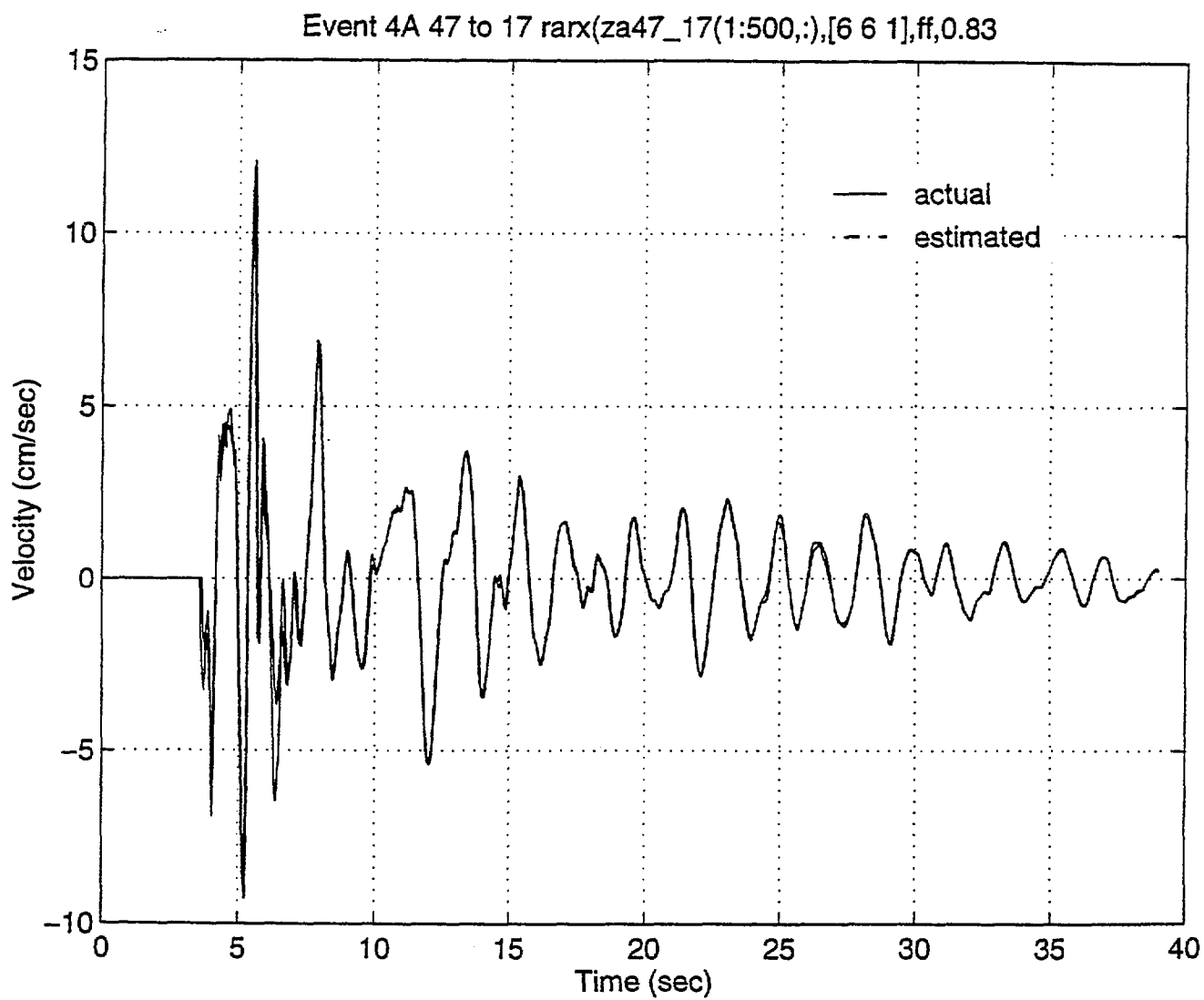Figure 3.18 "Best Fit" ARX model for Event 4, DHA, 47 m to 17 m depth interval, 6-DOF.

Figure 3.19   Recursive RARX model for Event 4, DHA, 47 m to 17 m depth, 3-DOF.

3.3 Meaning of the Estimated Damping Values

A question must be raised about the meaning of the damping values calculated in this, and other, studies – at this point the geotechnical engineer does not really know what the "correct" answer should be! A common practice is to hold up "damping" values that work well in SHAKE (Schnabel et al., 1972) as the "real" answer, but these values are also a numerical "nicety" to make a given model work. The parameters calculated in this study represent the weights that can transfer input into output through convolution. These parameters can be represented in the frequency domain as poles and zeros, and in turn as resonant frequency and damping. The detailed congruence between actual system outputs and modeled outputs will be discussed in this chapter, and are presented for all studied events in Appendix E. The values calculated, reasonable compared to other modal studies (e.g., Iemura et al., 1990) and many laboratory studies (Vucetic and Dobry, 1991), are better seen as "effective" damping coefficients which capture all forms of frequency-dependent mechanical losses, rather than an 'intrinsic' material property.

A problem common to all estimation techniques is that the damping is being modeled as viscous damping of a lumped-mass system because it is the most amenable to calculation (Pandit, 1991). In actuality "damping" is measuring cumulative energy dissipation which will include viscous damping, plastic deformation, friction and attendant heat generation (Kramer, 1995). Even with a perfect technique, the damping values estimated by the model will not truly represent what is physically occurring in the soil

Damping estimates are often very sensitive to subtle changes in the modeling of the system, especially for recursive estimates which have very different system parameters changing rapidly. In this case a limited number of data points enter directly into the calculation and variance is inversely proportional to the square root of the number of data points. The physical interpretation of the instantaneous mechanical values is also not immediately clear. The ARMA parameters recursively calculated at any given time define the filter needed to transform that time step of input data into the next output value. The mechanical characteristics are mathematically

extracted from the filter based on a limiting set of assumptions, and an "instantaneous frequency" or damping has no physical meaning. The ARX estimates are made with more input data points than the Kalman estimates, but the Kalman assumptions better model the changing system.

Damping is inherently harder than natural frequency to identify by any method or calculation. A study was done by Gersch (1974) in order to determine the greatest degree of accuracy with which a proper order ARMA model can estimate the damping ratio and natural frequency of a structure, using the Maximum Likelihood method. He notes that as the number of data points (N) becomes large, the estimates approach the actual, and the model errors approach the Cramer-Rao lower bound of variance. For both parameters, the coefficient of variation is inversely proportional to N and length of the period sampled, and relatively insensitive to noise. For one thousand data points, the coefficient of variation was less than 0.01 for natural frequency, but greater than 0.2 for damping ratio; this is an order of magnitude difference. In summary:

- error in damping estimates will be one to two orders of magnitude larger than for natural frequency.
- error for both factors are inversely proportional to the number of data points included in the analysis and the sampling period
- error for both factors are insensitive to additive noise when a MLE procedure is used and the number of modes of the system being modeled

3.4 The Pseudo-Stiffness

As the pore pressure ratio increases, the effective stress acting among the sand grains decreases, and the shear modulus (G) decreases. Since it has been impossible to accurately measure stress and strain inside the soil body, the ratio of applied force to displacement (stiffness) is used to characterize material behavior.

The here-proposed pseudo-stiffness is calculated by the following algorithm.

1)   *All horizontal motions from the surface (s) accelerometers are accounted for by taking the Euclidean norm of the north-south and east-west surface acceleration records –* $a_{hs} = \sqrt{a_{s,(N-S)}^2 + a_{s,(E-W)}^2}$.

2) *All horizontal motions from the buried (b) accelerometers are accounted for by taking the Euclidean norm of the north-south and east-west buried acceleration records* $- a_{hb} = \sqrt{a_{b,(N-S)}^2 + a_{b,(E-W)}^2}$.

3) *The relative acceleration of the surface to buried transducer is determined from the step-by-step difference between the surface and buried horizontal accelerations* $-$ $a_{rel_{(i)}} = a_{s,h_{(i)}} - a_{b,h_{(i)}}$

4) *The relative accelerations are converted into forces by multiplying the differential accelerations acting at the top and bottom of the layer of interest by the soil column mass, which should change relatively little during the softening process (e.g. Udwadia, 1985)* $- F_i = a_{rel_{(i)}} \cdot \gamma \cdot H_l$

5 *The running total of the amount of force is computed for the system during each time step $-$ sum(t)=sum(t-1)+{force(t)-force(t-1)} $-$ yielding the cumulative horizontal unit force.*

6) *Steps 1, 2, 3, and 5 are applied to the displacement records to yield the cumulative horizontal displacement.*

7) *The ratio of the resulting cumulative horizontal unit force to displacement are two independent variables that combine to give a pseudo-stiffness.*

The use of a single transducer to provide acceleration and displacement measurements is not problematic since the derived displacement (Brady et al., 1989) is generally assumed to be identical to what would be recorded by an independent displacement transducer placed next to the accelerometer. The calculations do not distinguish between active (external, inertial) and restorative (internal, stiffness) forces acting on the soil. The pseudo-stiffness is a convenient representation of the system behavior, combining load, time, and displacement information in a simple curve.

CHAPTER 4 PARAMETRIC MODELING OF LOTUNG DATA

4.1 Introduction

As discussed in Chapter 2, eight earthquakes of varying characteristics were chosen for this study. The selected temblors represent two classes - large and small. The estimated mechanical parameters for the small (low energy/acceleration) events can be seen as a linear baseline against which to judge whether the larger events exhibited nonlinear behavior. This chapter will begin with a general discussion of the results of the study, followed by general discussions on modal frequency, damping, and soil-structure interaction for the lotung site as a whole. The two similar small events (events 7 and 8) and the large events (events 4 and 16) will then be discussed in detail.

All pertinent intervals for the Lotung events were modeled during this study. The comparisons of all actual interval outputs to estimated system outputs are presented in Appendix E. An example of the congruence between estimated and actual output is given in Fig. 4.1. This result is for the top six meters for the free-field DHB array due to Event 4, using a 2-DOF model.

4.2 Discussion of Results

A summary of the estimated fundamental frequencies for the earthquakes analyzed for this report is given in Table 4.1. The corresponding estimates of system damping are given in Table 4.2. As demonstrated in Tables 4.1 and 4.2, when subjected to greater seismic energy the modal frequencies do systematically decrease and damping ratios increase. In fact, the results strongly support the concept of threshold strain (Dobry, 1973). The modal frequencies and damping ratios are very close for small Events 3, 8, 9, and 10. These events all have values of Arias Intensity under 200 cm/sec and maximum acceleration values of 0.07 g and less. The higher energy events including Events 7, 4, 12 and 16, with Arias Intensities between 650 and 4000 cm/sec and maximum accelerations ranging from 0.17 to almost 0.5 g exhibit substantial and consistent decreases in fundamental frequency.
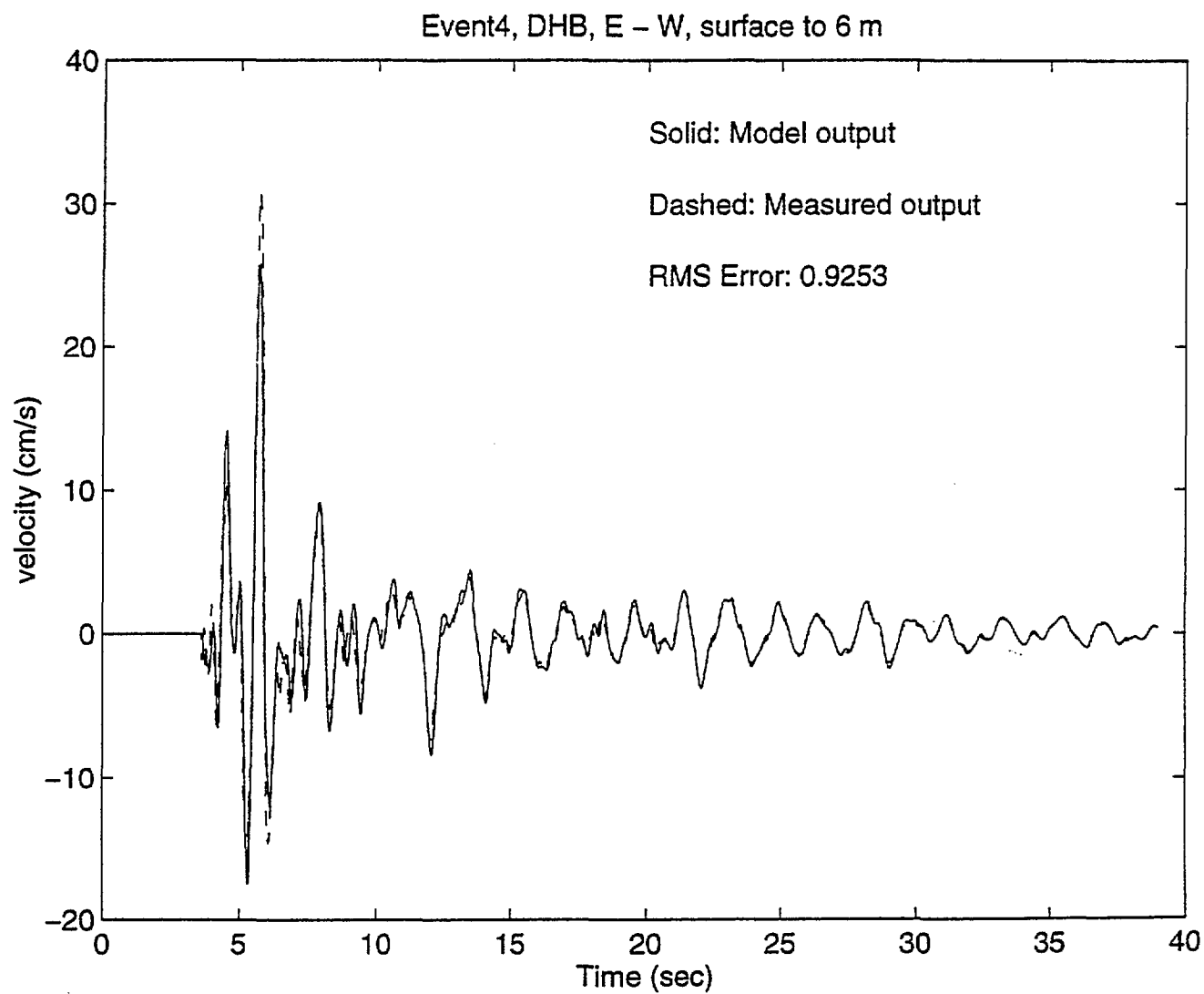
Figure 4.1   An example of "goodness-of-fit" between actual and modeled system output.

Table 4.1 Fundamental Resonant Frequencies Compared to Various Earthquake Metrics.

Earthquake		3		4		7		8		9		10		12		16	
Surface Peak Acceleration (PA)		0.01 g		0.49 g		0.21 g		0.03 g		0.07 g		0.04 g		0.20 g		0.17 g	
Surface Arias Intensity (AI)		74 m/s		1845 m/s		652 m/s		139 m/s		192 m/s		36 m/s		2710 m/s		3995 m/s	
Local Magnitude (M_L)		5.5		6.5		6.5		6.2		4.5		4.5		6.2		7.0	
Vertical Array		A	B	A	B	A	B	A	B	A	B	A	B	A	B	A	B
6 m to Surface	NS (Hz)	3.1	5.1	2.3	2.6	1.4	2.9	2.6	4.5	-	4.6	-	5.2	2.2	3.1	2.4	3.4
	EW (Hz)	3.3	5.1	2.1	2.9	1.8	3.6	-	-	-	4.7	-	5.1	2.4	3.5	2.4	3.9
	Input PA (g)	0.01	0.01	0.34	0.46	0.11	0.14	0.01	0.01	-	0.02	-	0.04	0.10	0.16	0.11	0.12
	Input AI (m/s)	11	15	2050	2170	329	386	37	56	-	35	-	25	1430	1224	2090	2028
11 m to 6 m	NS (Hz)	3.3	3.3	1.4	1.5	1.6	1.5	2.6	3.0	-	3.3	-	3.6	2.0	2.2	2.2	2.4
	EW (Hz)	3.1	3.4	1.3	1.4	1.7	1.8	-	-	-	3.0	-	3.1	1.9	2.2	2.0	2.4
	Input PA (g)	0.01	0.05	0.37	0.49	0.09	0.11	0.02	0.02	0.03	0.03	0.03	0.03	0.13	0.19	0.09	0.1
	Input AI (m/s)	14	23	1100	-	274	279	34	42	30	39	16	19	1581	1496	1205	1406
17 m to 11 m	NS (Hz)	2.4	2.5	1.3	-	1.4	1.6	2.2	2.4	-	2.6	-	2.5	1.7	1.8	1.5	1.6
	EW (Hz)	2.5	2.5	1.2	-	-	-	-	-	-	2.6	-	2.5	1.7	1.7	1.6	1.8
	Input PA (g)	0.01	0.01	0.48	-	0.08	0.09	0.02	0.02	-	0.02	-	0.01	0.17	0.19	0.08	0.08
	Input AI (m/s)	17	12	2040	-	225	250	28	33	-	21	-	9	1769	1258	1043	1058
47 m to 17 m	NS (Hz)	1.4	1.4	1.2	-	1.0	0.9	1.2	1.8	-	1.5	-	1.4	1.0	0.8	0.9	-
	EW (Hz)	1.4	1.4	1.3	-	-	-	-	-	-	1.4	-	1.4	1.0	-	0.8	-
	Input PA (g)	0.01	0.01	0.26	0.27	0.09	0.1	0.01	0.01	0.02	0.02	0.03	0.02	0.22	-	0.08	-
	Input AI (m/s)	10	8	1760	1770	134	125	25	28	18	16	12	6	1422	-	1248	-
Surface to 11 m	NS (Hz)	3.2	3.6	1.5	1.6	-	-	-	-	3.1	3.4	3.3	3.2	1.8	3.2	1.7	2.3
	EW (Hz)	3.1	3.6	1.5	1.9	-	-	-	-	3.0	3.2	3.0	3.3	1.9	3.3	1.8	2.4
	Input PA (g)	0.01	0.05	0.37	0.49	0.09	0.11	0.02	0.02	0.03	0.03	0.03	0.03	0.13	0.19	0.09	0.1
	Input AI (m/s)	14	23	1100	-	274	279	34	42	30	39	16	19	1581	1496	1205	1406
47 m to 11 m	NS (Hz)	1.4	1.6	0.85	0.9	-	-	-	-	1.5	1.5	1.3	1.3	0.9	-	0.9	-
	EW (Hz)	1.4	1.3	0.90	0.84	-	-	-	-	1.5	1.4	1.3	1.4	1.0	-	1.0	-
	Input PA (g)	0.01	0.01	0.26	0.27	0.09	0.1	0.01	0.01	0.02	0.02	0.03	0.02	0.22	-	0.08	-
	Input AI (m/s)	10	8	1760	1770	134	125	25	28	18	16	12	6	2422	-	1248	-

Table 4.2   Damping for Fundamental Resonant Frequencies Compared to Various Earthquake Metrics.

Earthquake	3		4		7		8		9		10		12		16	
Surface Peak Acceleration (PA)	0.01 g		0.49 g		0.21 g		0.03 g		0.07 g		0.04 g		0.20 g		0.17 g	
Surface Arias Intensity (AI)	74 m/s		1845 m/s		652 m/s		139 m/s		192 m/s		36 m/s		2710 m/s		3995 m/s	
Local Magnitude (M_L)	5.5		6.5		6.5		6.2		4.5		4.5		6.2		7.0	
Vertical Array	A	B	A	B	A	B	A	B	A	B	A	B	A	B	A	B
6 m to Surface NS (% critical damping)	7	2	34	27	33	14	10	3	-	2	-	3	24	13	27	12
EW (% critical damping)	11	2	12	12	16	18	-	-	-	2	-	1	19	21	32	10
Input PA (g)	0.01	0.01	0.34	0.46	0.11	0.14	0.01	0.01	-	0.02	-	0.04	0.10	0.16	0.11	0.12
Input AI (m/s)	11	15	2050	2170	329	386	37	56	-	35	-	25	1430	1224	2090	2028
11 m to 6 m NS (% critical damping)	7	4	26	25	13	12	5	6	-	4	-	5	28	11	16	16
EW (% critical damping)	6	9	28	37	13	15	-	-	-	6	-	5	16	16	22	14
Input PA (g)	0.01	0.05	0.37	0.49	0.09	0.11	0.02	0.02	0.03	0.03	0.03	0.03	0.13	0.19	0.09	0.1
Input AI (m/s)	14	23	1100	-	274	279	34	42	30	39	16	19	1581	1496	1205	1406
17 m to 11 m NS (% critical damping)	4	6	33	-	13	22	3	6	-	14	-	16	17	18	17	20
EW (% critical damping)	3	8	38	-	-	-	-	-	-	10	-	7	16	18	17	16
Input PA (g)	0.01	0.01	0.48	-	0.08	0.09	0.02	0.02	-	0.02	-	0.01	0.17	0.19	0.08	0.08
Input AI (m/s)	17	12	2040	-	225	250	28	33	-	21	-	9	1769	1258	1043	1058
47 m to 17 m NS (% critical damping)	22	14	14	-	12	12	18	12	-	12	-	13	33	20	14	-
EW (% critical damping)	30	18	16	-	-	-	-	-	-	12	-	13	13	-	14	-
Input PA (g)	0.01	0.01	0.26	0.27	0.09	0.1	0.01	0.01	0.02	0.02	0.03	0.02	0.22	-	0.08	-
Input AI (m/s)	10	8	1760	1770	134	125	25	28	18	16	12	6	14	22-	1248	-
Surface to 11 m NS (% critical damping)	2	7	19	17	-	-	-	-	7	4	3	5	13	16	31	18
EW (% critical damping)	2	6	25	40	-	-	-	-	7	6	4	5	14	13	27	18
Input PA (g)	0.01	0.05	0.37	0.49	0.09	0.11	0.02	0.02	0.03	0.03	0.03	0.03	0.13	0.19	0.09	0.1
Input AI (m/s)	14	23	1100	-	274	279	34	42	30	39	16	19	1581	1496	1205	1406
47 m to 11 m NS (% critical damping)	13	17	21	23	-	-	-	-	15	11	12	13	12	-	13	-
EW (% critical damping)	17	15	21	21	-	-	-	-	17	15	11	13	11	-	19	-
Input PA (g)	0.01	0.01	0.26	0.27	0.09	0.1	0.01	0.01	0.02	0.02	0.03	0.02	0.22	-	0.08	-
Input AI (m/s)	10	8	1760	1770	134	125	25	28	18	16	12	6	2422	-	1248	-

58

Consider the results from the "free field" hole, DHB. The fundamental frequency for the 0-6 m interval exhibits a decrease from 4.6-5.2 Hz for Events 8, 9, 10 and 3 (Arias Intensity ranging from 36-192) to 2.6-3.9 Hz for Events 7, 4, 12 and 16 (Arias Intensities 652-3995.) This result is consistent with the calculations from deeper intervals. The 6-11 m segment shows a decrease from an average of 3.3 Hz for the moderate events to 1.4-2.4 Hz for the larger events. The trend continues to the 11-17 m interval where the fundamental frequency decreases from 2.6 Hz to 1.6 Hz. For DHB the only deep interval information is the result from Event 4, which also exhibits a decrease in frequency from 1.4 Hz to 0.9 Hz for the 17-47 m segment.

Figure 4.2 graphically compares estimates of fundamental modal frequency to peak acceleration for all events, while Fig. 4.3 graphically compares estimates of system damping to peak acceleration for all events. The decrease in fundamental frequency and increase in damping with increase in peak acceleration is readily evident. Close examination shows that the change in material properties is greater for the near-surface layers than for the deep one. It is expected that greater confinement of deeper soils would serve to smooth out changes in system behavior.

Figure 4.4 graphically compares estimates of fundamental modal frequency to Arias intensity input into the soil layers, while Fig. 4.5 graphically compares estimates of system damping to Arias intensity input into the soil layers. Surprisingly there is less correlation between system behavior and energy input into soil layers as measured by Arias Intensity. This leads to a conclusion that soil softening is more a function of peak acceleration (which causes peak strain) than total input energy (that is proportional to cumulative strains). This conclusion implies a minimum peak acceleration is needed to excite the soil past its threshold strain.

The estimates for system damping presented in this study are greater than values traditionally accepted by geotechnical engineers (see Appendix D). Estimated values range from less than 2% to almost 50%. As discussed in Chapter 3, these are the values that map system input into system output. A quick review of the estimation results in Appendix E show how well the estimation process was able to capture the essence of the soil systems in question. Damping values reported in Table 4.2 are generally higher than estimates of damping by Zeghal et al. (1995) for Events 7, 12, and 16 (see Figs. D.9 through D.18)
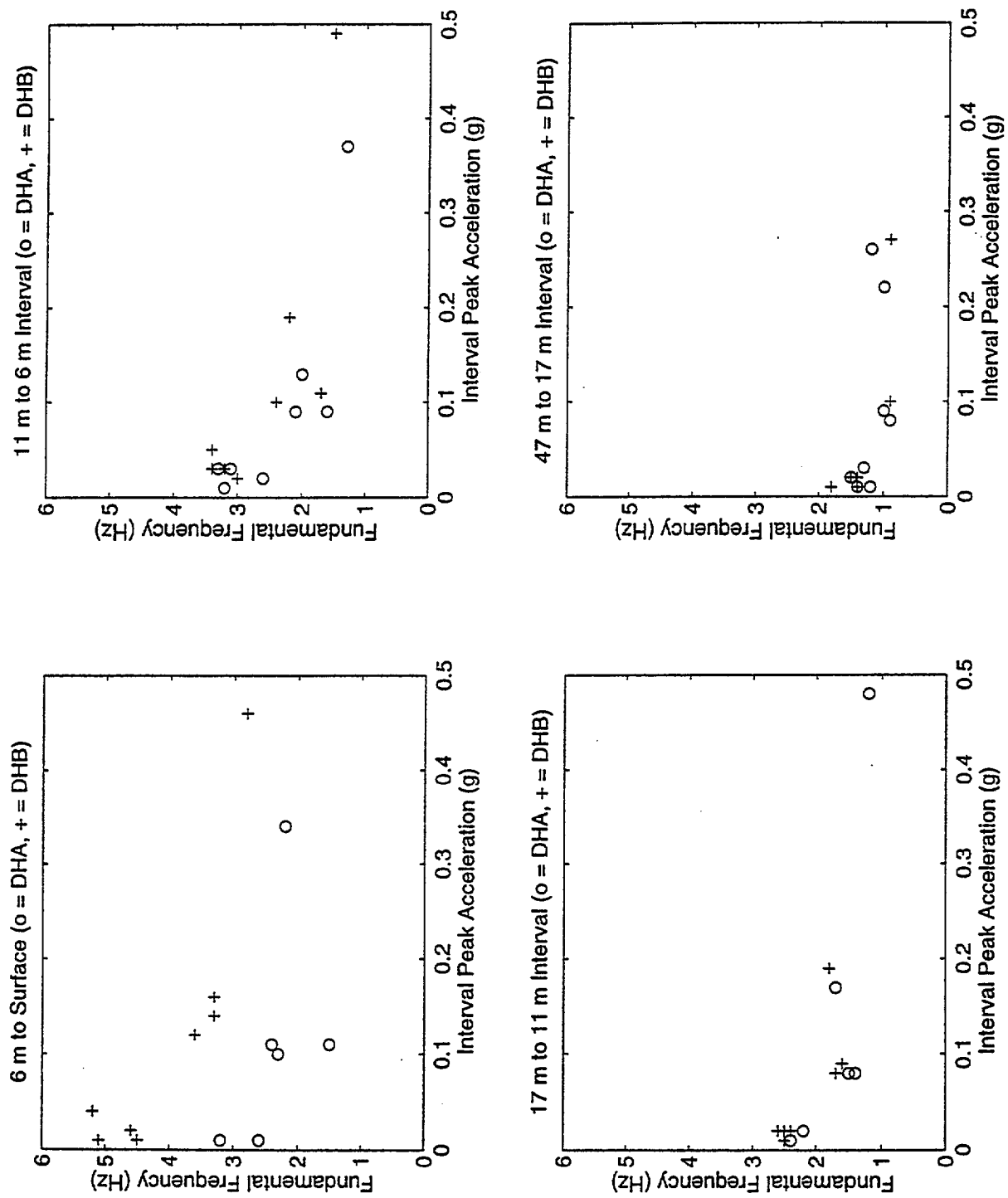
Figure 4.2   Comparison of estimates of fundamental modal frequency to peak acceleration for all events, presented by depth interval.
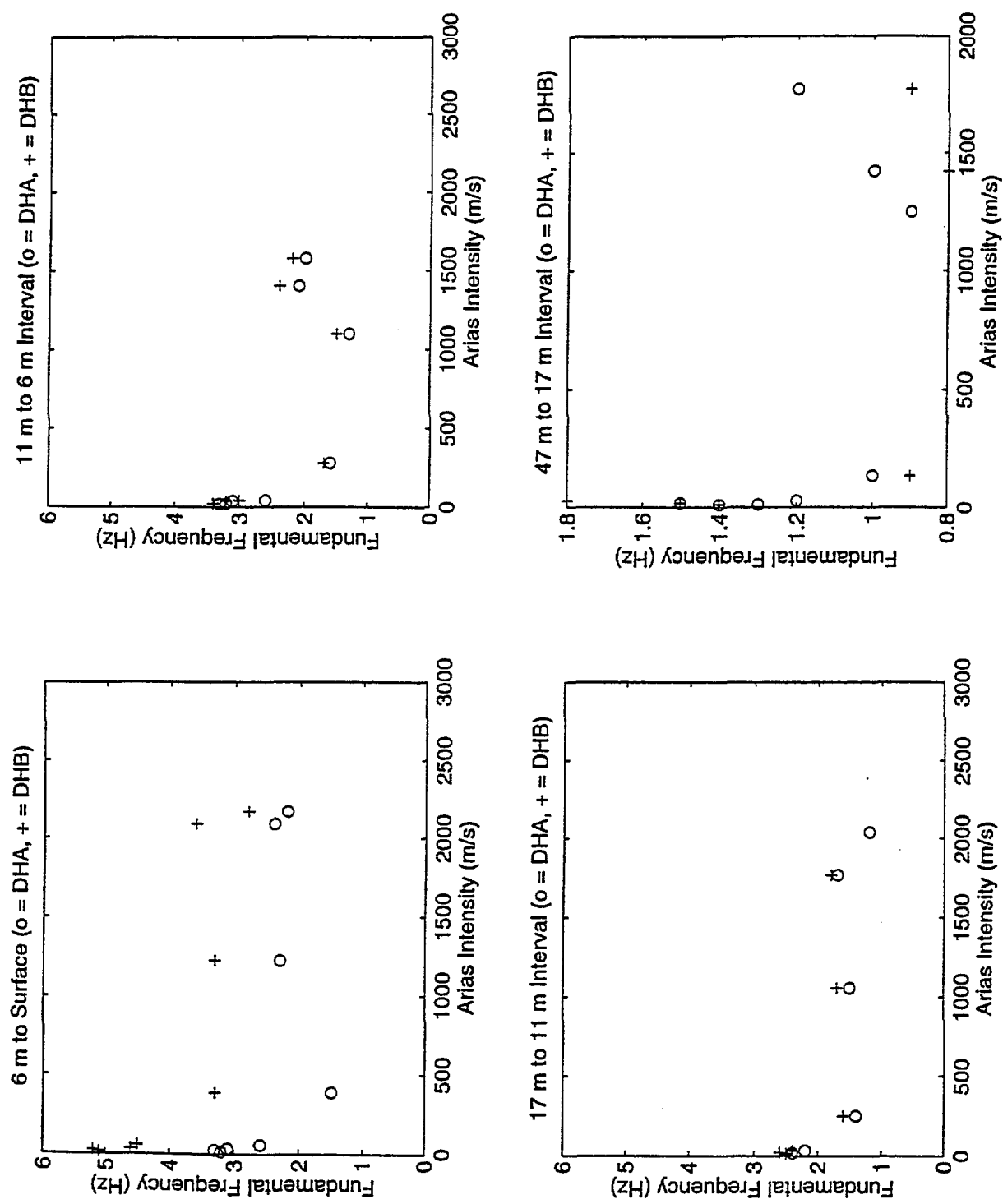
Figure 4.3   Comparison of estimates of fundamental modal frequency to Arias Intensity for all events, presented by depth interval.
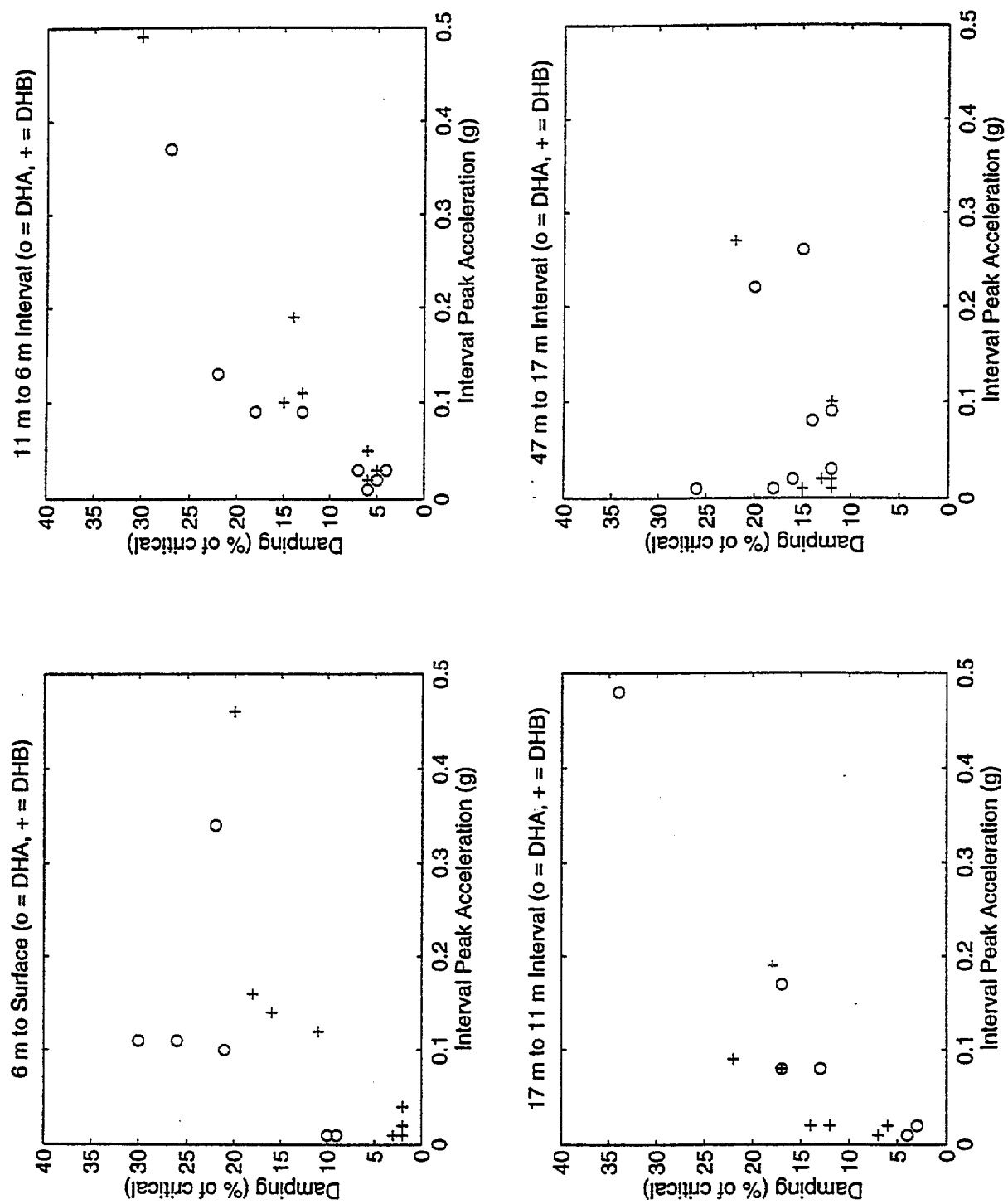
Figure 4.4   Comparison of estimates of damping to peak acceleration for all events, presented by depth interval.
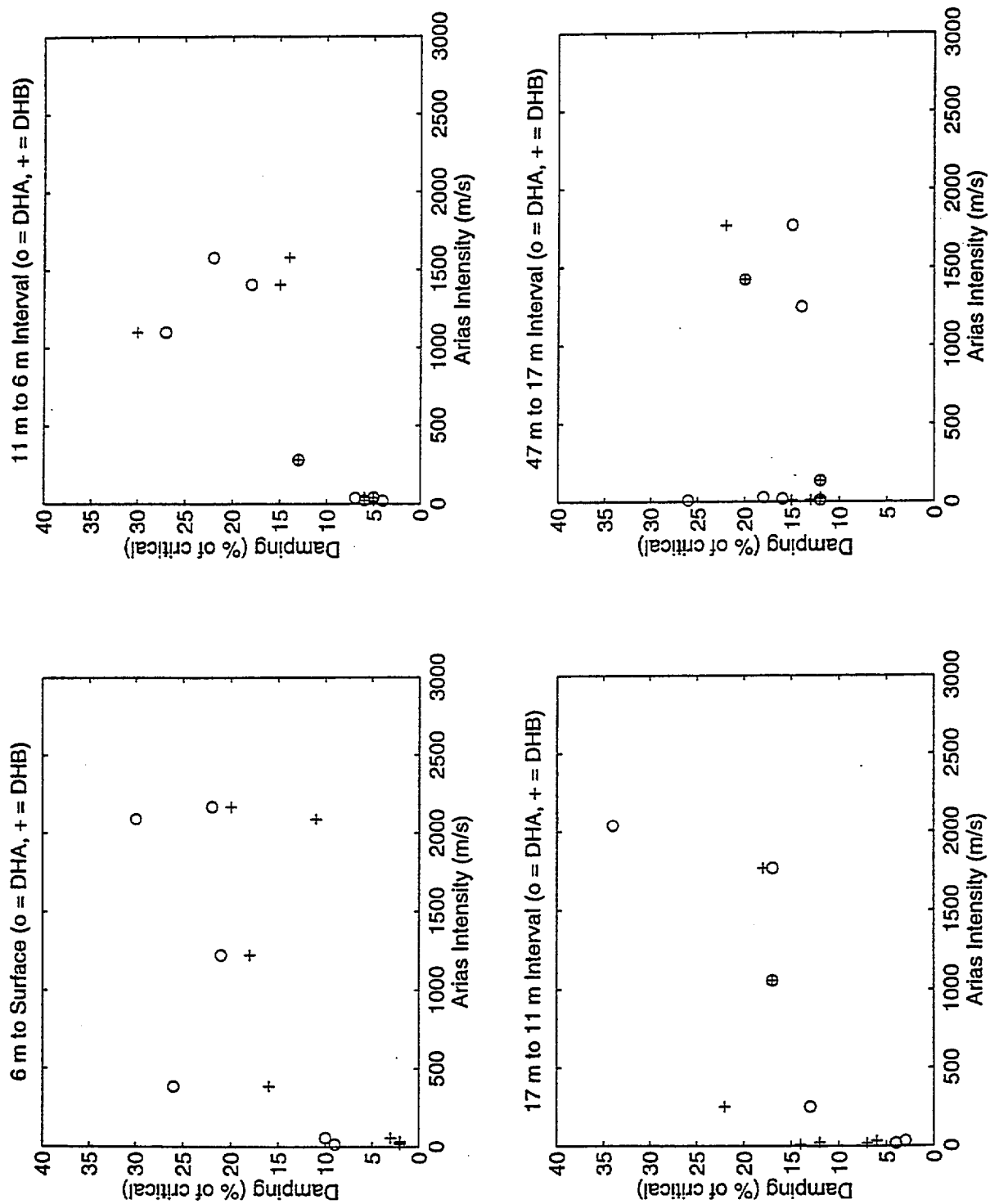
Figure 4.5   Comparison of estimates of damping to Arias Intensity for all events, presented by depth interval.

Table 4.3   Second Resonant Frequencies Compared to Various Earthquake Metrics.

Earthquake		3		4		7		8		9		10		12		16	
Surface Peak Acceleration (PA)		0.01 g		0.49 g		0.21 g		0.03 g		0.07 g		0.04 g		0.20 g		0.17 g	
Surface Arias Intensity (AI)		74 m/s		1845 m/s		652 m/s		139 m/s		192 m/s		36 m/s		2710 m/s		3995 m/s	
Local Magnitude (M_L)		5.5		6.5		6.5		6.2		4.5		4.5		6.2		7.0	
Vertical Array		A	B	A	B	A	B	A	B	A	B	A	B	A	B	A	B
6 m to Surface	NS (Hz) / EW (Hz)	6.7	7.2	5.8	-	6.0	6.9	-	8.7	-	7.2	-	6.9	5.2	5.8	6.0	8.8
		-	-	-	-	-	-	-	-	-	-	-	-	-	-	-	-
	Input PA (g)	0.01	0.01	0.34	0.46	0.11	0.14	0.01	0.01	-	0.02	-	0.04	0.10	0.16	0.11	0.12
	Input AI (m/s)	11	15	2050	2170	329	386	37	56	-	35	-	25	1430	1224	2090	2028
11 m to 6 m	NS (Hz) / EW (Hz)	-	6.5	5.5	5.0	7.4	6.1	5.0	8.2	-	8.8	-	8.9	7.2	5.5	6.8	6.8
		-	-	-	-	-	-	-	-	-	-	-	-	-	-	-	-
	Input PA (g)	0.01	0.05	0.37	0.49	0.09	0.11	0.02	0.02	0.03	0.03	0.03	0.03	0.13	0.19	0.09	0.1
	Input AI (m/s)	14	23	1100	-	274	279	34	42	30	39	16	19	1581	1496	1205	1406
17 m to 11 m	NS (Hz) / EW (Hz)	6.1	6.3	4.2	-	7	6.4	5.8	5.5	-	5.5	-	6.1	4.6	5.8	5.0	5.0
		-	-	-	-	-	-	-	-	-	-	-	-	-	-	-	-
	Input PA (g)	0.01	0.01	0.48	-	0.08	0.09	0.02	0.02	-	0.02	-	0.01	0.17	0.19	0.08	0.08
	Input AI (m/s)	17	12	2040	-	225	250	28	33	-	21	-	9	1769	1258	1043	1058
47 m to 17 m	NS (Hz) / EW (Hz)	5	5.3	-	-	7	7	7.5	7.4	-	6.9	-	5.2	4.0	-	7.7	-
		-	-	-	-	-	-	-	-	-	-	-	-	-	-	-	-
	Input PA (g)	0.01	0.01	0.26	0.27	0.09	0.1	0.01	0.01	0.02	0.02	0.03	0.02	0.22	-	0.08	-
	Input AI (m/s)	10	8	1760	1770	134	125	25	28	18	16	12	6	1422	-	1248	-
Surface to 11 m	NS (Hz) / EW (Hz)	-	-	-	-	-	-	-	-	-	-	-	-	-	-	-	-
		-	-	-	-	-	-	-	-	-	-	-	-	-	-	-	-
	Input PA (g)	0.01	0.05	0.37	0.49	0.09	0.11	0.02	0.02	0.03	0.03	0.03	0.03	0.13	0.19	0.09	0.1
	Input AI (m/s)	14	23	1100	-	274	279	34	42	30	39	16	19	1581	1496	1205	1406
47 m to 11 m	NS (Hz) / EW (Hz)	-	-	-	-	-	-	-	-	-	-	-	-	-	-	-	-
		-	-	-	-	-	-	-	-	-	-	-	-	-	-	-	-
	Input PA (g)	0.01	0.01	0.26	0.27	0.09	0.1	0.01	0.01	0.02	0.02	0.03	0.02	0.22	-	0.08	-
	Input AI (m/s)	10	8	1760	1770	134	125	25	28	18	16	12	6	2422	-	1248	-

Table 4.4 Damping for Second Resonant Frequencies Compared to Various Earthquake Metrics.

Earthquake	3		4		7		8		9		10		12		16	
Surface Peak Acceleration (PA)	0.01 g		0.49 g		0.21 g		0.03 g		0.07 g		0.04 g		0.20 g		0.17 g	
Surface Arias Intensity (AI)	74 m/s		1845 m/s		652 m/s		139 m/s		192 m/s		36 m/s		2710 m/s		3995 m/s	
Local Magnitude (M_L)	5.5		6.5		6.5		6.2		4.5		4.5		6.2		7.0	
Vertical Array	A	B	A	B	A	B	A	B	A	B	A	B	A	B	A	B
6 m to Surface — NS (% critical damping)	8	19	24	-	15	21	29	10	-	20	-	19	24	24	7	13
EW (% critical damping)	-	-	-	-	-	-	-	-	-	-	-	-	-	-	-	-
Input PA (g)	0.01	0.01	0.34	0.46	0.11	0.14	0.01	0.01	-	0.02	-	0.04	0.10	0.16	0.11	0.12
Input AI (m/s)	11	15	2050	2170	329	386	37	56	-	35	-	25	1430	1224	2090	2028
11 m to 6 m — NS (% critical damping)	-	7	10	27	15	20	26	6	-	5	-	3	37	13	10	10
EW (% critical damping)	-	-	-	-	-	-	-	-	-	-	-	-	-	-	-	-
Input PA (g)	0.01	0.05	0.37	0.49	0.09	0.11	0.02	0.02	0.03	0.03	0.03	0.03	0.13	0.19	0.09	0.1
Input AI (m/s)	14	23	1100	-	274	279	34	42	30	39	16	19	1581	1496	1205	1406
17 m to 11 m — NS (% critical damping)	13	-	25	-	23	17	17	5	-	3	-	2	13	20	23	15
EW (% critical damping)	-	-	-	-	-	-	-	-	-	-	-	-	-	-	-	-
Input PA (g)	0.01	0.01	0.48	-	0.08	0.09	0.02	0.02	-	0.02	-	0.01	0.17	0.19	0.08	0.08
Input AI (m/s)	17	12	2040	-	225	250	28	33	-	21	-	9	1769	1258	1043	1058
47 m to 17 m — NS (% critical damping)	4	3	-	-	34	33	19	12	-	2	-	2	41	-	17	-
EW (% critical damping)	-	-	-	-	-	-	-	-	-	-	-	-	-	-	-	-
Input PA (g)	0.01	0.01	0.26	0.27	0.09	0.1	0.01	0.01	0.02	0.02	0.03	0.02	0.22	-	0.08	-
Input AI (m/s)	10	8	1760	1770	134	125	25	28	18	16	12	6	14	22-	1248	-
Surface to 11 m — NS (% critical damping)	-	-	-	-	-	-	-	-	-	-	-	-	-	-	-	-
EW (% critical damping)	-	-	-	-	-	-	-	-	-	-	-	-	-	-	-	-
Input PA (g)	0.01	0.05	0.37	0.49	0.09	0.11	0.02	0.02	0.03	0.03	0.03	0.03	0.13	0.19	0.09	0.1
Input AI (m/s)	14	23	1100	-	274	279	34	42	30	39	16	19	1581	1496	1205	1406
47 m to 11 m — NS (% critical damping)	-	-	-	-	-	-	-	-	-	-	-	-	-	-	-	-
EW (% critical damping)	-	-	-	-	-	-	-	-	-	-	-	-	-	-	-	-
Input PA (g)	0.01	0.01	0.26	0.27	0.09	0.1	0.01	0.01	0.02	0.02	0.03	0.02	0.22	-	0.08	-
Input AI (m/s)	10	8	1760	1770	134	125	25	28	18	16	12	6	2422	-	1248	-

65

A summary of second mode frequency estimates is given in Table 4.3, and damping estimates in Table 4.4. The damping is in general higher than for the fundamental modes, although the there is a fair amount of scatter due to the estimation process. If a system needed more than 2-DOF to model the soil response well, the second mode is often a "phantom" mode that does not represent strong system behavior. Therefore, the participation factor must be examined to determine whether the second and higher modes are significant.

4.2.1 Soil-Structure Interaction

The basic understanding of soil-structure interaction (SSI) predicts two effects of a structure sitting on a non-rigid foundation: (1) the fundamental frequency of the soil/structure system would be lower than that of the structure on a rigid base and (2) the damping ratio of the soil structure system will be larger than that of the structure on a rigid base (Kramer, 1995). These effects are in terms of the building rather than for the soil itself. Rollins and Seed (1990) discuss the various changes to soil response possible but come to no firm conclusions. The same is true for the extensive study on SSI for the Lotung site (Tang, 1987).

Damping and modal frequency results for DHA are given in Tables 4.1, 4.2, 4.3, and 4.4. The results are summarized graphically in Figs. 4.2 through 4.5 in comparison to the free field results. It is interesting to note that the decrease in fundamental frequency is much less pronounced for the results from DHA, the array under the model containment structure. For the 0-6 m interval the fundamental resonant frequency shifts only from 3.1 Hz for Event 3 (maximum acceleration 0.01g) to 2.2-2.4 Hz for Events 4, 12 and 16 (maximum accelerations of 0.17-0.49 g). Note also that the fundamental frequencies for the same events in the 0-6 m interval are lower under the structure compared to the free field values. This difference is no longer evident by the 6-11 m level. In fact, examination of the data for the 6-11 m, 11-17 m, 17-47 m and 11-47 m intervals indicate that modal frequencies are equivalent at DHA and DHB below 6 m. Other authors have predicted that the soil structure interaction would be evident to a depth of 17 m (Tang, 1987).

Examination of pseudo-stiffness provides another method of examining soil-structure interaction. While detailed analysis of this effect will follow in the sections on the individual

earthquakes, the results showed a clear effect for the top interval (6 m to the surface) and in rare occasions for the second interval (11 m to 6 m). For Events 4, 7, 8, and 16 the pseudo-stiffness is smaller at the structure than in the free-field. For event 12, the surface layer of soil appears to have a greater pseudo-stiffness than in the free-field.

4.3 Event 4

Event 4 subjected the Lotung site to the highest peak acceleration of any recorded event in the LSST suite (0.49 g), although the strong motion for Event 4 was very brief (about 1.6 seconds) as opposed to event 16 (about 12 seconds). This lead to a much lower Arias Intensity (1845 m/s vs. 3995 m/s) and a slightly smaller magnitude (M_L = 6.5 vs. 7.0). Because of the high peak acceleration and other properties (Elgamel, 1995) researchers thought that the pore water pressure generated during this event must be at least as great as that recorded during event 16. Since there is no pore water pressure record for Event 4, other methods must be found to estimate system behavior.

The Event 4 surface layer (6 m to the surface) signal from DHA proved difficult to model using stationary techniques, indicating some degree of non-linear behavior that can be captured using recursive techniques. It was found that the system could be well modeled as a 3-DOF ([6 6 1]) system using a forgetting-factor of 0.83 (Ljung, 1987). Figure 4.6 shows the congruency between the actual and modeled system, while the evolution of the three modal frequencies (1 Hz, 3.5 Hz, and 7.3 Hz) is given in Fig. 4.7. It is seen that the system behaves very erratically for the first 10 seconds, or the period of strong shaking. It is evident from the velocity history shown in Fig. 4.6 that the signal becomes more regular and lower in frequency content at this point. The change is reminiscent to that of a soil undergoing liquefaction, such as the time histories from the Wildlife site, Superstition Hills, earthquake (e.g. Glaser, 1996, 1995). The evolution of the Event 4 surface layer system damping could be estimated, and is given in Fig. 4.8.

Figure 4.5 Comparison of Event 4 surface layer actual and modeled (RARX [6 6 1]) outputs.
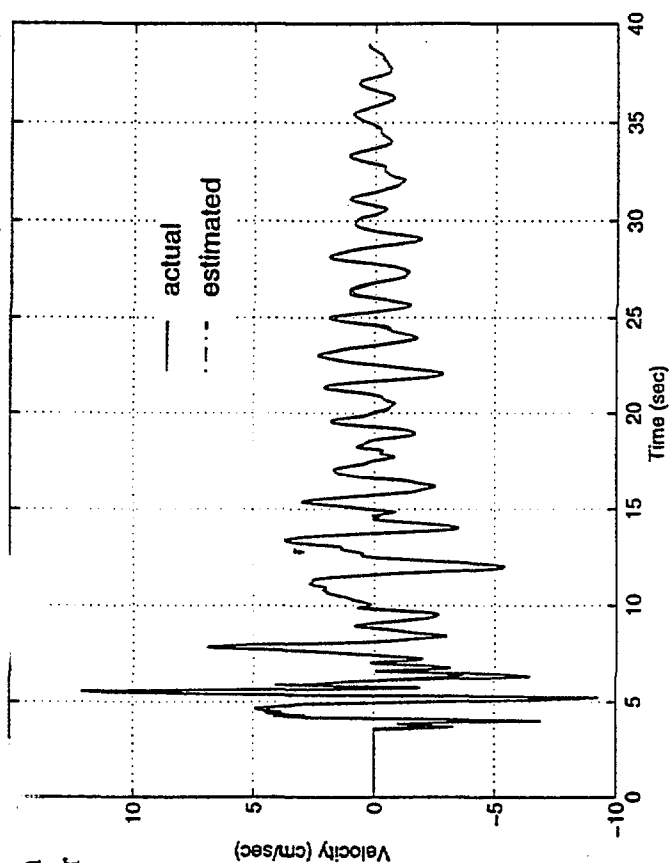
Figure 4.7 Evolution of the three modal frequencies (1 Hz, 3.5 Hz, and 7.3 Hz).
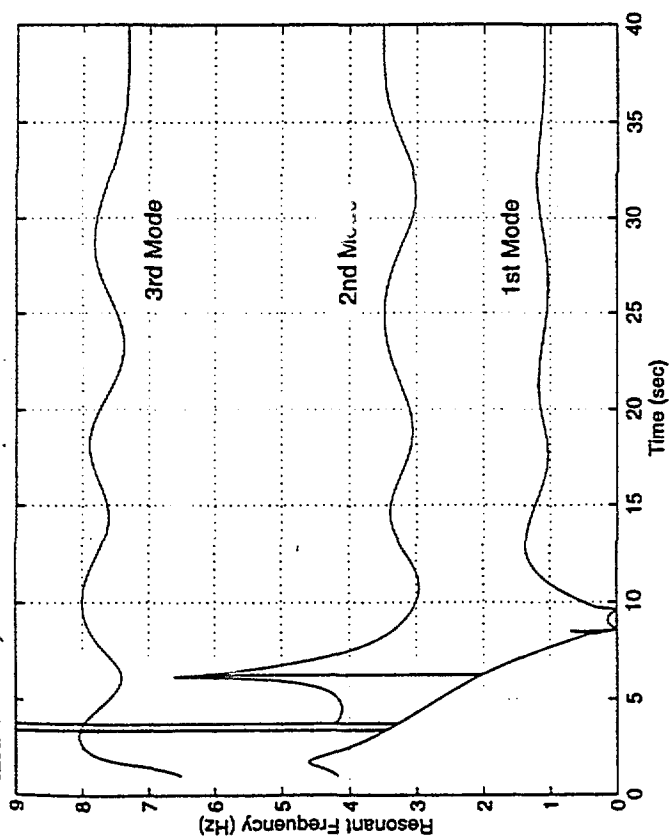
Figure 4.8 Evolution of the Event 4 surface layer system damping.

68
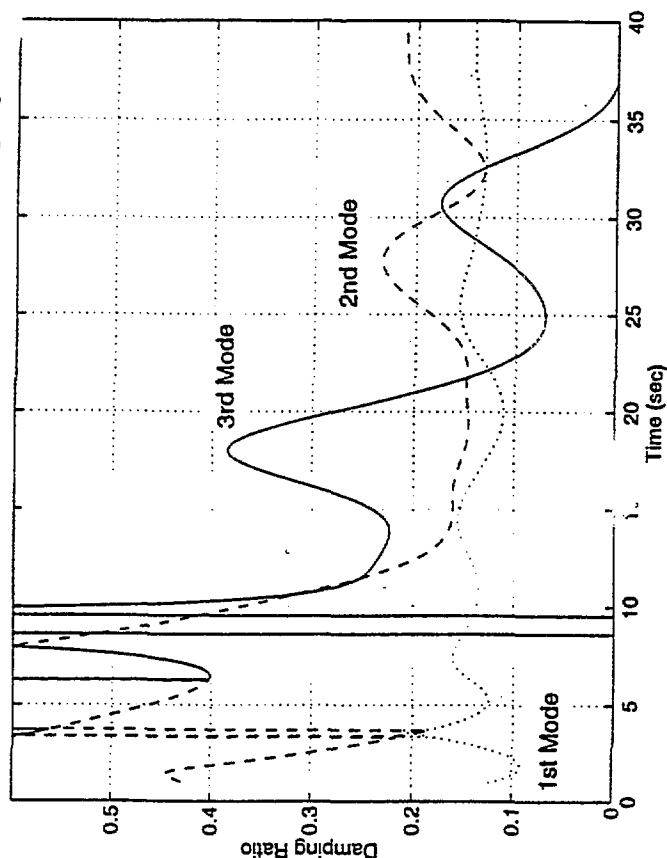
Figure 4.9   Event4, DHB vs. Event8, DHB; 6 m to Surface
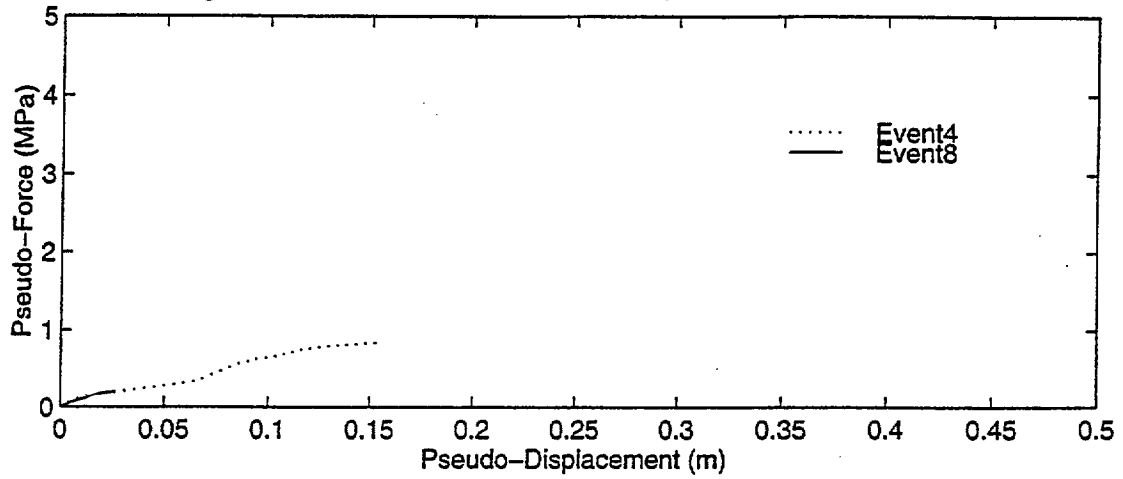
Figure 4.10 Event4, DHB vs. Event8, DHB; 11 m to 6 m
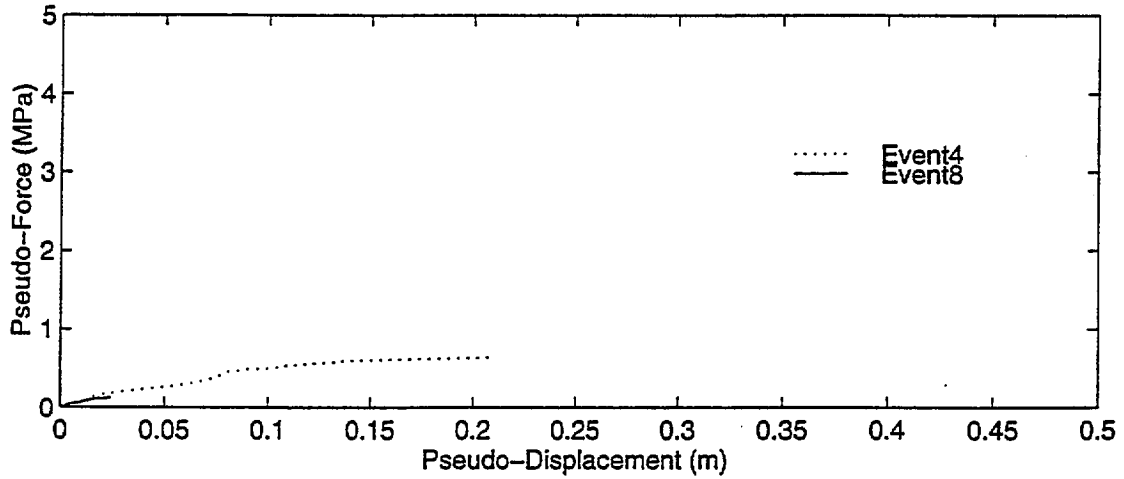
Figure 4.11 Event4, DHB vs. Event8, DHB; 47 to 11 m
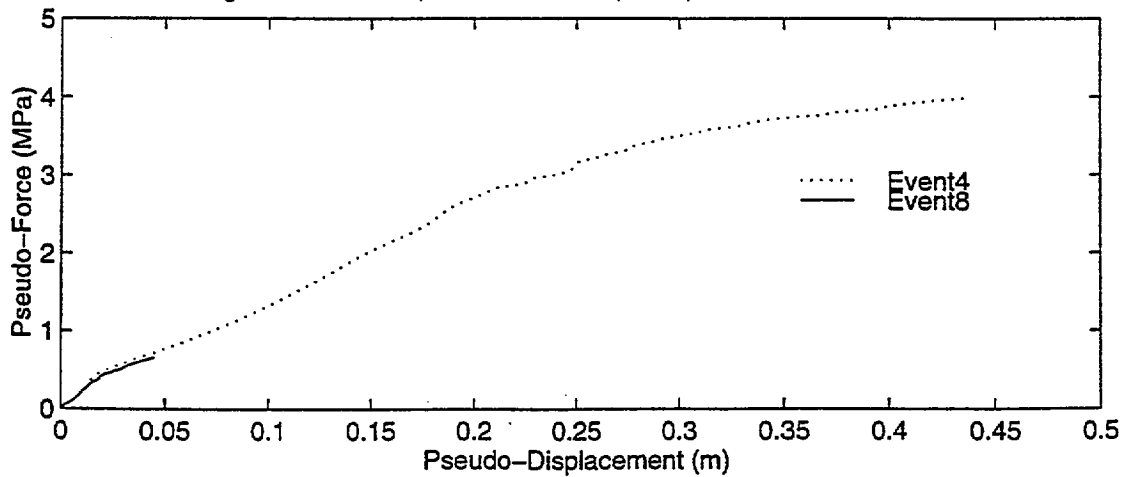
4.3.1 Event 4 Pseudo-Stiffness and Soil-Structure Interaction

One method is to compare the pseudo-stiffness behavior of the two events to determine if there was comparable softening taking place, in particular a comparison with a very small event such as Event 8. Figure 4.9 shows a comparison of the pseudo-stiffness for the deep interval, 47 m to 11 m (due to the confinement it is expected that this interval would show no loosening, as shown in Sect. 4.2). It is seen in detail that initially the pseudo-stiffness is identical for both Event 8 and 4, with slight reduction in pseudo-stiffness after the soil absorbed most of the Event 4 energy. The same observation holds true for the 11 m to 6 m interval shown in Fig. 4.10 and the 6 m to surface interval shown in Fig. 4.11.

However, when Event 4 pseudo-stiffness is compared to Event 16 pseudo-stiffness, the values are the same. Figures 4.12, 4.13, and 4.14 show a comparison in pseudo-stiffness between events 4 and 16 for the 47 m - 17 m, 11 m - 6 m, and 6 m to surface intervals, respectively. It is readily seen that the slopes shown (the pseudo-stiffness) are the same, although there was more total motion during Event 16 (AI≈ 4000 m/s) than Event 4 (AI≈ 1850 m/s).

Comparison of the pseudo-stiffness results from the free-field array (DHB) and the array adjacent to the containment vessel (DHA) show effects of soil-structure interaction. Figure 4.15 shows the pseudo-stiffness curve for both arrays, where it is seen that the slope is identical for the two. When the behavior for the 11 m to 6 m interval is examined in Fig. 4.16, there is evidence that the structure acted to smooth and constrain the soil behavior, although the soil ends up behaving the same in both locations. For the top interval, 6 m to the surface shown in Fig, 4.17, the soil adjacent to the structure shows significantly greater softening than that in the free-field.

This can be compared with values given in Table 4.1 for fundamental frequency. There is only a significant difference in fundamental mode for the top, 6 m to surface, interval - about 2.2 Hz at DHA and 2.8 Hz in the free-field. The damping estimates, from Table 4.2, are too erratic to yield any firm conclusions.

70

Figure 4.12 Event4, DHB vs. Event16, DHB; 11 m to 6 m
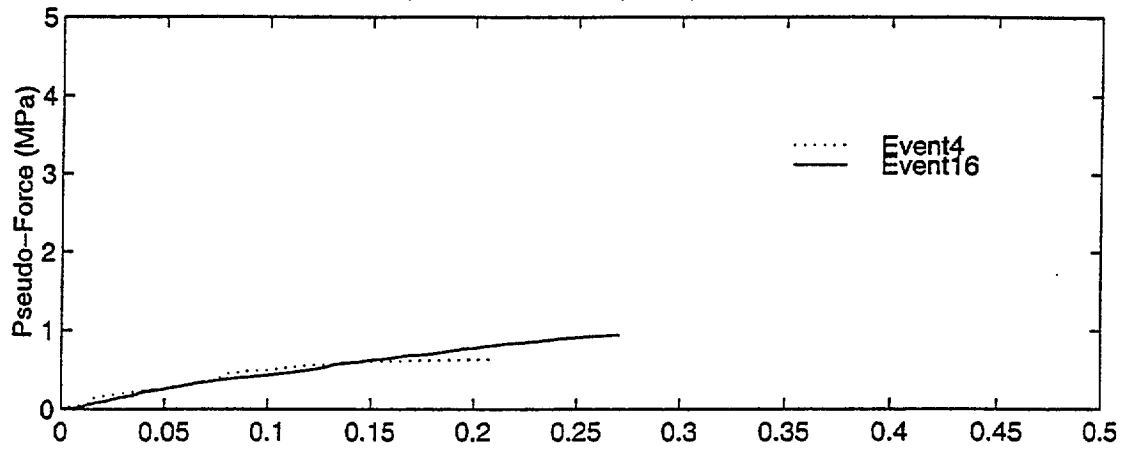
Figure 4.13 Event4, DHB vs. Event16, DHB; 11 m to 6 m
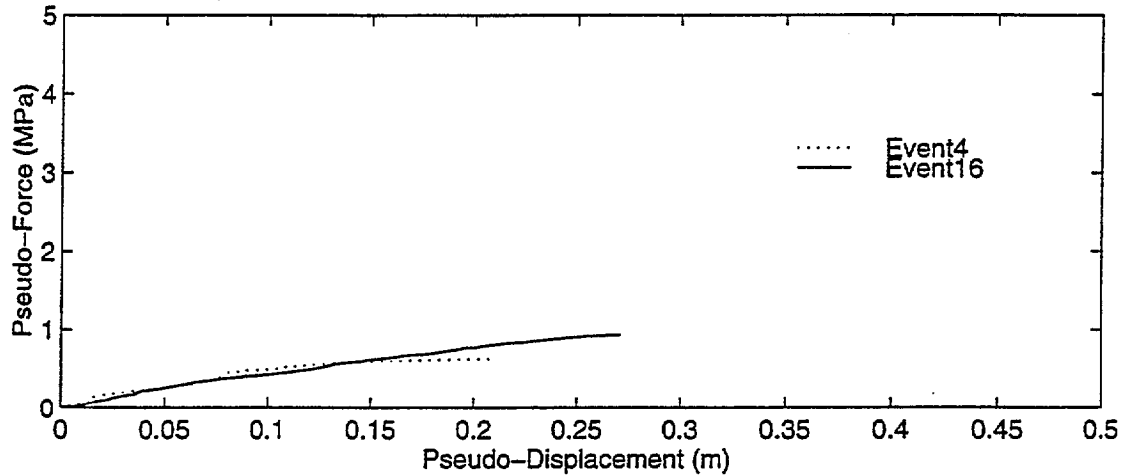
Figure 4.14 Event4, DHB vs. Event16, DHB; 47 m to 17 m

Figure 4.15 Event4 free-field vs. Event4 SSI; 6 m to surface
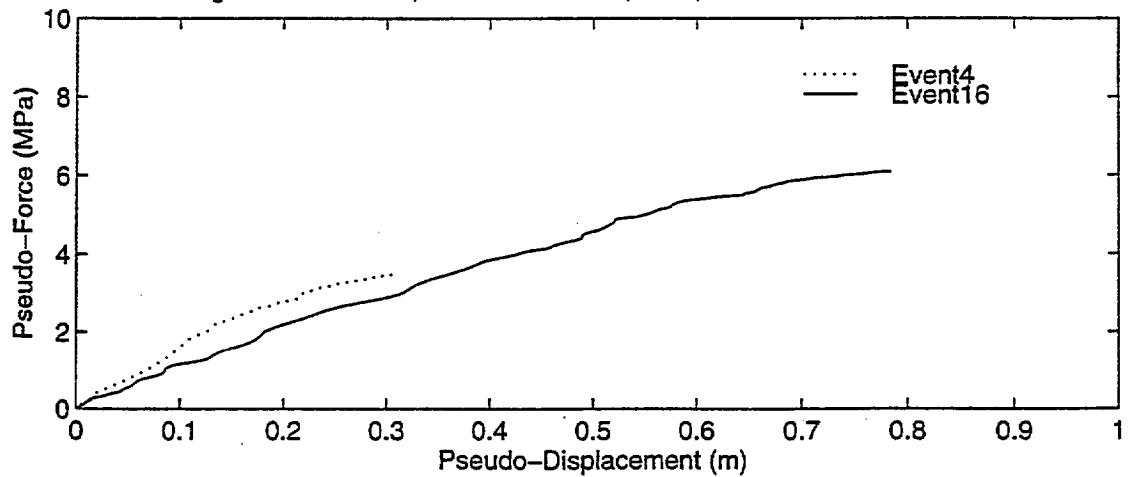
Figure 4.15 Event4 free-field vs. Event4 SSI; 6 m to surface

Figure 4.16 Event4 free-field vs. Event4 SSI; 11 m to 6 m
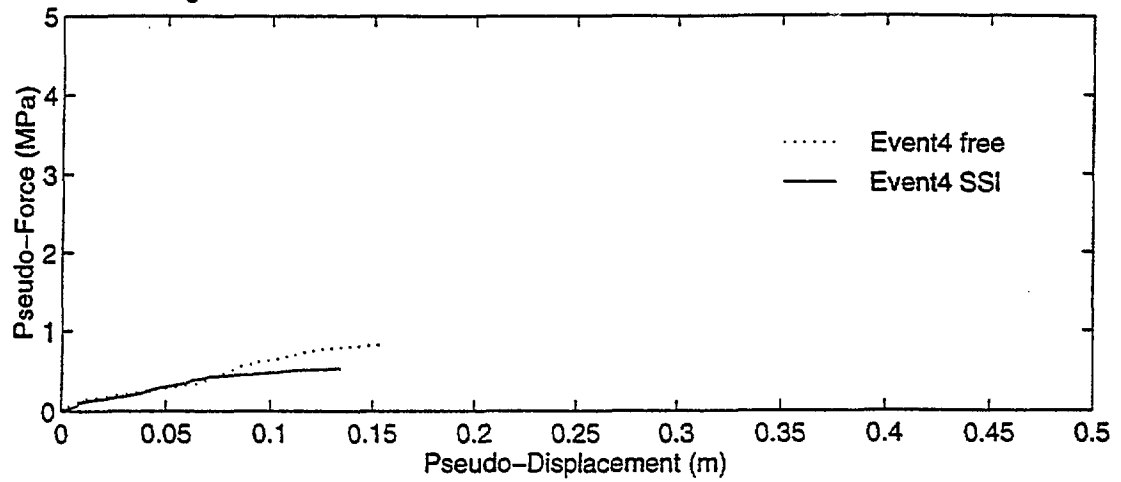
Figure 4.16 Event4 free-field vs. Event4 SSI; 11 m to 6 m

Figure 4.17 Event4 free-field vs. Event4 SSI; 47 m to 17 m
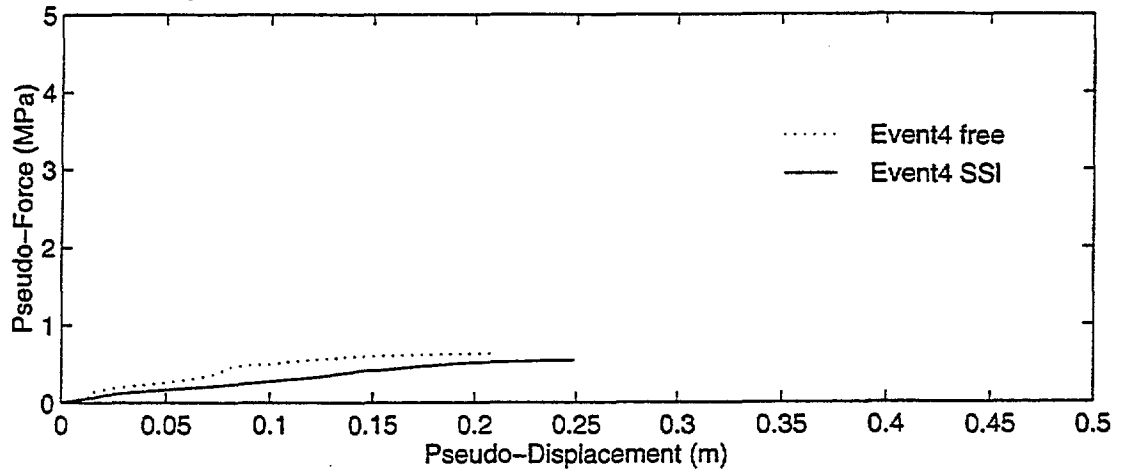
Figure 4.17 Event4 free-field vs. Event4 SSI; 47 m to 17 m
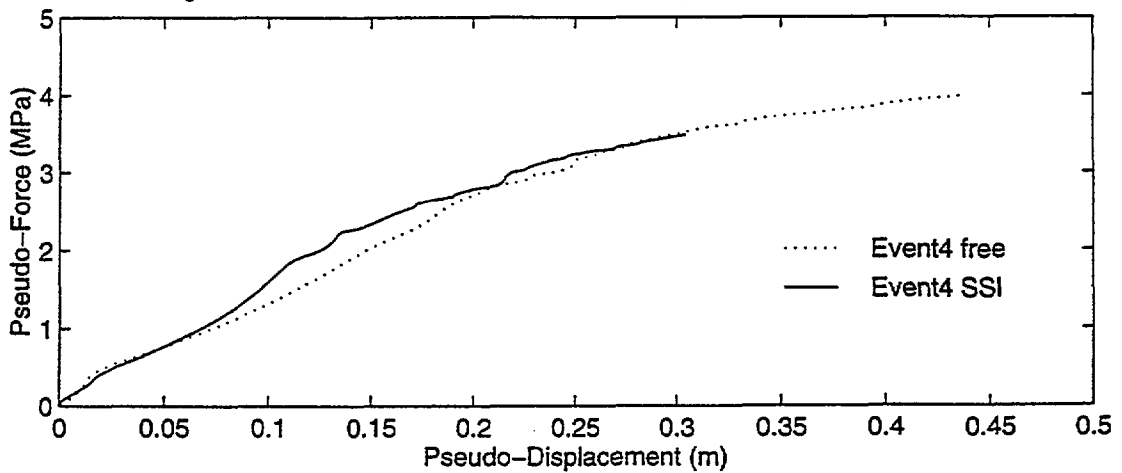
4.4 Events 7 and 8

Event 8 (M_L=6.2) is considered to be an aftershock of Event 7 (M_L=6.2) (see Section 2.4), so comparison of the results from these two events should cancel out any effects associated with hypocentral location and source parameters. Although both events had very similar magnitudes, peak acceleration for Event 7 was much greater than for Event 8 (0.21 g vs. 0.03 g) as was the Arias Intensity (652 m/s vs. 139 m/s).

However, the models for the low-energy Event 8 was able to capture the behavior of the various intervals well enough to accurately estimate the behavior of the Event 7 shaking. Figure 4.18 compares the actual Event 7 surface layer output to the output estimated from the appropriate Event 8 filter. The input to the model was the N-S 6 m velocity time history. Further evidence as to the model capturing the essence of the layer is given in Fig. 4.19 which is a comparison of the Event 7 E-W output to the Event 7 output modeled through the Event 8 N-S filter.

Figure 4.20 shows the results of modeling Event 8 N-S output through the Event 7 N-S filter. The filter captures the frequency information, with only a very slight (2 time step) phase lag, but tends to overestimate the early, high, amplitudes by about 10%. These results are consistent through all intervals, with the results of the 17 m to 11 m interval shown in Figs. 4.21 and 4.22.

As expected, the estimated resonant frequencies are lower for Event 7, and damping is higher. The ability for Event 8 filters to so well model Event 7 events causes additional difficulty is interpreting these results - what are the "correct" values? Models created for Event 7, even using recursive techniques, sometimes do not map the data as "well" as the filter calculated from Event 8, although results using the representative filter give physically satisfying results - we expect the damping to be greater for Event 7 since there was quite high peak acceleration and Arias intensity. Our interpretation is that the change in soil behavior between Event 7 and 8 is small enough that the low-strain filter captures the essence of the soil layer behavior. The statistical confidence of this estimate is illustrated in the graphs shown in fig. 4.23. This figure shows the 99% confidence interval in both the time and frequency domain. The slight change in soil properties between events is reflected in the Event 7 filter.
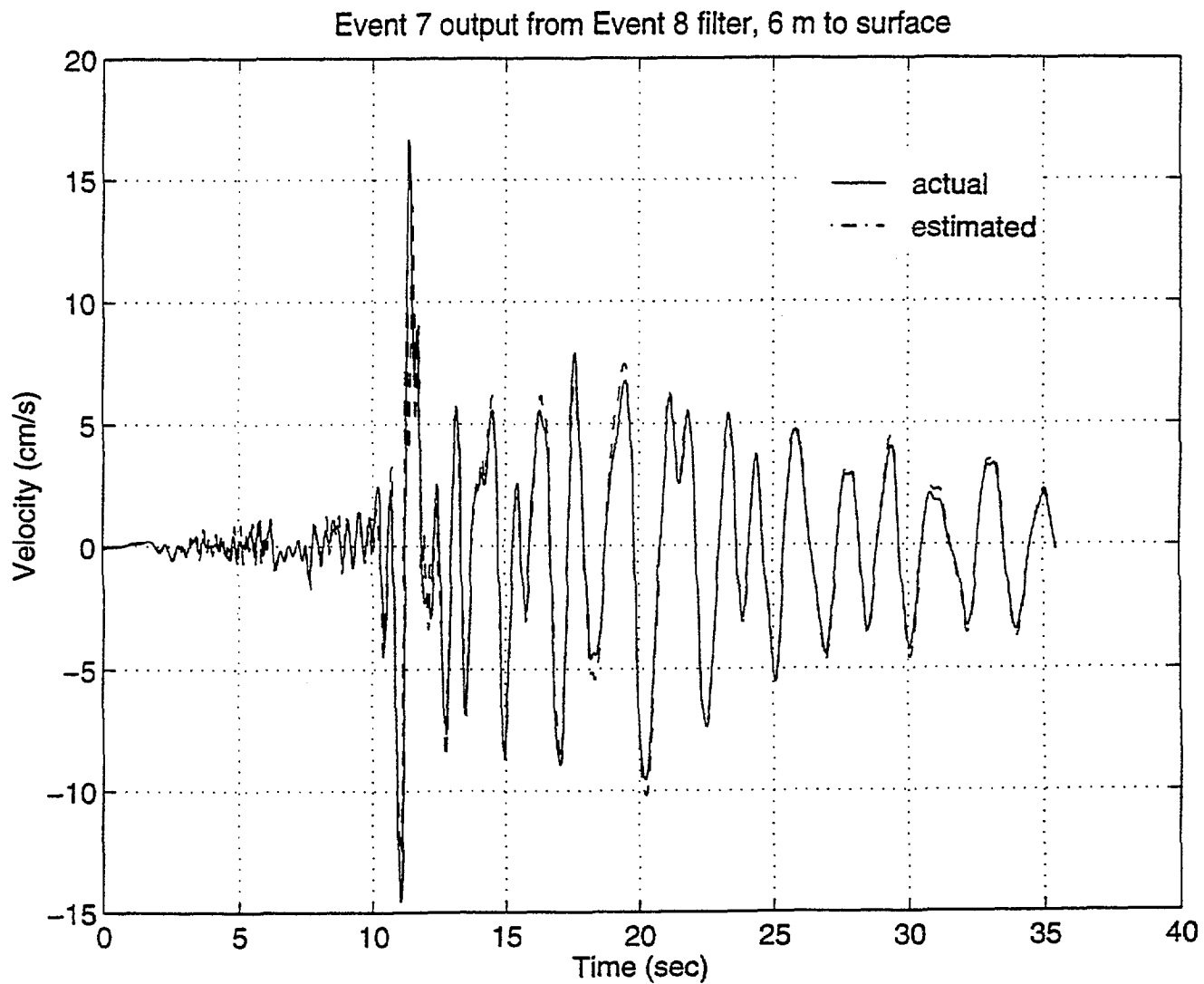
Figure 4.18 Comparison of the actual Event 7 surface layer output to the output estimated from
the appropriate Event 8 filter
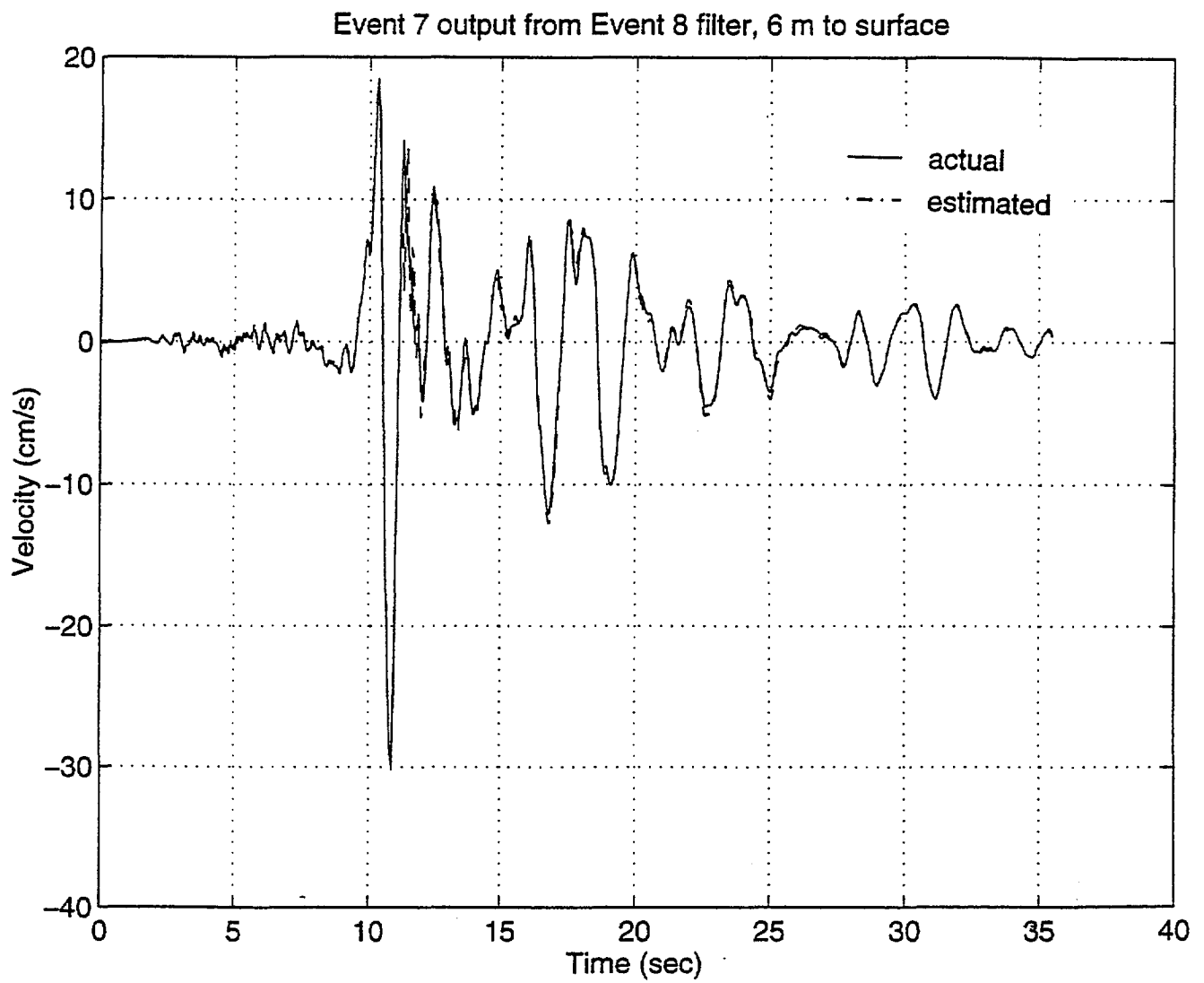
Figure 4.19   Comparison of the Event 7 E-W output to the Event 7 output modeled through the
Event 8 N-S filter

Event 8 output from Event 7 filter, 6 m to surface
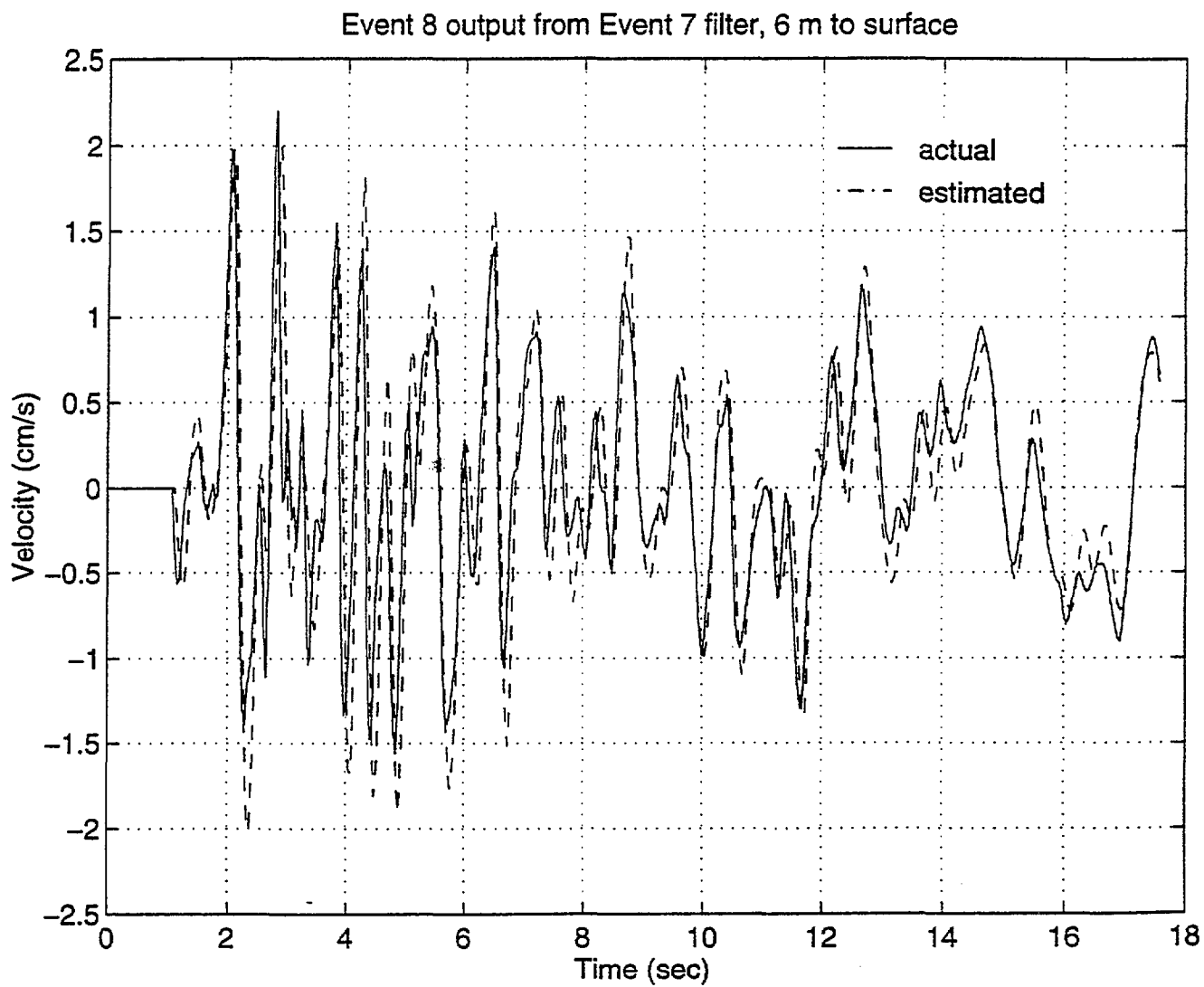
Figure 4.20   Results of modeling the Event 8 N-S output through the Event 7 N-S filter, 6 m to the surface.

Event 7 output from Event 8 filter, 17 m to 11 m
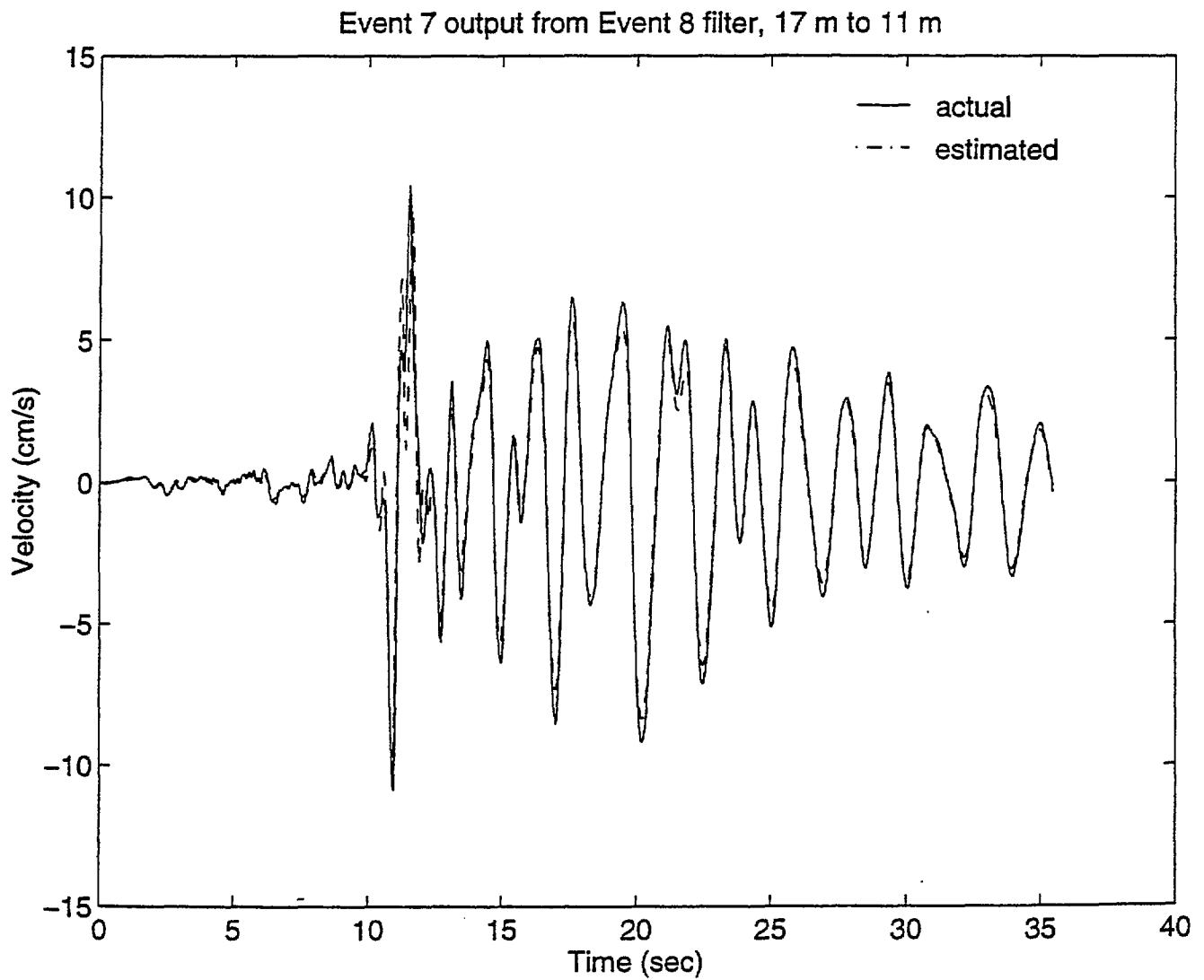
Figure 4.21   Results of modeling the Event 7 N-S output through the Event 8 N-S filter, 17 m to 11 m.
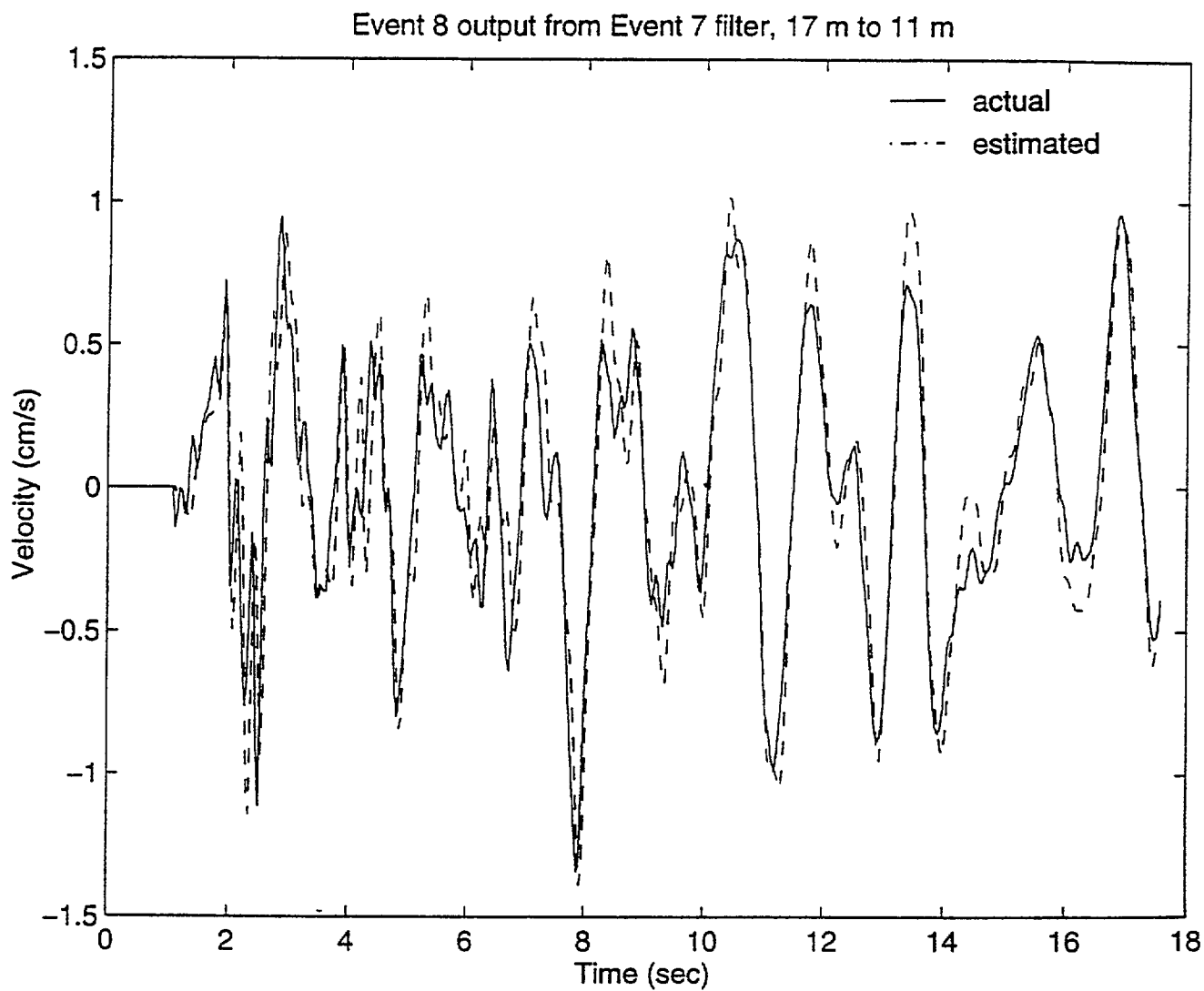
Figure 4.22 Results of modeling the Event 8 N-S output through the Event 7 N-S filter, 17 m to
11 m.
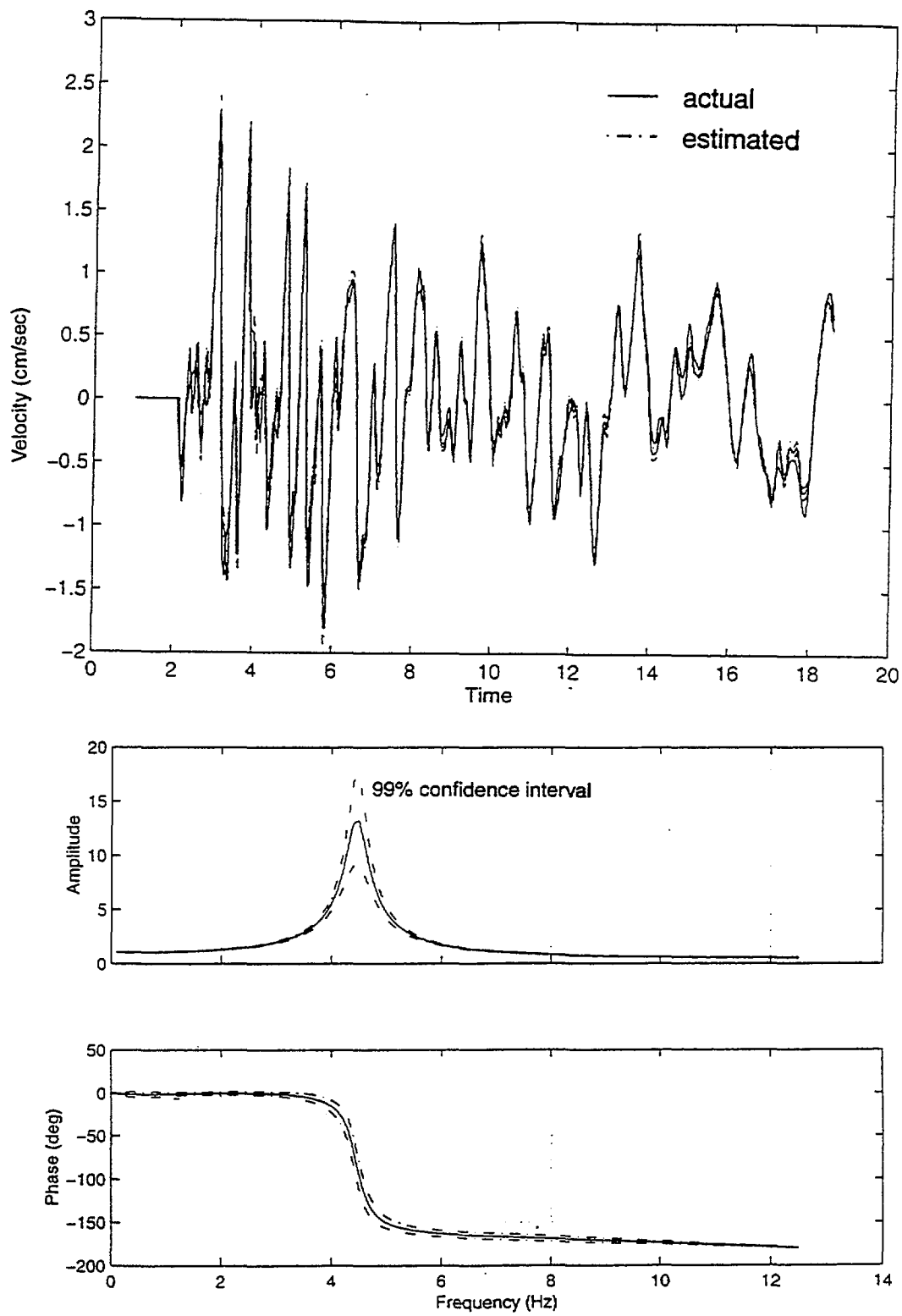
Figure 4.23 99% confidence interval for estimated output, Event 8, 6 m to the surface, in the time and frequency domain.
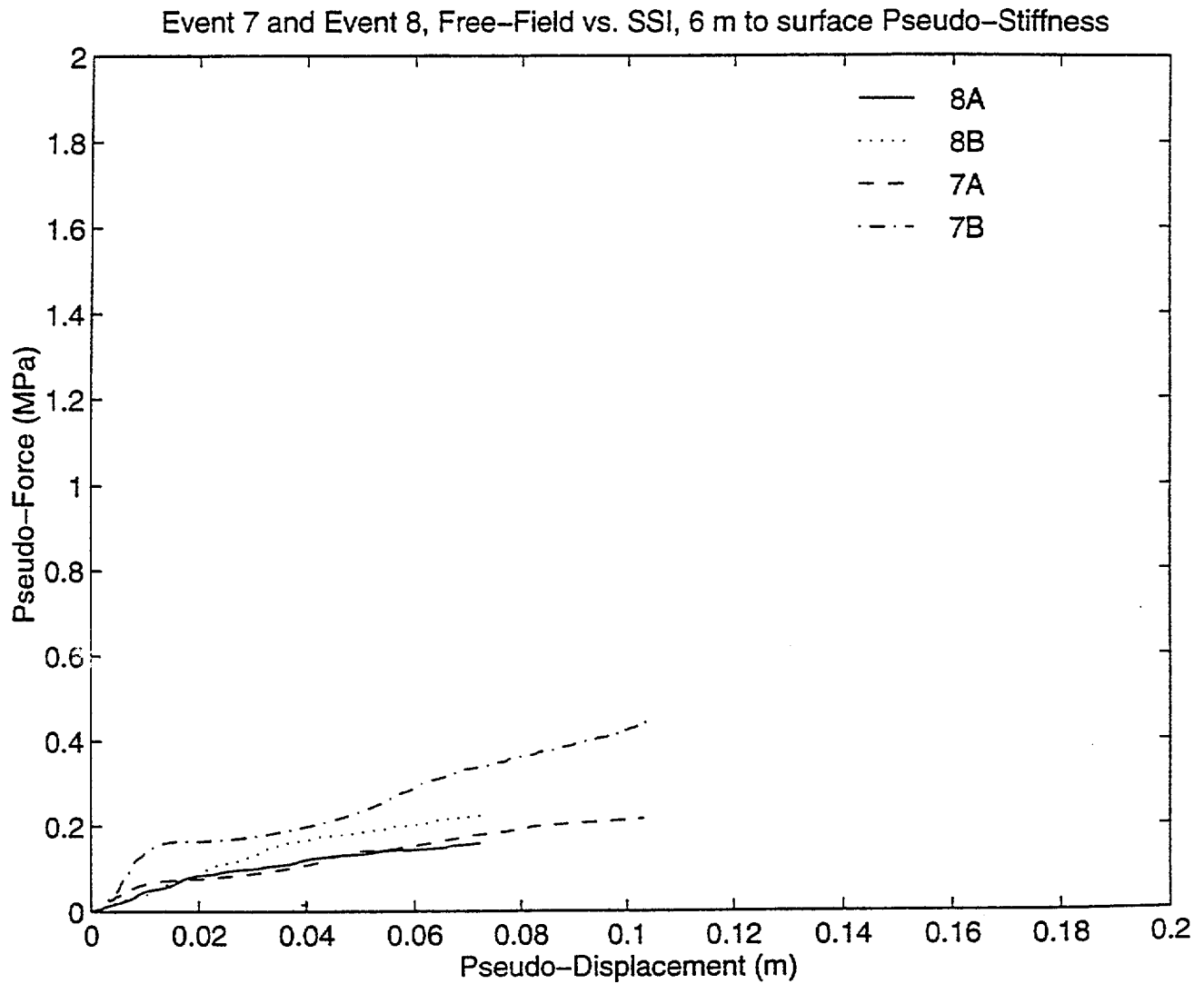
Figure 4.24   Comparison of pseudo-stiffness for DHA and DHB for Events 7 and 8.

4.4.1 Event 7 and 8 Soil-Structure Interaction

Effects of soil-structure interaction (SSI) on the stiffness and damping estimates are evident from entries in Tables 4.1 and 4.2. As for Event 4, all effects of SSI are gone by a depth of 17 m, and are hardly evident at 11 m. These effects are evident in Fig. 4.24, which is a comparison of pseudo-stiffness for DHA and DHB for Events 7 and 8. The pseudo-stiffness is the same for DHA for both events, implying that the structure mitigated much of the strain-induced effects. The free-field stiffness is initially much greater than for DHA, and then approaches the level of the soil affected by SSI. For the second interval, 11 m to 6 m, there is only slight effects of SSI evident for Event 7, as shown in Fig. 4.25. For the deep two intervals, Figs. 4.26 and 4.27 show identical behavior for both arrays and both events.

4.5 Event 16

Event 16 was the highest magnitude ($M_L = 7.0$) event recorded at Lotung, and also had the greatest Arias Intensity (3995 m/s). Pore water pressure was recorded for this event, and is included in Appendix C. A summary of response in comparison to estimated strain is given in Fig. 4.28 (Zeghal and Elgamel, 1993). Although the strain was large enough that the estimated damping ratios were greater than for low energy events and the resonant frequency was greater (see Tables 4.1 and 4.2), it would be of tremendous interest to actually track softening of the soil throughout the event. An obvious indication of softening would be phase shift between the deepest layer and the surface record (e.g. Glaser, 1996). Figure 4.29 is a comparison of N-S velocity for the 47 m and surface layers. It is seen that the greatest effect of 47 m of soil is an "amplification" of velocity at the surface, which is evident for the 47 m to 17 m interval as well, Fig. 4.30. The only indication of phase offset is between about 24 s and 27 s, and it is not a systematic offset such as would occur from serious softening of the intervening soil layers.

Another method of looking for changes in the system through time is to use a segmentation algorithm which uses parallel recursive algorithms to find parametric changes within stated limits (e.g. Ljung, 1993; Andersson, 1985). Figure 4.31 presents the fundamental frequency and damping estimates for the 6 m to surface interval, and shows a change in the system that can be
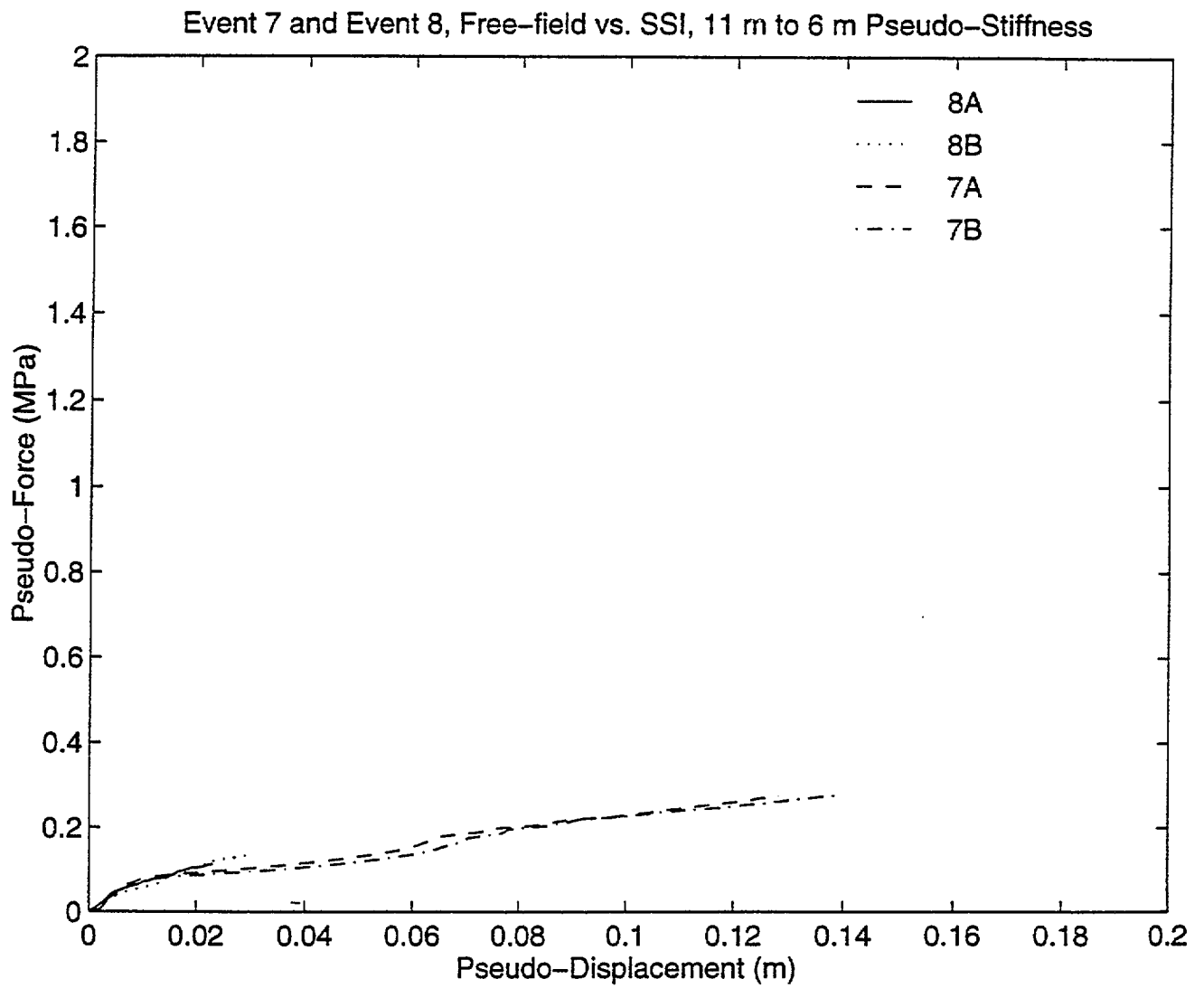
Figure 4.25   Comparison of pseudo-stiffness for DHA and DHB for Events 7 and 8, 11 m to 6 m.
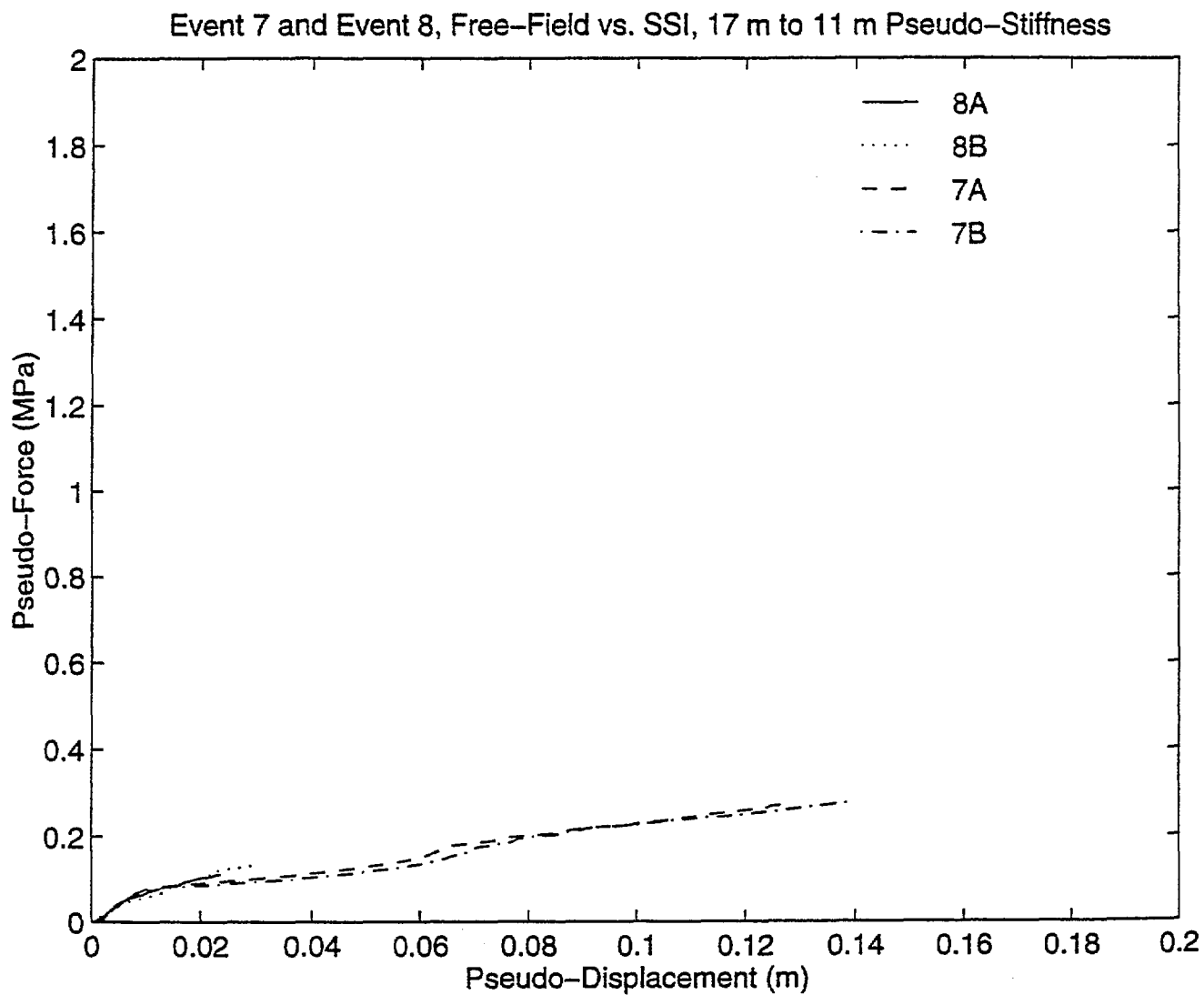
Figure 4.26 Comparison of pseudo-stiffness for DHA and DHB for Events 7 and 8, 17 m to 11 m.
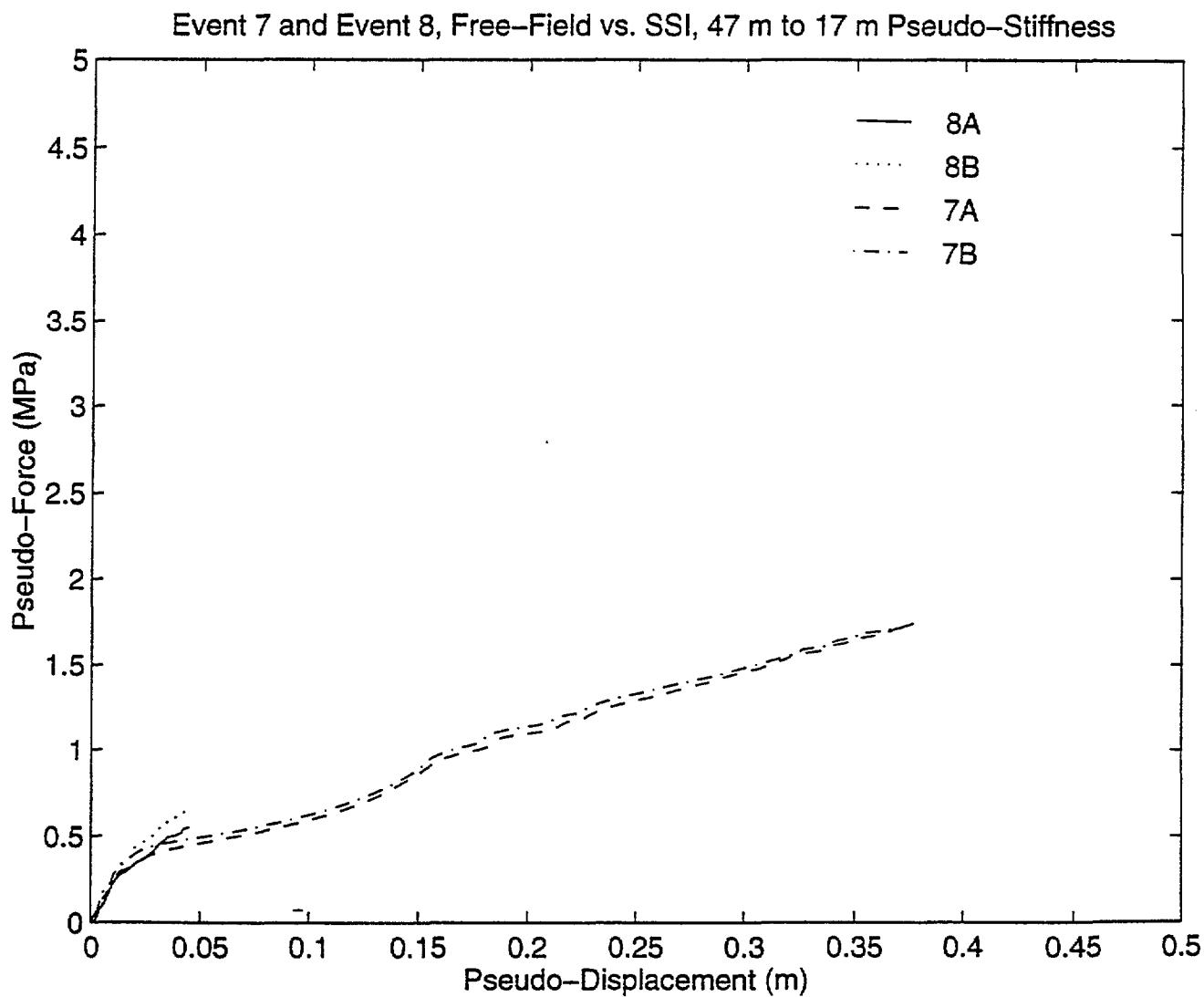
Figure 4.27 Comparison of pseudo-stiffness for DHA and DHB for Events 7 and 8, 47 m to 17 m.
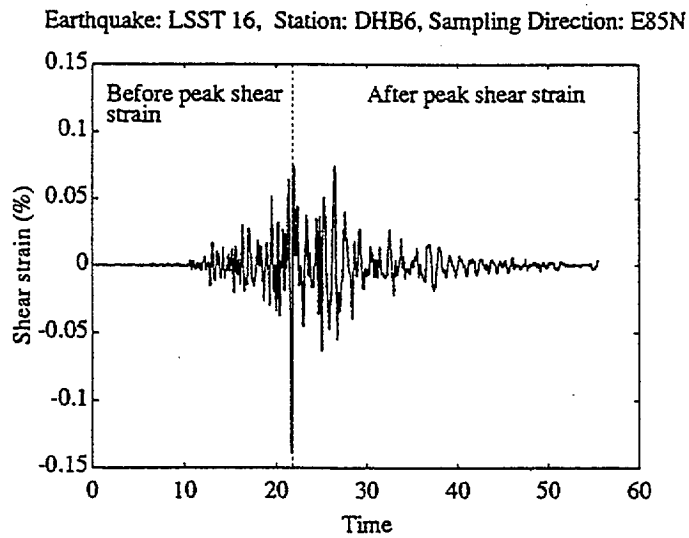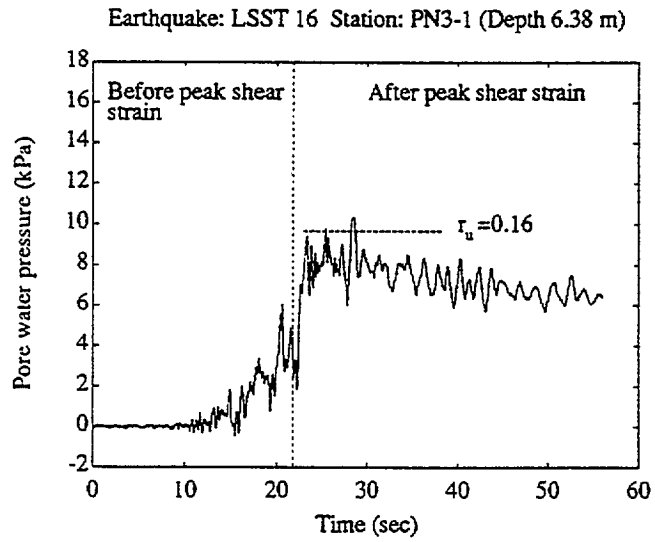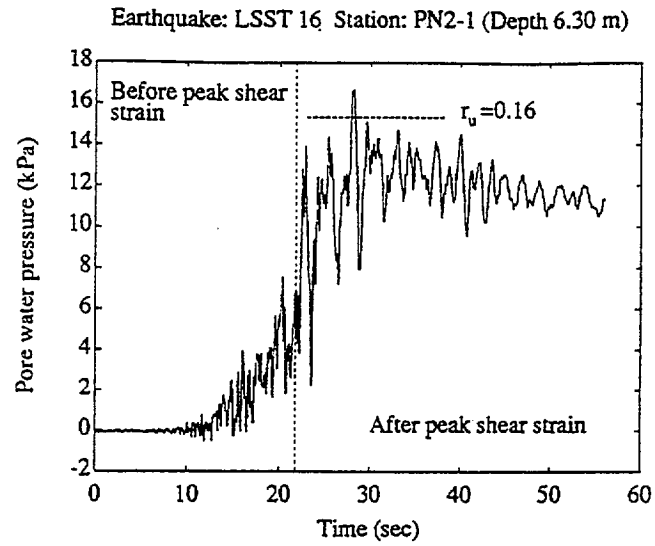
Figure 4.28 Pore water pressure buildup and shear strain history, Event 16, DHA, 6 m depth (from Zaghel et al., 1995).

Event 16, DHA, comparison of 47 m to surface interval
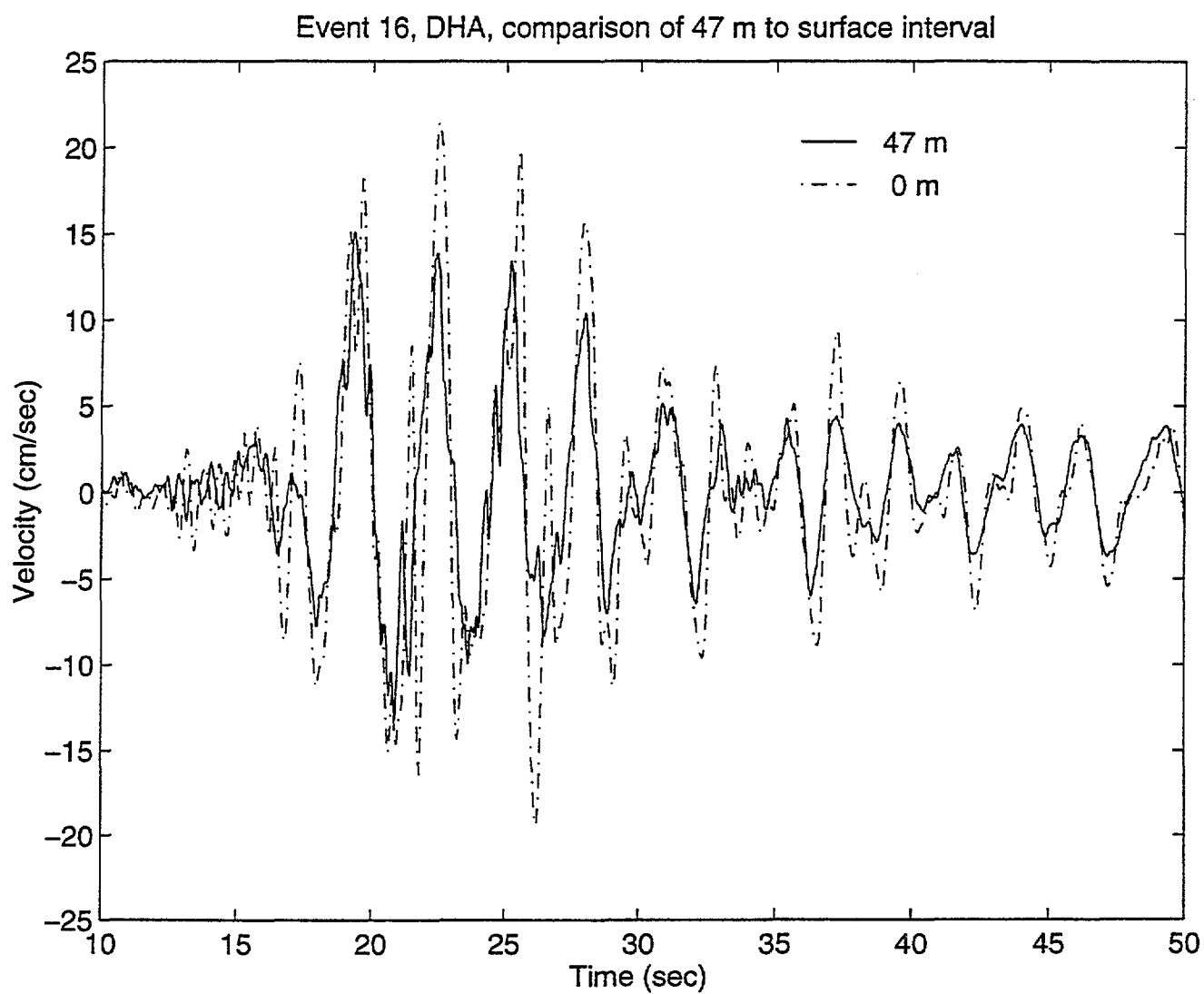
Figure 4.29   Comparison of N-S velocity for the 47 m and surface layers, DHA, Event 16.
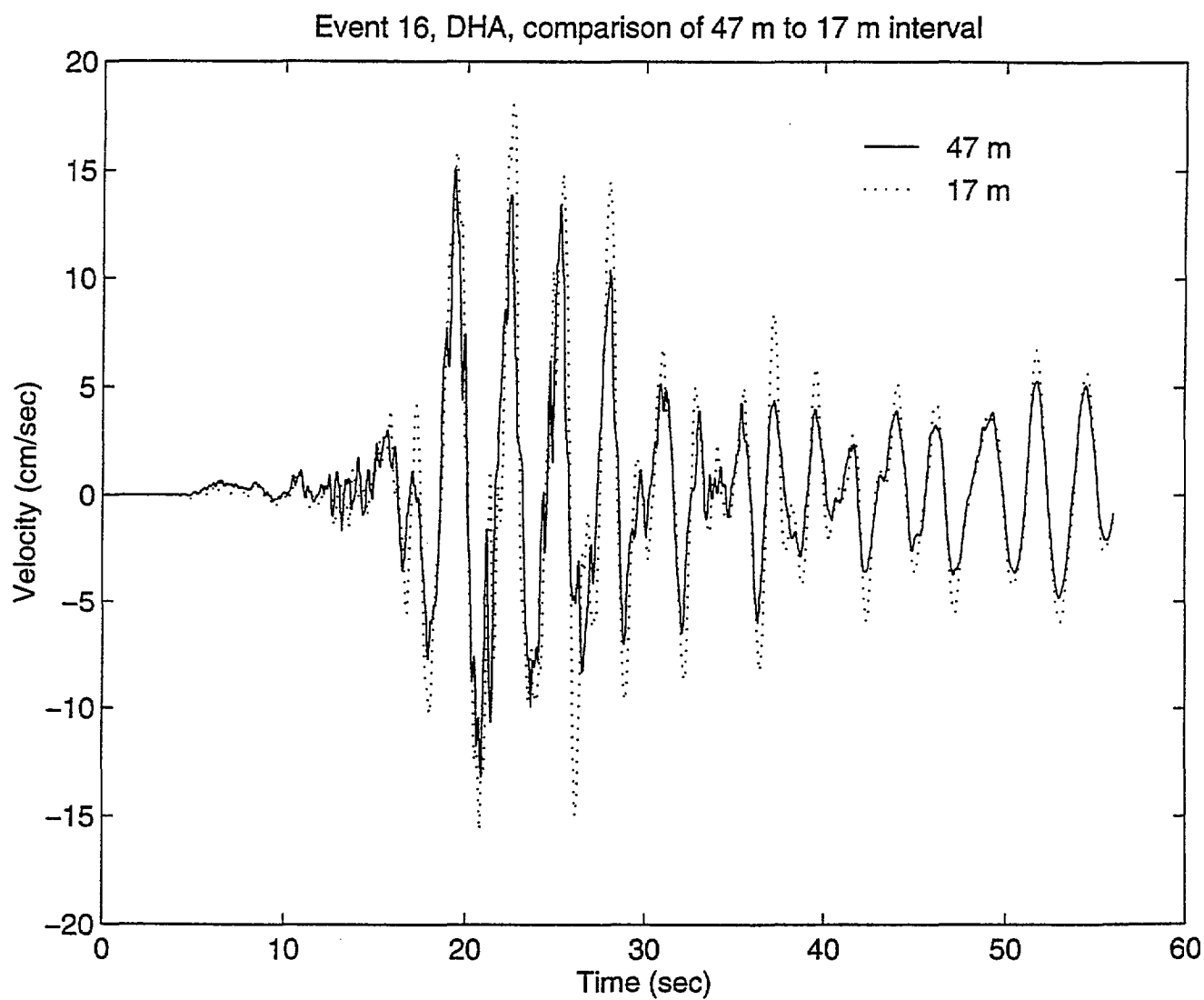
Figure 4.30 Comparison of N-S velocity for the 47 m and 17 m layers, DHA, Event 16.
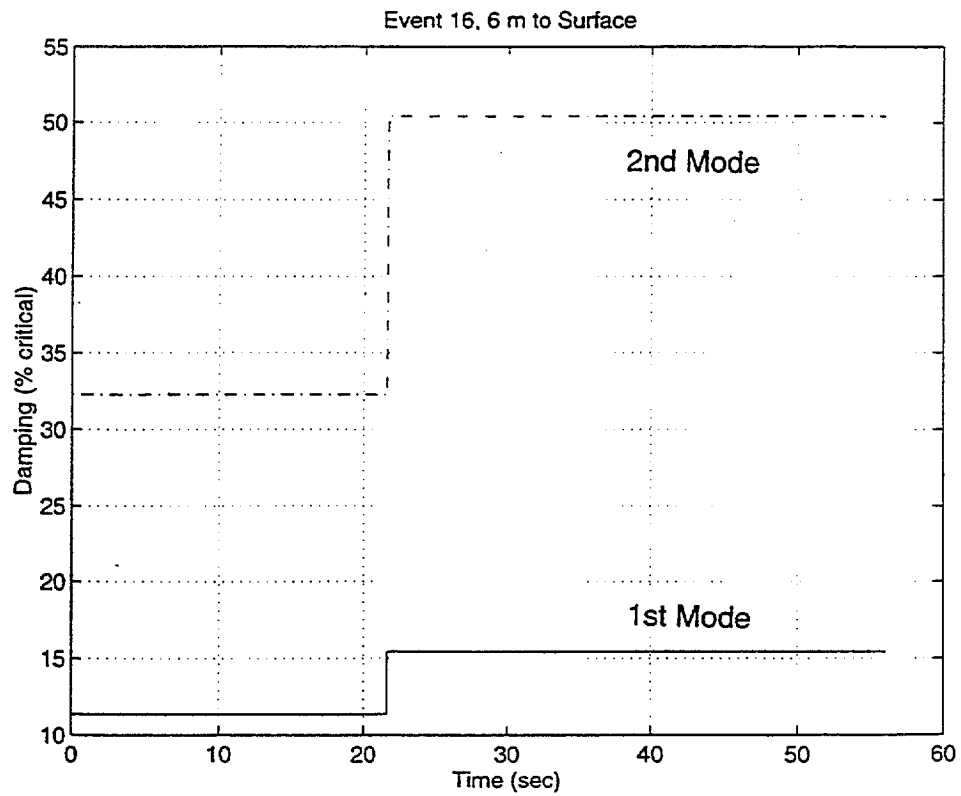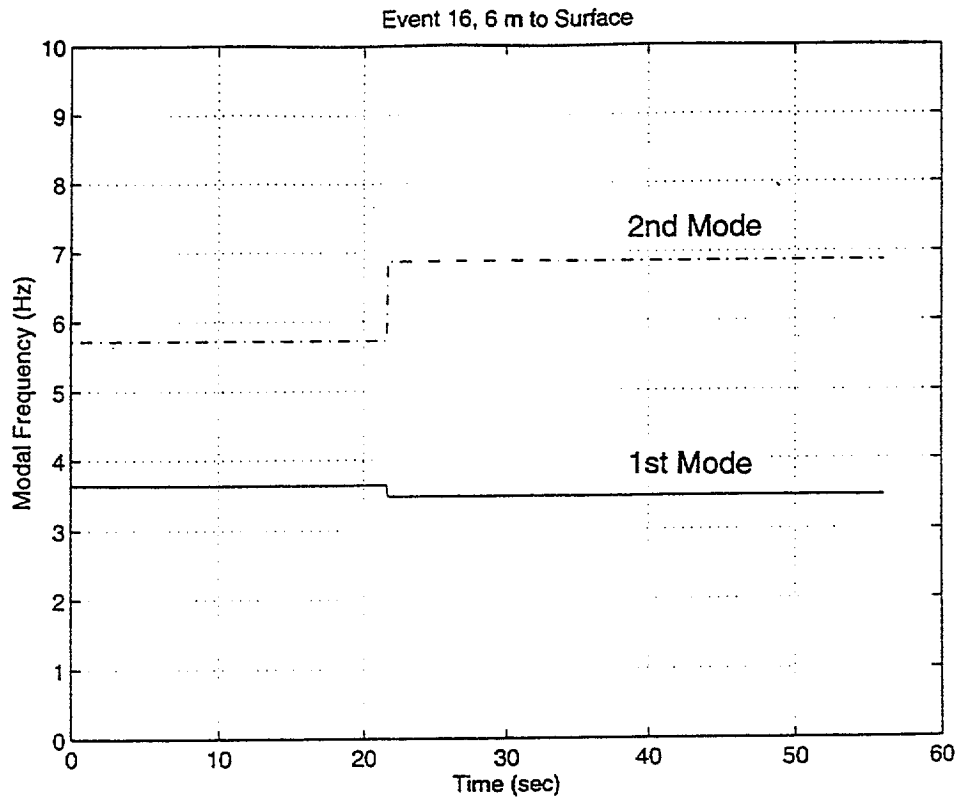
Figure 4.31 Fundamental frequency and damping estimates for 6 m to surface interval, Event 16.
Note change that can be attributed to softening at about 22 seconds into the temblor.

88
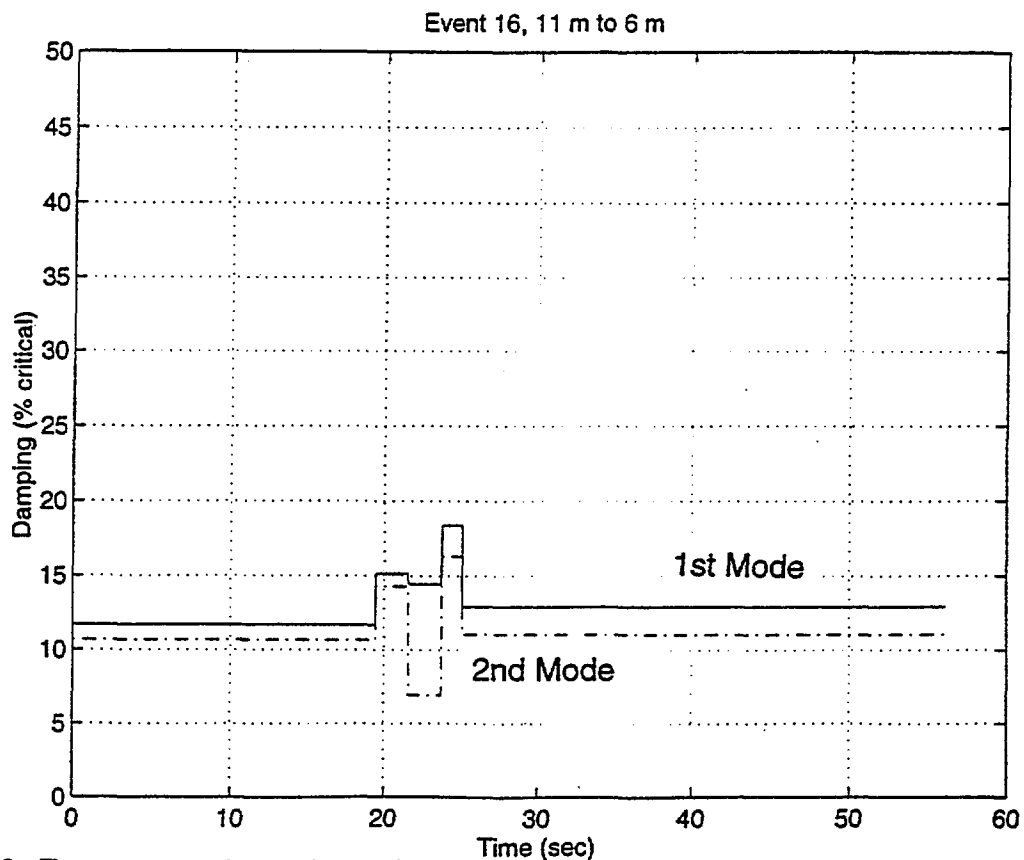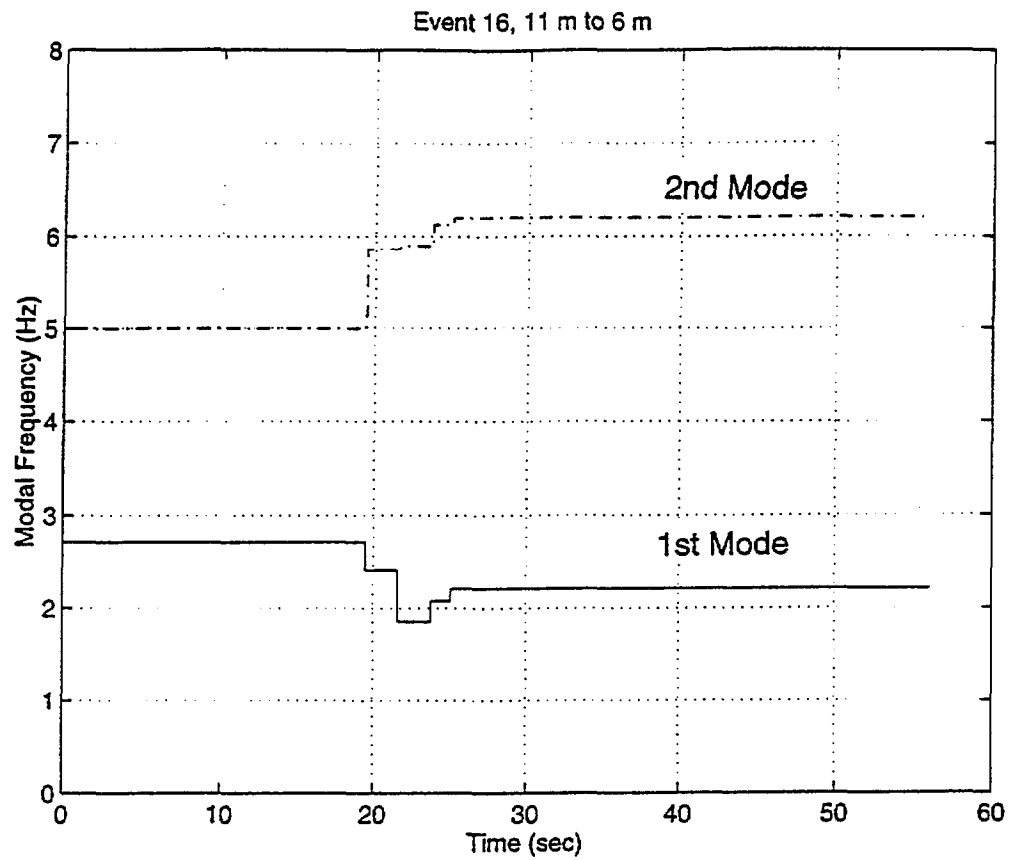
Figure 4.32 Frequency and damping estimates for 11 m to 6 m interval, Event 16. The variance needed indicate a system change is lower than for Fig. 4.31.

attributed to softening at about 22 seconds into the temblor, as per Zeghal et al. (1995). Figure 4.32 is a similar presentation for the 11 m to 6 m interval, but with the required change in parameters to indicate a system change held to closer tolerance. The change in system parameters correlates very nicely with the increase in pore pressure shown in Appendix C and Fig. 4.28.

However, the change in parameters throughout the event is tenuous and sensitive to analysis method. The "average" values, although they reflect softening, can easily "overpower" the subtle temporal changes. An example is shown in Fig. 4.32, which shows the excellent fit for the 6 m to surface interval using a time-invariant model, and the frequency response for this system. The goodness-of-fit in the frequency domain is indicated by the 99% confidence interval given by the dashed lines. The question remains as to which model - time invariant or non-stationary - better "captures" the nature of soil behavior.
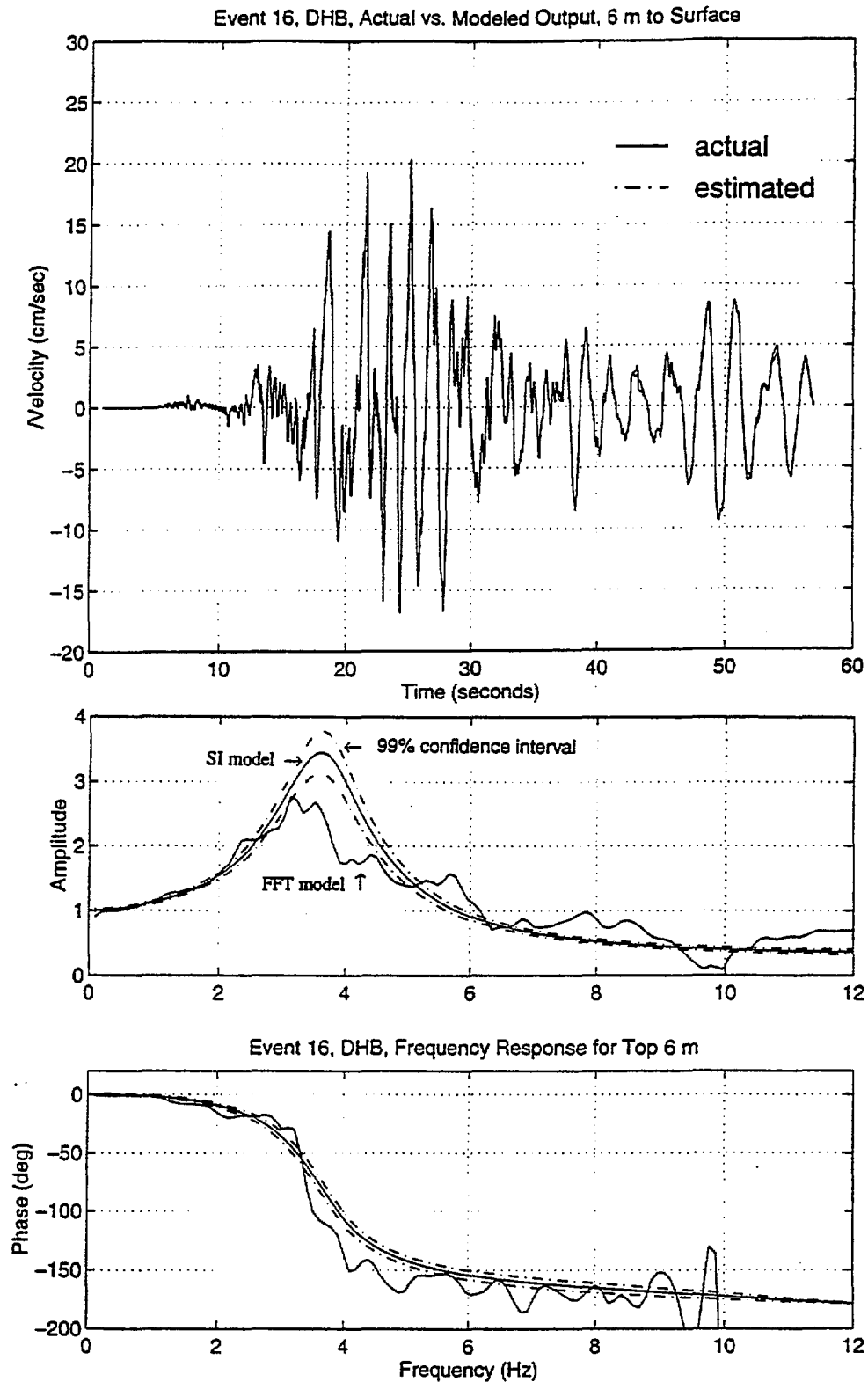
Figure 4.32 Event 16, 6 m to surface, in the time and frequency domain using a time-invariant model, and the frequency response for this system. The goodness-of-fit in the frequency domain indicated by the 99% confidence interval in dashed lines.

CHAPTER 5 - CONCLUSIONS

This report describes the process and results of using system identification to calculate soil system parameters for eight earthquakes of varying intensities recorded at the Lotung Large Scale Seismic Test Site in northeastern Taiwan. For this study the modal frequencies and damping ratios were calculated for depth intervals of 0-6 m, 6-11 m, 11-17 m, 17-47 m, 0-11 m and 11-47 m for events 3, 4, 7, 8, 9, 10, 12 and 16 with local magnitudes ranging from 4.5 to 7.0. The modal frequencies and damping ratios calculated are examined for the effect of local energy intensity and soil-structure interaction. Modal frequencies are seen to decrease with increasing intensity once a certain threshold of acceleration/intensity is reached. This result is consistent with the data obtained by other authors using different techniques. For the 0-6 m interval the decrease in frequency with event energy is less pronounced under a model containment structure than in the free field. This soil-structure effect is increasingly diminished with depth and absent by the 17-47m interval. Calculated damping values demonstrate an expected increase with input seismic energy. For the 0-6 m and 6-11 m intervals the damping values are higher under the model structure than in the free field. This distinction is completely missing in the 17-47 m results. The transition to non-linear behavior, while less pronounced with increasing depth, consistently occurs above a peak acceleration of 0.05 g or Arias Intensity of 100 m/sec.

System identification was used to calculate modal frequencies and damping values for various intervals for eight earthquakes of a range of ground intensities. System identification is a technique that identifies the important parameters of a mechanical system by modeling the effect of the system on an input signal. Comparing the expected output predicted by an SI model with the actual output determines which modeled mechanical system is an accurate representation of the system being studied. This method was used to characterize the behavior of the soil at the Wildlife site in the Imperial Valley for the Elmore Ranch and Superstition Hills earthquakes of 1987 (Glaser, 1996). The same author has also written a paper describing the potential advantages of parametric modeling (system identification) over spectral ratio descriptions of a system transfer function (Glaser, 1995). Essentially, parametric models give a more reliable estimate of signal spectral content when short, and/or non-stationary signals are being considered. A specific

parametric model, the ARMA (autoregressive-moving-average) model, is ideally suited for this problem because it can be derived from the equations of motion for an N degree of freedom (N-DOF) oscillator. The vibrating soil layer is the system of interest, the natural frequency and damping ratio information are contained in the system parameters.

The results clearly indicate some non-linear response over the intervals studied. Evidence of a decrease in specific interval fundamental frequency and an accompanying general trend of increased damping with higher seismic energy are clear. Comparison of the results of this study with previous work considered with the inherent superiority of parametric modeling for transient and/or non-stationary time series such as earthquakes indicate that system identification is a more robust method for identifying fundamental frequencies and damping values for layers of earth materials when borehole information is available.

CHAPTER 6 BIBLIOGRAPHY

Abdel-Ghaffar, A. M., & Scott, R. F. (1979). Shear moduli and damping factors of earth dam. *Journal of the Geotechnical Engineering Division*, ASCE, 105(GT12), pp. 1405-1426.

Anderson, D.G. (1993). Geotechnical Synthesis for the Lotung Large-Scale Seismic Experiment, *Report TR-102362*, Palo Alto: Electric Power Research Institute.

Anderson, D. G. and Tang, Y. K. (1989). Summary of Soil Characterization Program for the Lotung Large-Scale Seismic Experiment. *Proceedings: EPRI/NRC/TPC workshop on seismic soil-structure interaction analysis techniques using data from Lotung, Taiwan, Report NP-6154*, Palo Alto: Electric Power Research Institute.

Andersson, P. (1985). Adaptive Forgetting in Recursive Identification Through Multiple models. *International Journal of Control*, 42(11), pp. 1175-1194.

Astrom, K. J., and Eykhoff, P. (1971). System identification — a survey. *Automatica*, 7(2), pp. 123-162.

Bracewell, R. N. (1978). *The fourier transform and its applications*. New York: McGraw-Hill.

Bohlin, T. (1987). Model validation. *Encyclopedia of systems and control* (ed. Singh, M.) Oxford: Pergamon Press.

Chang, C.-Y., Mok, C. M., and Power, M. S. (1991a) Analysis of ground response data at Lotung large-scale soil-structure interaction experiment site, *Report NP-7306-M*, Palo Alto: EPRI.

Chang, C.-Y., Mok, C. M., Power, M. S., Tang, Y. K., Tang, H. T., and Stepp, J. C. (1991b). Development of shear modulus reduction curves based on Lotung down-hole ground motion data. S. Prakash, ed., *Second international conference on recent advances in geotechnical earthquake engineering and soil dynamics. Vol. I*, St. Louis, MO. pp. 111-118. Rolla, MO: University of Missouri-Rolla.

Chang, C.-Y., Mok, C. M., Power, M. S., Tang, Y. K., Tang, H. T., & Stepp, J. C. (1990). Equivalent linear versus nonlinear ground response analyses at Lotung seismic experiment site. *Proc. fourth U.S. national conference on earthquake engineering. V.3* pp. 327-336. Oakland, CA: EERI.

Chang, C.-Y., Power, M. S., Tang, Y. K., & Mok, C. M. (1989). Evidence of nonlinear soil response during a moderate earthquake. *Proceedings of the twelfth international conference on soil mechanics and foundation engineering. Vol. 3*, Rio De Janeiro. pp. 1927-1930. Rotterdam: Balkema.

Converse, A.M. and Brady, A.G. (1992). BAP: basic strong-motion accelerogram processing software; version 1.0. *Open File Report 92-296A*, Denver: U.S. Geological Survey.

Elgamal, A.W., (1994). Personal communication.

Elgamal, A.-W., Zeghal, M., Tang, H. T., and Stepp, J. C. (1995). Evaluation of los-strain site characteristics using the Lotung seismic array. *ASCE Journal of Geotechnical Engineering*, 121(4), pp. 350-362.

EPRI (1989). Proceedings: EPRI/NRC/TPC workshop on seismic soil-structure interaction analysis techniques using data from Lotung, Taiwan, *Report NP-6154*, Palo Alto: Electric Power Research Institute.

Figueroa, J.L., Saada, A.S., Liang, L., and Dahisaria, M.N. (1994). Evaluation of Soil Liquefaction by Energy Principles. *ASCE Journal of Geotechnical Engineering*, 120(9), pp. 1554-1569.

Gersch, W. (1974). On the achievable accuracy of structural system parameter estimates. *Journal of sound and vibration*, 34(1), pp. 63-79.

Gersch, W., and Luo, S. (1972). Discrete time series synthesis of randomly excited structural system response. *Journal of the acoustic society of America, 51*(1), pp. 402-408.

Ghanem, R. G., Gavin, H., and Shinozuka, M. (1991). *Experimental Verification of a number of structural system identification algorithms*. p. 302. Technical Report NCEER-91-0024.

Glaser, S. (1993). *Estimating soil parameters important for lifeline siting using system identification techniques*. NISTIR 5145. p. 91. Gaithersburg, MD:NIST.

Glaser, S. D. (1995). System identification and its application to estimating soil properties. *ASCE Journal of Geotechnical Engineering*, 121(7), pp. 553-560.

Glaser, S.D. (1996). Insight Into Liquefaction by System Identification. *Géotechnique*. Accepted for publication.

Glaser, S. D. and Leeds, A. (1996). *Preliminary Processing of the Lotung LSST Data*. NIST GCR 96-690.

Iemura, H., Yamada, Y., Izuno, K., Iwasaki, Y., and Ohno, S., (1990). Phase-adjusted control of structures with identification of random earthquake ground motion. *Proceedings, U.S. national workshop on structural control research*, UCLA: Los Angeles. (Ed. G.W. Housner and S. Masri), 116-124.

Johansson, R. (1993). *System identification and modeling*. Englewood Cliffs, NJ: Prentice-Hall.

Jong Shing Boring Services Company (1984). Geological Exploration and Soil Testing for EPRI/ TPC Large-Scale Seismic Testing Program. *Submitted to EPRI/TPC.*

Kalman, R. E. (1960). A new approach to linear filtering and prediction problems. *Transactions of the ASME, journal of basic engineering*, (3), pp. 35-45.

Kalman, R. E., & Bucy, R. (1961). New results in linear filtering and prediction theory. *Transactions of the ASME, journal of basic engineering*, (3), pp. 83-95.

Kramer, S.L. (1995). *Geotechnical Earthquake Engineering.* Prentice-Hall.

Krauss, T.P., Shure, L., and Little, J.N. (1994). *Signal processing toolbox.* Natick, MA: MathWorks.

Lee, M. K. W., and Finn, W. D. L. (1978). *DESRA-2. Dynamic effective stress response analysis of soil deposits with energy transmitting boundary including assessment of liquefaction.* Vancouver, B.C.: Dept. Civil Engineering, University of British Columbia. (Soil Mechanics Series No. 38)

Liu, C.C. and Yeh, Y.T. (1985). Final instrument installation report for Lotung LSST program, *Report ASIES-ER8510*, Institute of Earth Sciences, Academia Sinica.

Ljung, L. (1987). System identification: theory for the user. Englewood Cliffs, NJ: Prentice-Hall.

Ljung, L. (1979). Asymptotic behavior of the extended Kalman filter as a parameter estimator for linear systems. *IEEE transactions on automatic control, AC-24*(1), 36-50.

Ljung, L.J., (1993). *System identification toolbox.* Natick, MA: The MathWorks.

Marple, S.L. Jr. (1987). Digital spectral analysis with applications. Englewood Cliffs: Prentice-Hall.

MathWorks, (1993). *MATLAB.* Natick, MA: The MathWorks.

National Taiwan University (1989). *Final testing report of foundation soils for Phase 3 Lotung LSST, Taiwan, ROC.* Submitted to the Taiwan Power Company.

National Taiwan University (1987). *Final testing report of foundation soils for Lotung nuclear power plant model, Taiwan, ROC.* Submitted to the Taiwan Power Company.

Nau, R. F., and Oliver, R. M. (1979). Adaptive filtering revisited. *Journal of the Operational Research Society*, 30(9), pp. 825-831.

Pandit, S. M., (1991). *Modal and spectrum analysis: data dependent systems in state space.* p. 415. New York: Wiley.

Pierce, J.R. (1980). *An introduction to information theory.* Dover Press.

Robinson, E. A. (1982). A historical perspective of spectrum estimation. *Proceedings of the IEEE,* 70(9), pp. 885-907.

Rollins, K. M., and Seed, H. B. (1990). Influence of buildings on potential liquefaction damage. *Journal of the geotechnical engineering division,* ASCE, 116(2), pp. 165-185.

Safak, E. (1988). *Analysis of recordings in structural engineering: adaptive filtering, prediction, and control.* (Open-File Report 88-647). Menlo Park, CA: U.S. Geological Survey.

Schnabel, P. B.; Lysmer, J., and Seed, H. B. (1972). *SHAKE* [Computer Program]. Berkeley, CA: Earthquake Engineering Research Center. (No. 72-12)

Seed, H. B., and Idriss, I. M. (1970). *Soil moduli and damping factors for dynamic response analyses.* (EERC 70-10): University of California, Berkeley, EERC.

Shannon, C.E. (1949). Communication in the Presence of Noise. *Proceedings of the Institute of Radio Engineers,* 37, pp. 10-21.

Shannon, C.E. and Weaver, W. (1949). The Mathematical Theory of Communication. University of Illinois Press.

Shen, C.K., Chan, C.K., Li, X.S., Yang, H.W., Ueng, T.S., Wu, W.T., and Chen, C.H. (1987). Field Pore Pressure Response Measurements During Earthquakes. *University of California and Taiwan National University, submitted to the National Science Foundation/Navel Civil Engineering Laboratory, and EPRI.*

Sorenson, H. W. (1970). Least-squares estimation: from Gauss to Kalman. *IEEE spectrum,* 7(7), 63-68.

Tang, H. T. (1987). Large-scale soil-structure interaction. *Report NP-5513-SR.* Palo Alto, CA: Electric Power Research Institute.

Tang, Y.K. and Tang, H.T. (1992). Lotung Large-Scale Seismic Test strong motion records, Vol. 1-8. Report NP-7496, Palo Alto: Electric Power Research Institute.

Tang, H.T., Tang, Y.K., Stepp, J.C., Wall, I.B., Lin, E., Cheng, S.C., Lee, S.K., and Hsiau, H.M., (1989). EPRI/TPC large-scale seismic experiment at Lotung, Taiwan, *Proceedings: EPRI/ NRC/TPC workshop on seismic soil-structure interaction analysis techniques using data from Lotung, Taiwan, Report NP-6154*, Palo Alto: Electric Power Research Institute.

Udwadia, F. E. (1985). Some uniqueness results related to soil and building structural identification. *SIAM Journal of Applied Mathematics*, 45(4), pp. 674-685.

Vucetic, M., and Dobry, R. (1991). Effect of Soil Plasticity on Cyclic Response. *Journal of Geotechnical Engineering*, 117(1), pp. 89-107.

Wen,. K.L. and Yeh, Y.T. (1984). Seismic Velocity Structure Beneath the SMART 1 Array. *Bulletin of the Institute of Earth Science*, Academia Sinica, Vol. 4.

Zeghal, M. and Elgamal, A.-W. (1993). Lotung Site: Downhole Seismic Data Analysis. *Report*. Palo Alto, CA: Electric Power Research Institute.

Zeghal, M., Elgamal, A.-W., Tang, H. T., and Stepp, J. C. (1995). Lotung downhole array. II: Evaluation of soil nonlinear properties. *ASCE Journal of Geotechnical Engineering*, 121(4), pp. 363-378.

APPENDIX A: PROCEDURES FOR DATA PROCESSING

A.1 Data Processing

A.1.1 Cataloging

The EPRI-supplied data consists of 10 pc-format floppy disks of data. The data supplies ground motions, structural motions, dynamic earth pressure, and ancillary data for 18 earthquake events (Tang and Tang, 1992). The data set consists of 2,103 individual files. Pore water pressure values are available for events 12, 16, and 17 only.

The first step of the data processing was to enter the relevant data files into MATLAB and group them into corresponding event files. Files event01 through event18 were created. A simplified naming convention was developed for each data record. The first letter of the name is an a, v, or d, for acceleration, velocity, and displacement, respectively. The next three letters are dha or dhb for downhole array a or b. The following number refers to the depth in meters - 0, 6, 11, 17, and 47. The second number, following the underscore refers to the event number. The last letter - e, n, or u, refers to accelerometer orientation - east-west, north-south, or up-down.

An example of the naming convention is adha47_18u. This record is the acceleration time history at a depth of 47 m at downhole array a, event 18. The record gives the vertical ground motion for this location and event.

A.1.2 Filtering, Resampling, and Integration

The data as received from EPRI is in the form of raw acceleration records, which we processed following standard U.S.G.S. method (Converse and Brady, 1992). The acceleration records are digitized at a rate of 200 samples per second (s/s), for a bandwidth of 100 Hz. This relatively high Nyquist frequency causes the event records to be very long, 8,000 data points for each 40 s trace. In addition, there is little useful information for our study above 10-15 Hz, and this region would be very noisy. Resampling greatly reduces the amount of data to be later analyzed, and eliminates time-domain aliasing of the band-passed signals. It was therefore

decided to low-pass filter and resample the data at a rate of 25 s/s, yielding a Nyquist frequency of 12.5 Hz. Previous work indicated that the information of interest would be contained in this band (Glaser, 1993, 1995a,b).

The data was resampled using the *resample* algorithm from the MATLAB Signal Processing Toolbox (Krauss et al., 1994). The data is first low-pass filtered using a Kaiser-windowed linear-phase FIR filter using ten terms on either side of the timestep in the calculation. The low-pass filter is applied both forward and reverse to eliminate phase shift, and the data resampled at 25 Hz. The same process was carried out for every strong motion record as well as for the pore water pressure records.

The acceleration records were then processed and integrated to provide velocity records, and the velocity records similarly reprocessed and integrated to yield displacement time histories. The acceleration record is first high-pass filtered at 0.15 Hz using a 4th order bi-directional Butterworth filter to remove dc offset and low frequency drift. A best-fit straight line from the arrival of the strong motion is then subtracted from the data, followed by the sample mean. The pre-arrival data is then set to zero. The processed acceleration data is now integrated using the trapezoidal method (Converse and Brady, 1992). The same steps are carried out on this newly formed velocity time history to yield the strong motion displacement.

APPENDIX B - MATLAB PROCEDURE TO INTEGRATE ACCELERATION RECORDS TO VELOCITY AND DISPLACEMENT.

```
function [a,v,d]=vd(f,Lcut,dT,n,pre,name)
% function [a,v,d]=vd(f,Lcut,dT,n,pre)
%
% detrends and filters the input acceleration,
% and integrates twice to give velocity and displacement.
% The results are plotted so they can be reviewed.
%
% f is the input acceleration vector
% Lcut is the low-end cutoff frequency in Hz.
% dT is the time step
% n is the order of the Butterworth filter;
% pre is the pre-event segment length to be zeroed.
%
% since the acceleration is filtered twice, the
% effective order of the filter is double the value of n.
%
zip=(1:pre);
zip=zeros(size(zip));
%
[b,c]=butter(n, Lcut*dT*2.0, 'high');
a=filtfilt(b,c,f);
a=dtrend(a(:,1),1,pre);
a=detrend(a);
a=a-a(pre+1);
a(1:pre)=zip;
%
v=inttrap(a,dT);
v=filtfilt(b,c,v);
v=dtrend(v(1,:)',1,pre);
v=detrend(v);
v=v-v(pre+1);
v(1:pre)=zip;
%
d=inttrap(v,dT);
[b,c]=butter(n, (Lcut*dT*2)/1.0, 'high');
d=filtfilt(b,c,d)'; d=dtrend(d(:,1),1,pre);
d=detrend(d);
d=d-d(pre+1);
d(1:pre)=zip;
%
time=(length(f)*dT)/1.0;
t=[dT: dT: time];
temp=name(1:(length(name)-6));
clf
subplot(3,1,1), plot(t,a(1:length(t))), title([temp,':   acceleration']), grid on
subplot(3,1,2), plot(t,v(1:length(t))), title([temp,':   velocity']), grid on
subplot(3,1,3), plot(t,d(1:length(t))), title([temp,':   displacement']), grid on, xlabel('Time (seconds)')
```

APPENDIX C: PORE WATER PRESURE TIME HISTORIES FOR EVENTS 12, 16, 17.
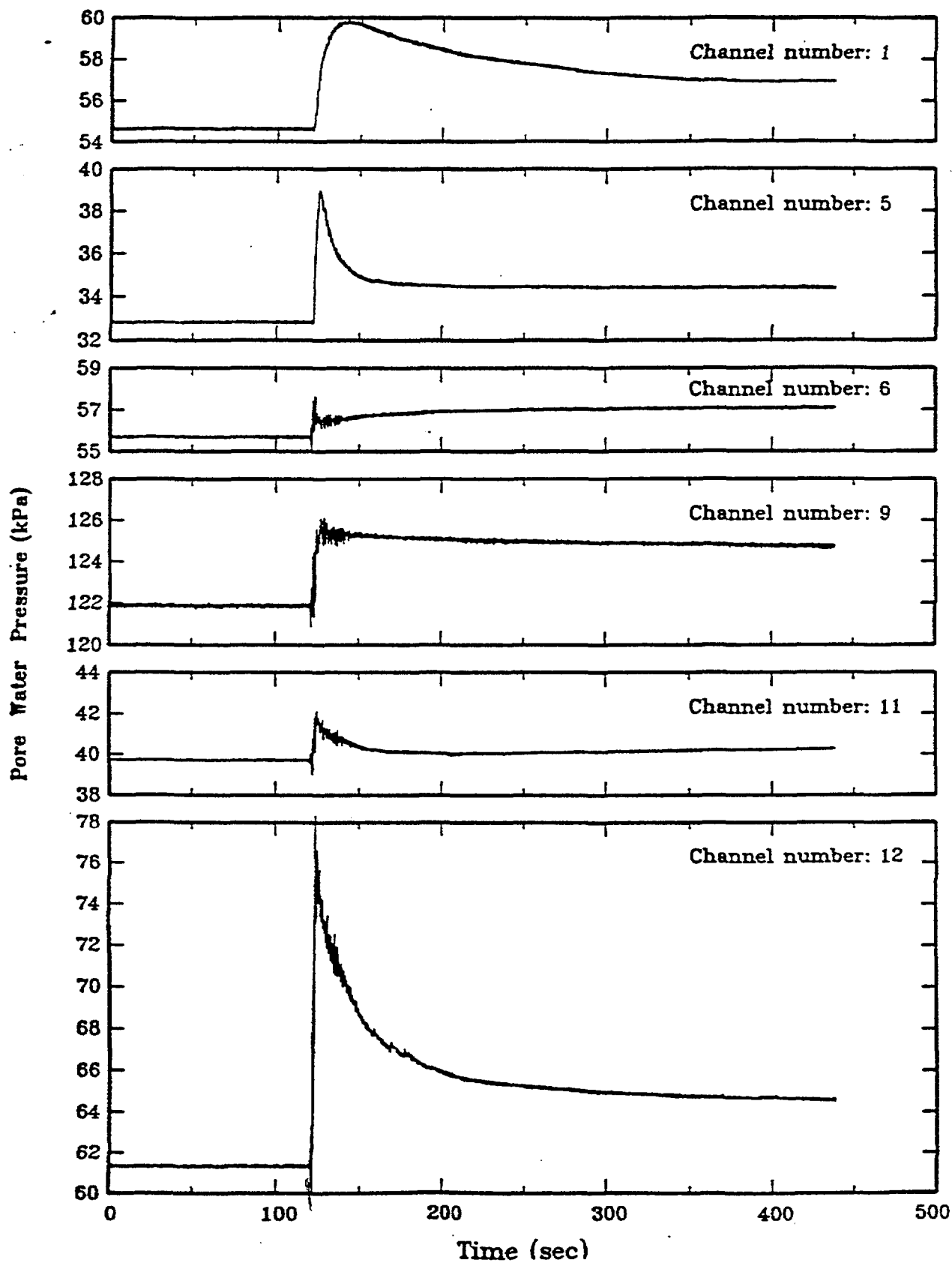
Pore Water Pressure Time Histories, Event LSST No. 12 (7/30/1986)
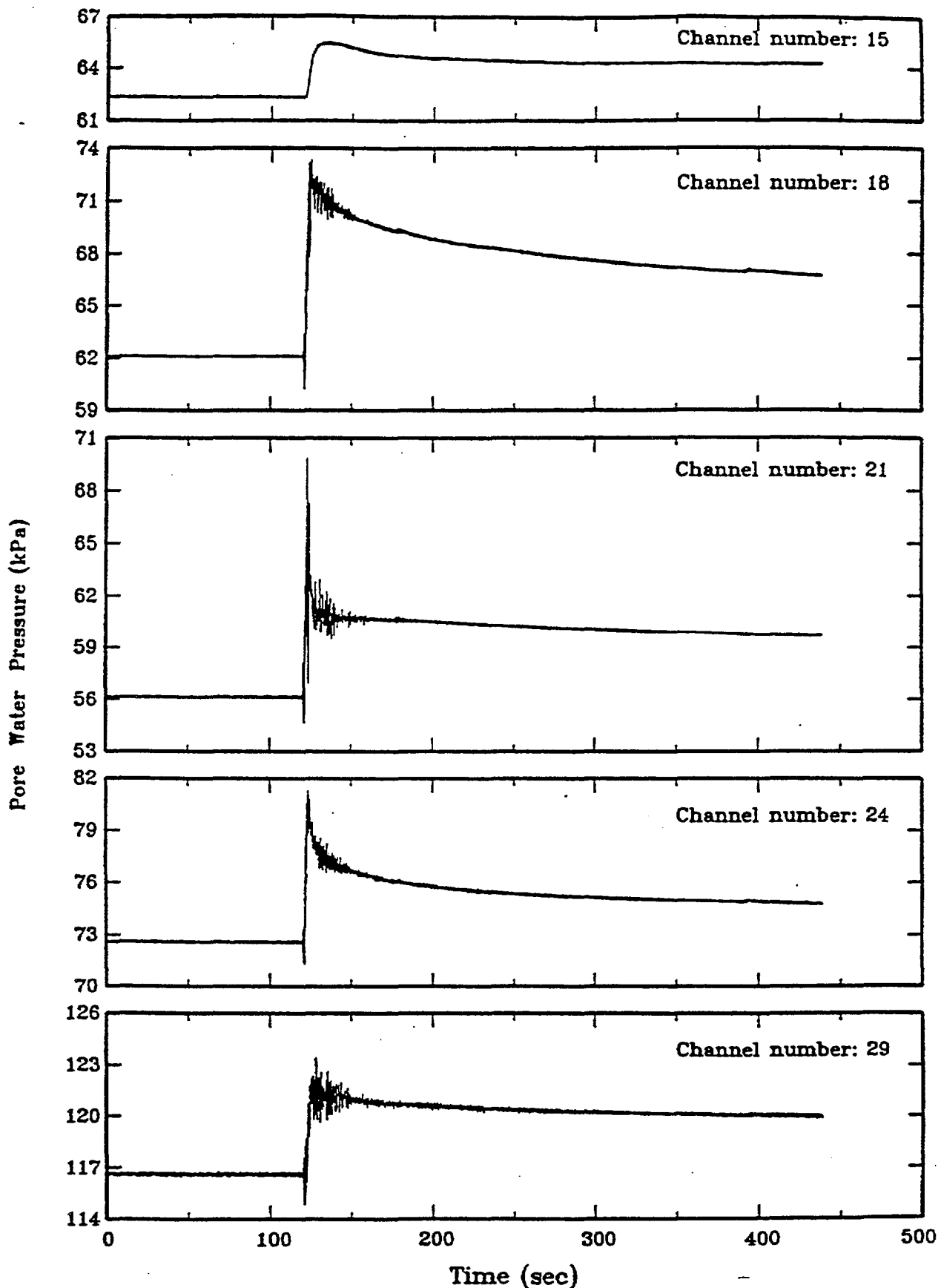
(Tang et al., 1992)

Pore Water Pressure Time Histories, Event LSST No. 12 (7/30/1986)
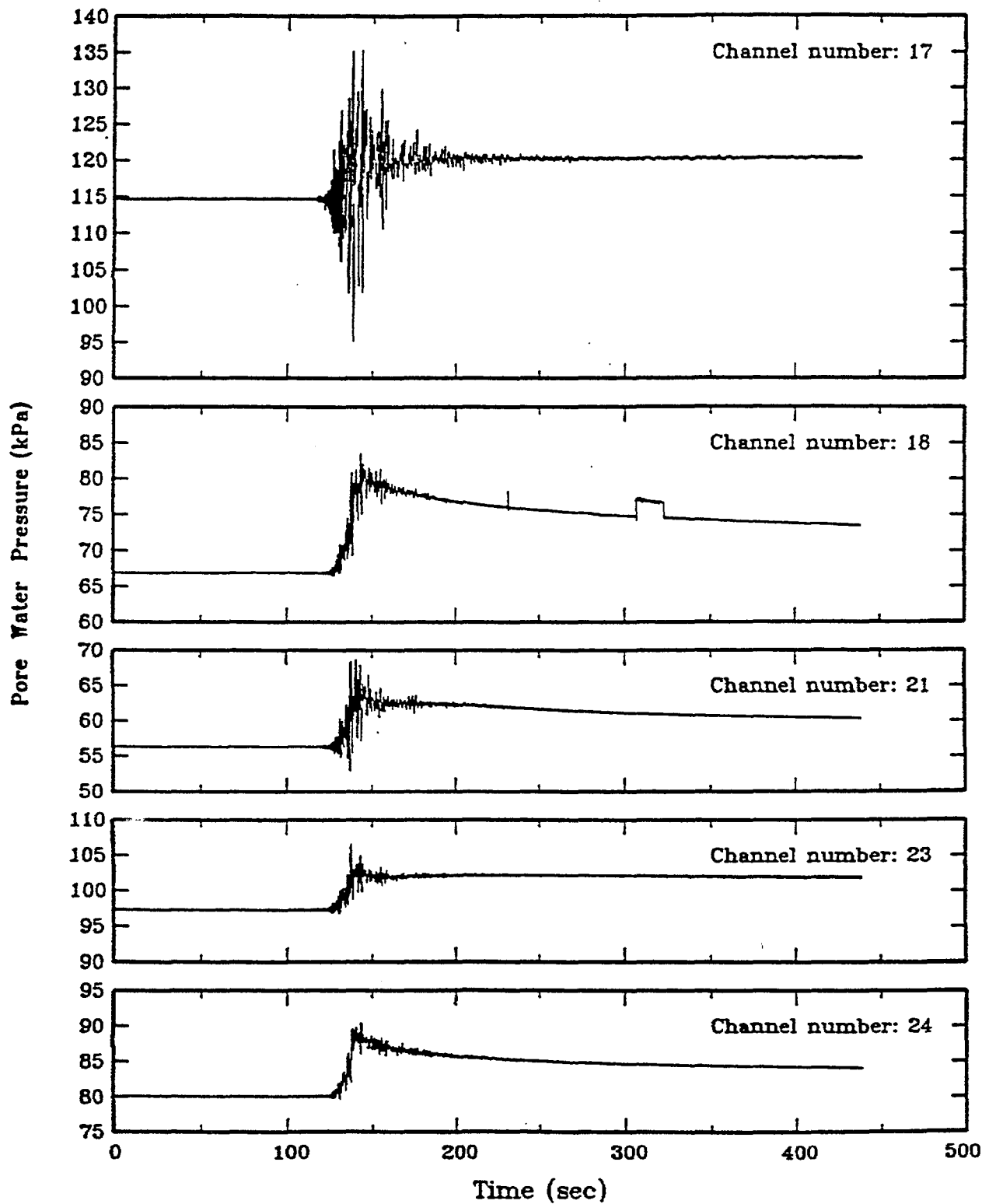
(Tang et al., 1992)

Pore Water Pressure Time Histories, Event LSST No. 16 (11/14/1986)

(Tang et al., 1992)
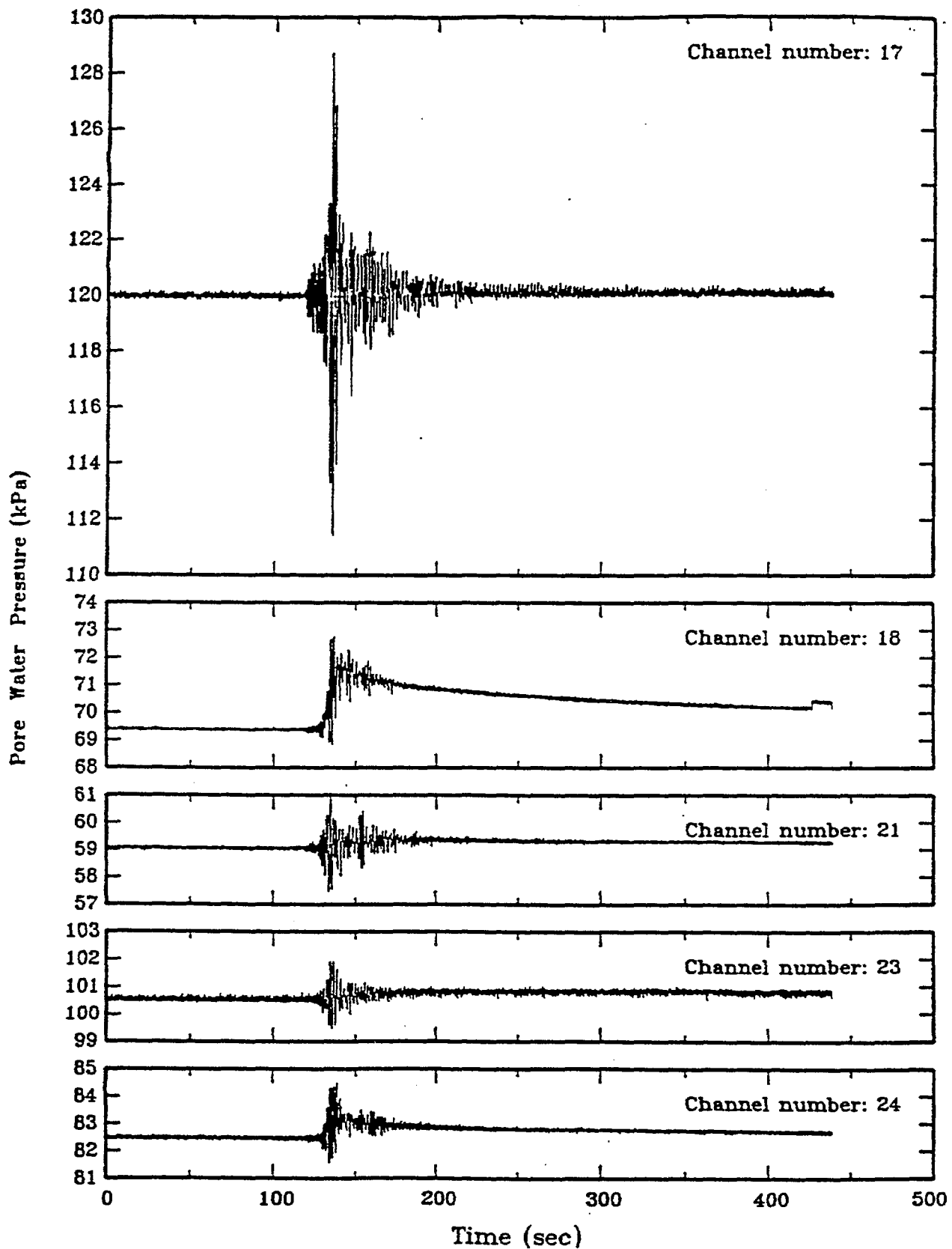
Pore Water Pressure Time Histories, Event LSST No. 17 (11/14/1986)

(Tang et al., 1992)

109

APPENDIX D: REVIEW OF DAMPING VALUES MEASURED IN THE FIELD AND LABORATORY

D.1 Introduction

In order to put the damping estimates made in this report in context, it is important to review previous estimates of soil damping. Measurements have been made in the laboratory as well as the field. Advantages of laboratory tests include full control over loading paths and strain, including large-strain measurements. Laboratory tests will all yield at best approximate results since no one can run a laboratory test on an *undisturbed* loose sand. The preliminary reports from back-calculating earthquake response imply that the laboratory degradation curve might be too high at intermediate strains. In addition, the results from two independent methods (Chang et al., 1990; Abdel-Ghaffar and Scott, 1979) show that the customary hyperbolic shape of the laboratory damping curve might be incorrect, and actually is S-shaped. Laboratory tests also examine a very small volume of soil, giving a point estimate compared to the site of interest.

Field testing avoids the disturbance issues associated with laboratory testing. In principle, geophysical field testing methods measure damping of undisturbed expanses of soil. However, the system damping thus calculated is the small strain damping, or D_{min}, and is only valid for the elastic region of the soil (Dobry et al., 1982). The limitation is due to the inability to reliably impart strains into the soil much greater than 1×10^{-6}. Therefore, it has been impossible to measure threshold strain, γ_T, and the soil degradation curve, D/D_{min}, in situ.

Attempts to input enough energy into the ground to cause intermediate to large strains have not been very successful. The amount of energy needed would destroy a bore-hole, and would be destructive on the surface as well. There is also the problem of the transducers being in the near-field if they are close to a source large enough to cause large strains in an immediate area. One exception was a project undertaken for the Nuclear Regulatory Commission (Shannon-Wilson, 1976) where intermediate-to-large strains were input in a large scale field experiment.

The optimum situation would be the ability to make measurements during different magnitudes of earthquake excitement. In this case shear strain in the layers of interest, and stiffness (velocity), would be continually monitored. This approach is optimal since it allows nondestructive (in as much as an earthquake is nondestructive) evaluation of soil properties in the actual situation of interest. Since earthquakes can not be made-to-order, the chances of this situation happening are virtually nonexistent. The instrumentation would also be extremely difficult. However, use of inverse theory allows the soil parameters of interest to be calculated from attainable data — the ground motion records of the motion going into the layers of interest, and above the layer itself.

The following sections present a non-exhaustive compilation of damping estimates made in the laboratory, in the field using geophysical methods, and in the field using strong motion excitation. The "Source" column in the accompanying tables refers to the publications tabulated at the end of this appendix.

D.2 Laboratory Estimates of Soil Damping:

Table D.1 presents a summary of some laboratory estimates of soil damping available in the literature. The values given are "average" representative values commonly accepted by the geotechnical community. The low-strain (< 0.001%) damping estimates for soils, whether cohesive or non-cohesive, lie in a very close range from about 1% to 5%. Even at a large strain of 0.1%, damping is estimated to be 10 - 12% or less. At large strains, sand displays significantly higher damping than clay, as would be expected from application of Mindlin's theory (Dobry et al., 1982). Details of the relationship between strain and damping for sands measured in the laboratory are given in Fig. D.1 (Seed et. al., 1986), while Fig. D.2 presents a similar relationship for normally consolidated clay (Dobry and Vucetic, 1987).

A comparison of the strain dependent damping for sands and clayss based on an earlier compilation (Seed and Idriss, 1970) is shown in Fig. D.3, where it can be seen that damping increases with strain faster for sand than clay. A similar relationship is shown in Fig. D.4, which is based on laboratory measurements done by Japanese researchers (Kokusho, 1987). The results

from the extensive laboratory testing done for the Lotung project is given in Fig. D.5, where it is seen that damping is a bit higher than the Seed and Idriss approximation. While there has not been as much work done on gravelly soils, Fig. D.6 implies that these soils have a damping response much the same as sand (Seed et al., 1986). These Figures show that there actually is significant scatter of soil damping above the threshold strain.

Table D.1: Laboratory estimates of Soil Damping

SOIL	DAMPING(%)	STRAIN(%)	SOURCE
clay	0.9 - 2.4	10^{-3}	20
cohesive	3 (1 - 5)	10^{-3}	17
cohesionless	0.5 - 2	10^{-4} - 10^{-3}	16
sand	1 - 4 2 - 8 4 - 16	10^{-3} 10^{-2} 10^{-1}	15
sand	1.5	10^{-3}	5
sand	1	10^{-3}	14
silty sand	1 - 3 3 - 10 10 - 21	10^{-3} 10^{-2} 10^{-1}	15
silty sand, Wildlife site	2 1.5 - 3.7 6.5	10^{-4} 10^{-2} 10^{-1}	4
silty sand, Lotung site	1 - 2 2.5 - 5 18 - 25	10^{-3} 10^{-2} 10^{-1}	2
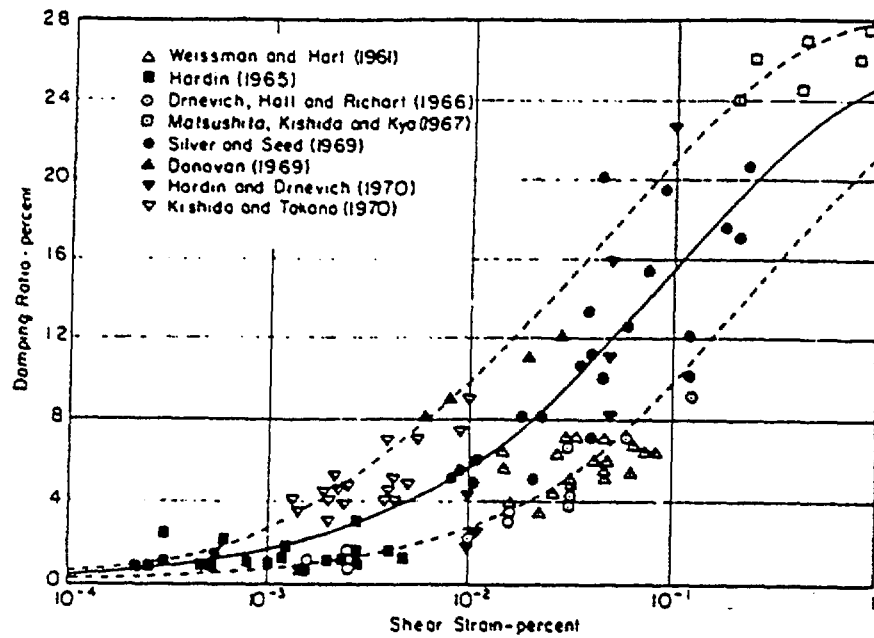
Figure D.1   Damping ratios for sands based on laboratory measurements (Seed et al., 1986).
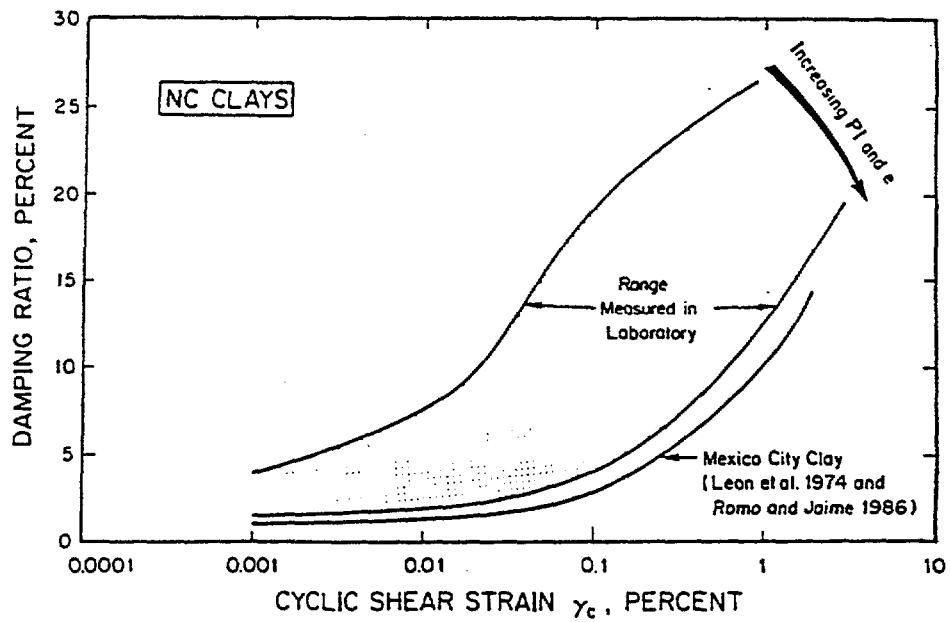
Figure D.2   Damping ratios for normally consolidated clays based on laboratory meaurements (Dobry and Vucetic, 1987).
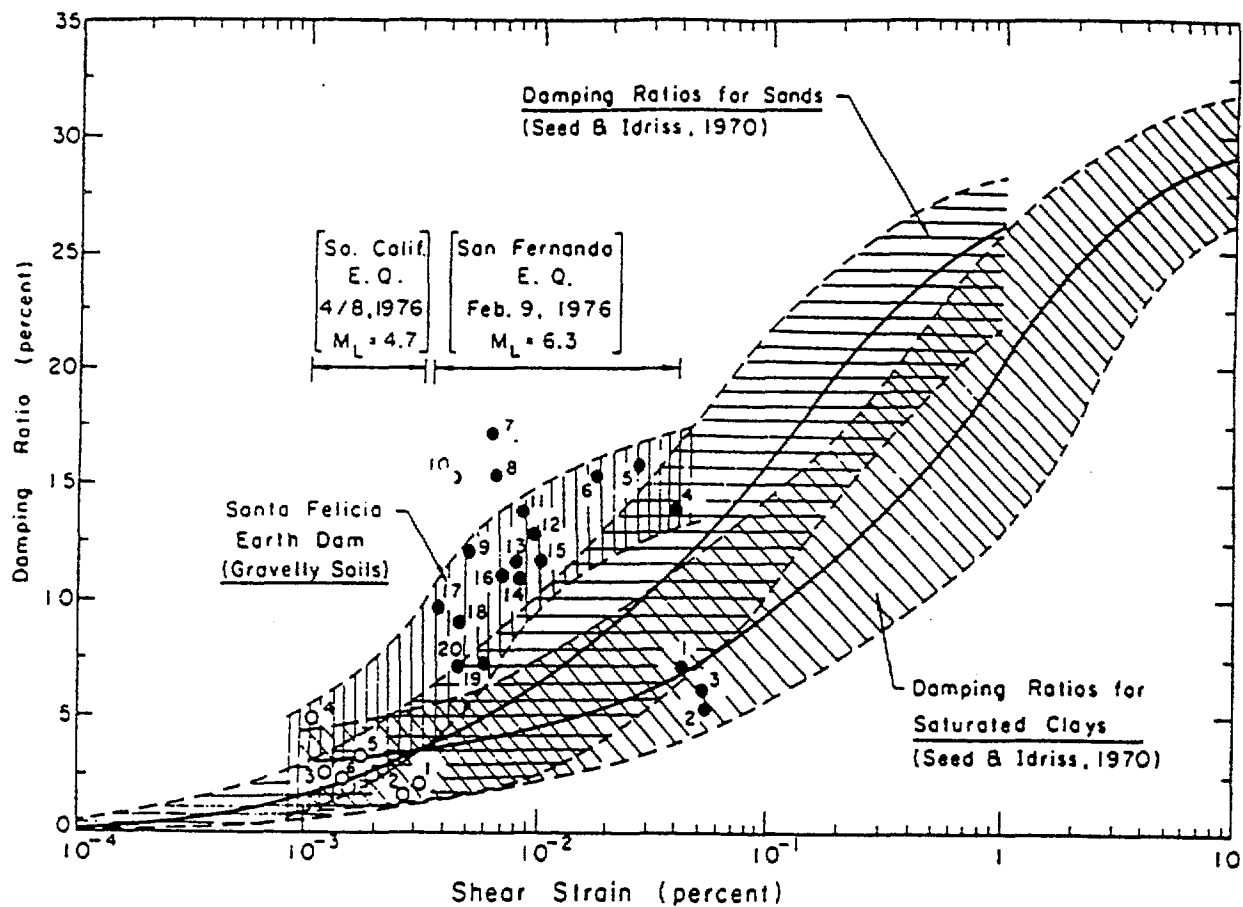
Figure D.3   Comparison between damping ratios obtained from 2 earthquake records (field) and those obtained for sands and saturated clays (laboratory) (Abdel-Ghaffar and Scott, 1979).
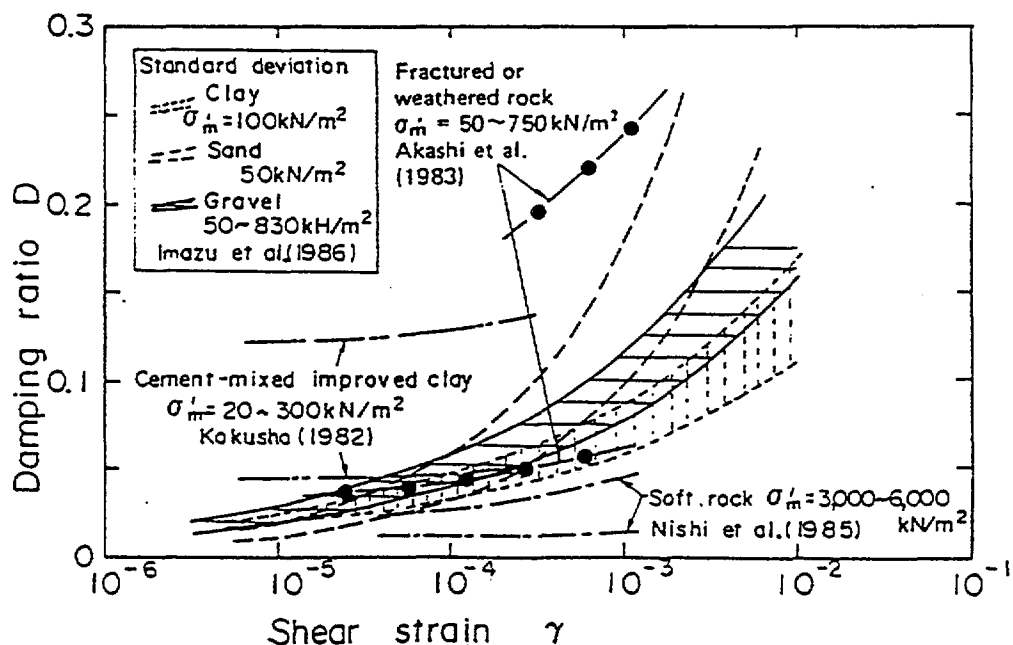
Figure D.4   Damping ratios for various soils obtained from field tests (Kokusho, 1987).
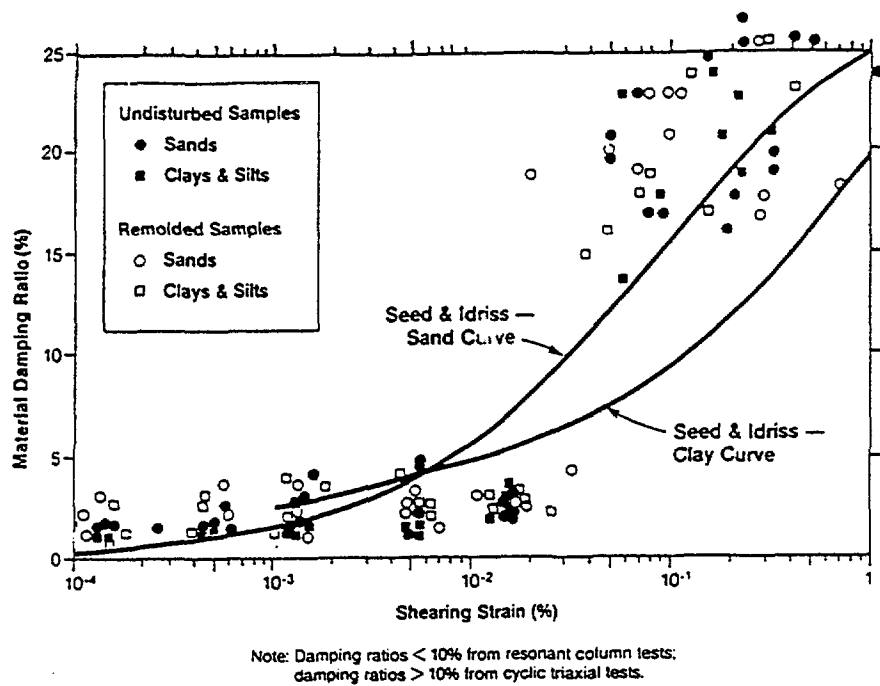
Damping Ratio Data for Lotung Site (1987 Program).
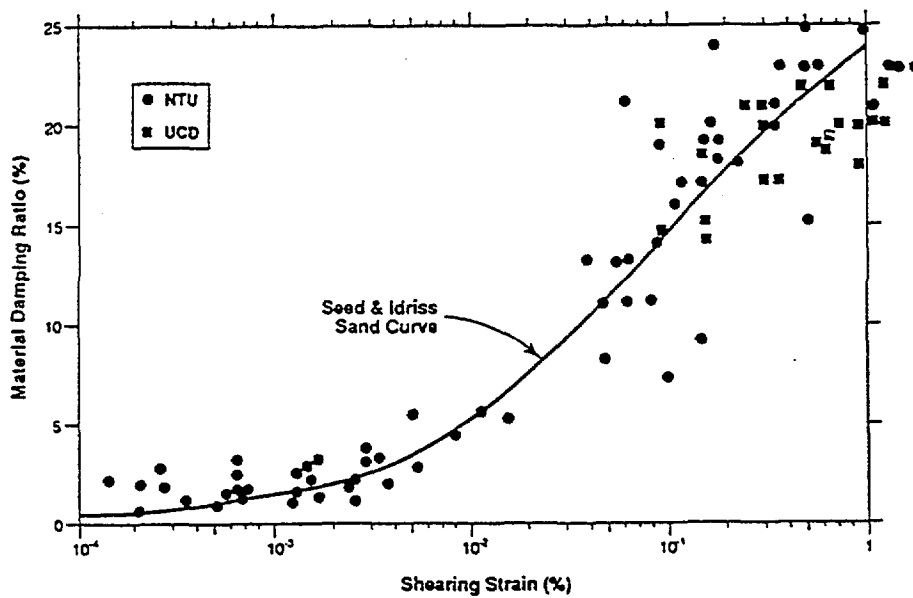
Damping Ratio Data for Lotung Site (1989-1990 Programs).

Figure D.5   Summary of laboratory damping estimates for the Lotung site (Anderson, 1993).

D.3 Field Geophysical Estimates of Soil Damping:

Representative values culled from the literature for field geophysical estimates of soil damping are presented in Table D.2. Note that these estimates were made for displacements well below the threshold strain, so there is no evidence of damping increase. The value of these estimates is that they were made on "undisturbed" soil, and should therefore be a more accurate measure of soil physical properties. Details on some of field tests in Japan are given in Table D.3 (Kokusho, 1987). The estimates are more scattered than from the laboratory, with damping estimates higher than in the lab. This relationship is presented graphically in Figure D.7, which compares laboratory and field damping from Japanese researchers (Kokusho, 1987). Clay damping is seen to measure higher in the lab than the field, while for non-cohesive soils field measurements are much higher when measured in the field. Which values are "correct" is not known.

D. 4 Field Estimates of Soil Damping Made From Strong Motion:

A detailed study of damping at the Lotung site was done by Zeghal et al. (1995). Summary plots of results from the field results are given in Figure D.8. Detailed results for Events 7, 12, and 16 are given in Figures D.9 through D.17. The other major studies using field excitation are Glaser (1996) at the wildlife site, and Qi et al. (1989) at Mexico City using the random decrement method. Table D.4 presents summaries of the values estimated by these studies. It can be seen that the damping values estimated from strong motion excitation of field sites are higher than laboratory estimates.
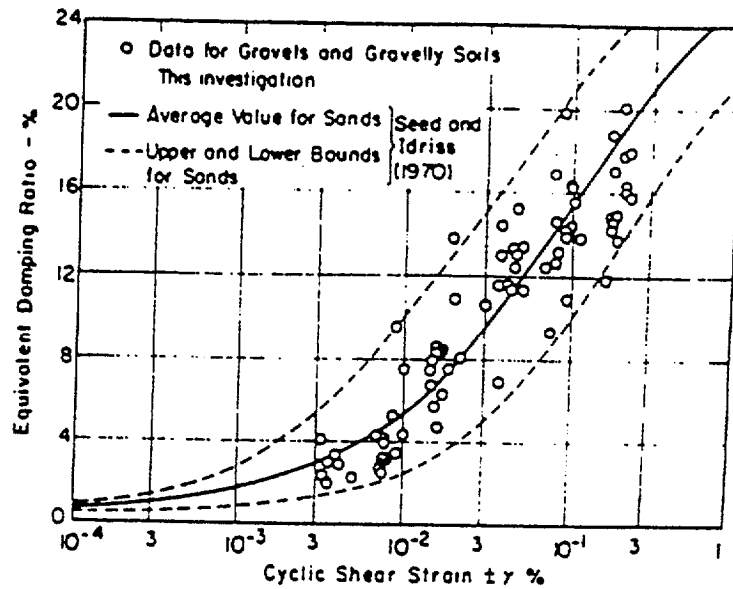
Figure D.6 Comparison of damping ratios for gravelly soils and sands (Seed et al., 1986).
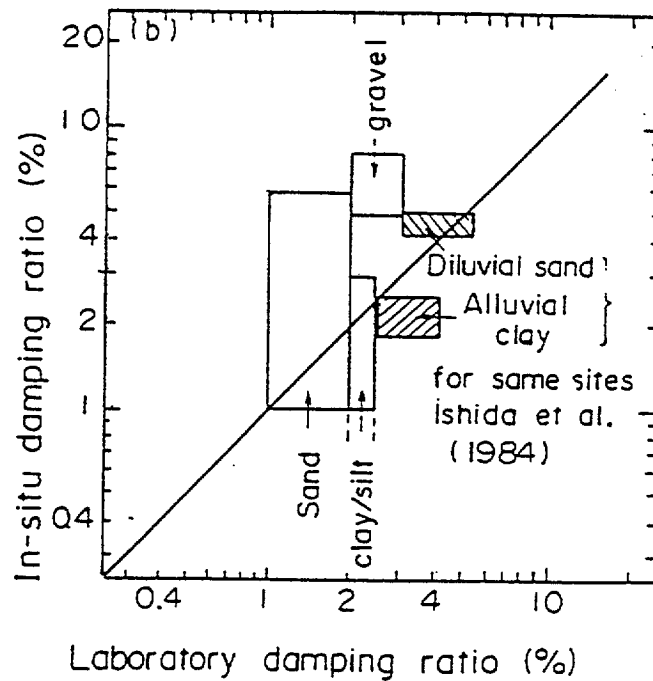
Figure D.7 Comparison of in situ and laboratory damping ratios from Japan (Kokusho, 1987).

Table D.2: Field Geophysical Estimates of Soil Damping

SOIL	DAMPING (%)	STRAIN (%)	SOURCE	NOTES
soft rock	6 - 8	$\approx< 10^{-4}$	6	
bay mud	4	$\approx< 10^{-4}$	13	2.5% in the lab
bay mud	9	$\approx< 10^{-4}$	10	
clayey	1.7	$\approx< 10^{-4}$	18	
clay/silt	1 - 3	$\approx< 10^{-4}$	6	
loam	5 - 10	$\approx< 10^{-4}$	6	
silt	2.5	$\approx< 10^{-4}$	7	
sandy silt	2.5	$\approx< 10^{-4}$	18	
alluvium, silt & clay	12 (<25 m)	$\approx< 10^{-4}$	12	1.5 - 3.5% in the lab
alluvium, silt & clay	3.5 (>25 m)	$\approx< 10^{-4}$	12	1.5 - 3.5% in the lab
sandy	5	$\approx< 10^{-4}$	18	
fine sand	1.7	$\approx< 10^{-4}$	18	
sand	1 - 6	$\approx< 10^{-4}$	6	
sand	6	$\approx< 10^{-4}$	7	
sand	4	$\approx< 10^{-4}$	9	
sand (P-wave)	2 - 3	$\approx< 10^{-4}$	10	0.7% in the lab
gravel	5 - 8	$\approx< 10^{-4}$	4	

Table D.3 Damping ratios of various soils measured in the field by Japanese researchers (Kokusho, 1987).

Damping ratio (%)	Soil	Shear wave velocity, V_s (m/sec.)	Depth (m)	Measuring method
6	Diluvial sand	260		Down-hole survey
2.5	Alluvial clay/silt	80 ∿ 100		
10	Loam	150		
8	Mudstone	420	10 ∿ 20	
5	Silt/sand	150 ∿ 200	25 ∿ 40	Down-hole survey
6	Clay core of dam	500	15	
8	Gravel	350	30	Vibrator test (S_H-wave)
6	Sandstone	800		
1 ∿ 3	Ariake Clay			Vibrator test (Surface wave)
2	Alluvial silt	80 ∿ 100	2 ∿ 6	
5 ∿ 7	Loam			Down-hole survey
1 ∿ 3	Clay			
1 ∿ 4	Sand		40 ∿ 51	
1.5 ∿ 2	Alluvial silt	160	14 ∿ 28	
3.1	Alluvial sand	210	12 ∿ 25	
0.3	Alluvial silt	140	25 ∿ 35	
2	Alluvial clay	20 ∿ 100	0 ∿ 20	Optimization of earthquake records
2 ∿ 5	Sand	120 ∿ 400		
5	Gravel	300 ∿ 600		

Note: Soil strain is in the order of 10^{-6} or less.

Table D.4: Estimates of Soil Damping Made From Strong Motion

SOIL	DAMPING (%)	STRAIN (%)	SOURCE
Mexico City clay	2	1.5×10^{-2}	11
Mexico City clay	2.7	1.5×10^{-2}	11
Mexico City clay	3.5	4.0×10^{-2}	11
Mexico City clay	3.7	5.0×10^{-2}	11
silty sand w/ gravel, Wildlife site	15	strong motion	3
silty sand w/ gravel, Wildlife site	28 - 66	liquefied	3
silty sand, w/ gravel, Lotung SST	3.5 10 21	10^{-3} 10^{-2} 10^{-1}	21
silty sand, w/ gravel, Lotung SST	3 63 20	10^{-3} 10^{-2} 10^{-1}	8
gravelly soils	1 - 5 9 - 15 12 - 18	10^{-3} 10^{-2} 10^{-1}	1

D.5 References for Damping Measurements Cited in Tables D.1, D.2, and D.4

1. Abdel-Ghaffar, A. M., & Scott, R. F. (1979). Shear moduli and damping factors of earth dam. Journal of Geotechnical Engineering 105(GT12), pp. 1405-1426.

2. Anderson, D.G. (1993). Geotechnical Synthesis for the Lotung Large-Scale Seismic Experiment, Report TR-102362, Palo Alto: Electric Power Research Institute.

3. Glaser, S. D. (1996). Insight Into Liquefaction by System Identification. Géotechnique. In press.

4. Haag, E.D. (1985). Laboratory Investigation of Static and Dynamic Properties of Sandy Soils Subjected to the 1981 Westmoreland Earthquake. Geotechnical Engineering Center Report GR85-11, Department of Civil Engineering, University of Texas at Austin.

5. Ishihara, K. (1982). Evaluation of Soil Properties in Earthquake Response Analysis. Proceedings, International Symp. Numerical Models in Geomechanics, Zurich, pp. 237-259.

6. Kokusho, T. (1987). In Situ Dynamic Soil Properties and Their Evaluations. Proceedings, 8th Asian Regional Conference on Soil Mechanics and Foundation Engineering, 2, pp. 215-240.

7. Kudo, K. and Shima, E. (1981). Attenuation of Shear Waves in Soil. Seismic Wave Attenuation, ed. Toksoz, M.N. S.E.G. reprint No. 2, pp. 325-338.

8. Lin, J.-S. (1994). Extraction of Dynamic Soil Properties Using Extended Kalman Filter. Journal of Geotechnical Engineering 120(12), pp. 2100-2117.

9. Meissner, R. and Theilen, F. (1986). Experimental Studies of the Absorption of Seismic Waves. Absorption of Seismic Waves (ASW), DGMK Project 254, Hamburg.

10 Mok, Y.J , Sanchez-Salinero, I., Stokoe, K.H. II, and Roesset, J.M. (1988). In Situ Damping Measurements by Crosshole Seismic Methods. Earthquake Engineering and Soil Dynamics II. ASCE GSP No. 20, pp. 305-320.

11. Qi, G.Z., Yang, J.C.S., Durelli, A.J., and Esteva, L. (1989). In Situ Determination of the Strain Dependence of the Soil Dynamic Properties. Structural Dynamics and Soil-Structure Interaction, pp. 431-442.

12. Redpath, B.B., Edwards, R.B., Hale, R.J., and Kintzer, F.C. (1982). Development of Field Techniques to Measure Damping Values for Near-Surface Rocks and Soils. NSF grant report PFR-7900192.

13. Redpath, B.B. and Lee, R.C. (1986). In Situ Measurement of Shear-Wave Attenuation at a Strong-Motion Recording Site. Report for U.S.G.S. contract 14-08-001-21823.

14. Saxena, S.K. and Reddy, K.R. (1989). Dynamic Moduli and Damping Ratios for Monterey No. 0 sand by resonant column method. Soils and Foundations, 29(2), pp. 37-51.

15. Seed, H. B., & Idriss, I. M. (1970). Soil moduli and damping factors for dynamic response analyses. (EERC 70-10): University of California, Berkeley, EERC.

16. Seed, H. B., Wong, R.T., Idriss, I.M. & Tokimatsu, K. (1986). Moduli and Damping Factors for Dynamic Analyses of Cohesionless Soils. Journal Geotech. Eng., 112(11), pp. 1425-1445.

17. Sun, J.I., Golesorkhi, R., and Seed, H.B. (1988). Dynamic Moduli and Damping Ratios for Cohesive Soils. Report UCB/EERC-88/15.

18. Tonouchi, K., Sakayama, T., and Imai, T. (1983). S-Wave velocity and the Damping Factor. Bulletin of the International Association of Engineering Geology, 26/27, pp. 327-333.

19. Vucetic, M., and Dobry, R. (1991). Effect of Soil Plasticity on Cyclic Response. <u>Journal of Geotech. Eng.</u>, 117(1), pp. 89-107.

20. Zavoral, D. (1990). <u>Dynamic Properties of an Undisturbed Clay From Resonant Column Tests</u>. Thesis, Department of Civil Engineering, University of British Columbia, Vancouver.

21. Zeghal, M., Elgamal, A.-W., Tang, H.T., and Stepp, J.C. (1995). Lotung Downhole Array. II: Evaluation of Soil Nonlinear Properties. <u>Journal of Geotech. Eng.</u>, 121(4), pp. 363-378.

LSST 7, 12 & 16; DHB 6, 11 & 17

Comparison of Equivalent Shear Moduli and Damping Ratios Evaluated from Stress-Strain Histories with Those Estimated from NTU Laboratory Tests (EPRI 1993)

Comparison of Equivalent Shear Moduli and Damping Ratios Evaluated from Stress-Strain Histories with Those Estimated from UT Laboratory Tests (EPRI 1993)

O O O Estimates before peak shear strain

• • • Estimates after peak shear strain

+ + + Low confidence damping ratio estimate

■ ■ ■ NTU laboratory estimates: sand (EPRI 1993)

♦ ♦ ♦ NTU laboratory estimates: clay (EPRI 1993)

▨▨▨ UT range of estimates (EPRI 1993)

———— Statistical fit (stress-strain history estimates)

– – – – Sand modulus reduction and equivalent damping curves[1]

–·–·– Gravel modulus reduction curve[1]

———— Sand and gravel upper and lower bound damping curves[1]

1 after Seed et al. 1970, 1984

Figure D.8   Summary of Lotung field estimates of soil damping made from strong motion (Zeghal et al., 1995).
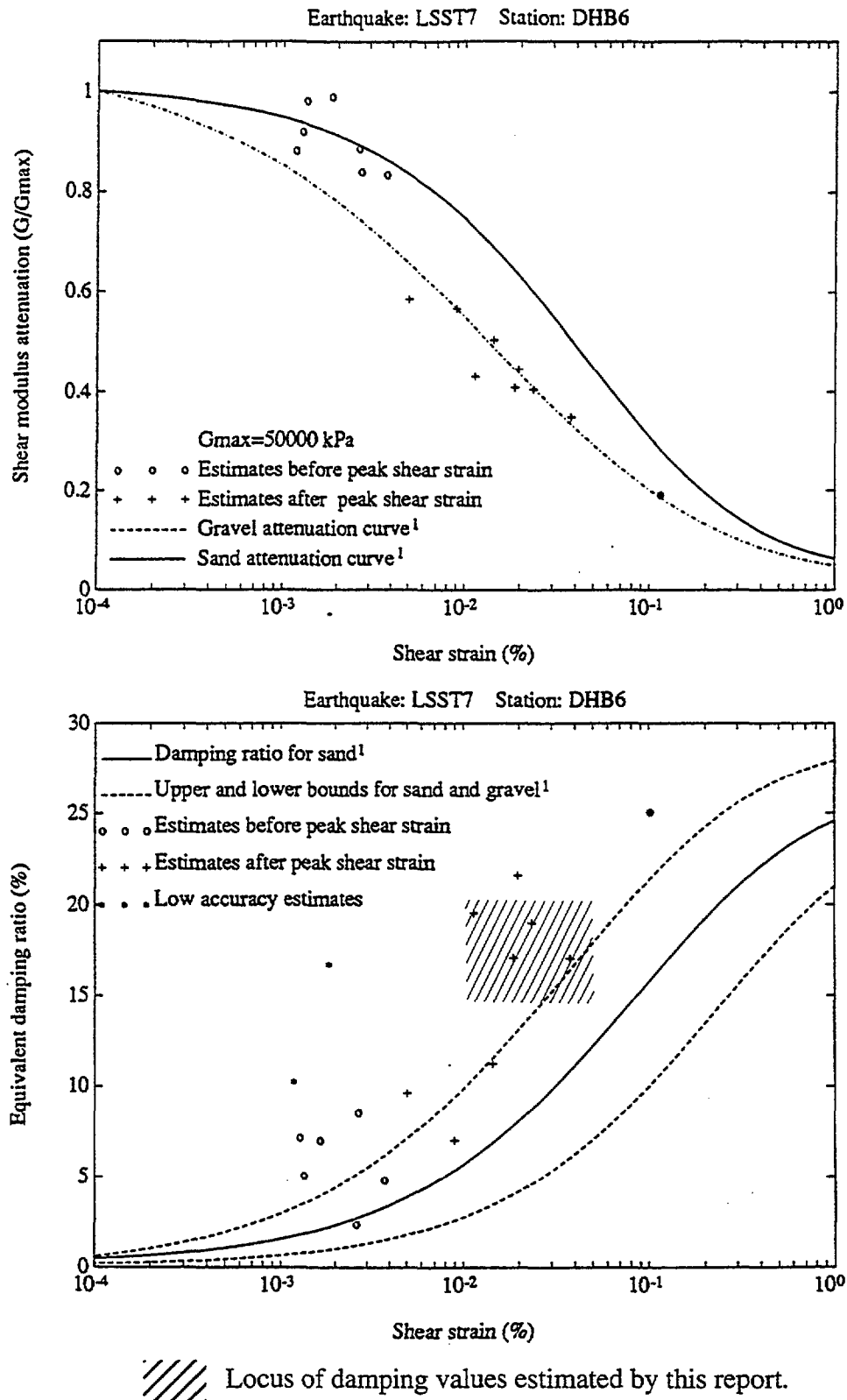
Figure D.9 Equivalent shear moduli and damping ratios at Event 7, 6 m depth, DHB (Zeghal et al., 1995).

Earthquake: LSST7   Station: DHB11

Earthquake: LSST7   Station: DHB11
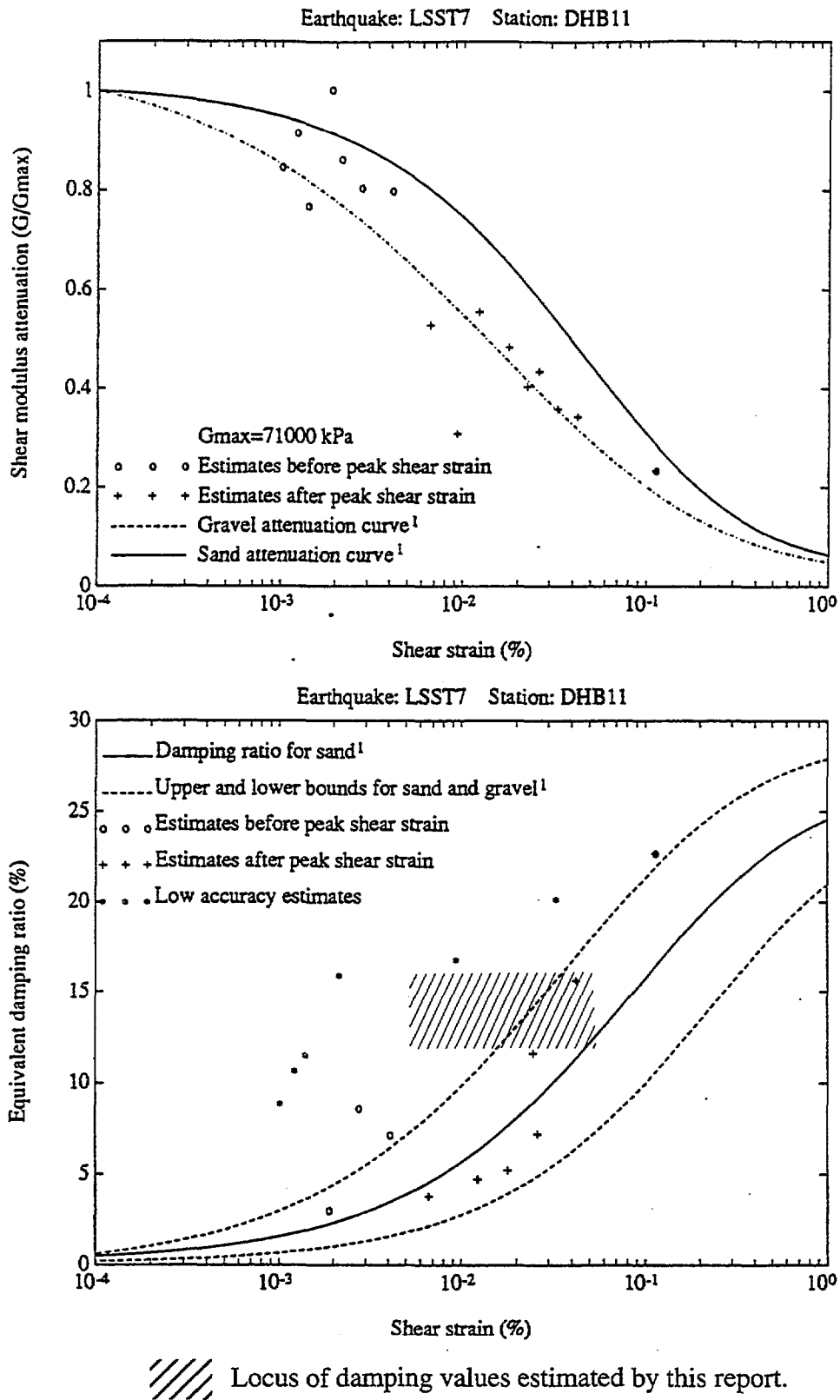
Figure D.10   Equivalent shear moduli and damping ratios at Event 7, 11 m depth, DHB (Zeghal et al., 1995).

Earthquake: LSST7   Station: DHB17

Earthquake: LSST7   Station: DHB17

//// Locus of damping values estimated by this report.
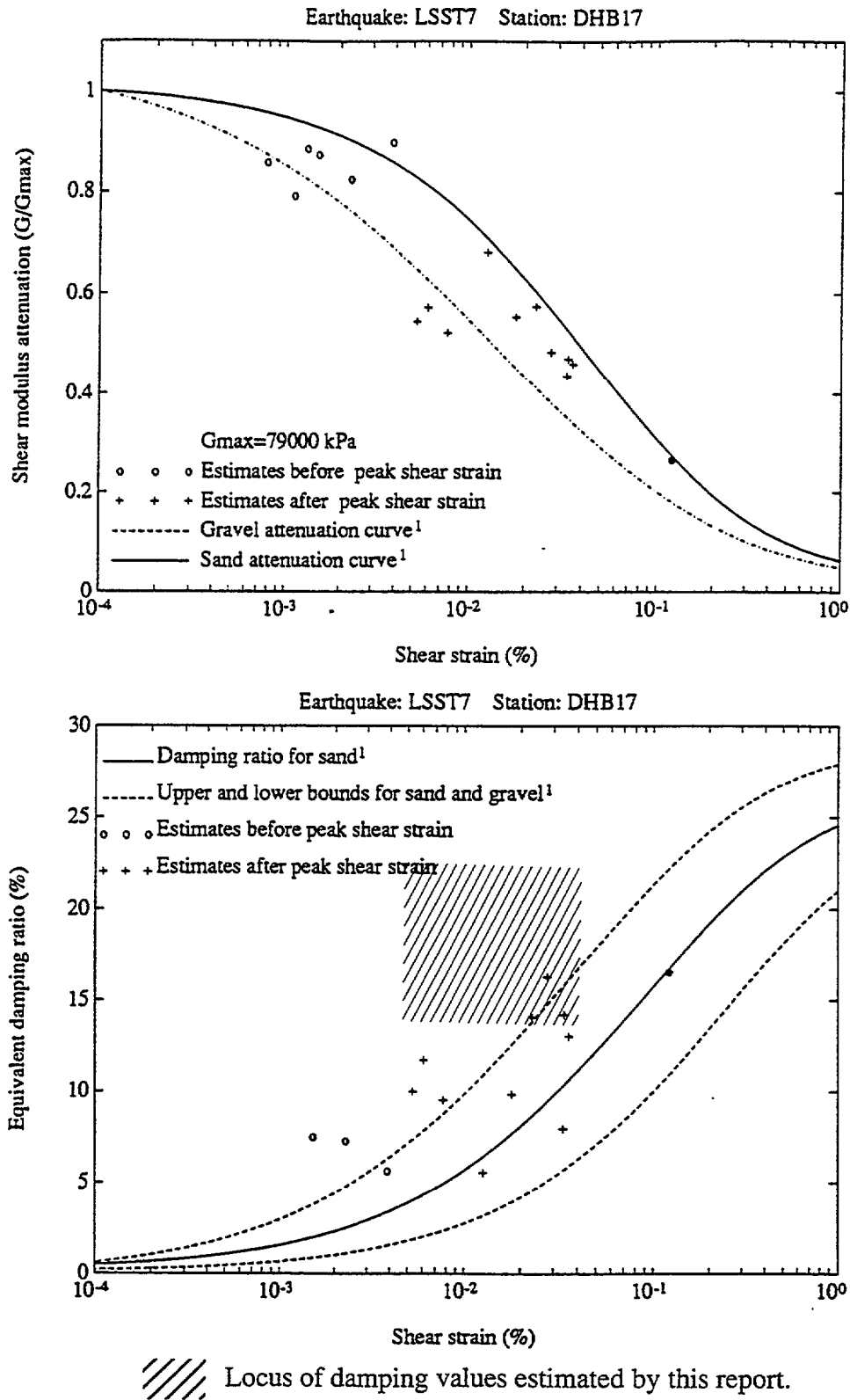
Figure D.11   Equivalent shear moduli and damping ratios at Event 7, 17 m depth, DHB (Zeghal et al., 1995).

126

Earthquake: LSST12   Station: DHB6

Shear modulus attenuation (G/Gmax)

Gmax=50000 kPa
o   o   o Estimates before peak shear strain
+   +   + Estimates after peak shear strain
------- Gravel attenuation curve[1]
——— Sand attenuation curve[1]

Shear strain (%)

Earthquake: LSST12   Station: DHB6

Equivalent damping ratio (%)

——— Damping ratio for sand[1]
----- Upper and lower bounds for sand and gravel[1]
o   o   oEstimates before peak shear strain
+   +   +Estimates after peak shear strain

Shear strain (%)

Locus of damping values estimated by this report.

Figure D.12   Equivalent shear moduli and damping ratios at Event 12, 6 m depth, DHB (Zeghal et al., 1995).

127

Earthquake: LSST12   Station: DHB11

Gmax=71000 kPa
o   o   o Estimates before peak shear strain
+   +   + Estimates after peak shear strain
------- Gravel attenuation curve[1]
——— Sand attenuation curve[1]

Earthquake: LSST12   Station: DHB11

——— Damping ratio for sand[1]
------ Upper and lower bounds for sand and gravel[1]
o   o   o Estimates before peak shear strain
+   +   + Estimates after peak shear strain
.   .   . Low accuracy estimates

//// Locus of damping values estimated by this report.

Figure D.13   Equivalent shear moduli and damping ratios at Event 12, 11 m depth, DHB (Zeghal et al., 1995).

128

Earthquake: LSST12   Station: DHB 17

///// Locus of damping values estimated by this report.

Figure D.14   Equivalent shear moduli and damping ratios at Event 12, 17 m depth, DHB (Zeghal et al., 1995).

Earthquake: LSST16   Station: DHB6

Earthquake: LSST16   Station: DHB6

Locus of damping values estimated by this report.
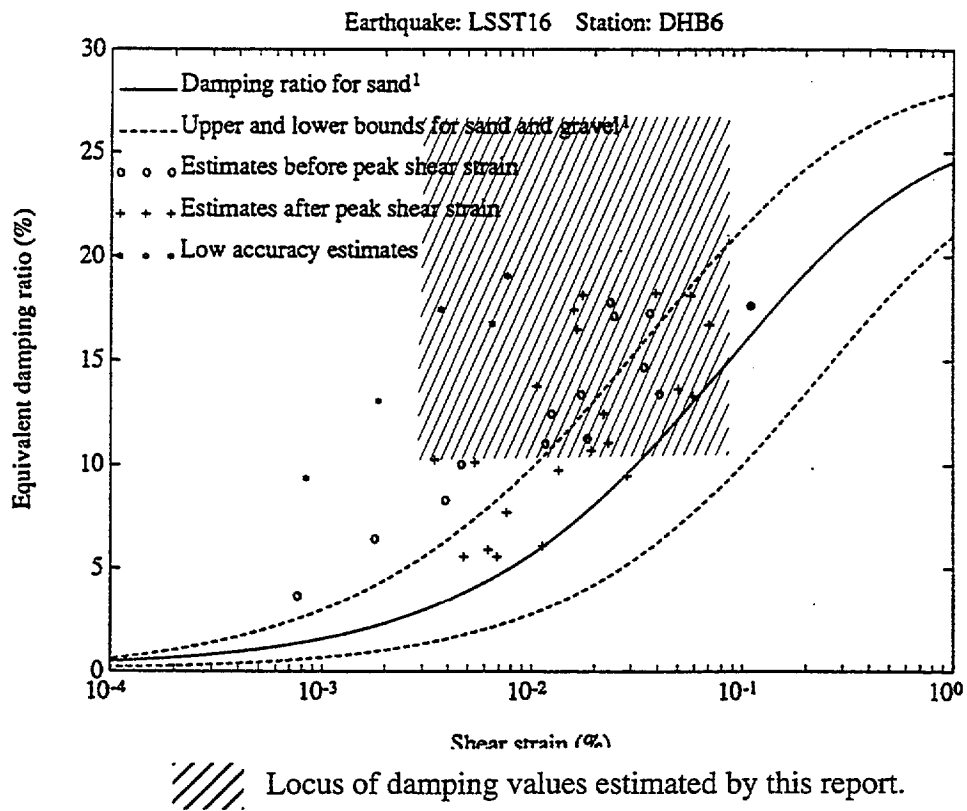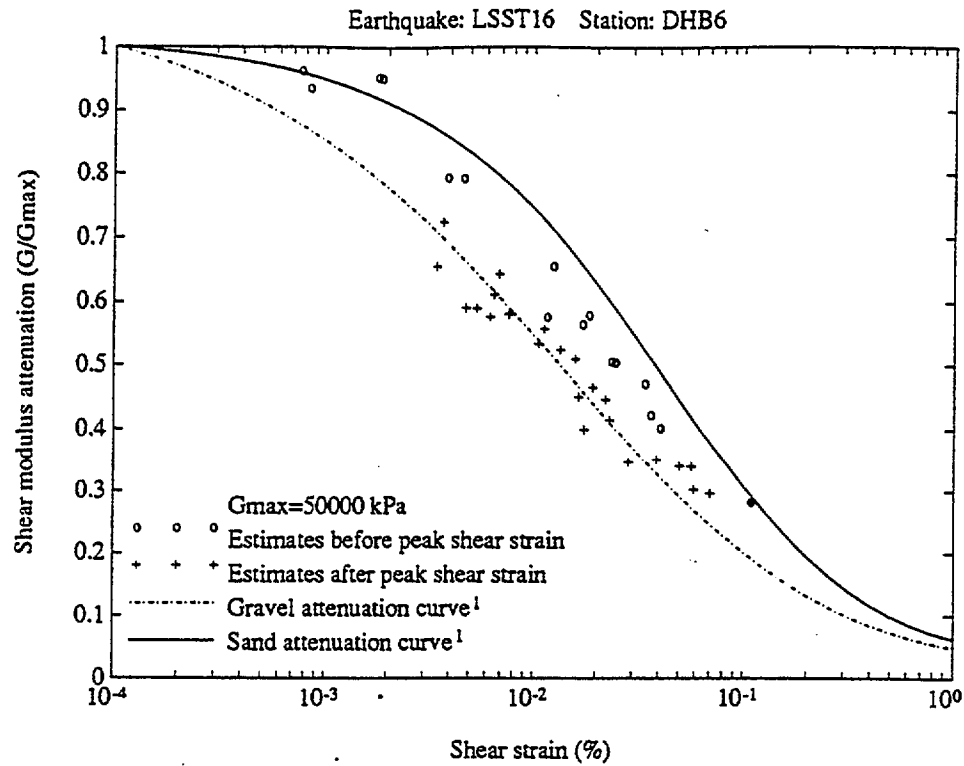
Figure D.15   Equivalent shear moduli and damping ratios at Event 16, 6 m depth, DHB (Zeghal et al., 1995).

130

Earthquake: LSST16   Station: DHB11

Earthquake: LSST16   Station: DHB11
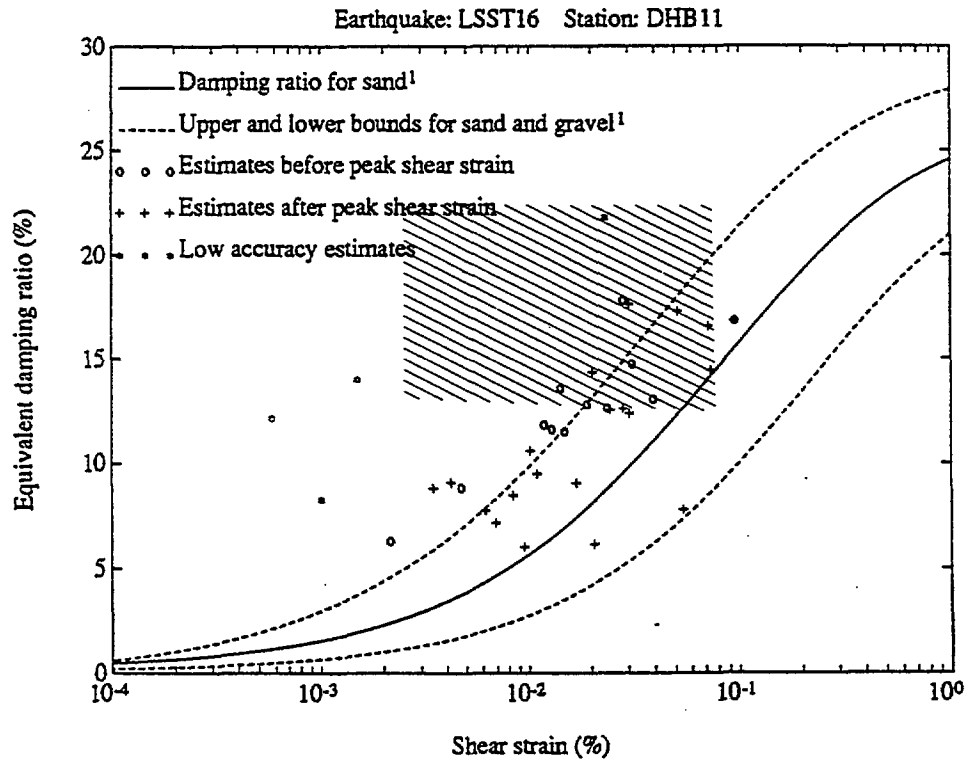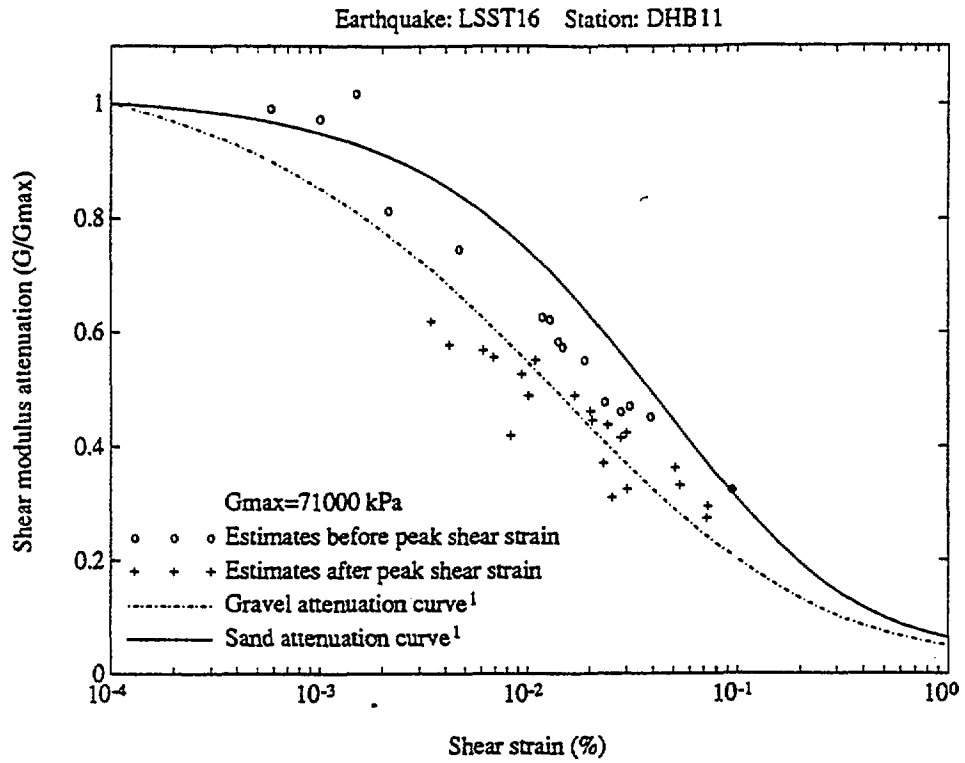
////. Locus of damping values estimated by this report.

Figure D.16   Equivalent shear moduli and damping ratios at Event 16, 11 m depth, DHB (Zeghal et al., 1995).

131

Earthquake: LSST16   Station: DHB17

Shear modulus attenuation (G/Gmax)

1

0.8

0.6

0.4

Gmax=79000 kPa

0.2
○   ○   ● Estimates before peak shear strain
+   +   + Estimates after peak shear strain
------- Gravel attenuation curve[1]
——— Sand attenuation curve[1]

0
10^{-4} 10^{-3} 10^{-2} 10^{-1} 10^{0}

Shear strain (%)

Earthquake: LSST16   Station: DHB17

30

Equivalent damping ratio (%)

——— Damping ratio for sand[1]
----- Upper and lower bounds for sand and gravel[1]
○ ○ ○ Estimates before peak shear strain
+ + + Estimates after peak shear strain
● ● ● Low accuracy estimates

25

20

15

10

5

0
10^{-4} 10^{-3} 10^{-2} 10^{-1} 10^{0}

Shear strain (%)

///// Locus of damping values estimated by this report.

Figure D.17   Equivalent shear moduli and damping ratios at Event 16, 17 m depth, DHB (Zeghal et al., 1995).

APPENDIX E: COMPARISON OF ACTUAL INTERVAL OUTPUTS TO MODELED INTERVAL OUTPUTS FOR ALL ANALYZED EVENTS

Actual (solid) VS. RARX Simulated (dashed) Out for [4 4 1]   Fit: 0.08735
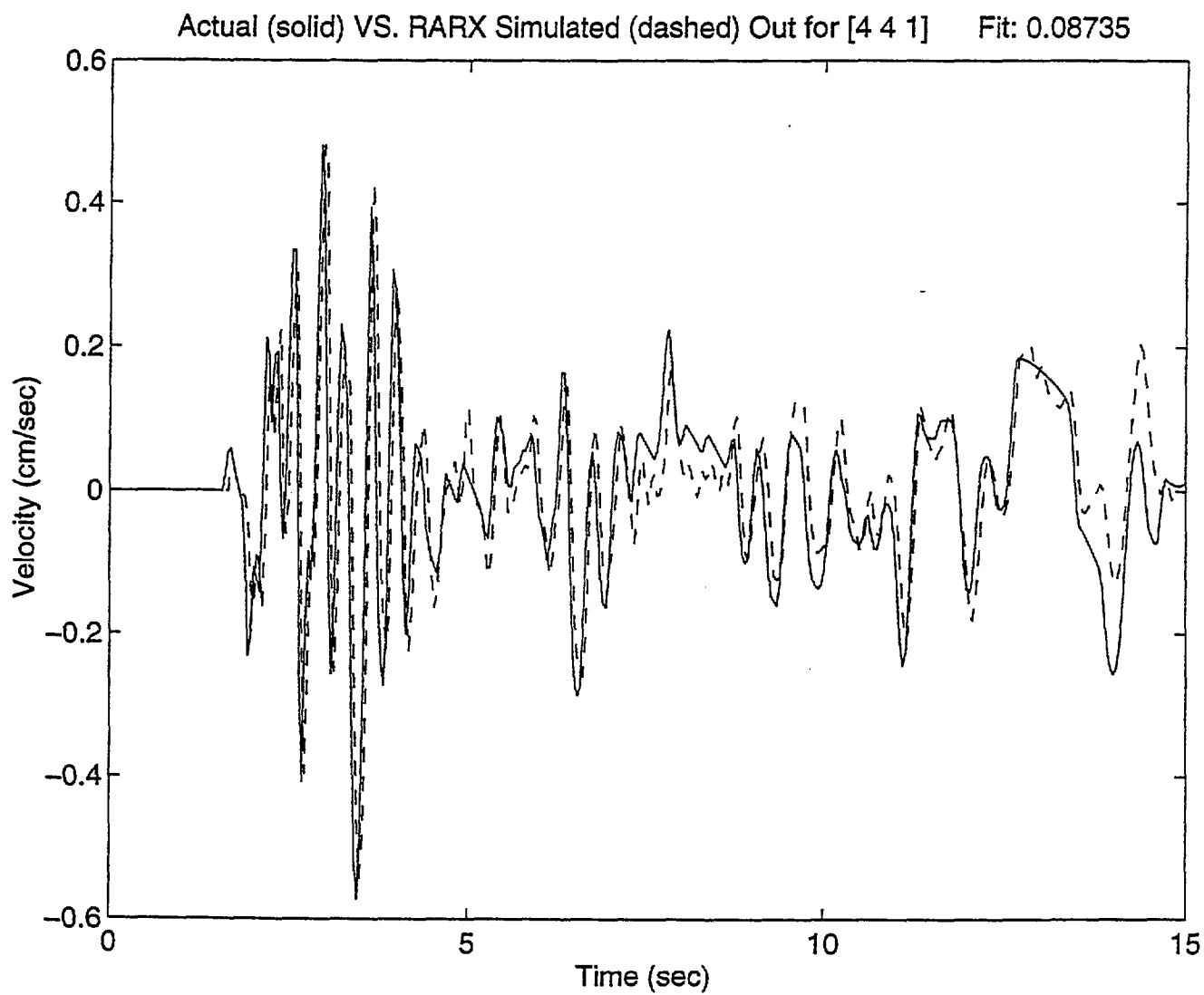
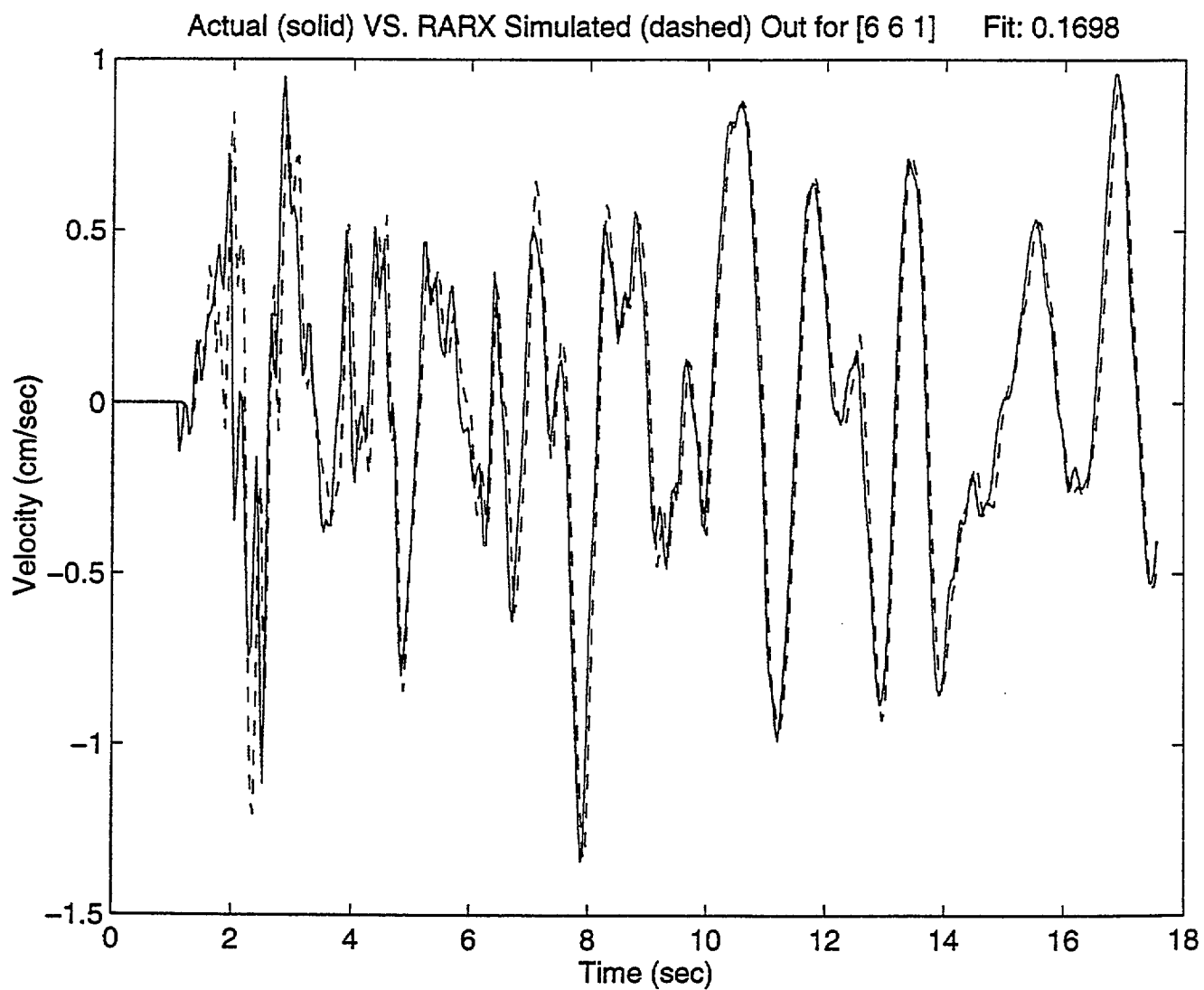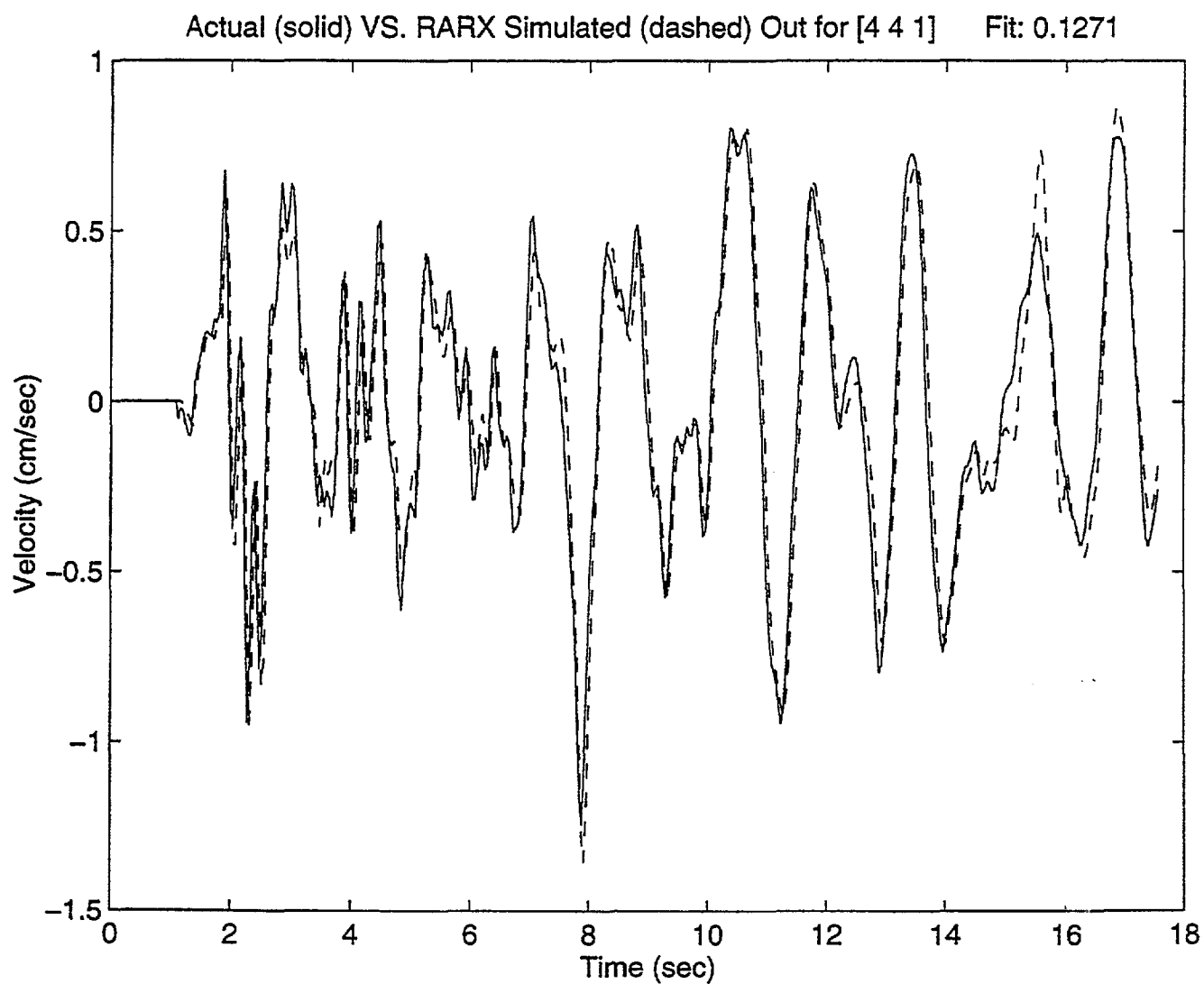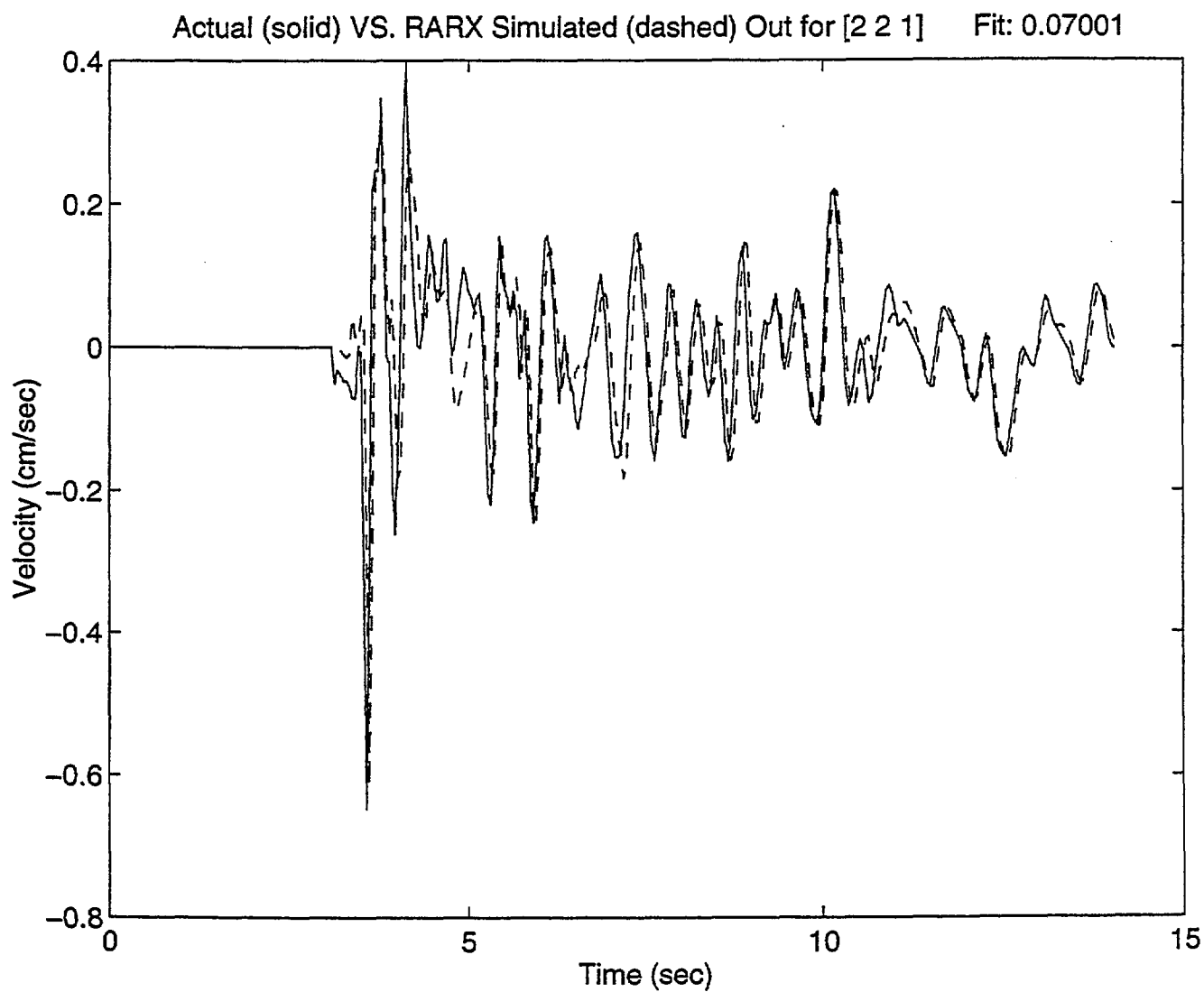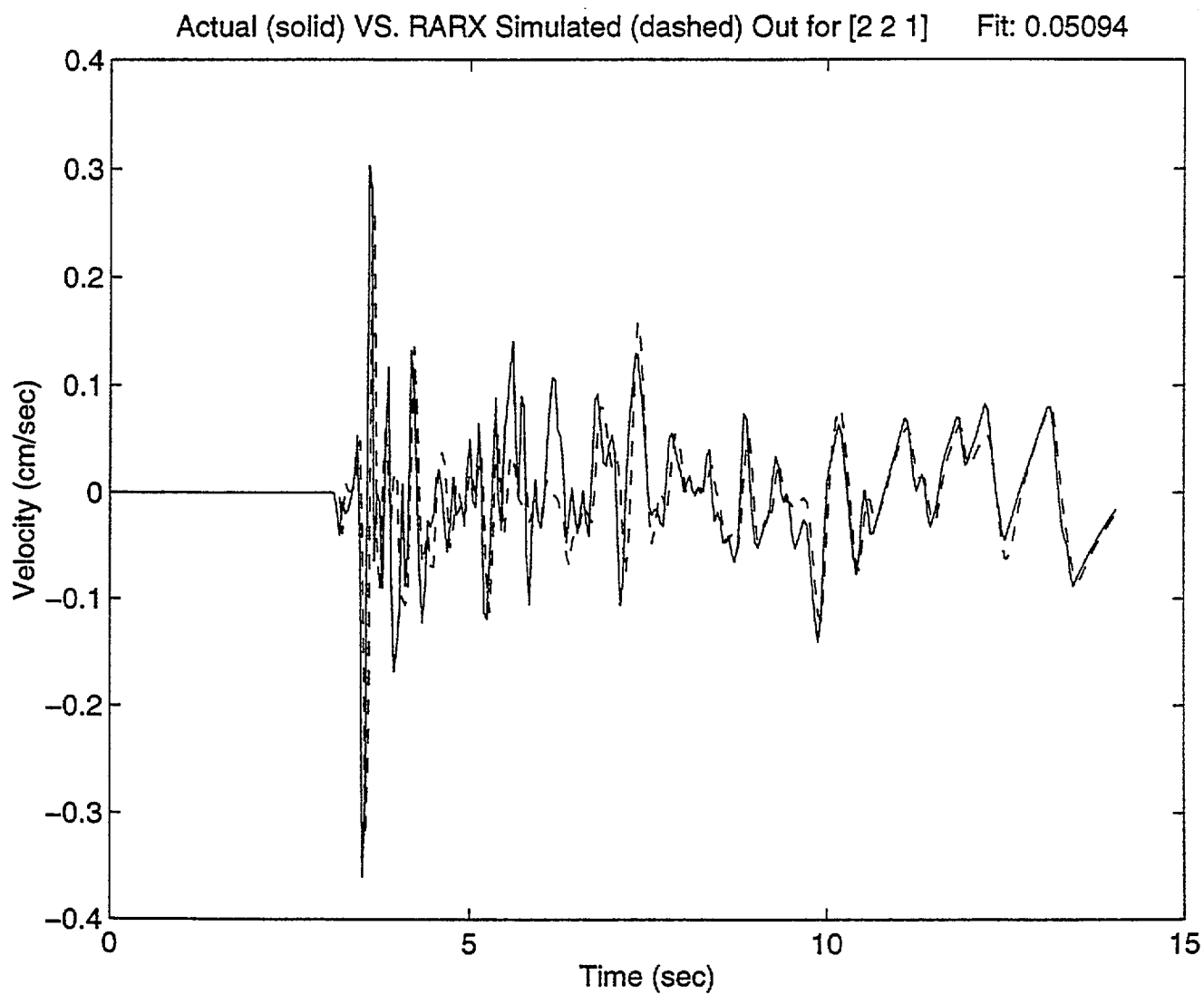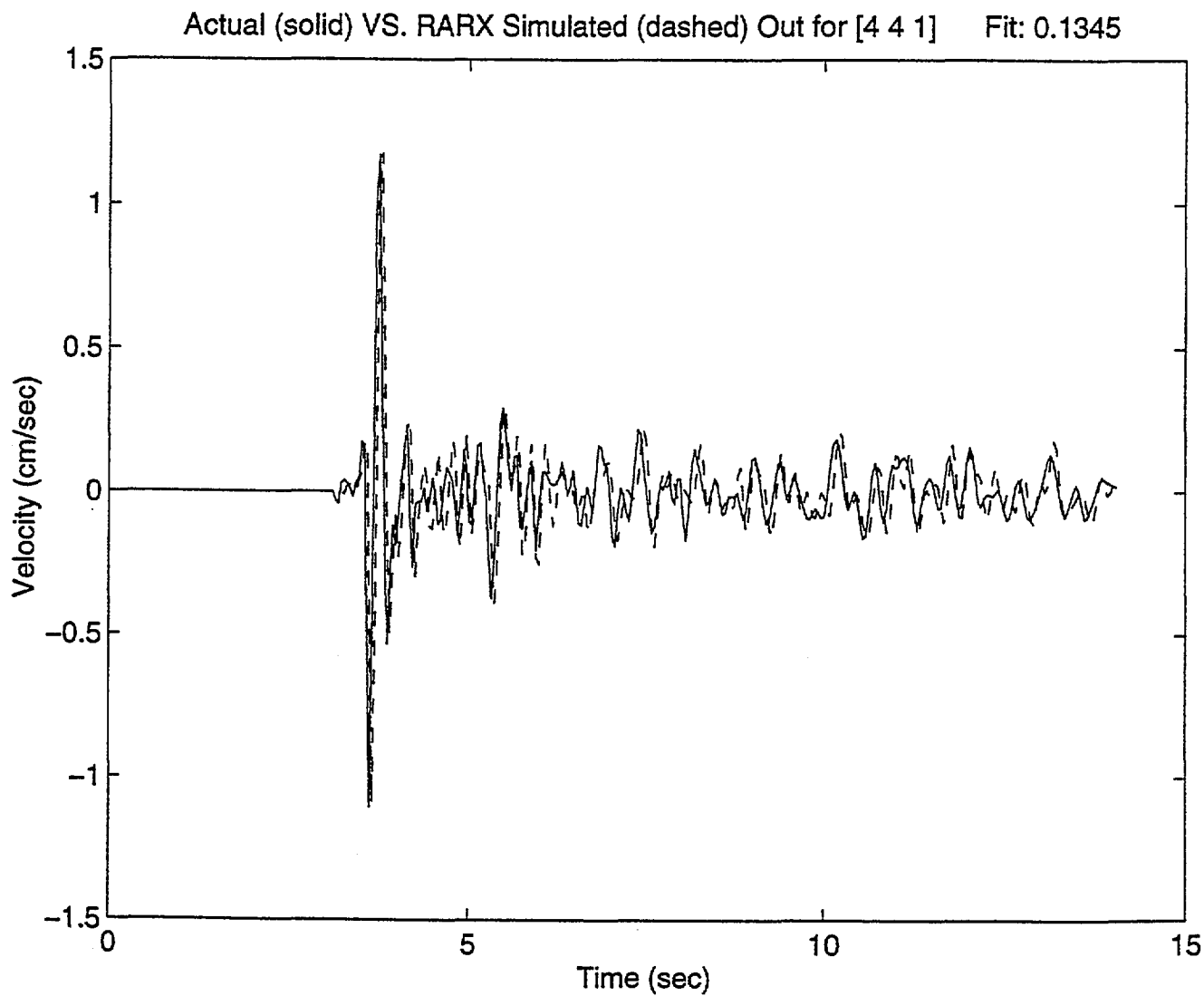Figure E.1   Modeled versus actual output, Event3, E - W, DHA, 0 to 6 m depth interval.
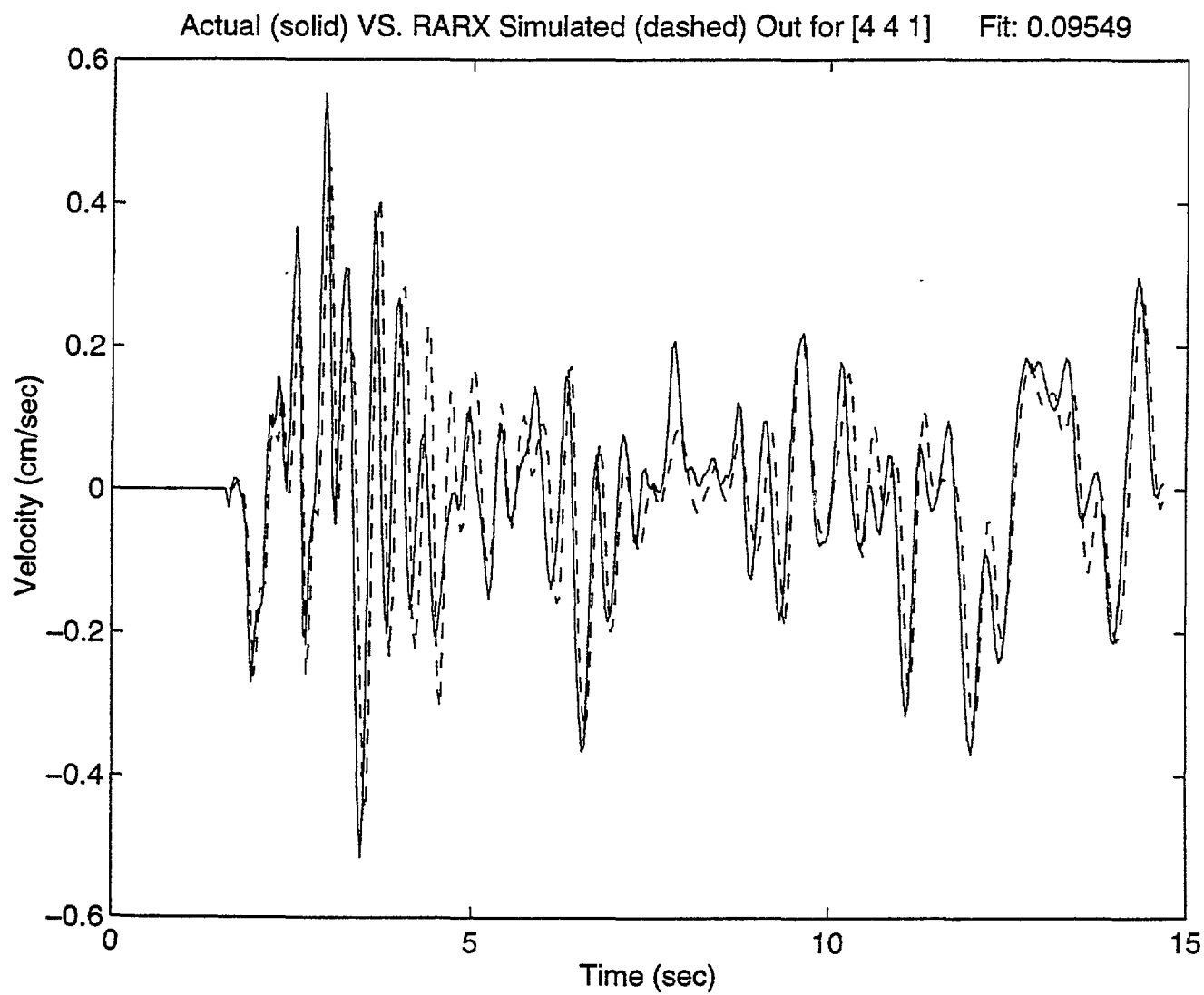
Figure E.2   Modeled versus actual output, Event3, E - W, DHA, 6 to 11 m depth interval.
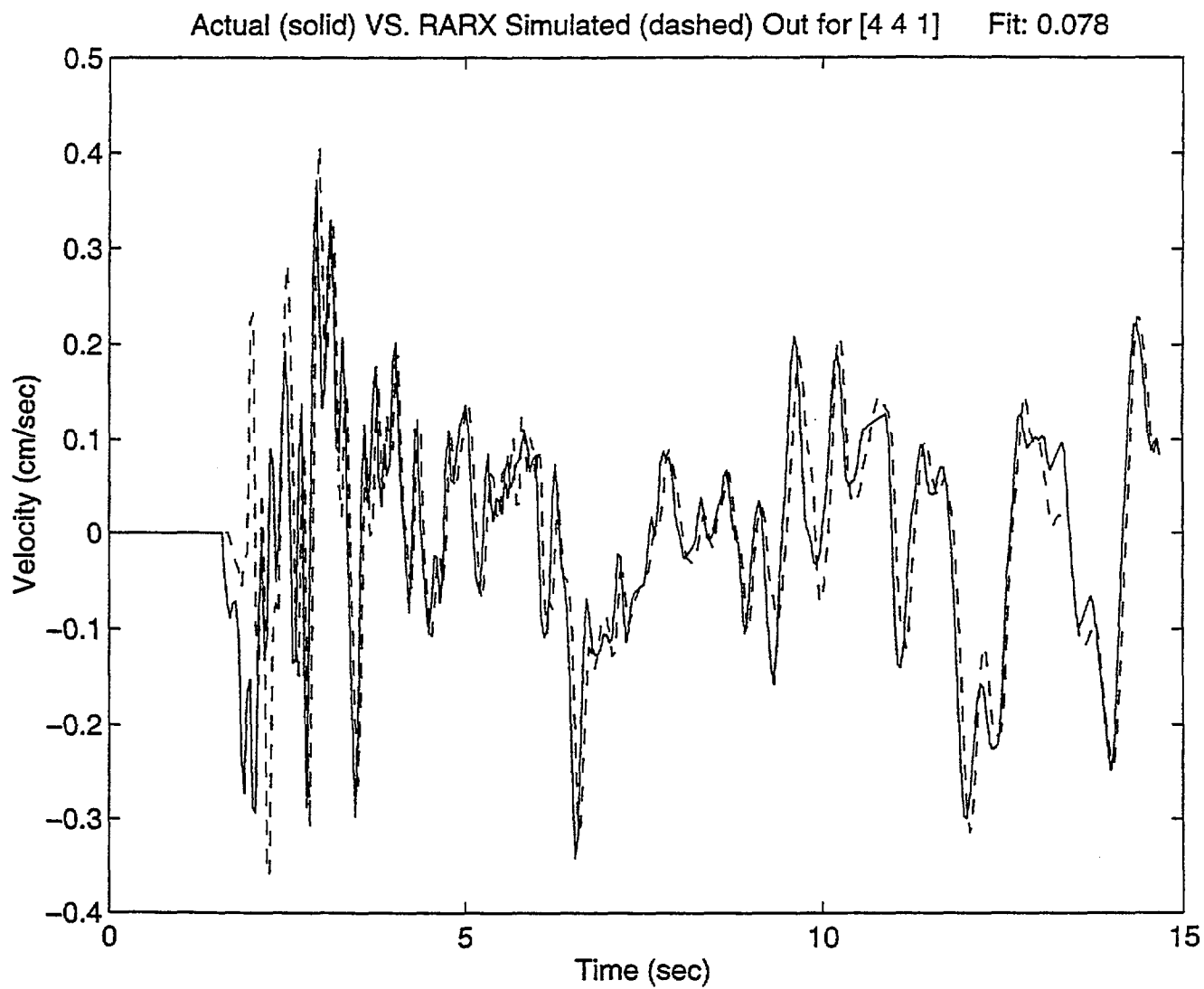
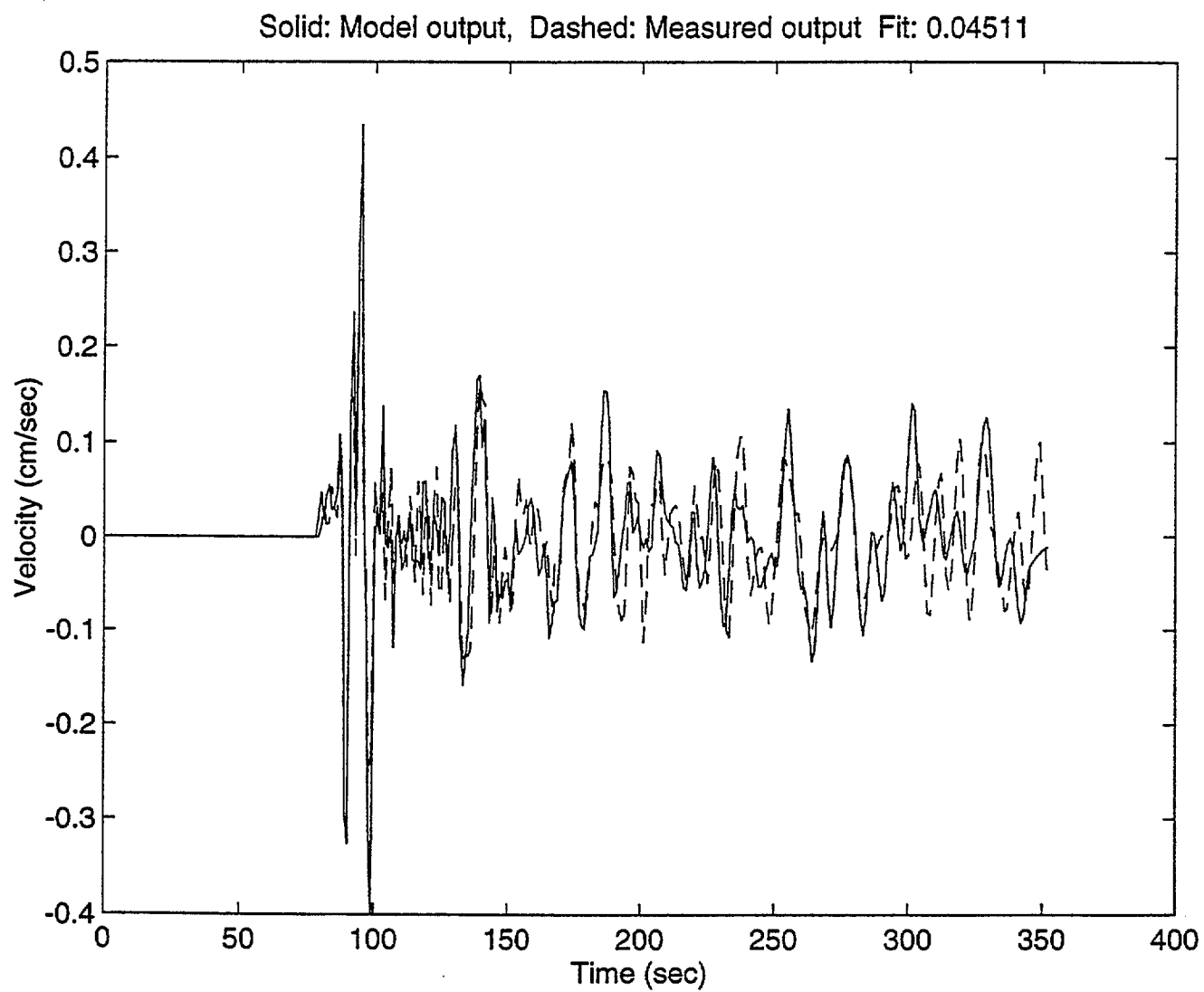Figure E.3   Modeled versus actual output, Event3, E - W, DHA, 11 to 17 m depth interval.
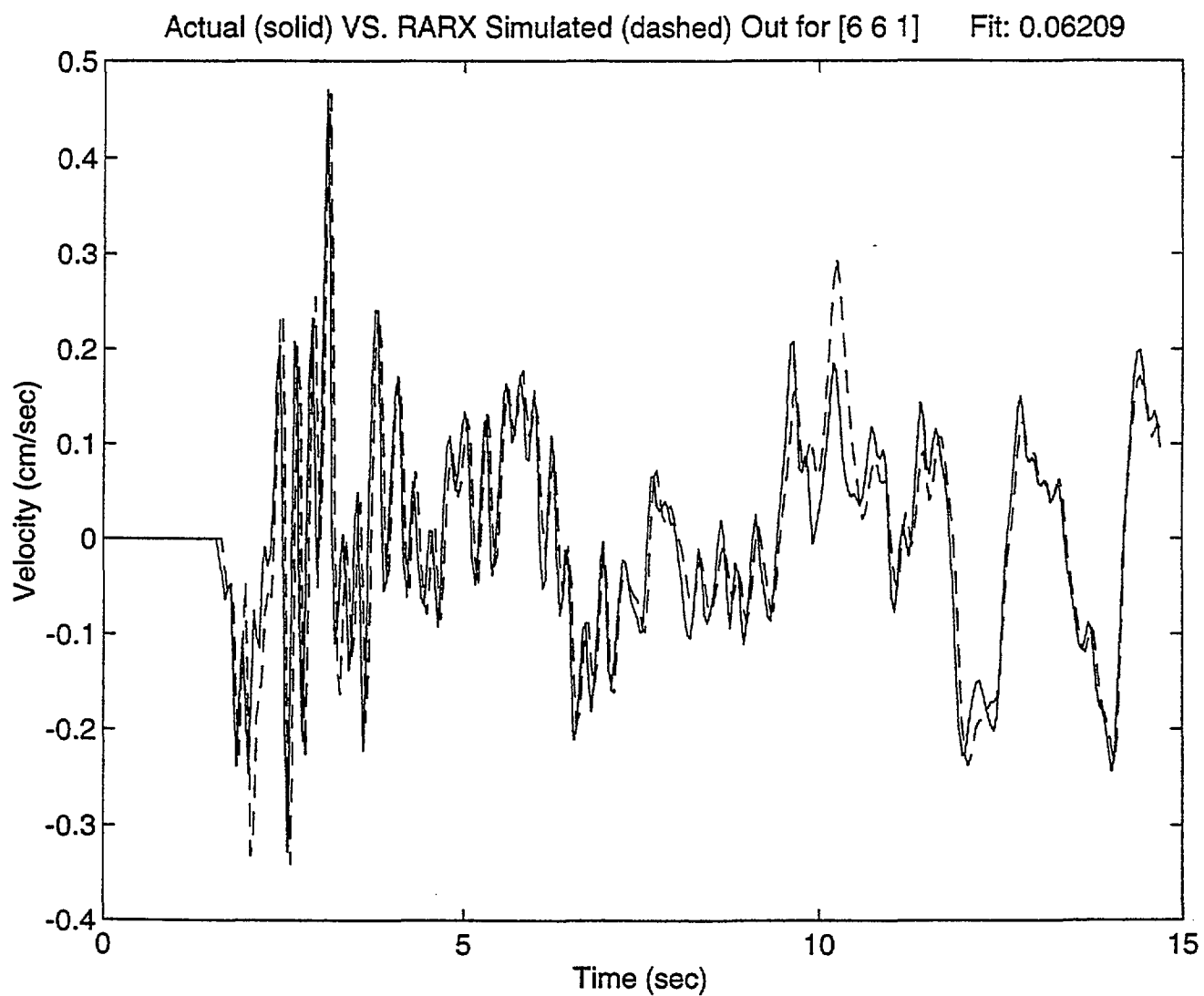
Figure E.4   Modeled versus actual output, Event3, E - W, DHA, 17 to 47 m depth interval.
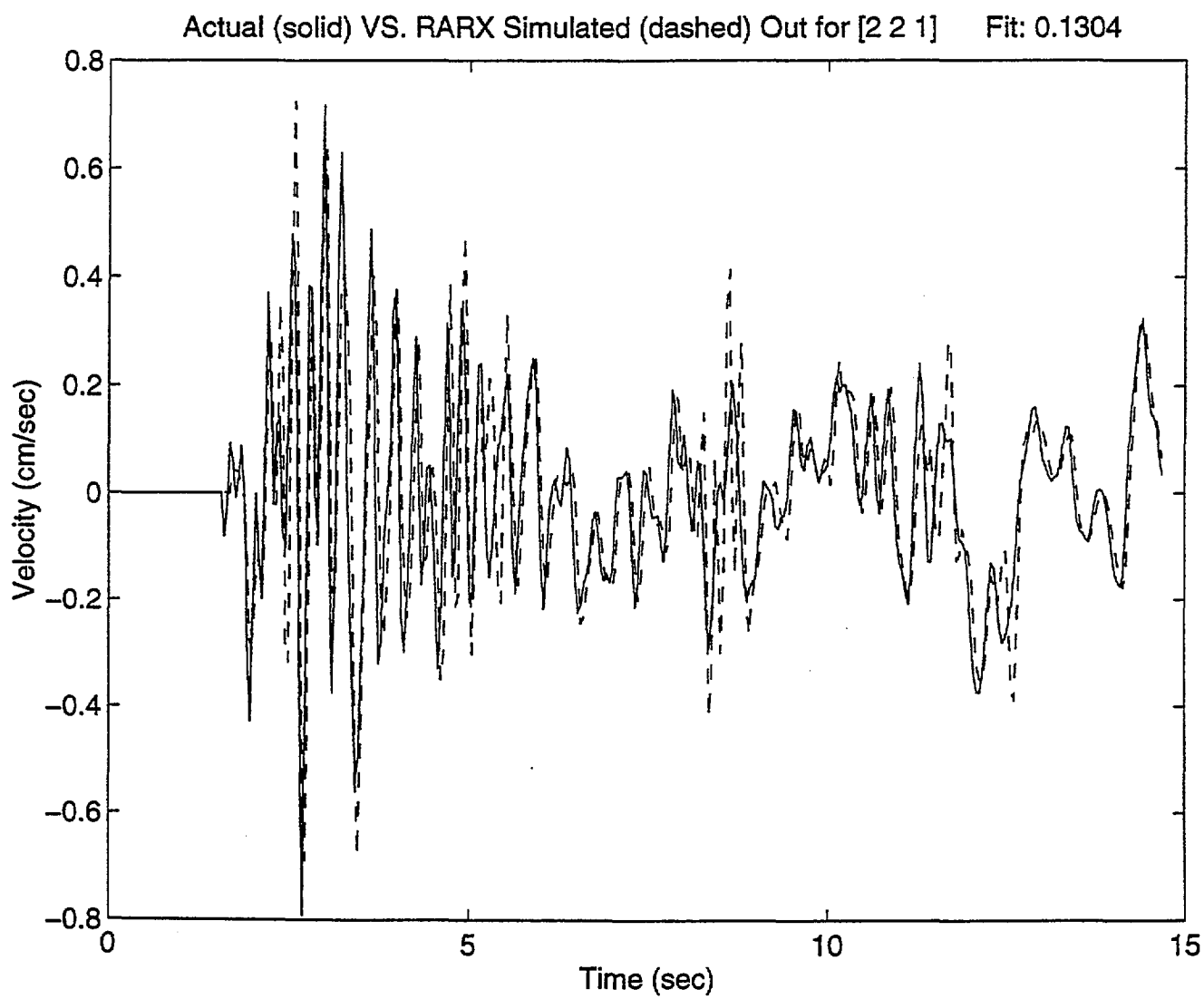
Figure E.5 Modeled versus actual output, Event3, E - W, DHB, 0 to 6 m depth interval.
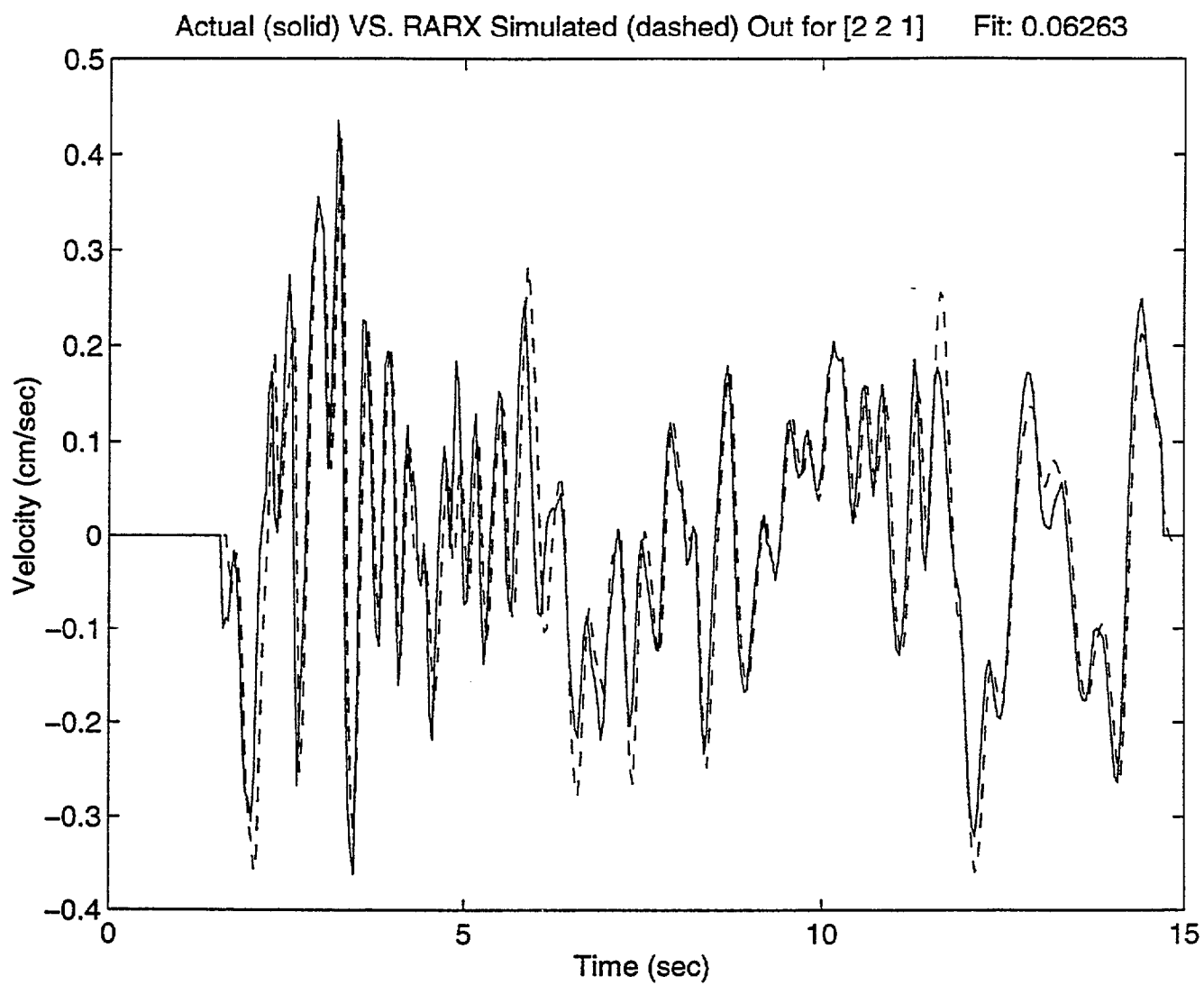
Figure E.6 Modeled versus actual output, Event3, E - W, DHB, 6 to 11 m depth interval.
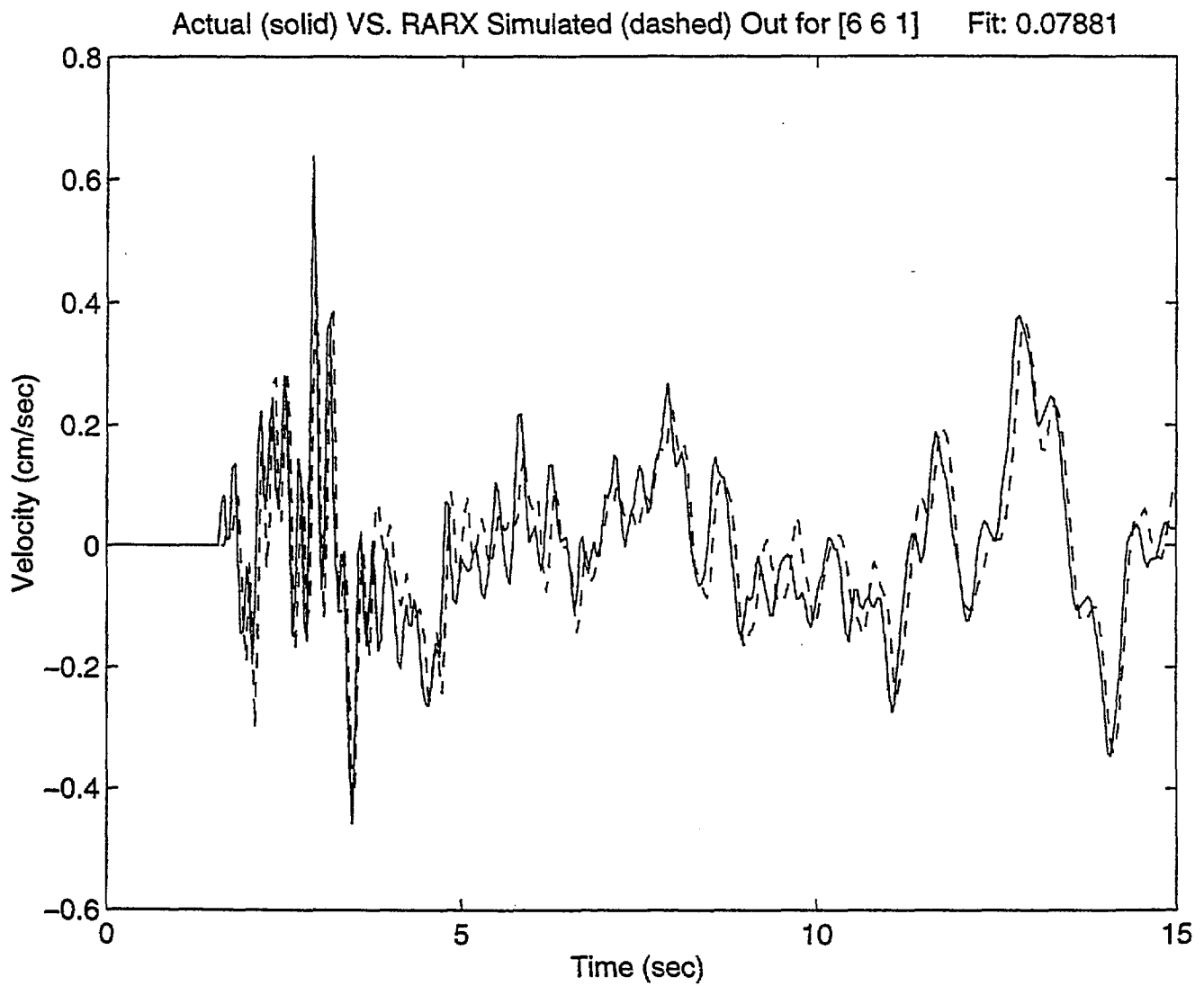
Figure E.7 Modeled versus actual output, Event3, E - W, DHB, 11 to 17 m depth interval.
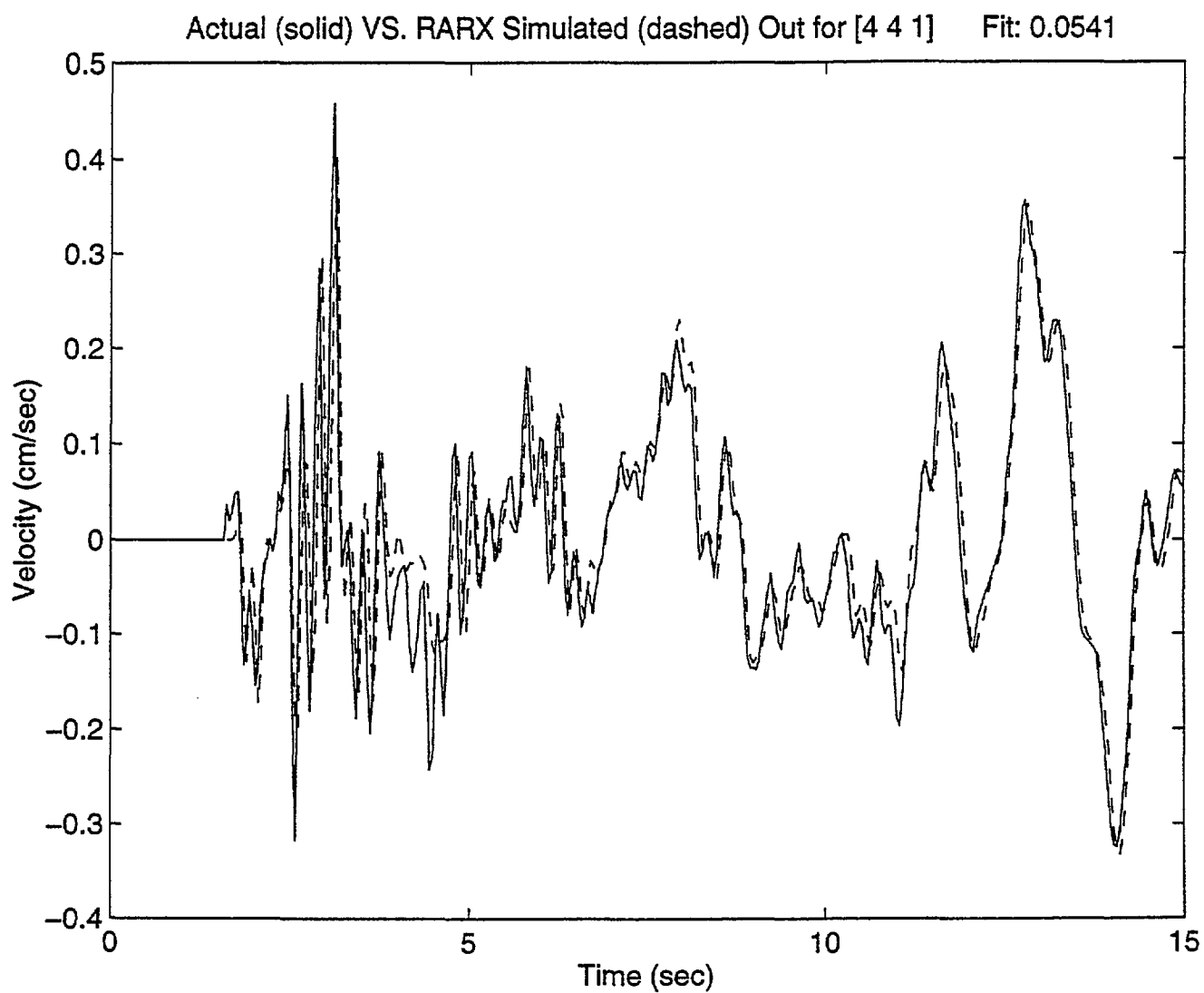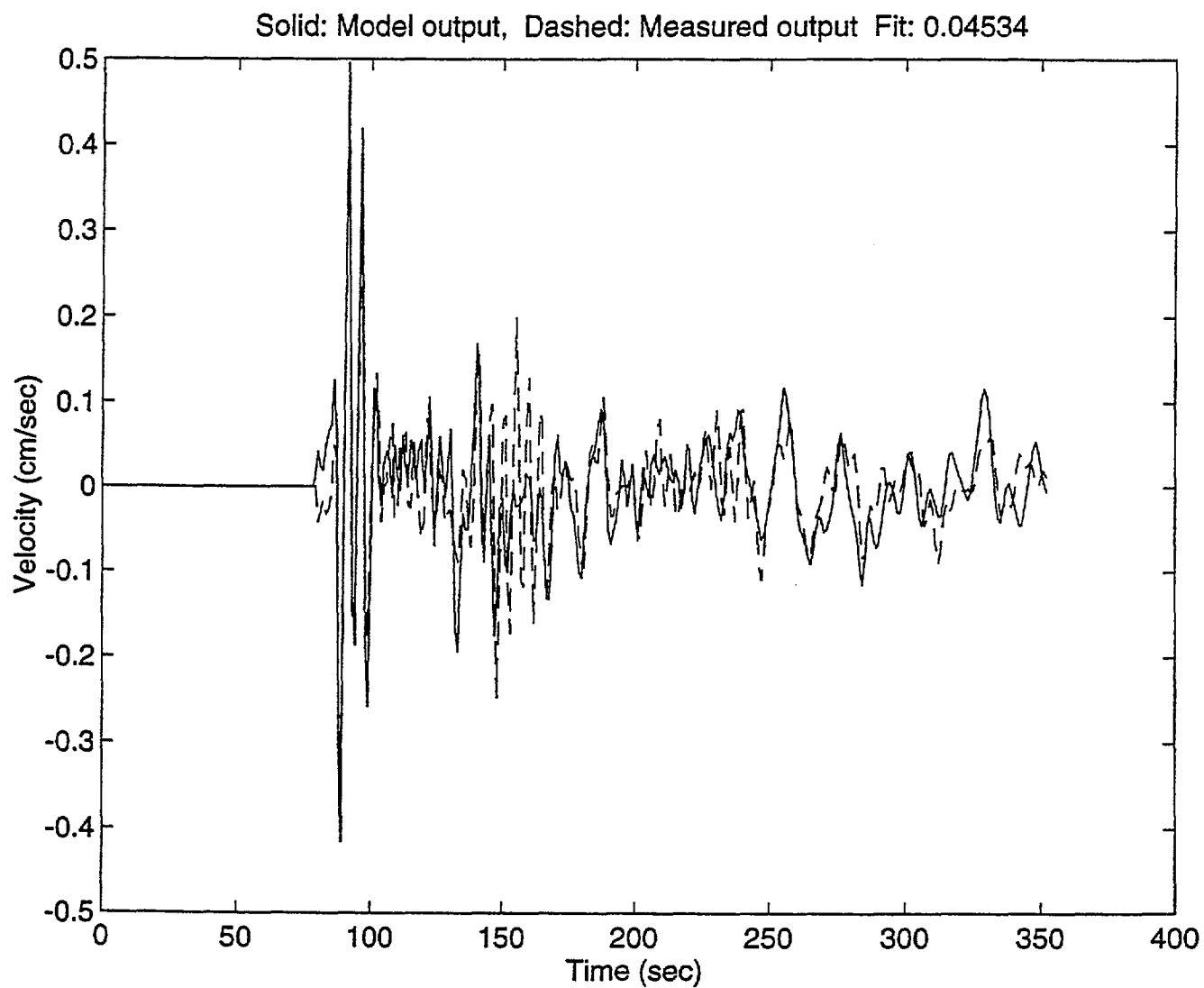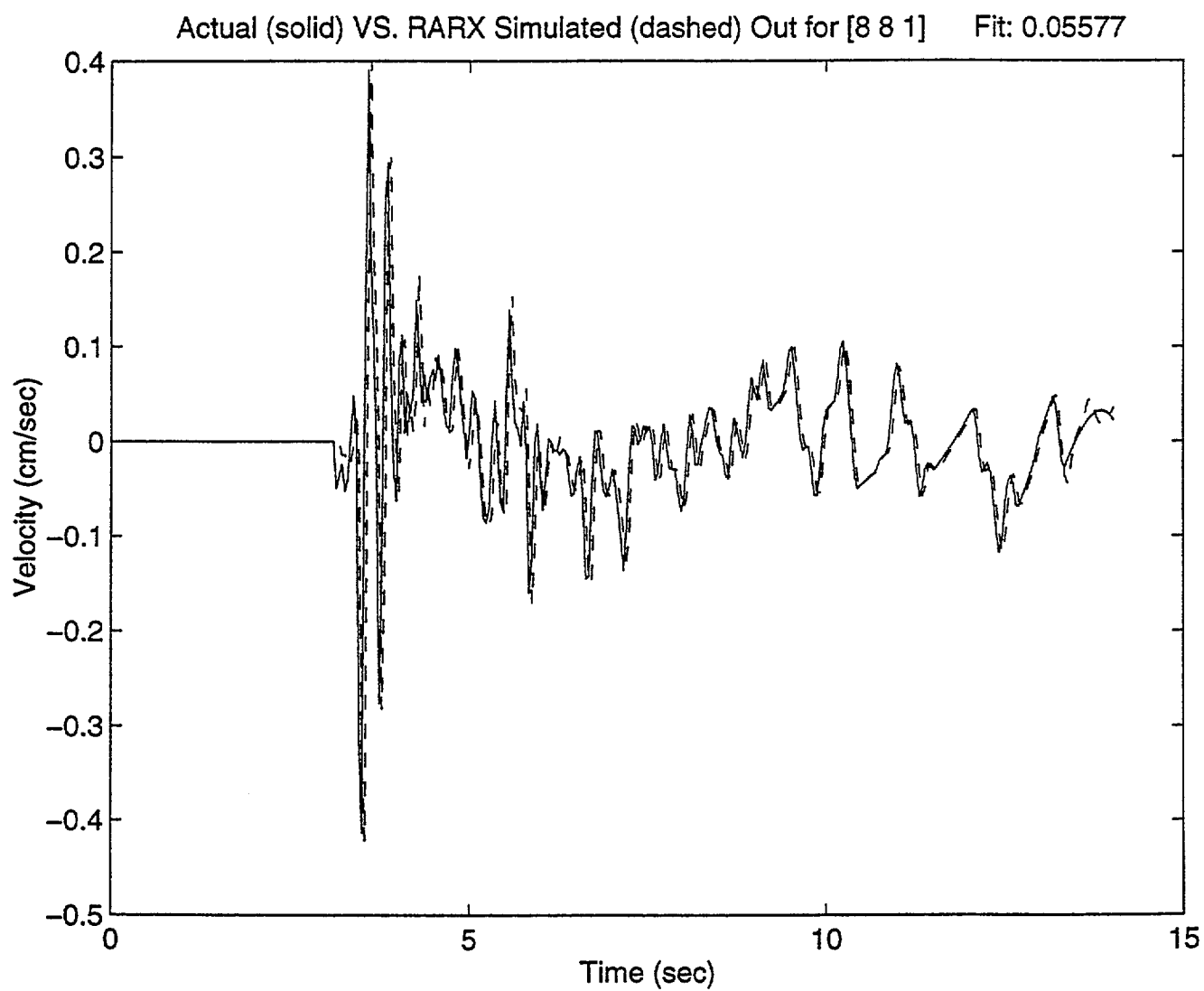
Figure E.8   Modeled versus actual output, Event3, E - W, DHB, 17 to 47 m depth interval.
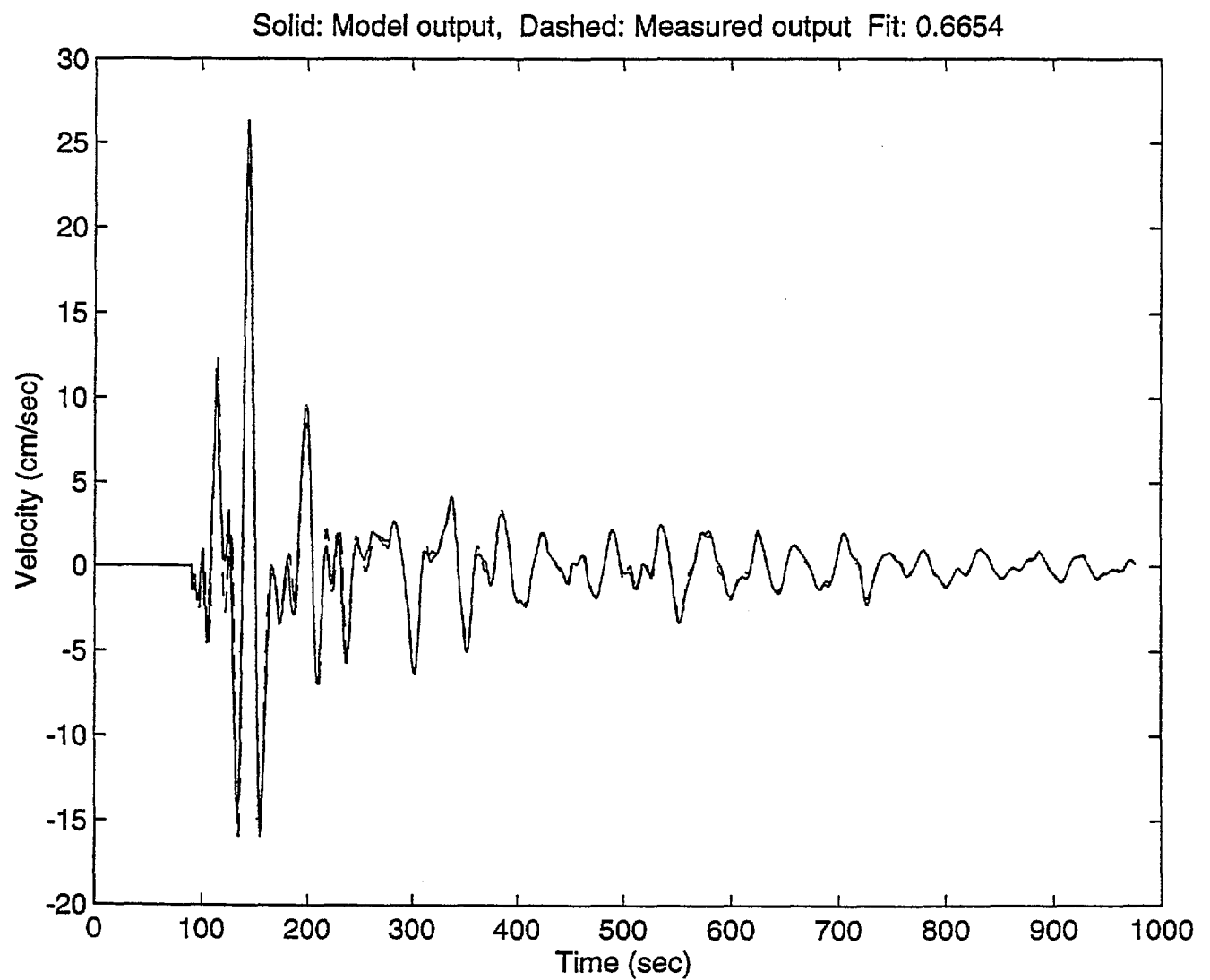
Figure E.9   Modeled versus actual output, Event4, E - W, DHA, 0 to 6 m depth interval.
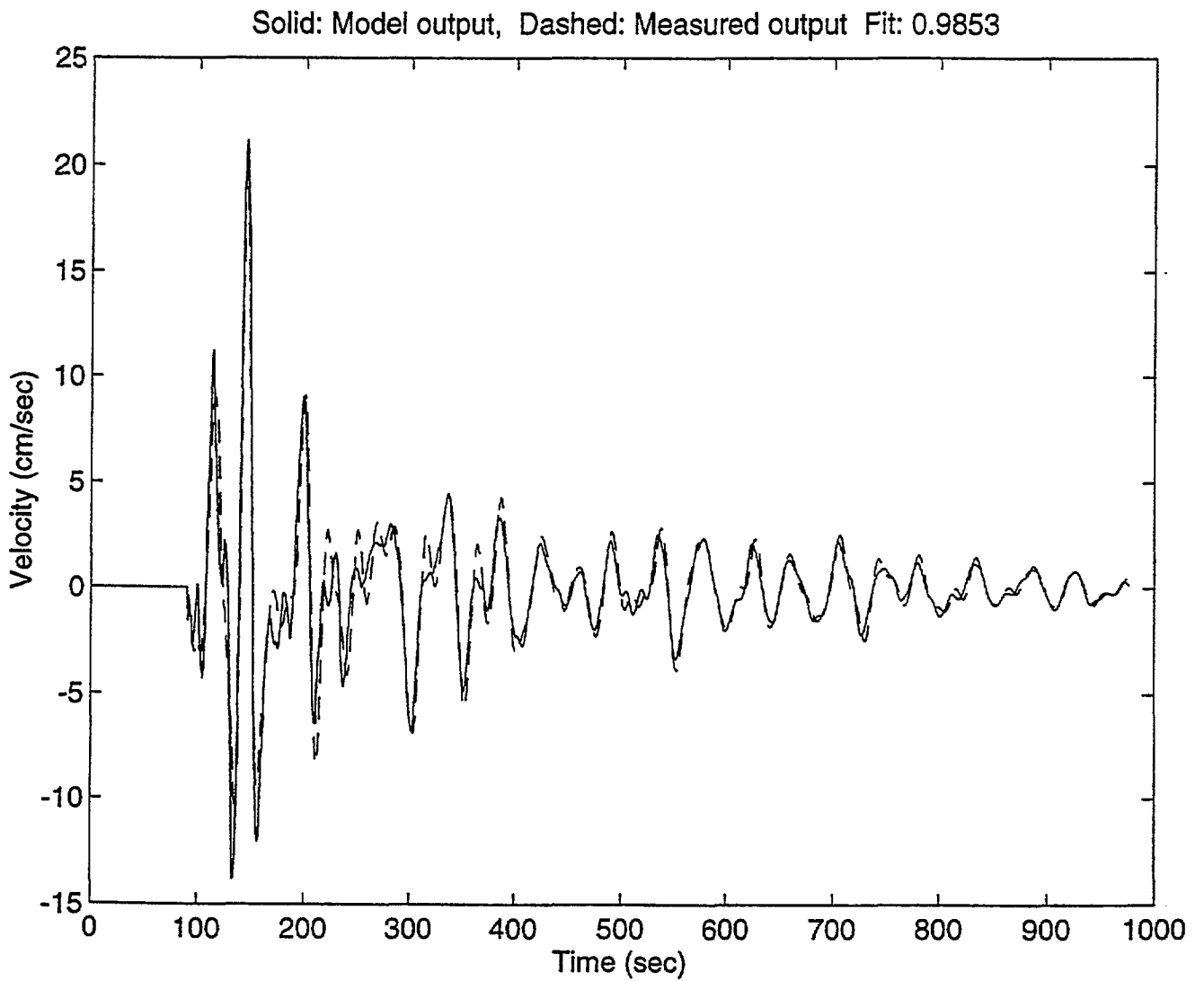
Figure E.10   Modeled versus actual output, Event4, E - W, DHA, 6 to 11 m depth interval.

Solid: Model output, Dashed: Measured output Fit: 0.6284
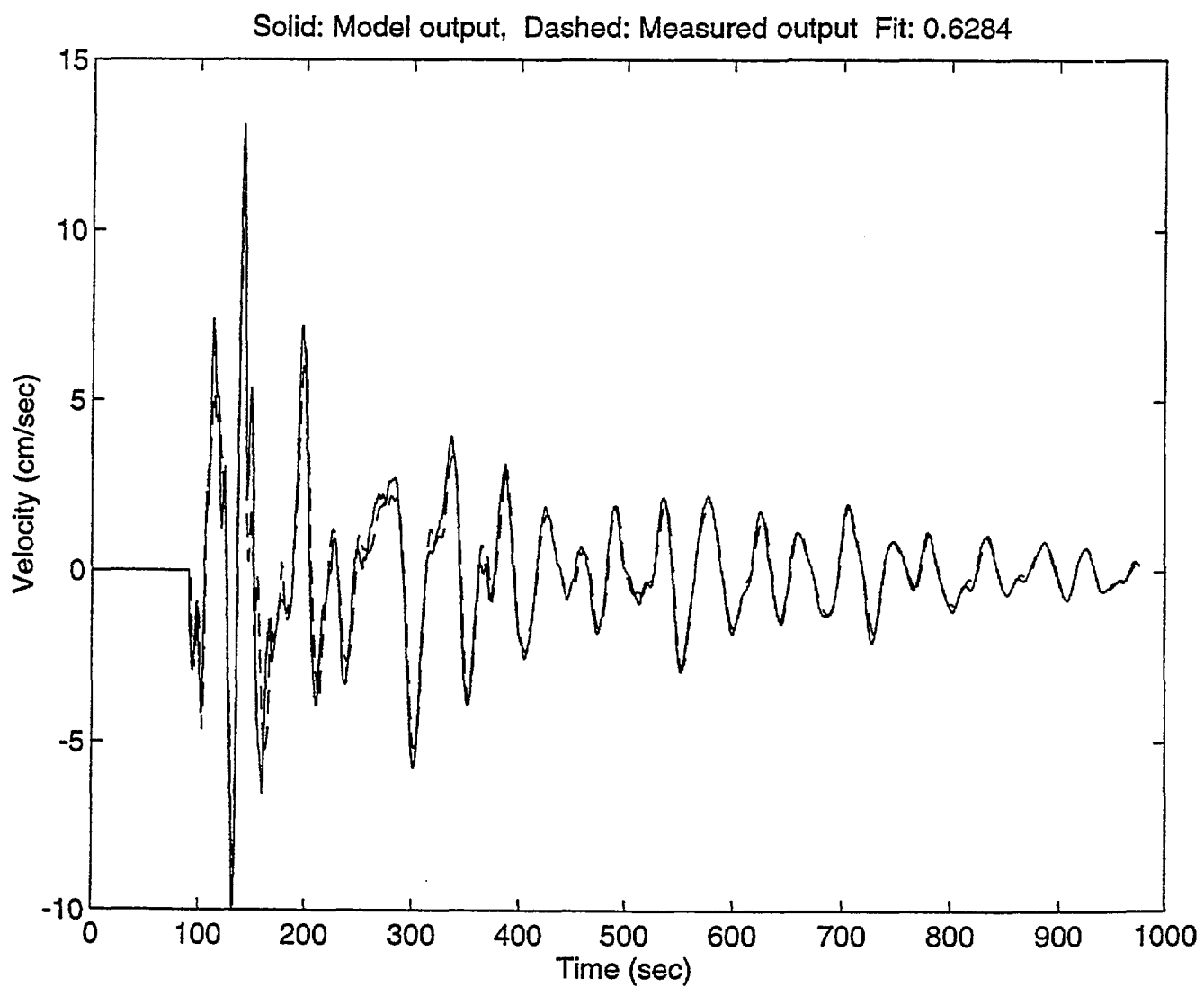
Figure E.11   Modeled versus actual output, Event4, E - W, DHA, 11 to 17 m depth interval.

Actual (solid) VS. RARX Simulated (dashed) Out for [2 2 1]   Fit: 0.6673
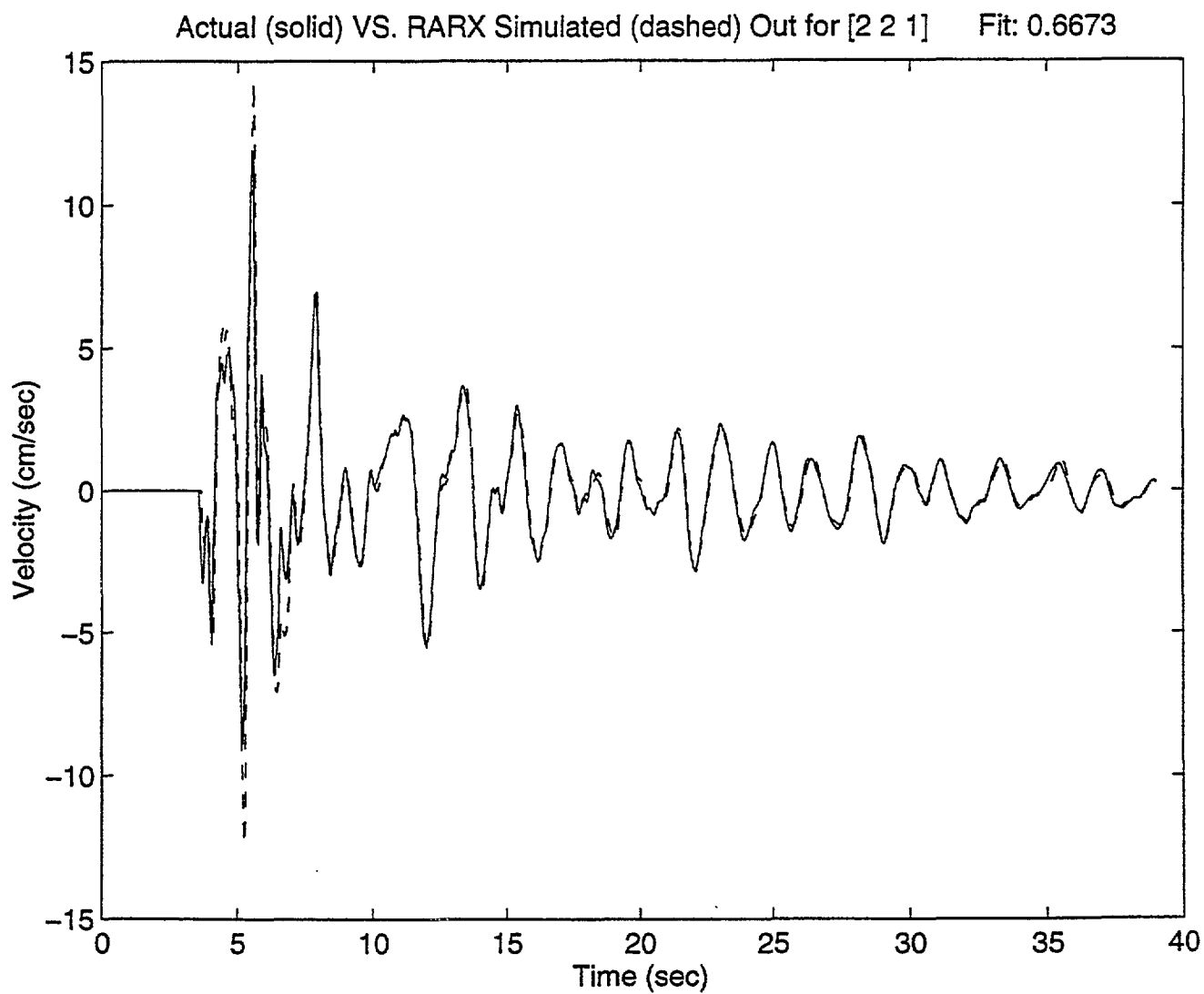
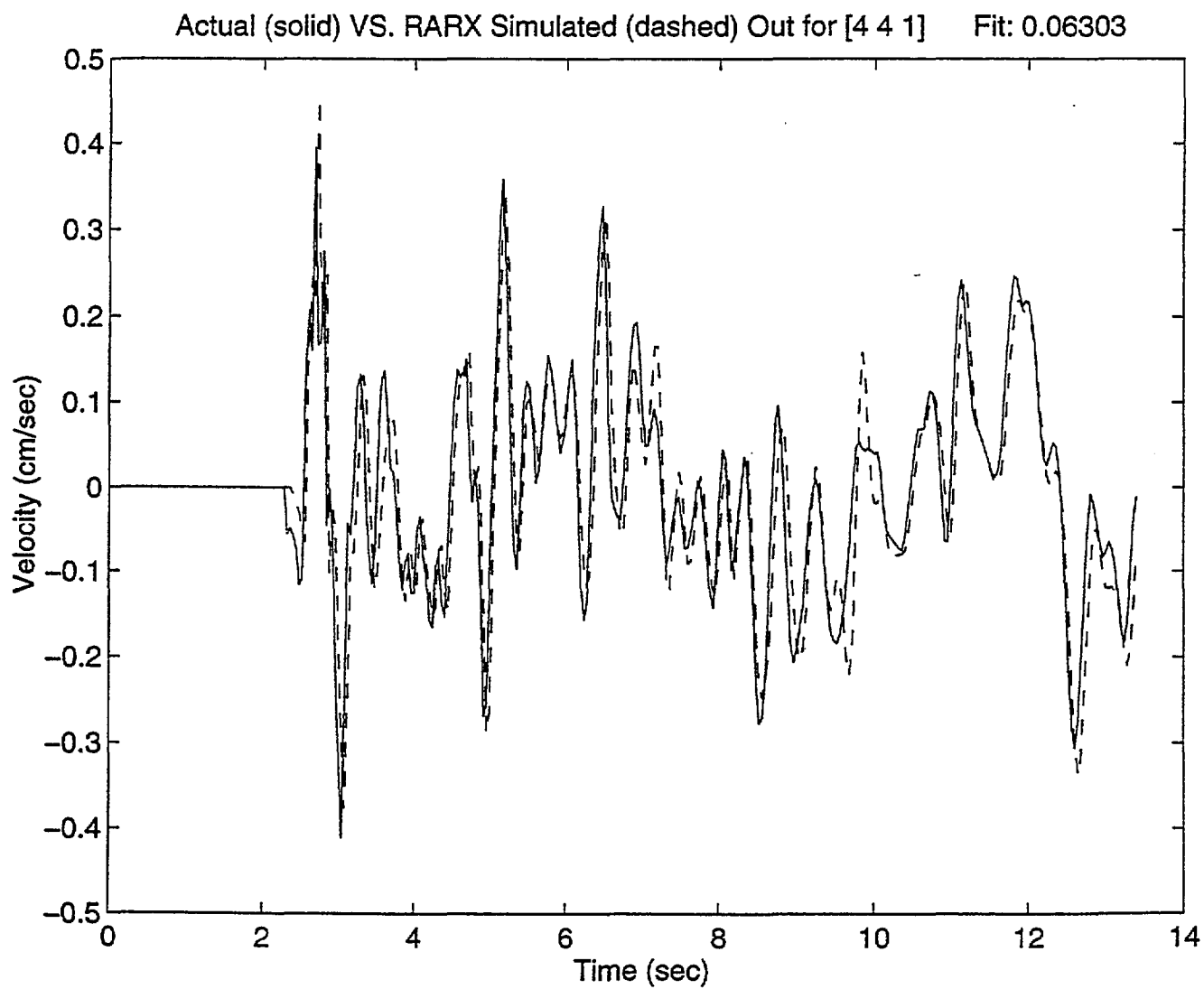Figure E.12   Modeled versus actual output, Event4, E - W, DHA, 17 to 47 m depth interval.
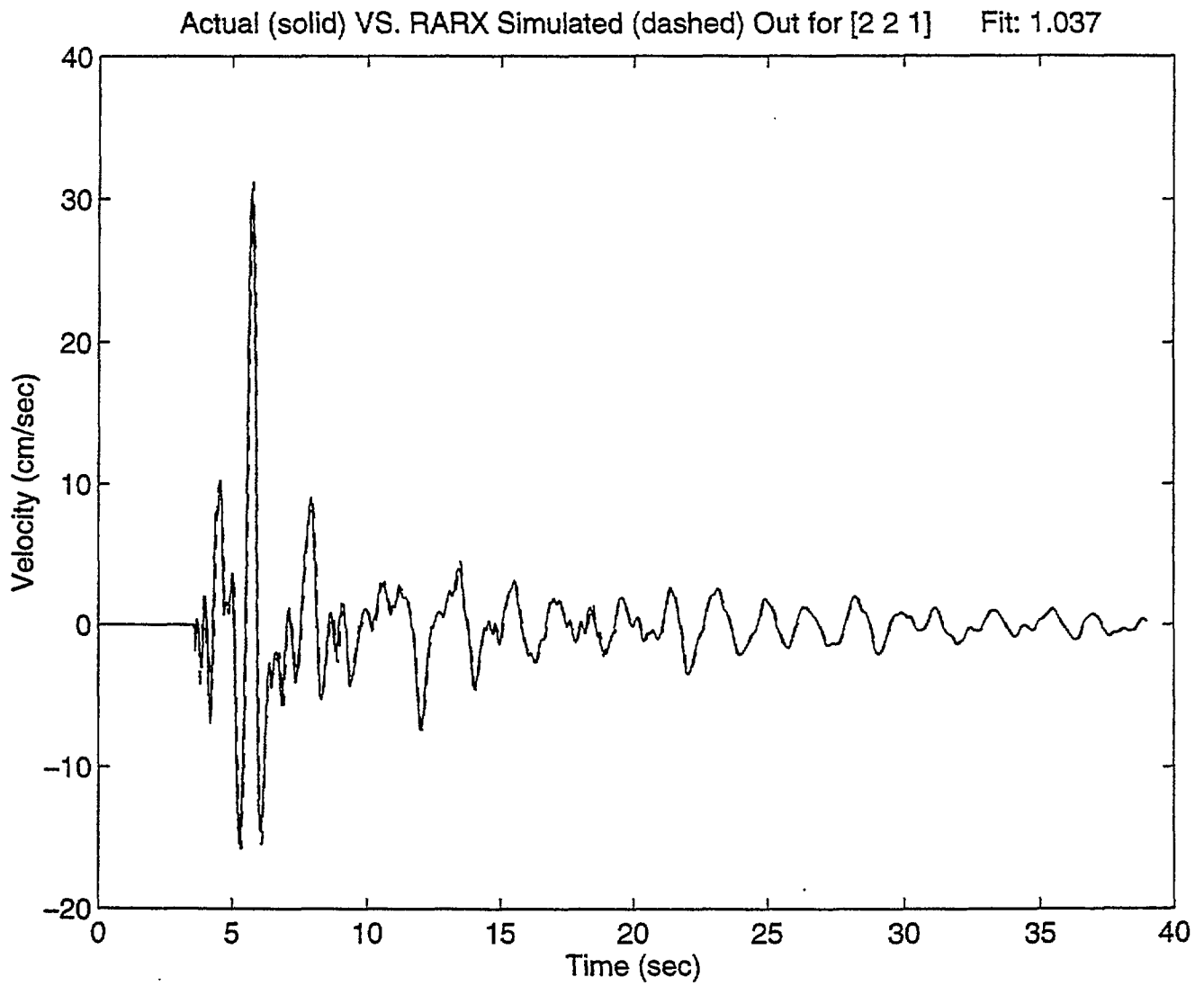
Figure E.13 Modeled versus actual output, Event4, E - W, DHB, 0 to 6 m depth interval.
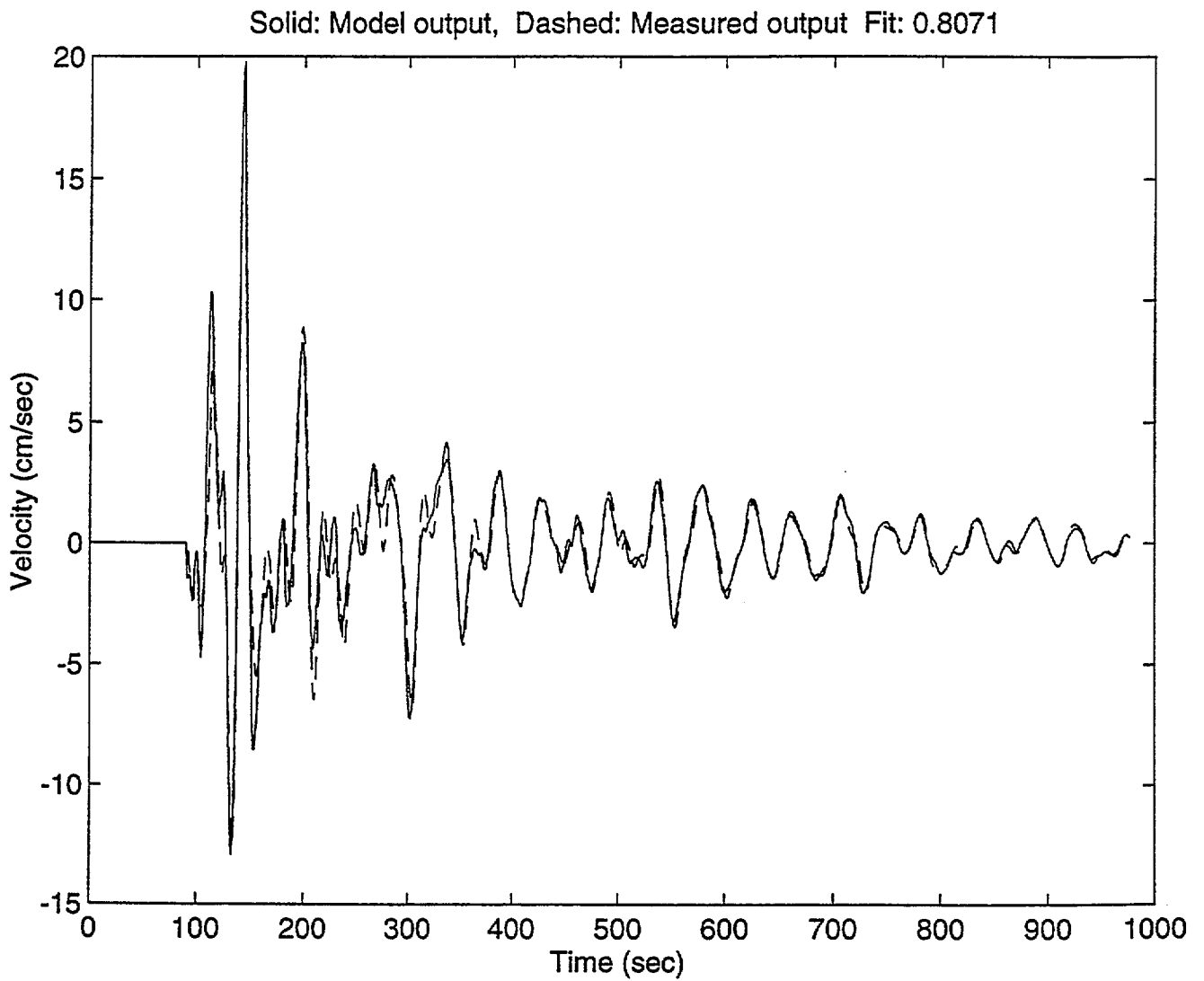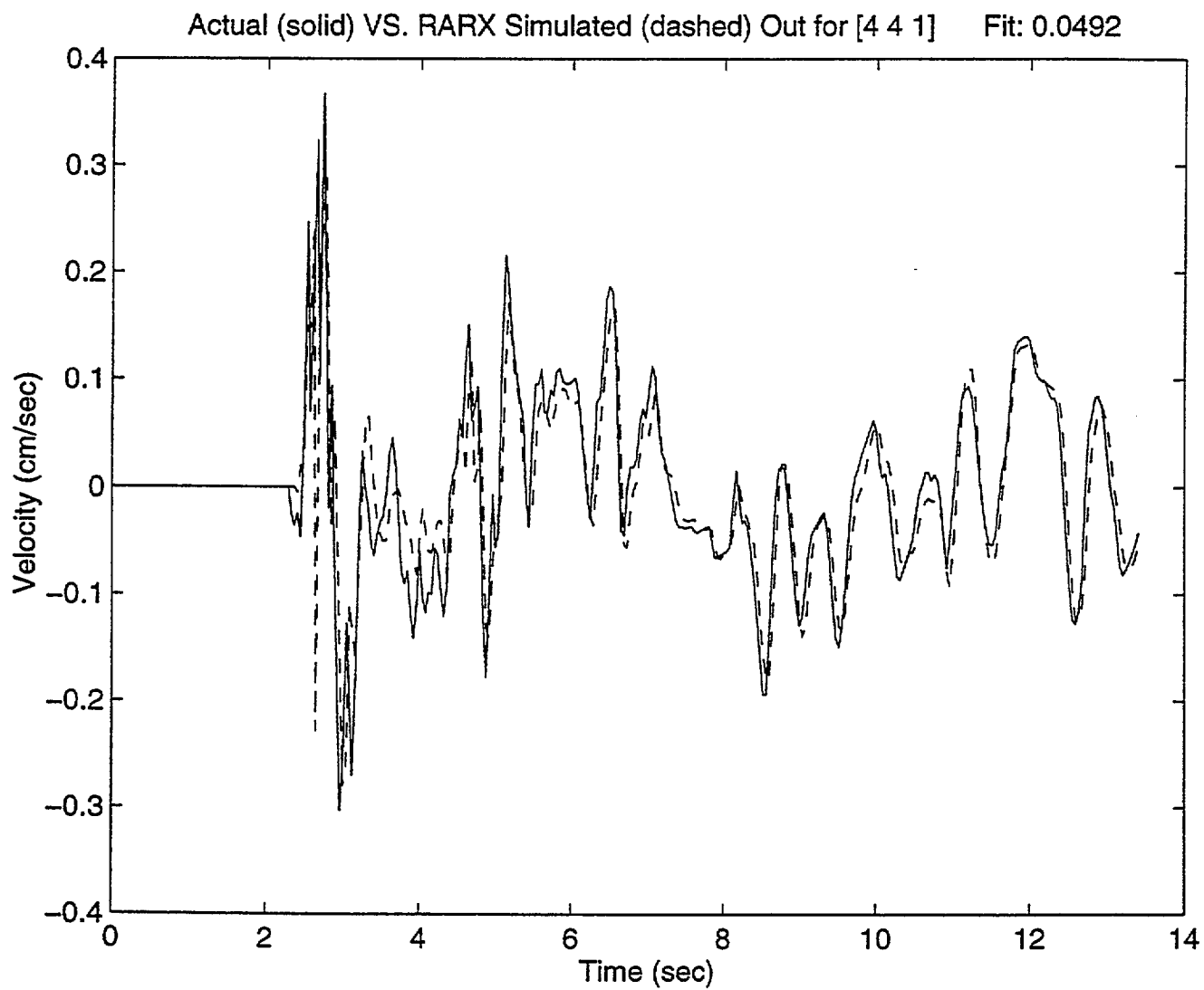
Figure E.14 Modeled versus actual output, Event4, E - W, DHB, 6 to 11 m depth interval.
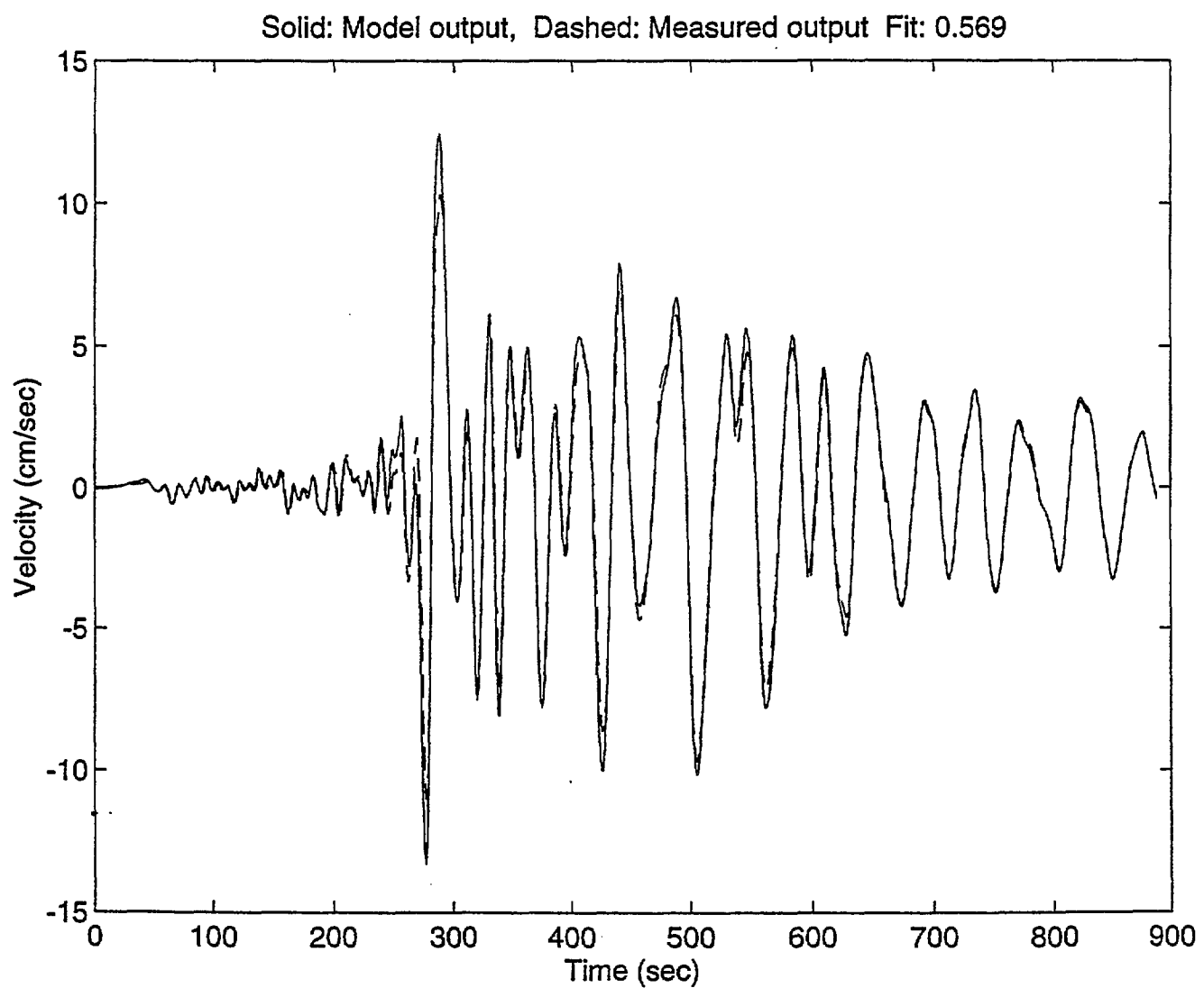
Figure E.15   Modeled versus actual output, Event7, E - W, DHA, 0 to 6 m depth interval.

Solid: Model output, Dashed: Measured output Fit: 0.6192
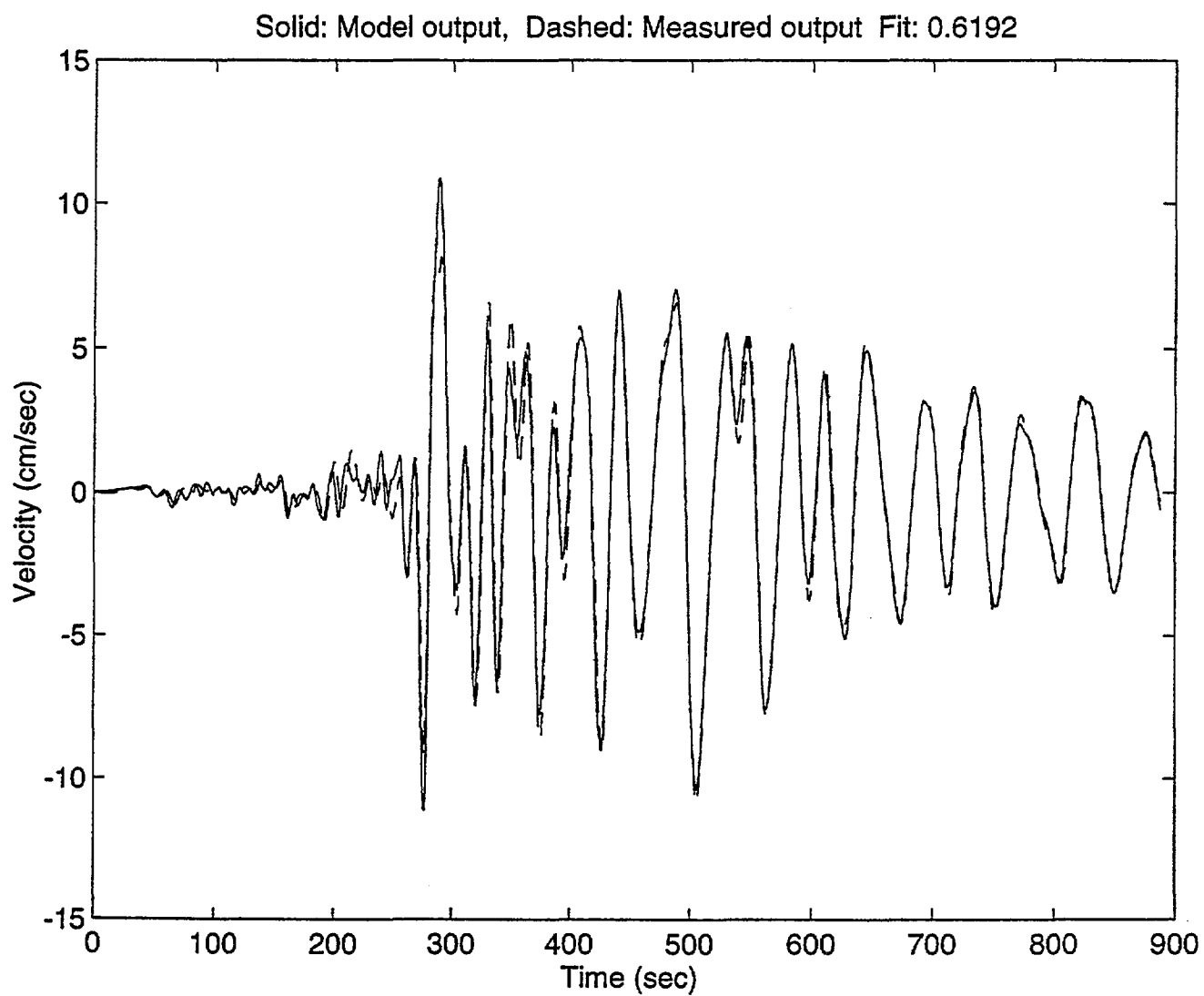
Figure E.16   Modeled versus actual output, Event7, E - W, DHA, 6 to 11 m depth interval.
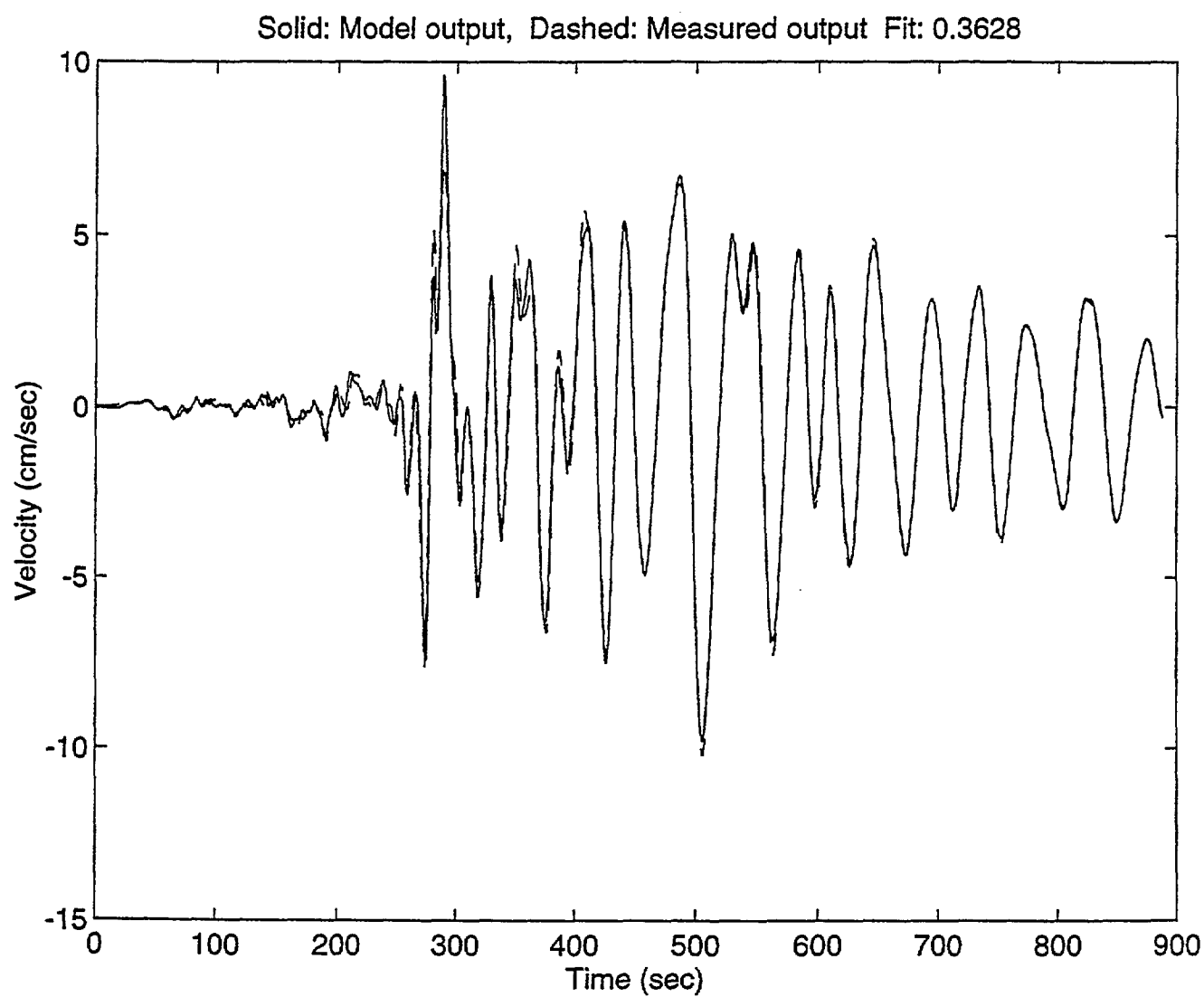
Figure E.17   Modeled versus actual output, Event7, E - W, DHA, 11 to 17 m depth interval.
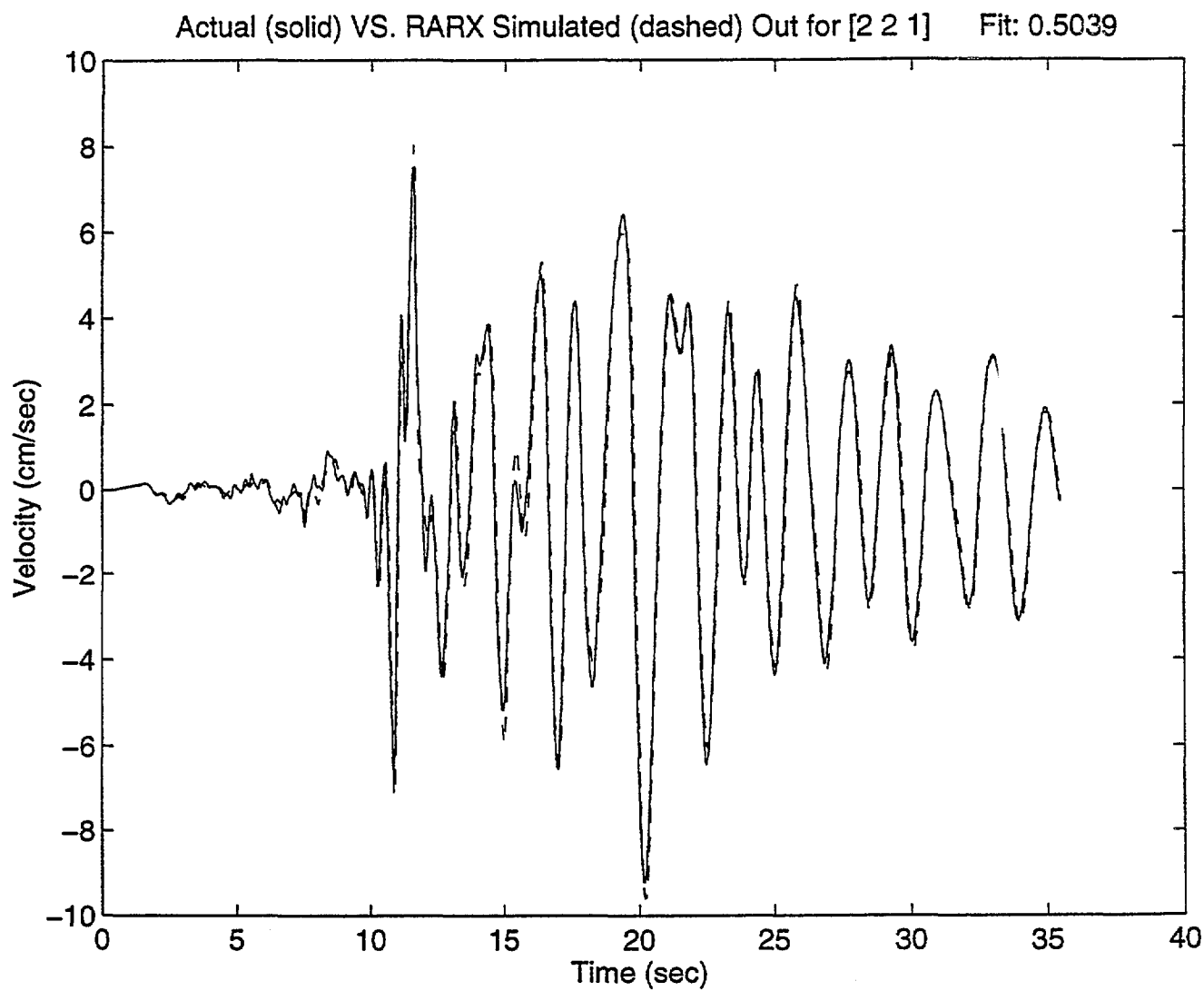
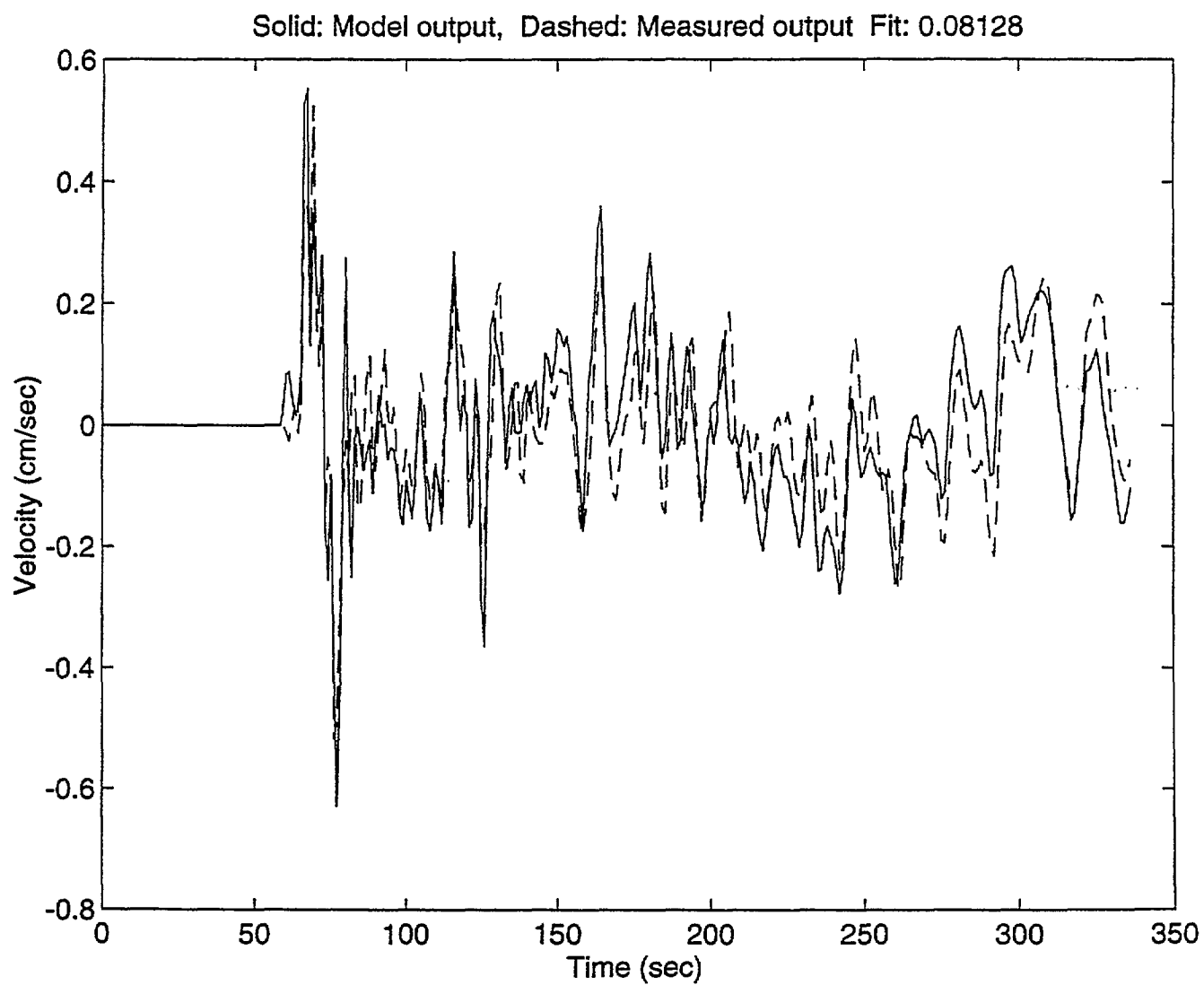Figure E.18   Modeled versus actual output, Event7, E - W, DHA, 17 to 47 m depth interval.
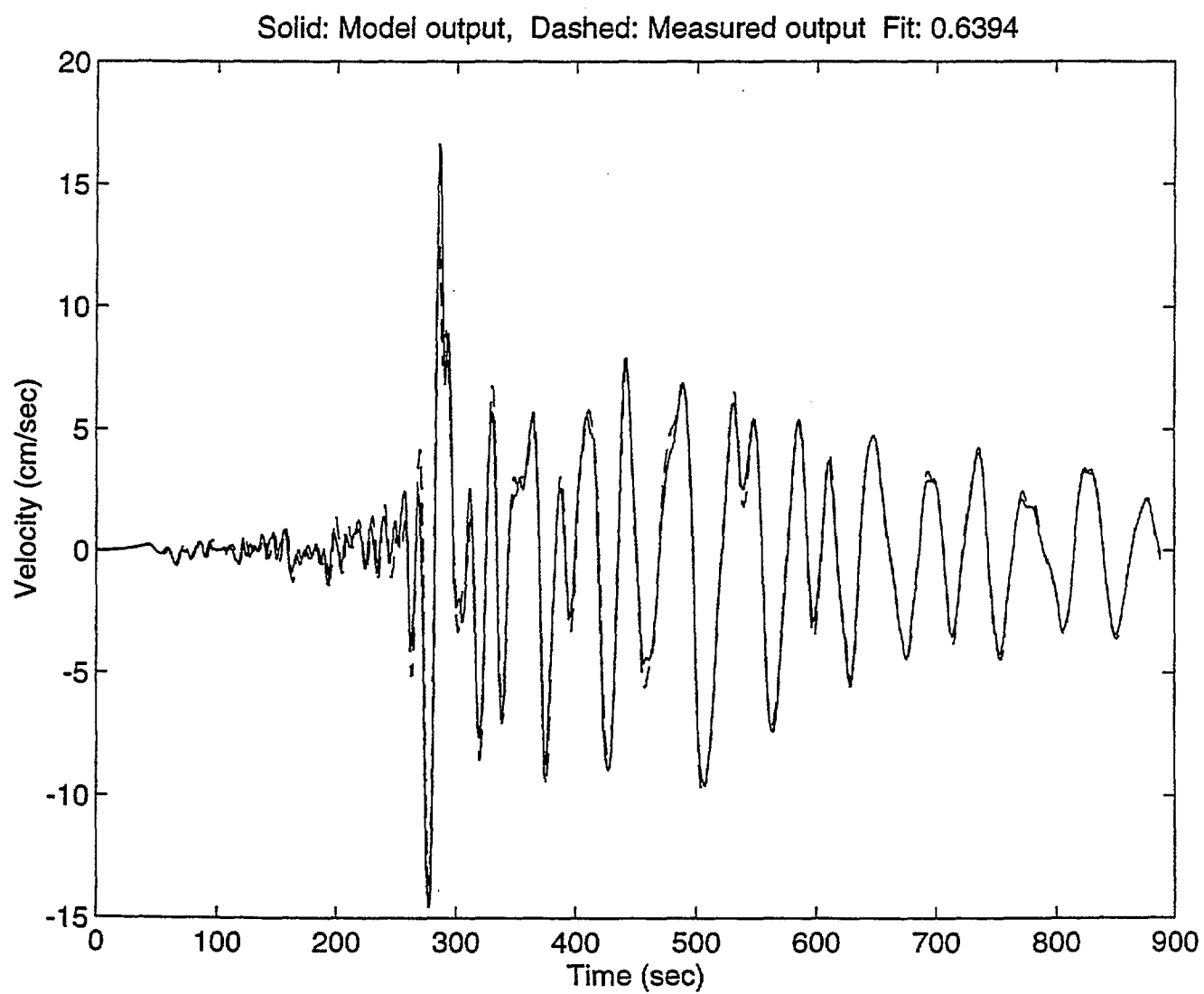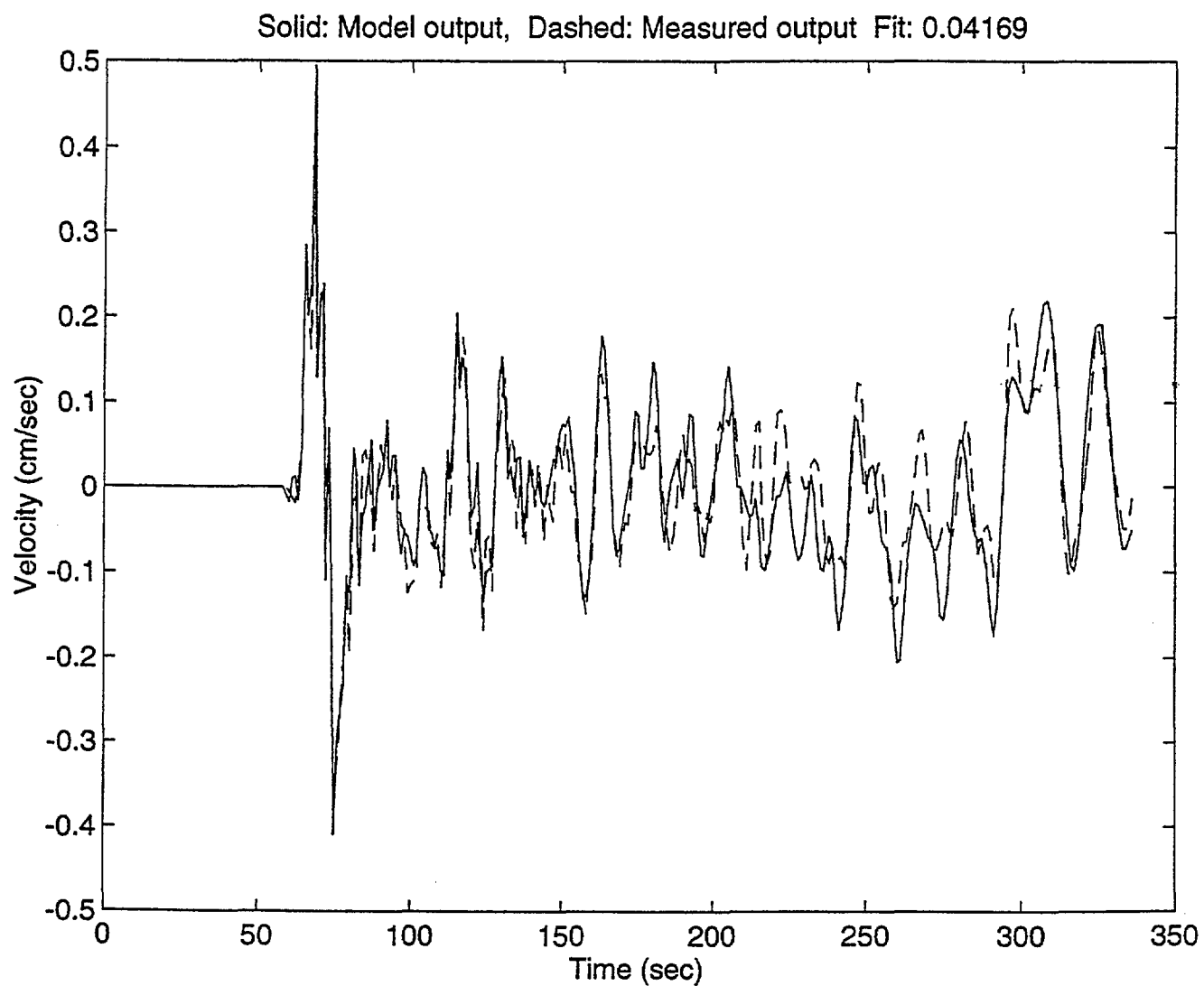
Figure E.19 Modeled versus actual output, Event7, E - W, DHB, 0 to 6 m depth interval.
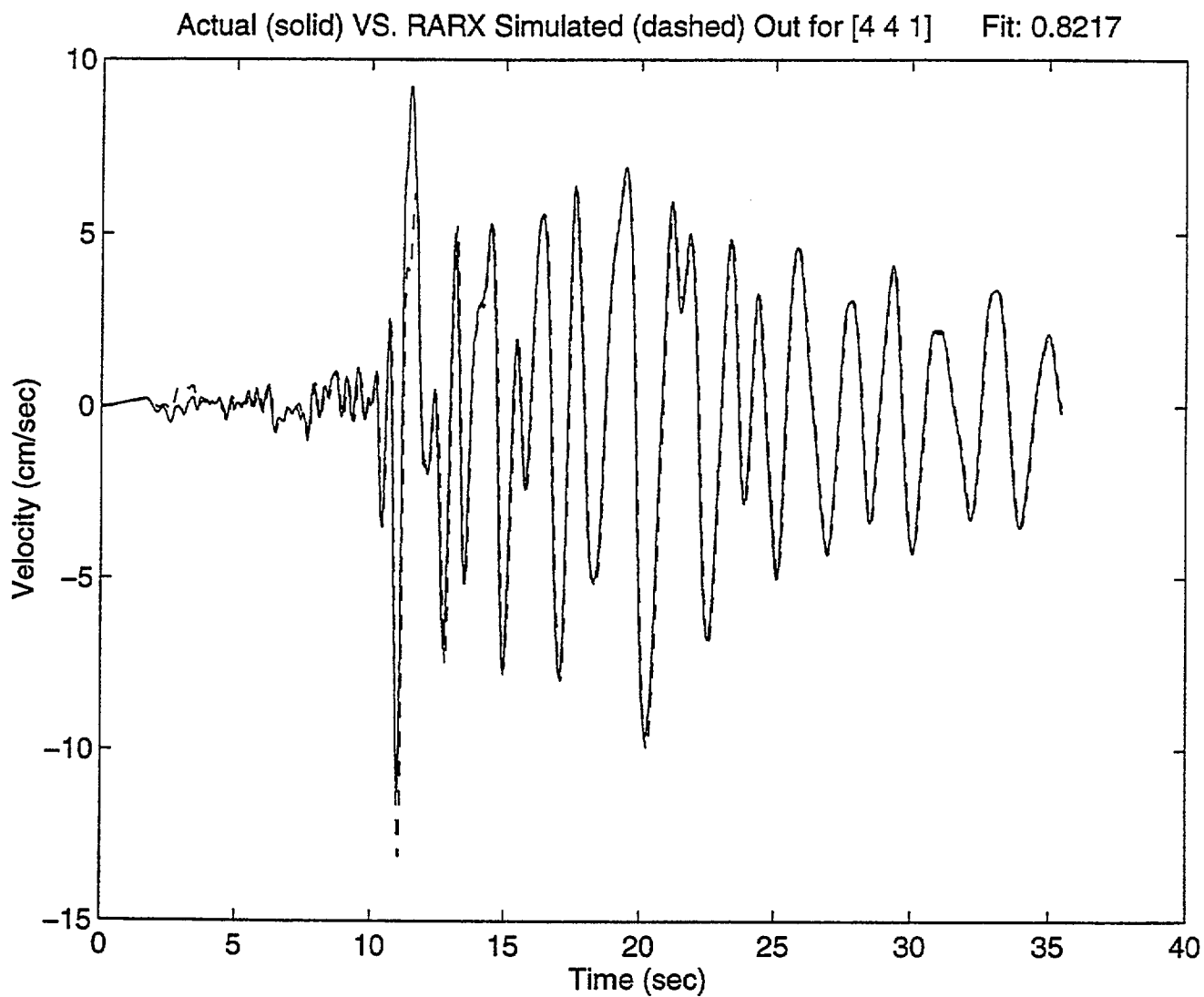
Figure E.20   Modeled versus actual output, Event7, E - W, DHB, 6 to 11 m depth interval.

154

Solid: Model output, Dashed: Measured output Fit: 0.3701
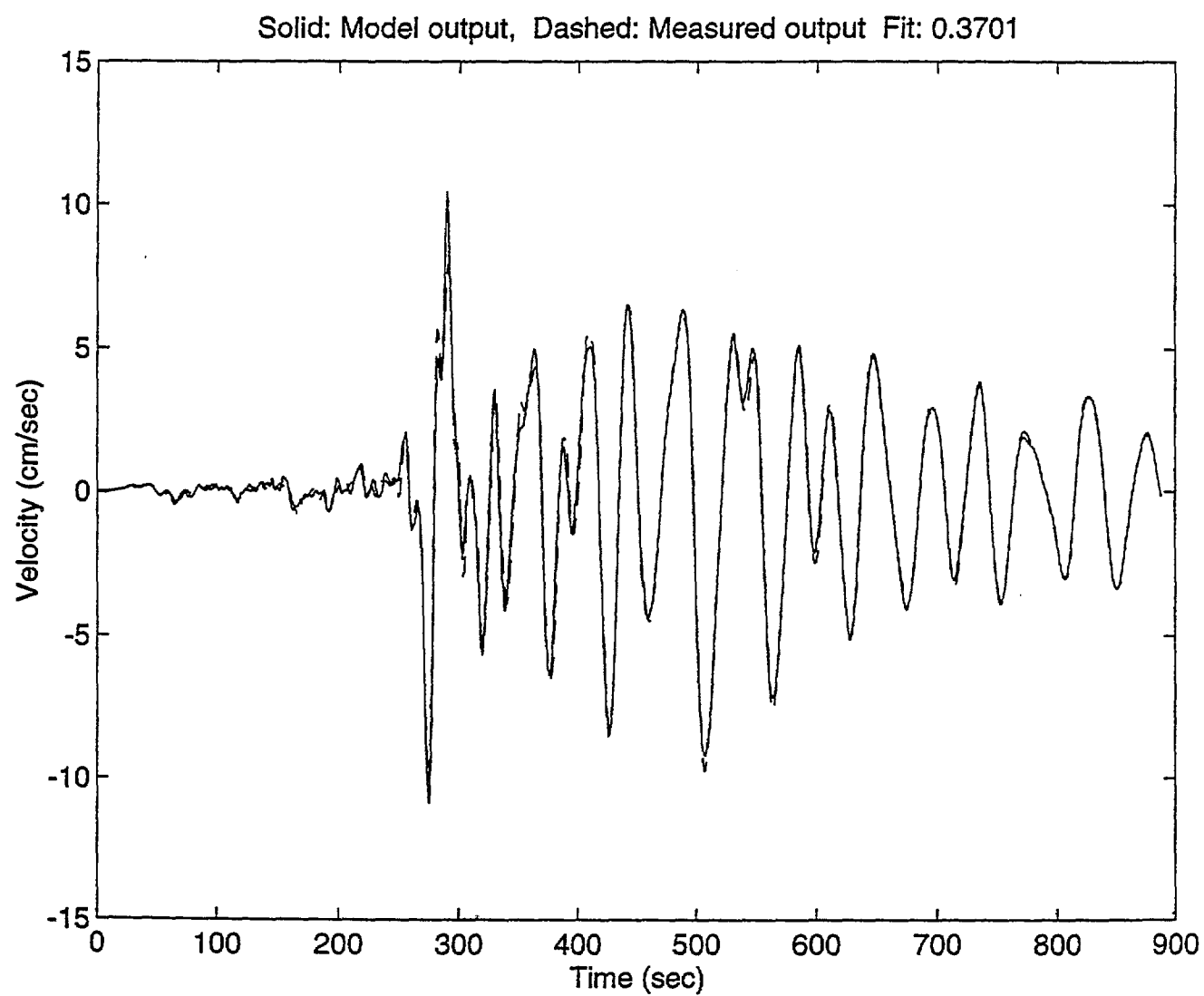
Figure E.21   Modeled versus actual output, Event7, E - W, DHB, 11 to 17 m depth interval.

Solid: Model output, Dashed: Measured output Fit: 0.8722
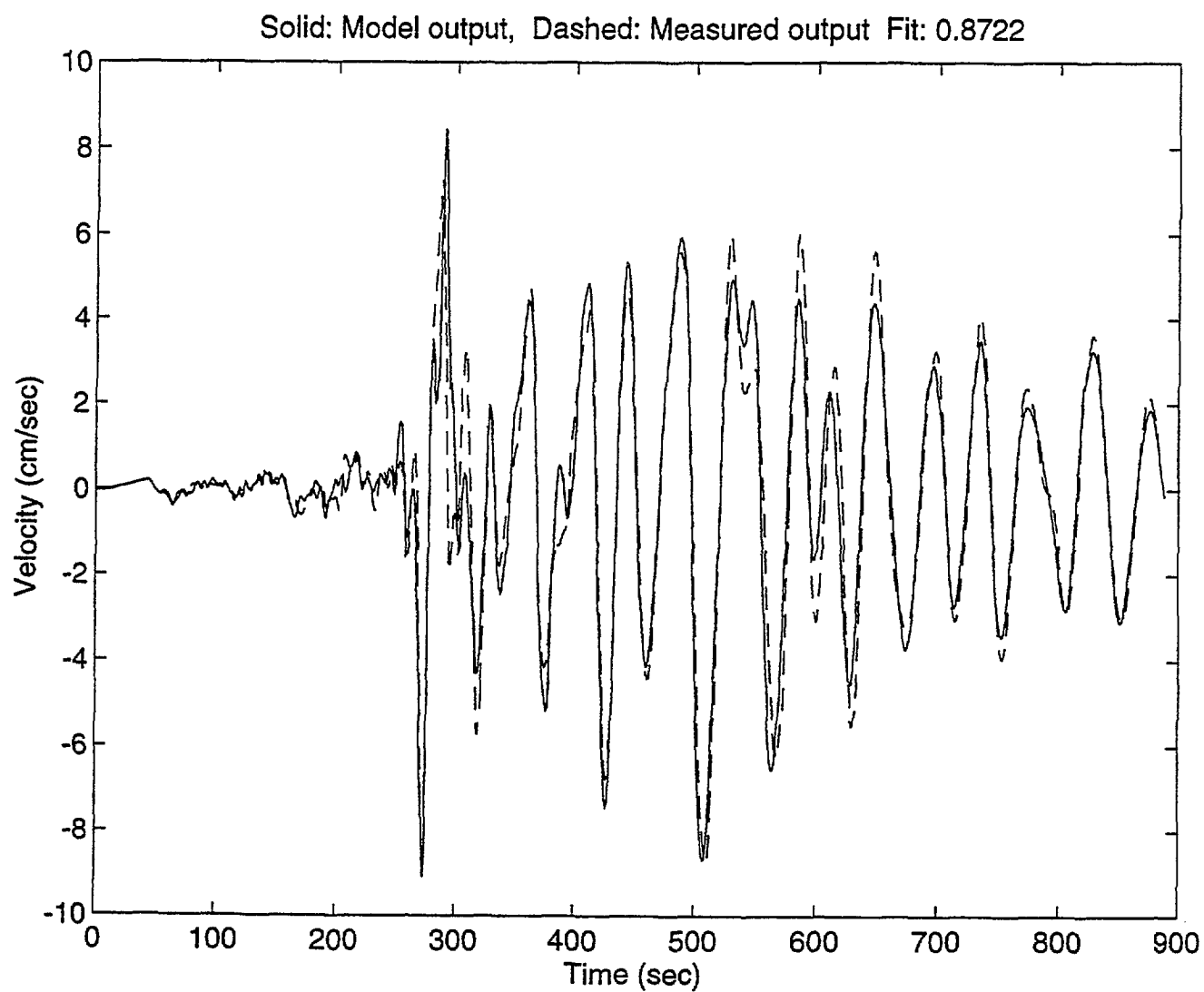
Figure E.22   Modeled versus actual output, Event7, E - W, DHB, 17 to 47 m depth interval.
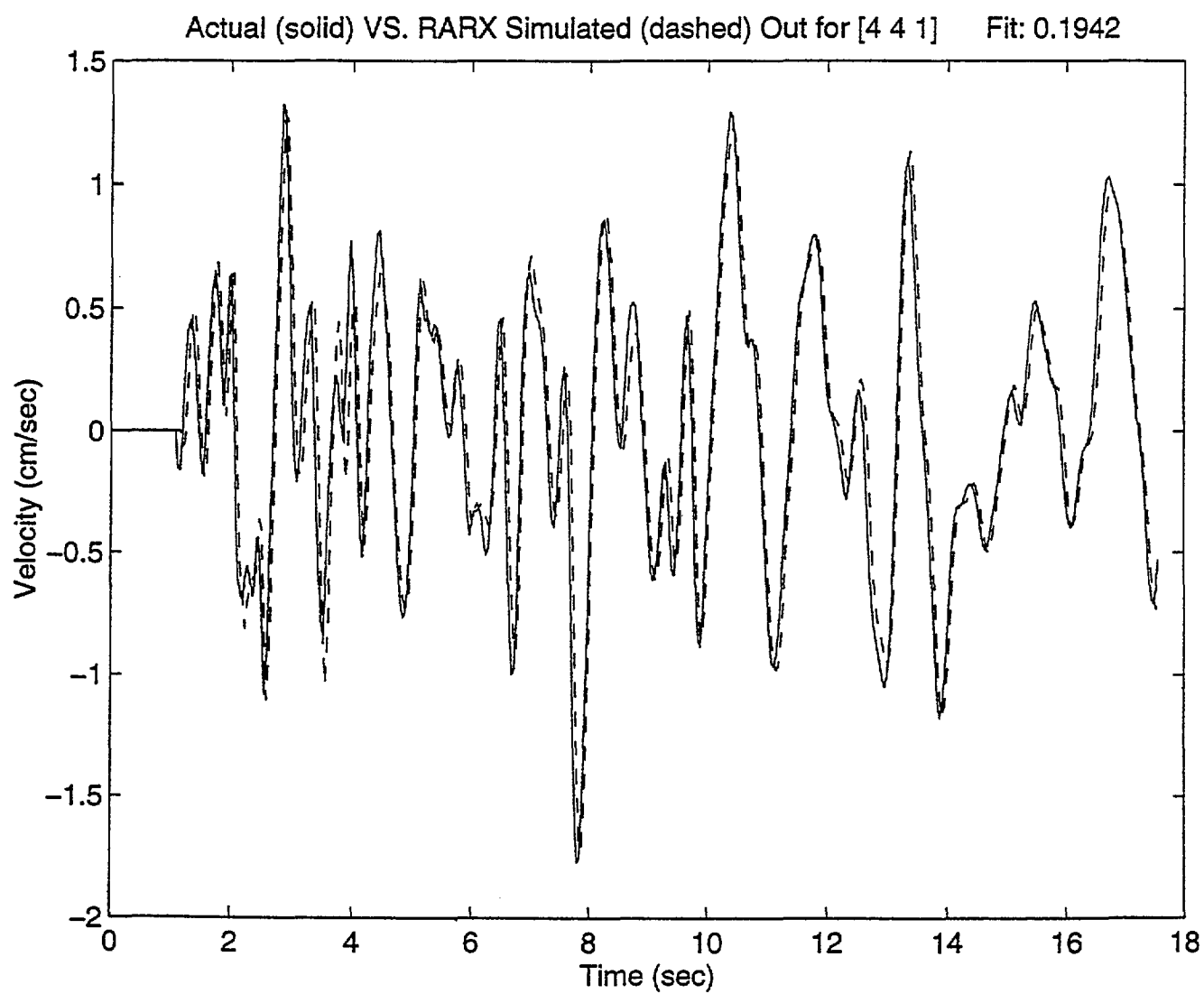
Figure E.23   Modeled versus actual output, Event8, E - W, DHA, 0 to 6 m depth interval.
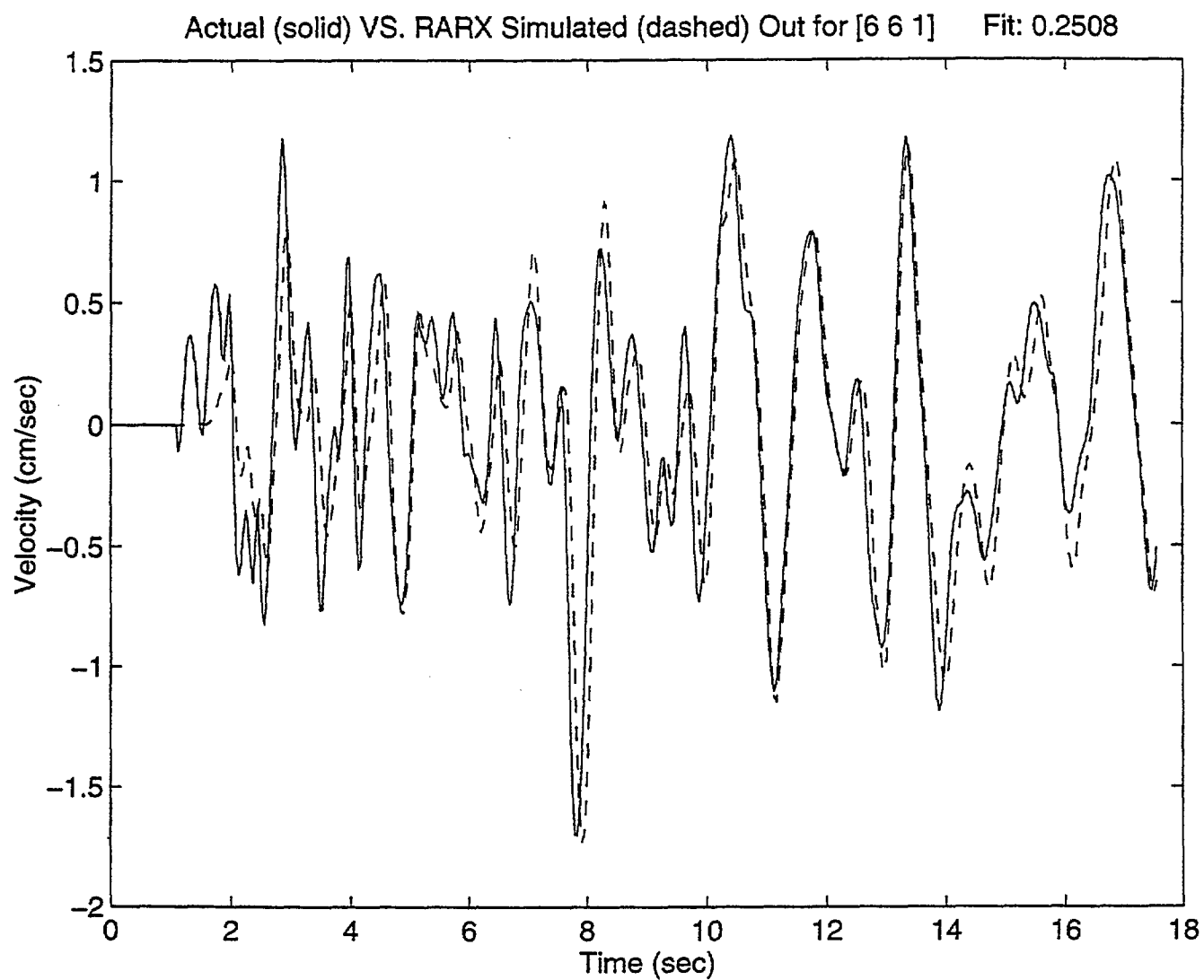
Figure E.24   Modeled versus actual output, Event8, E - W, DHA, 6 to 11 m depth interval.
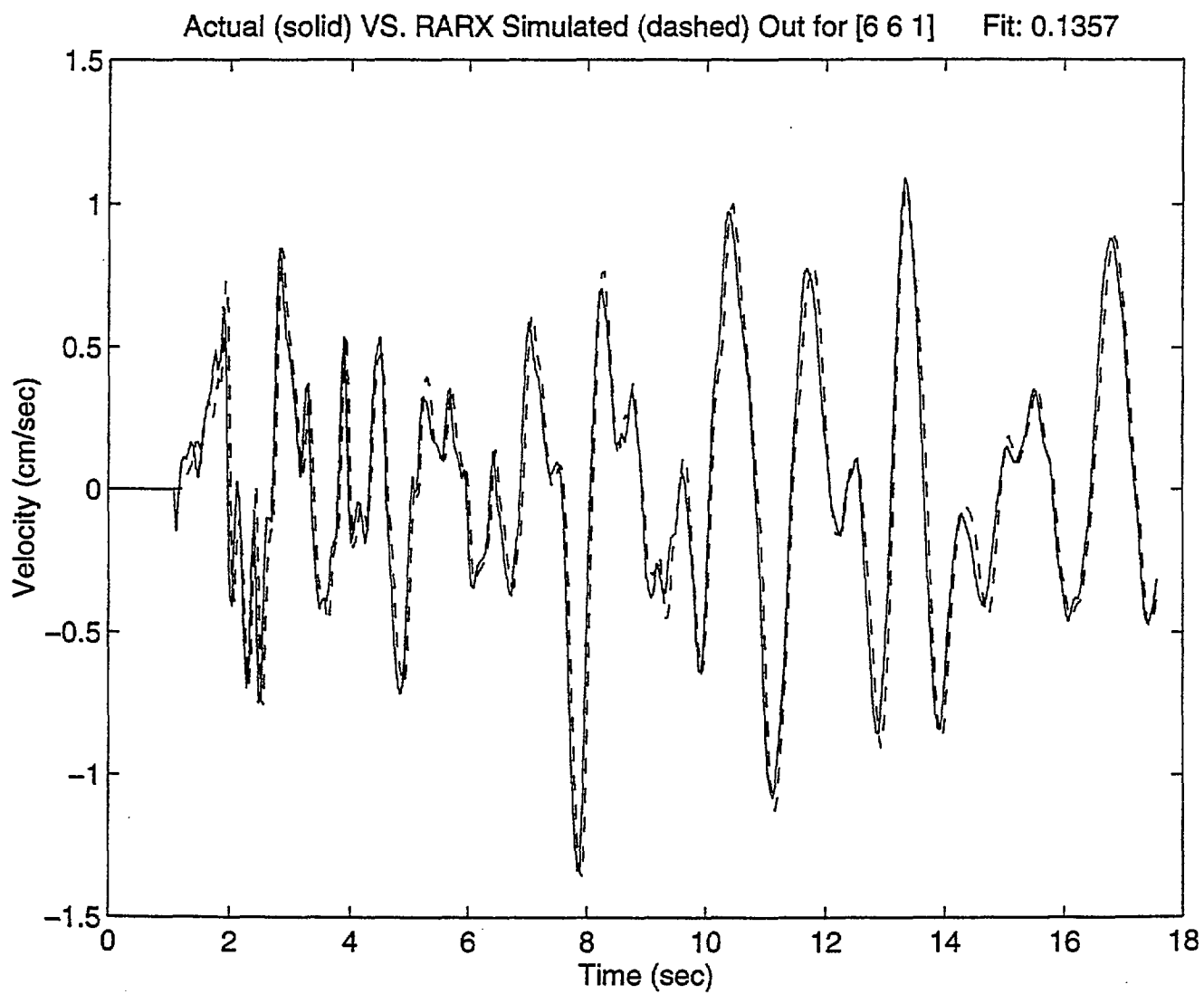
Figure E.25 Modeled versus actual output, Event3, E - W, DHA, 17 to 11 m depth interval.
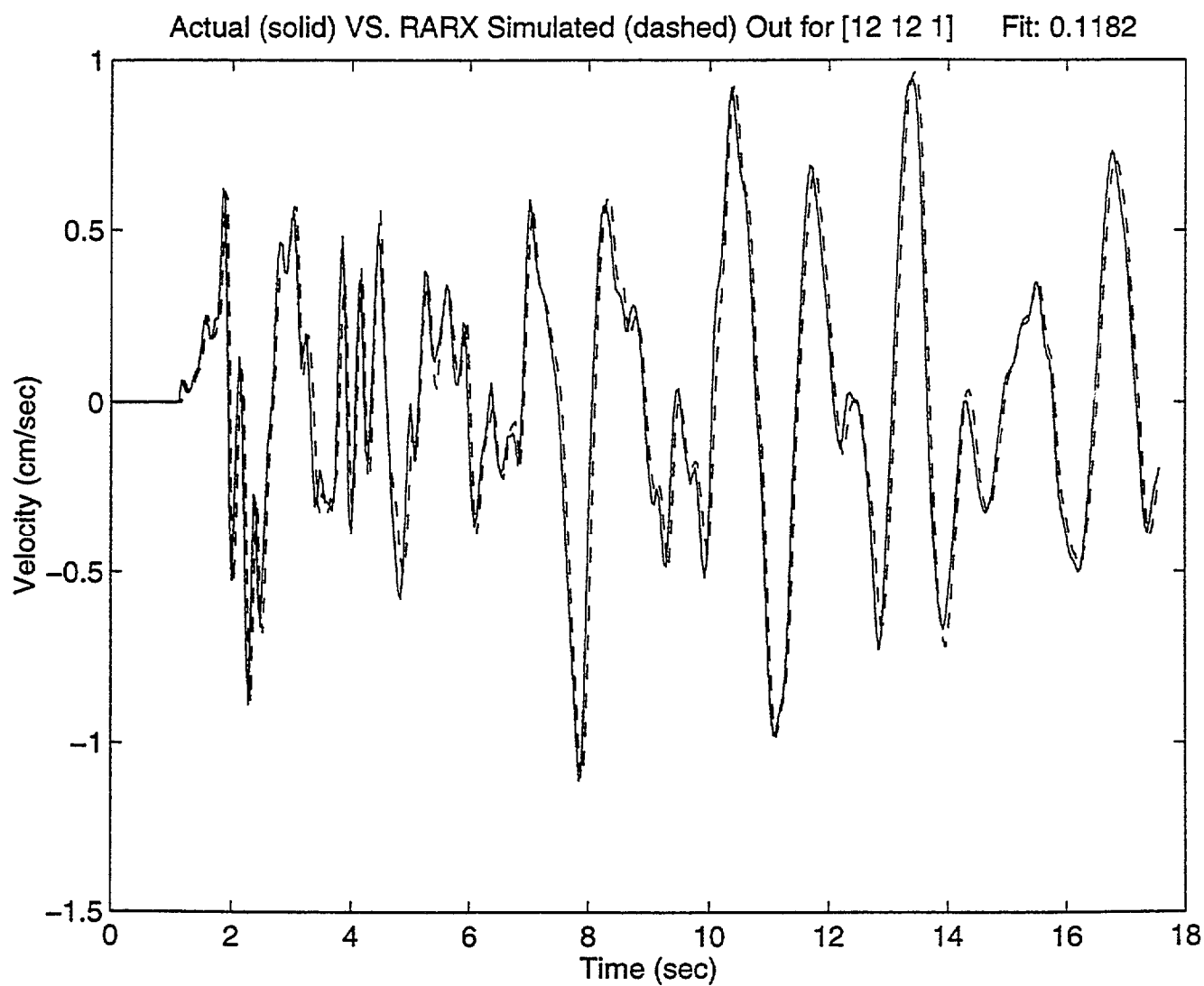
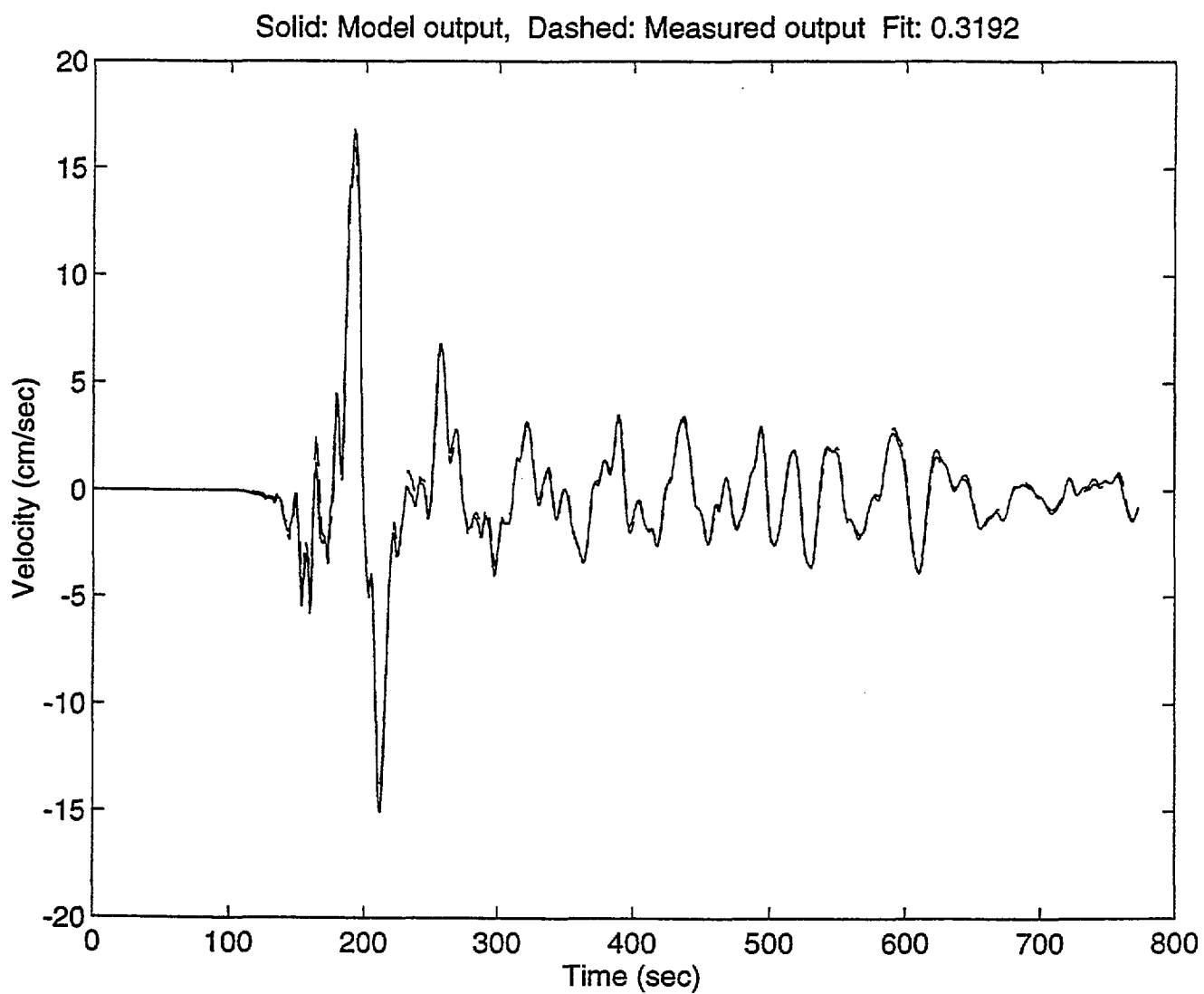Figure E.26   Modeled versus actual output, Event8, E - W, DHA, 47 to 17 m depth interval.
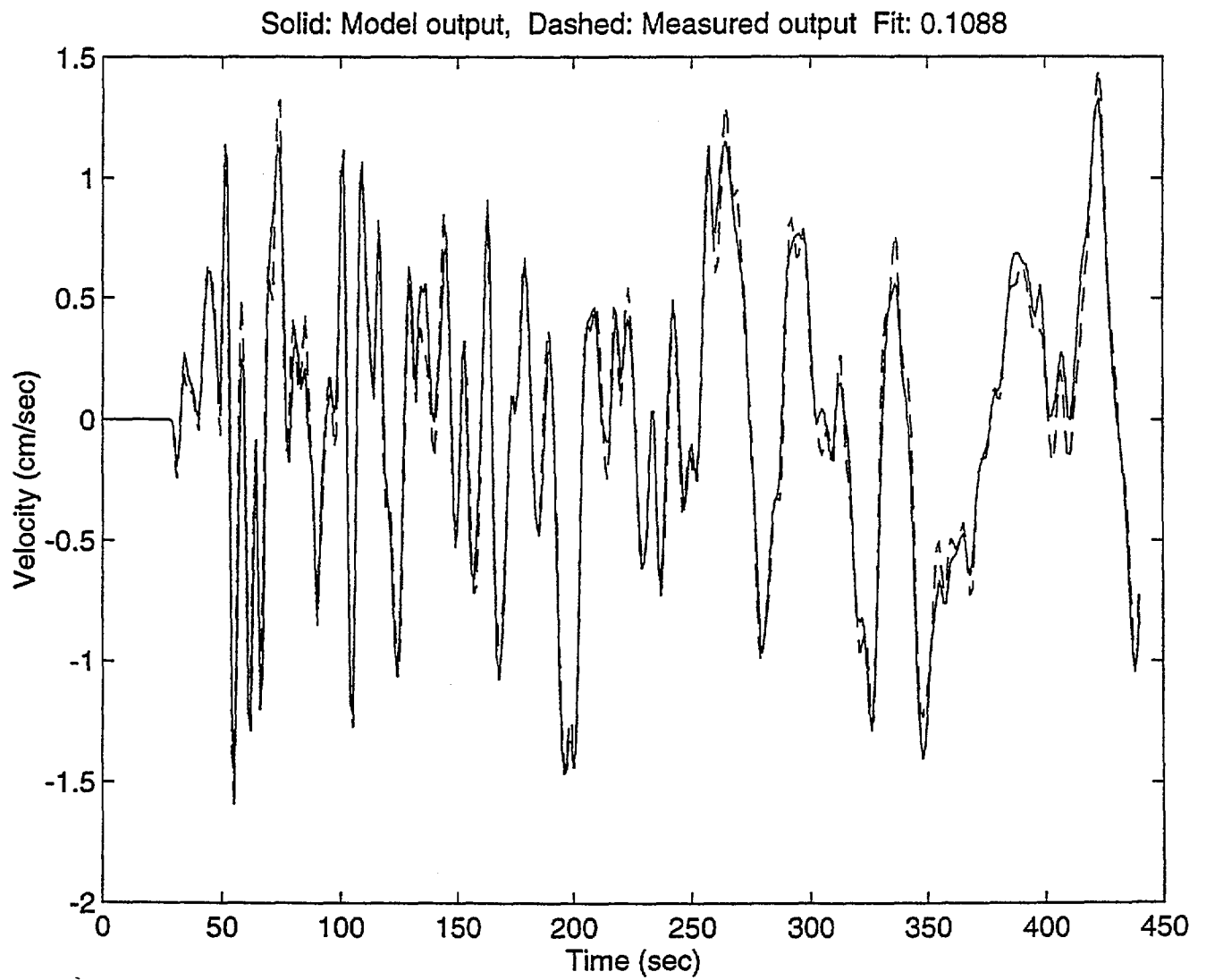
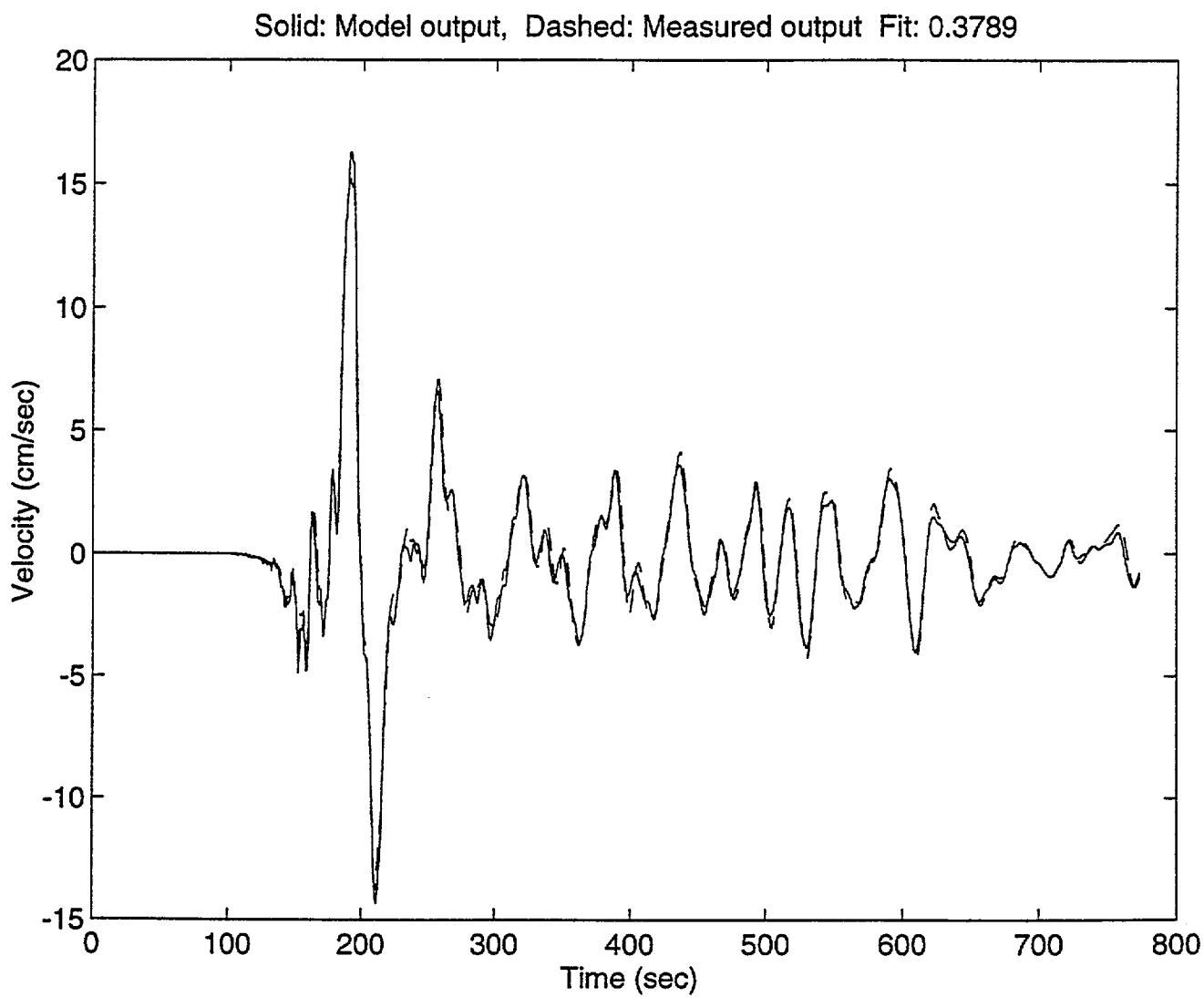Figure E.27   Modeled versus actual output, Event8, E - W, DHB, 6 to 0 m depth interval.
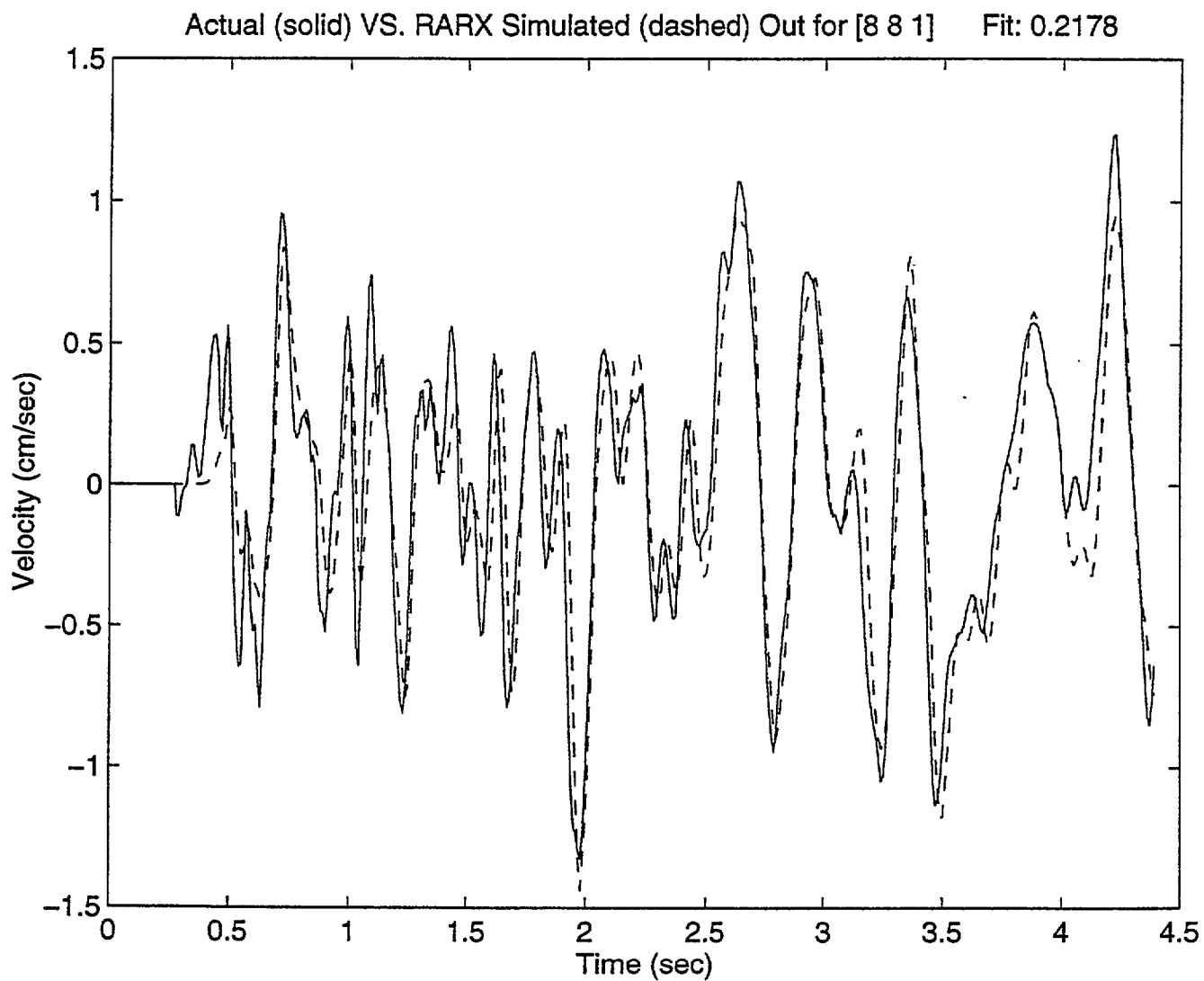
Figure E.28   Modeled versus actual output, Event8, E - W, DHB, 11 to 6 m depth interval.

162

Figure E.29   Modeled versus actual output, Event8, E - W, DHB, 17 to 11 m depth interval.

163

Figure E.30   Modeled versus actual output, Event8, E - W, DHB, 47 to 17 m depth interval.

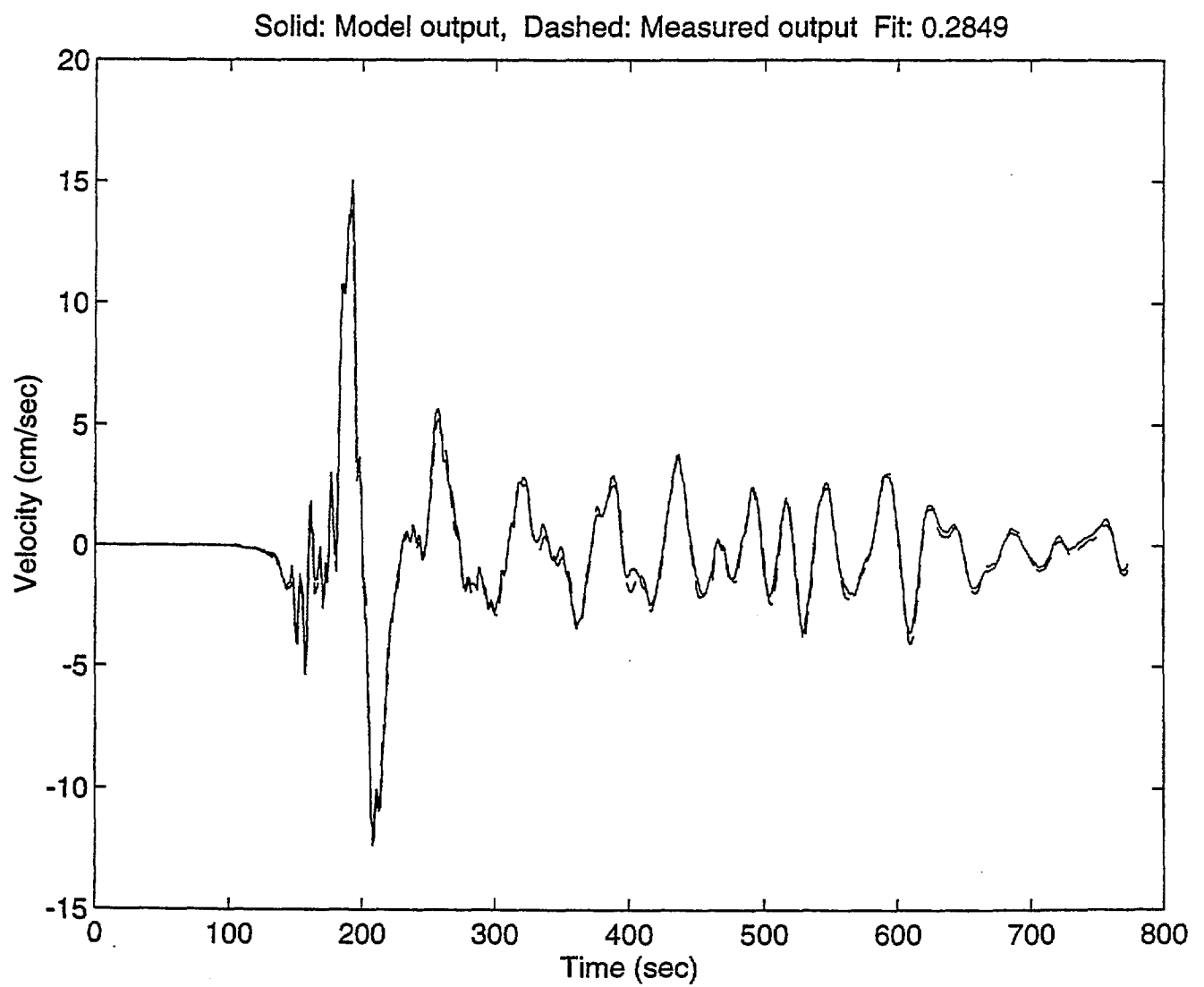Figure E.31 Modeled versus actual output, Event9, E - W, DHA, 11 to 0 m depth interval.

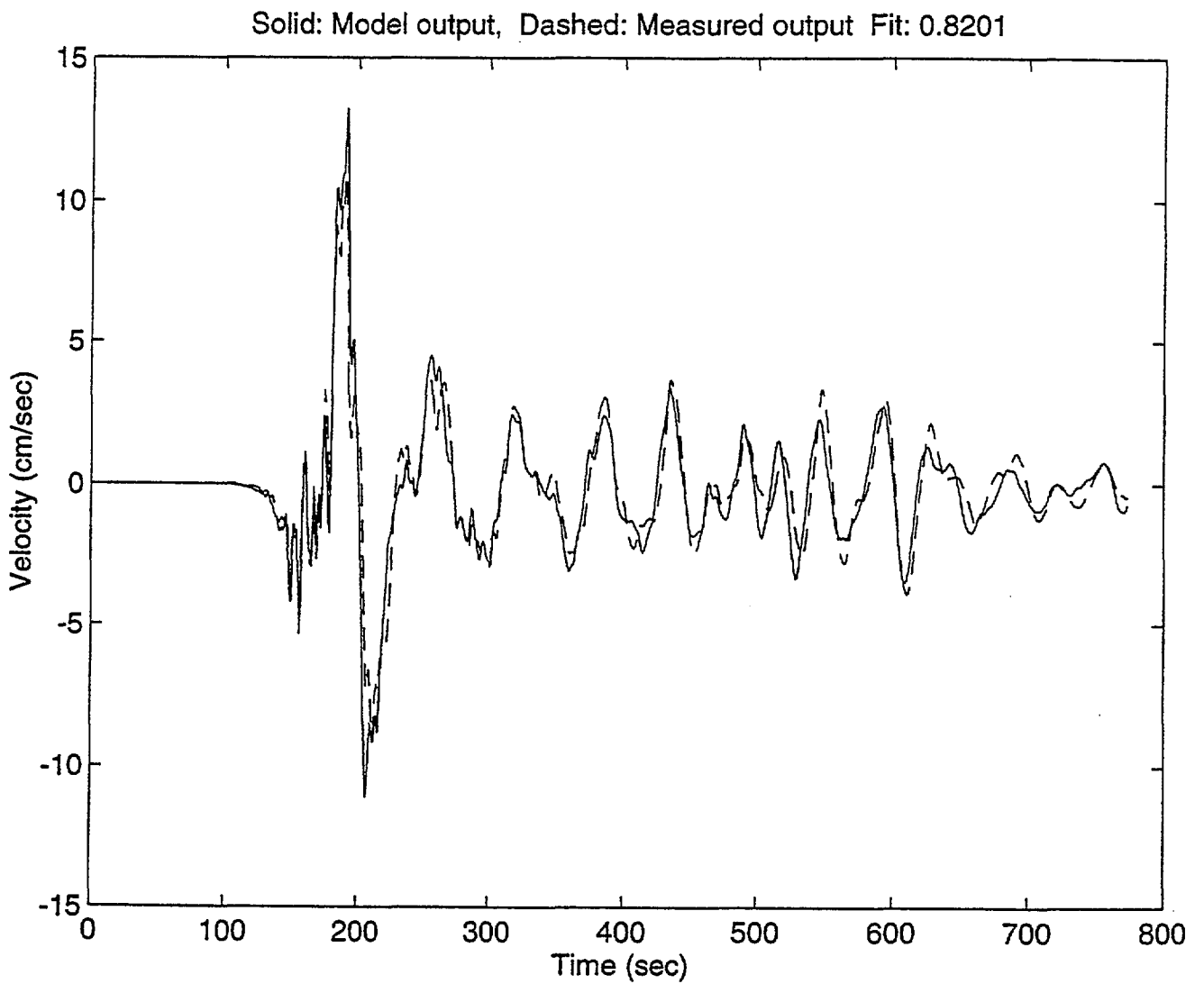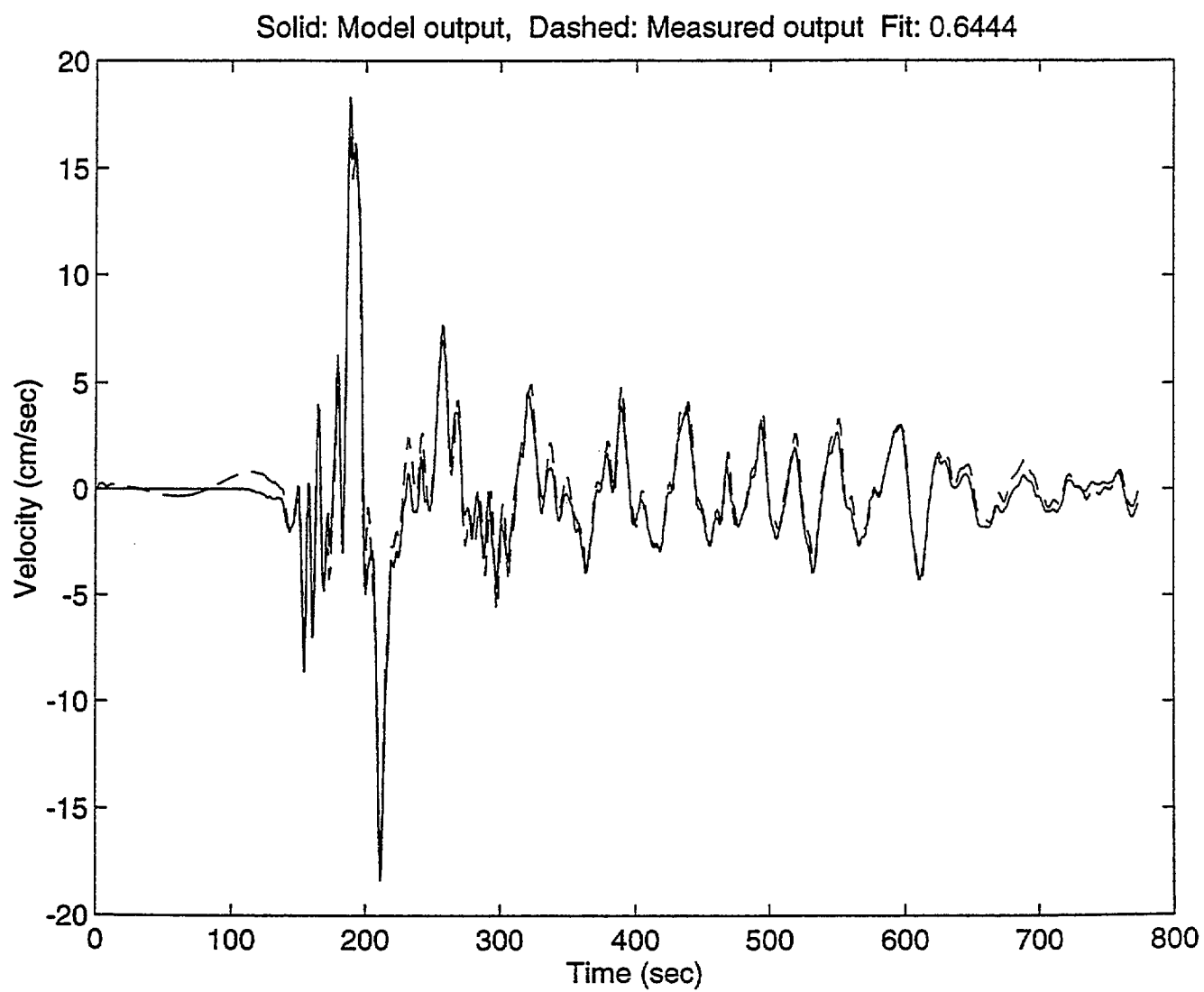Figure E.32 Modeled versus actual output, Event9, E - W, DHA, 47 to 11 m depth interval.

Figure E.33   Modeled versus actual output, Event9, E - W, DHB, 6 to 0 m depth interval.

Figure E.34   Modeled versus actual output, Event9, E - W, DHB, 11 to 6 m depth interval.

Figure E.35 Modeled versus actual output, Event9, E - W, DHB, 17 to 11 m depth interval.

Figure E.36   Modeled versus actual output, Event9, E - W, DHB, 47 to 17 m depth interval.

Figure E.37   Modeled versus actual output, Event10, E - W, DHA, 11 to 0 m depth interval.

Figure E.38 Modeled versus actual output, Event10, E - W, DHA, 47 to 11 m depth interval.

Figure E.39 Modeled versus actual output, Event10, E - W, DHB, 6 to 0 m depth interval.
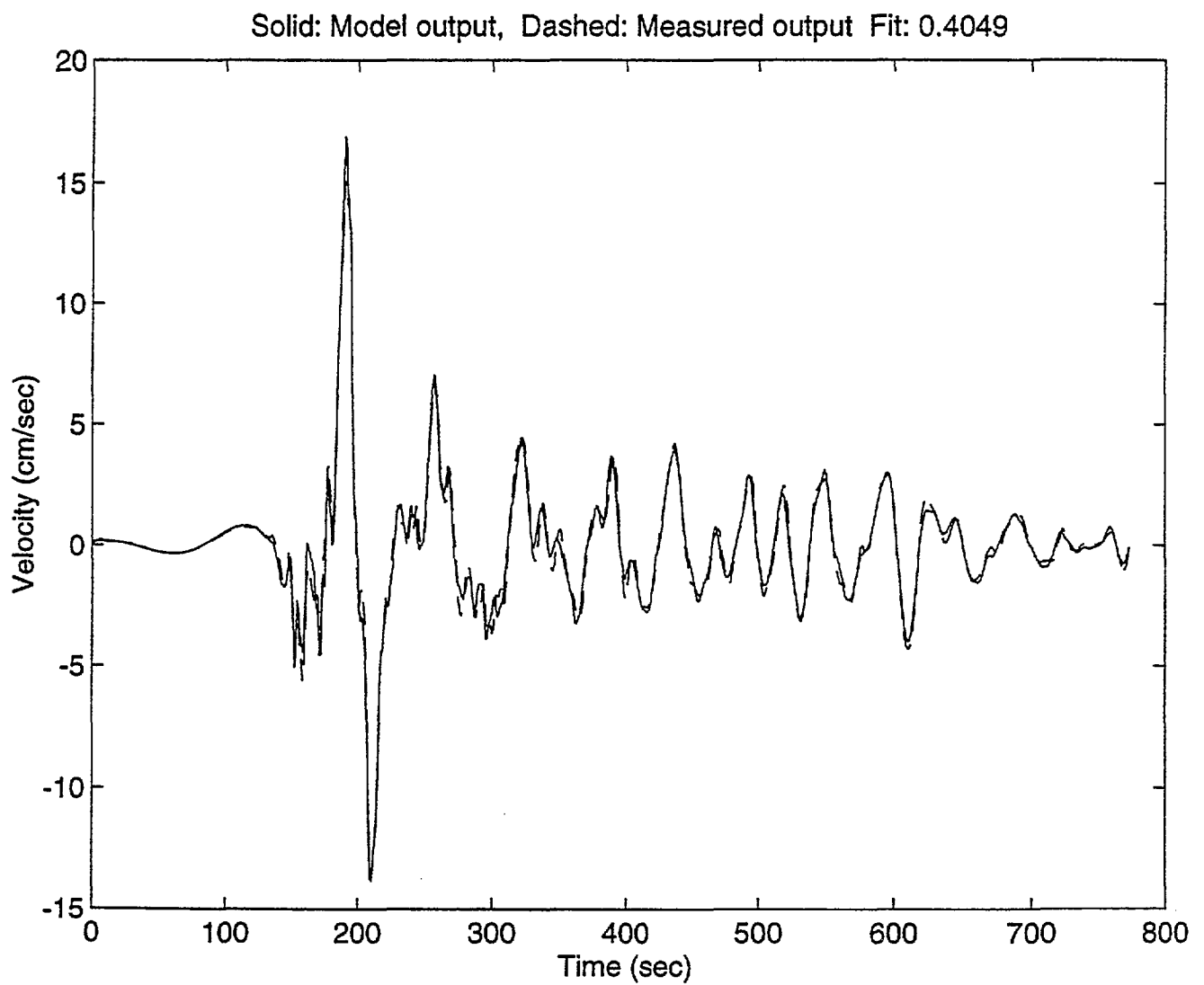
Figure E.40   Modeled versus actual output, Event10, E - W, DHB, 11 to 6 m depth interval.
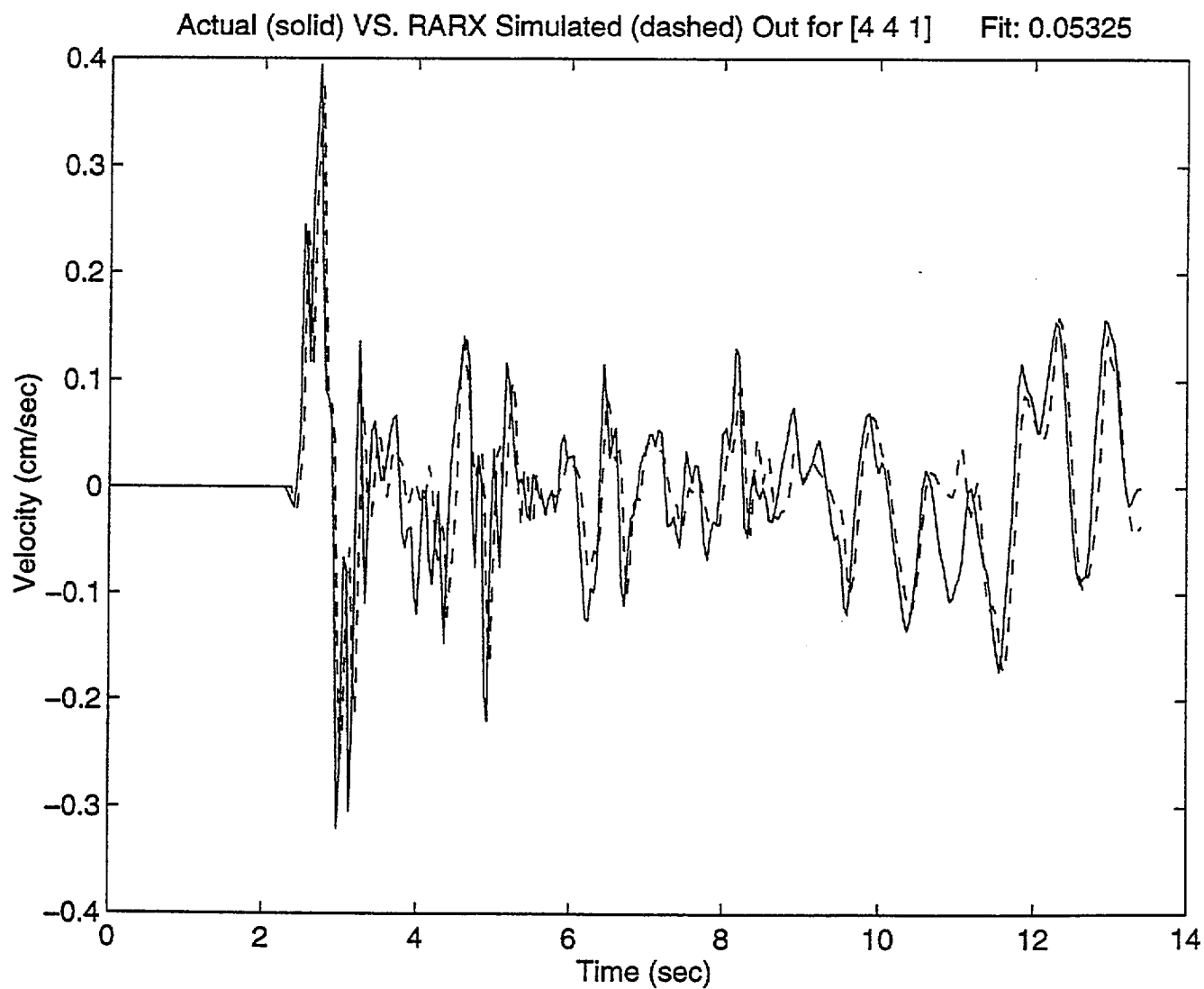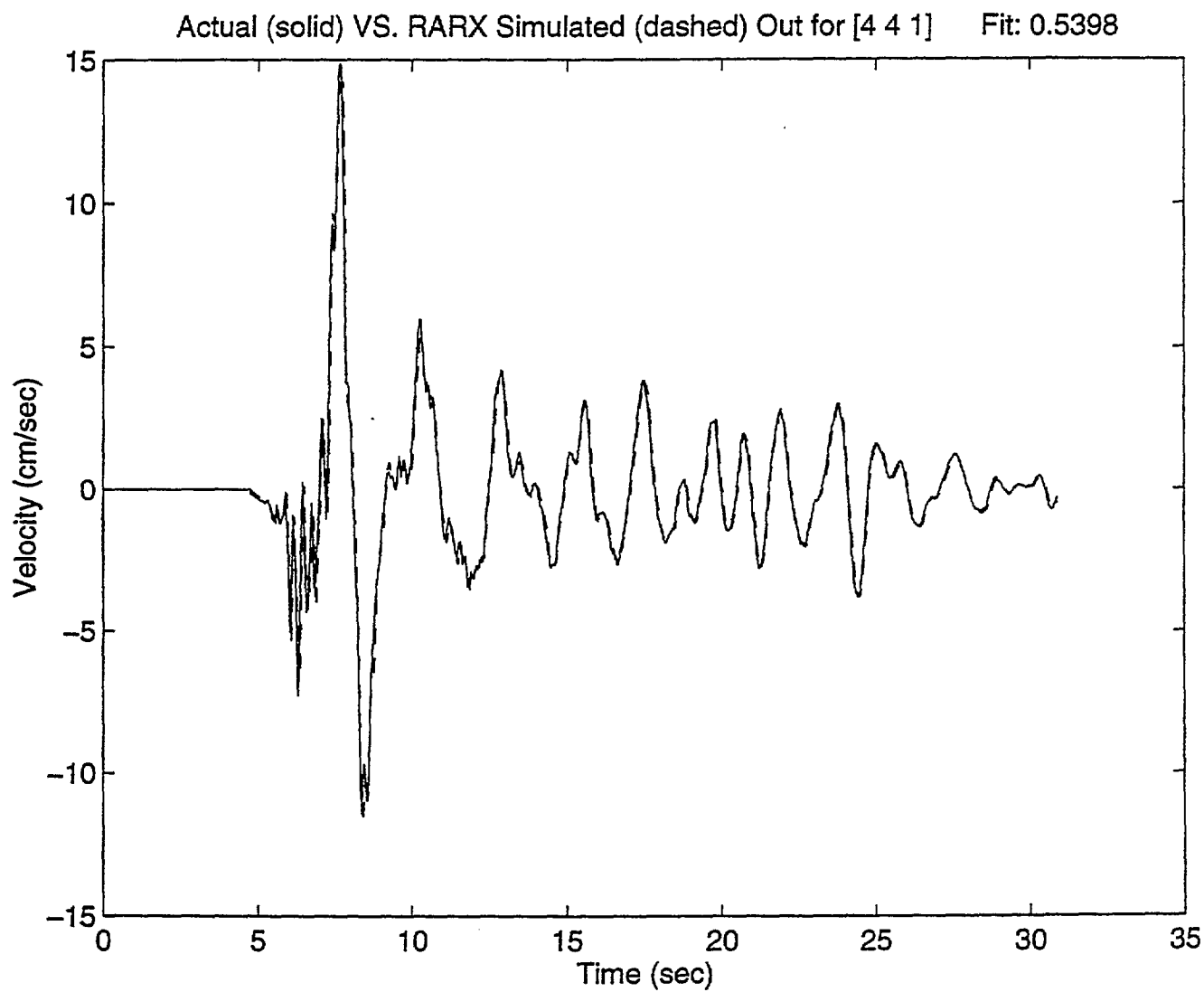
Figure E.41 Modeled versus actual output, Event10, E - W, DHB, 17 to 11 m depth interval.
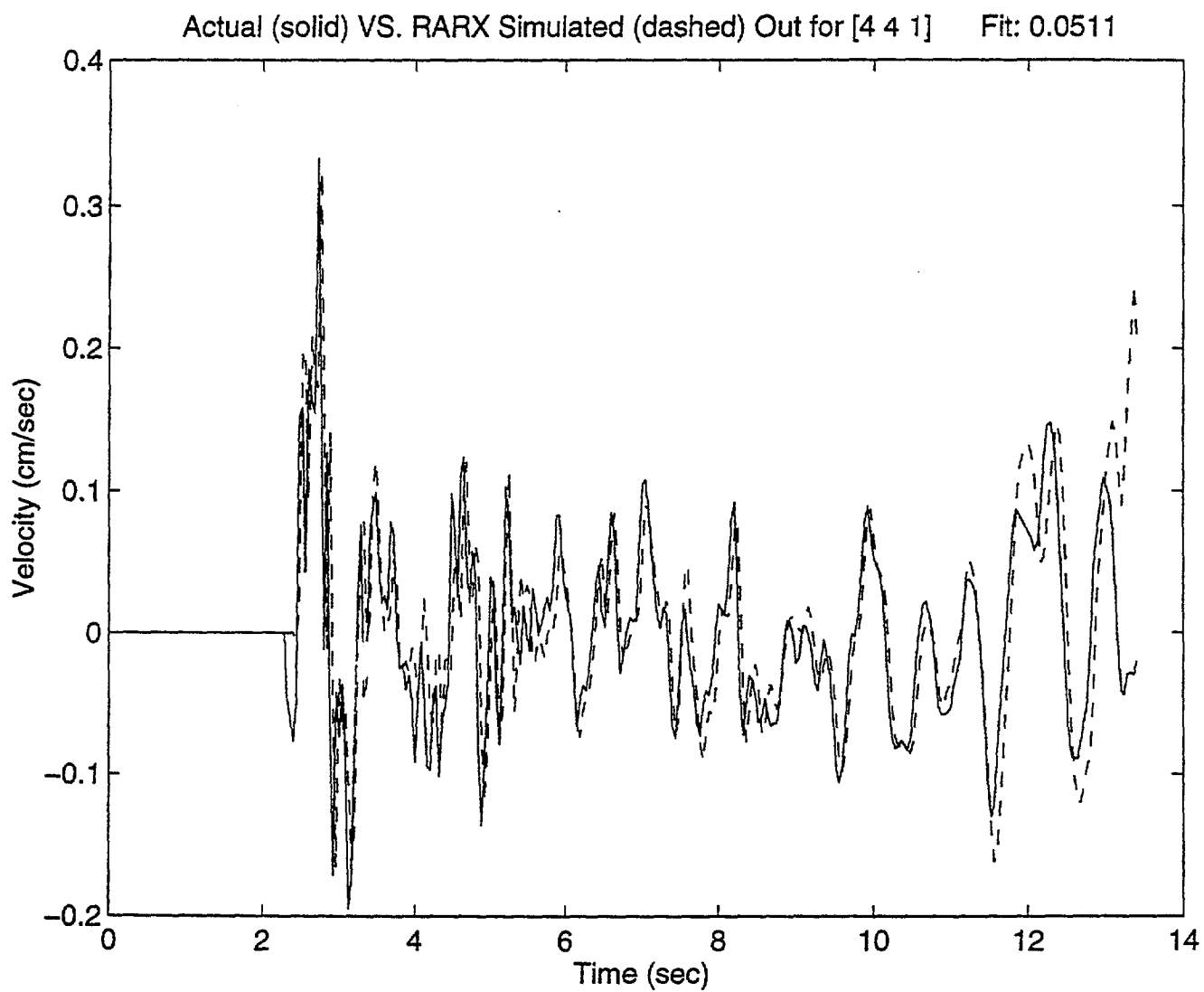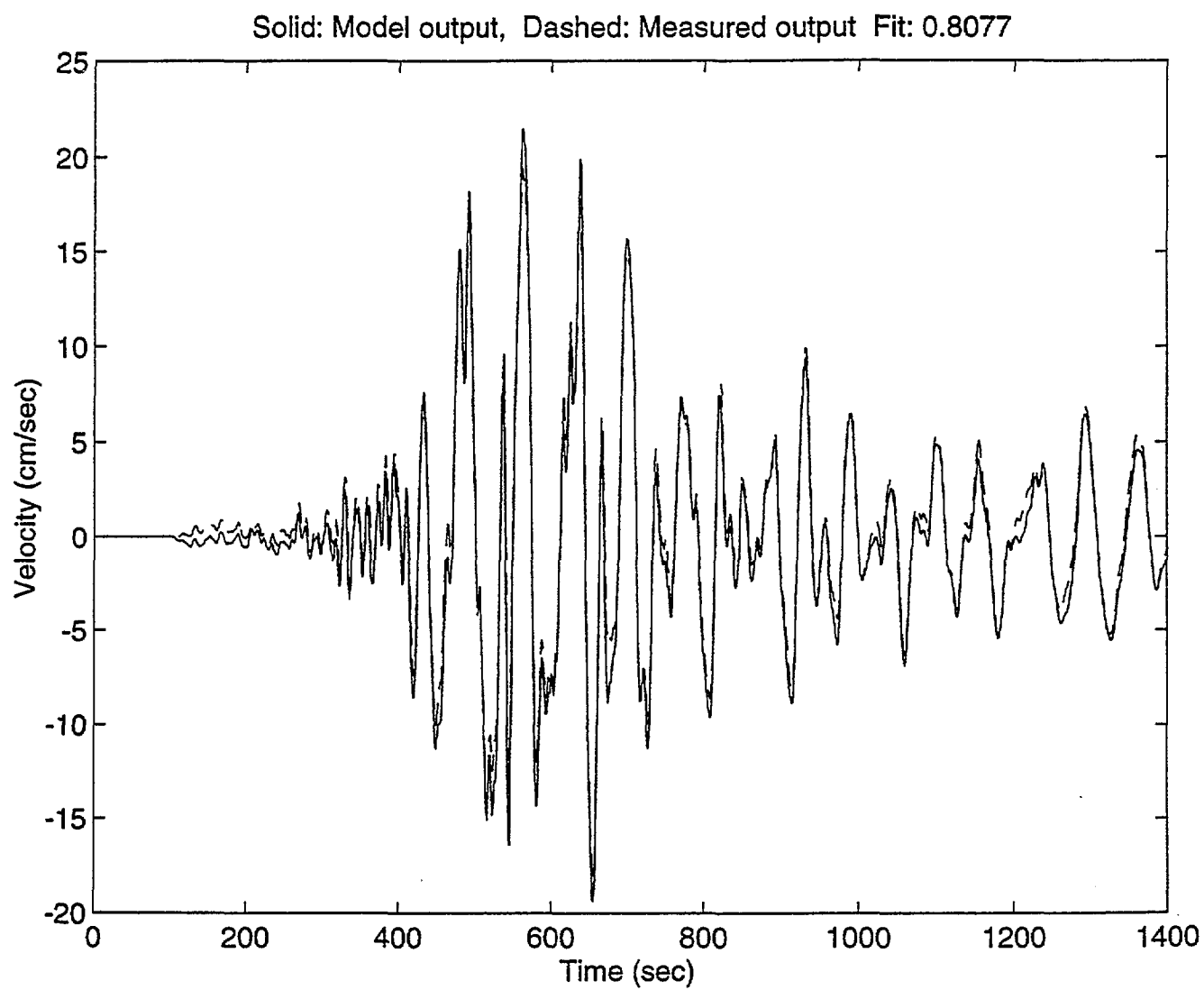
Figure E.42   Modeled versus actual output, Event10, E - W, DHB, 47 to 17 m depth interval.

Figure E.43 Modeled versus actual output, Event12, E - W, DHA, 6 to 0 m depth interval.

177

Figure E.44 Modeled versus actual output, Event12, E - W, DHA, 11 to 6 m depth interval.

Solid: Model output, Dashed: Measured output Fit: 0.2849

Figure E.45   Modeled versus actual output, Event12, E - W, DHA, 17 to 11 m depth interval.

Figure E.46   Modeled versus actual output, Event12, E - W, DHA, 47 to 17 m depth interval.

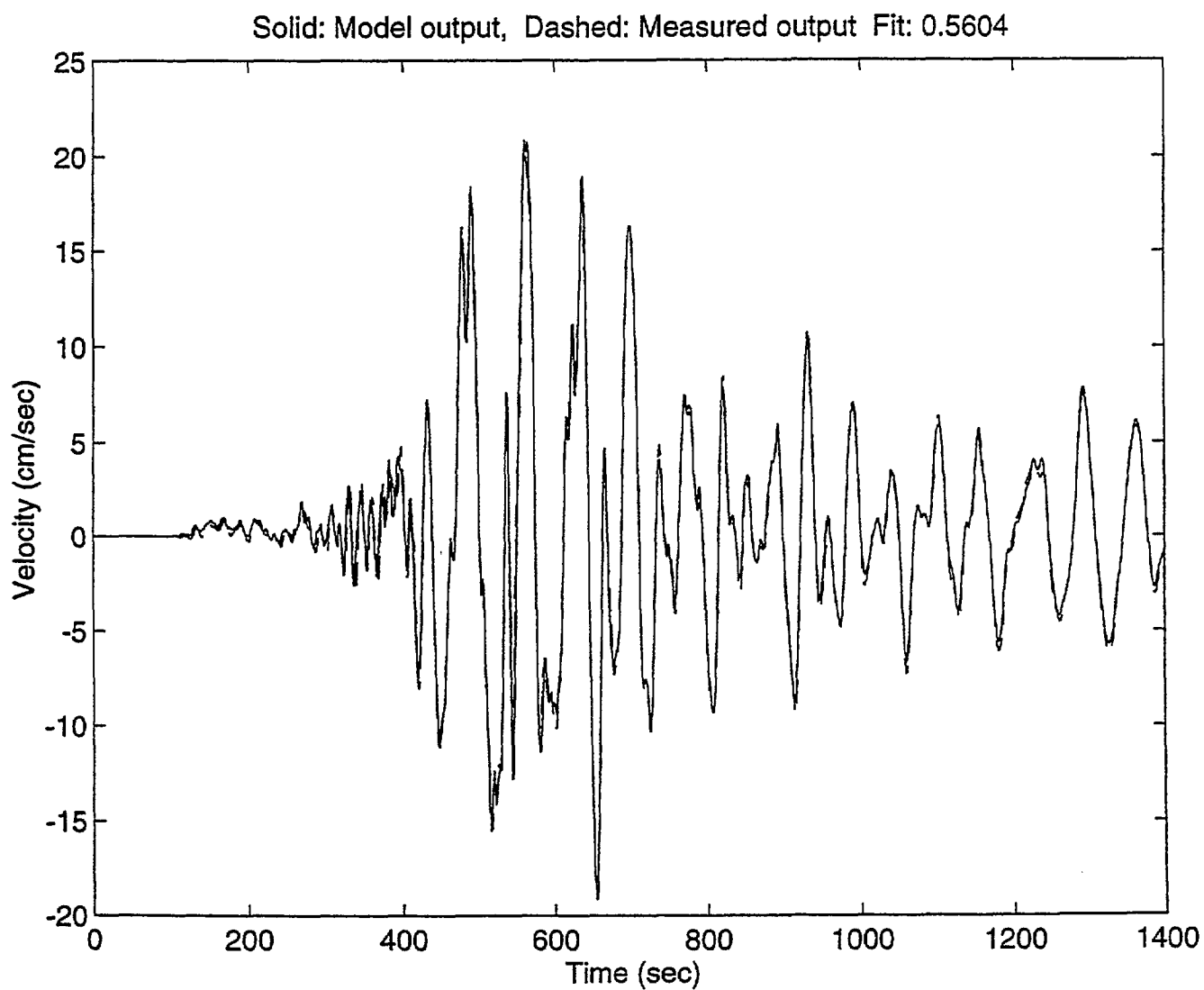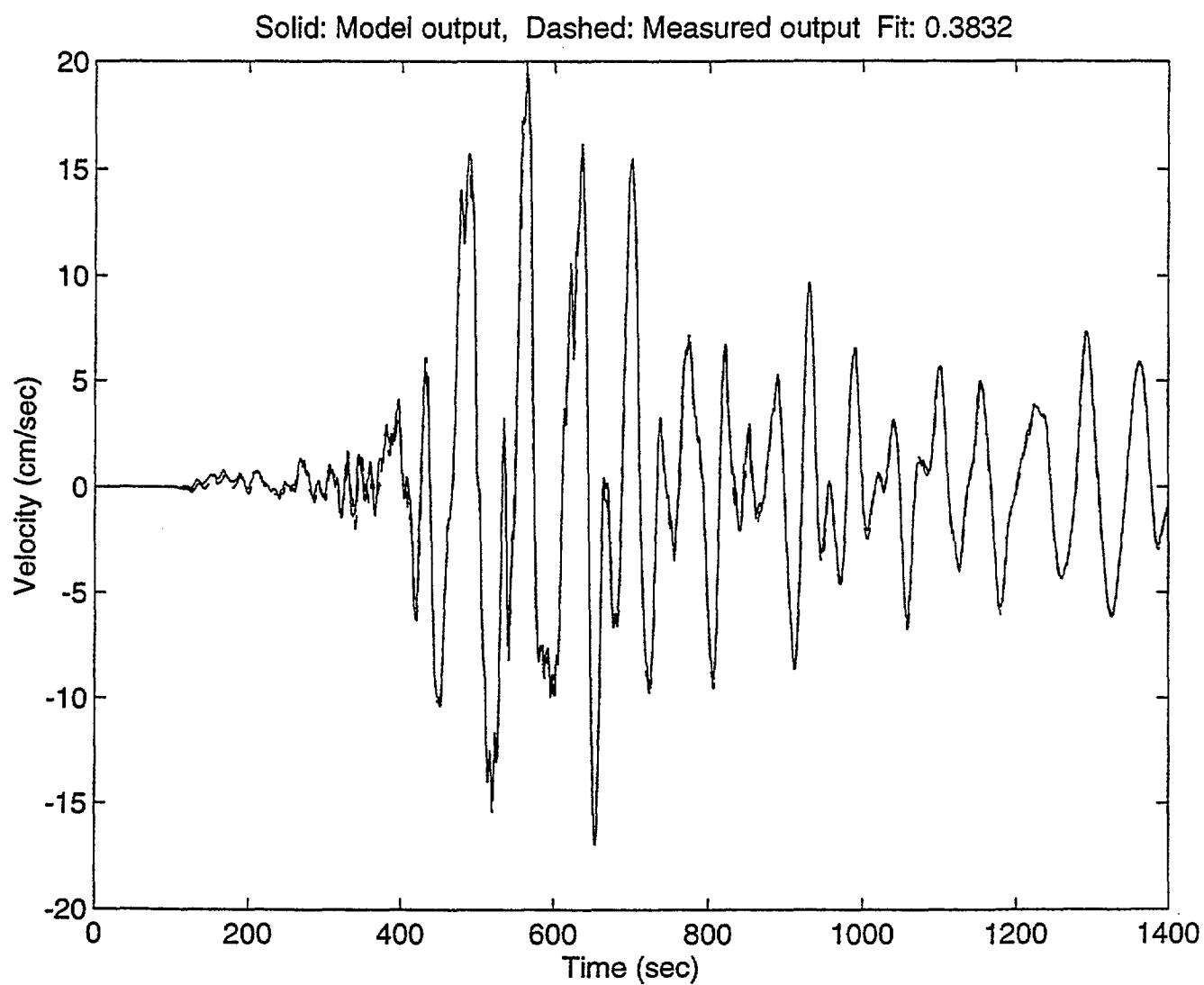Figure E.47   Modeled versus actual output, Event12, E - W, DHB, 6 to 0 m depth interval.

Solid: Model output, Dashed: Measured output Fit: 0.4049

Figure E.48   Modeled versus actual output, Event12, E - W, DHB, 11 to 6 m depth interval.

Figure E.49   Modeled versus actual output, Event12, E - W, DHB, 17 to 11 m depth interval.
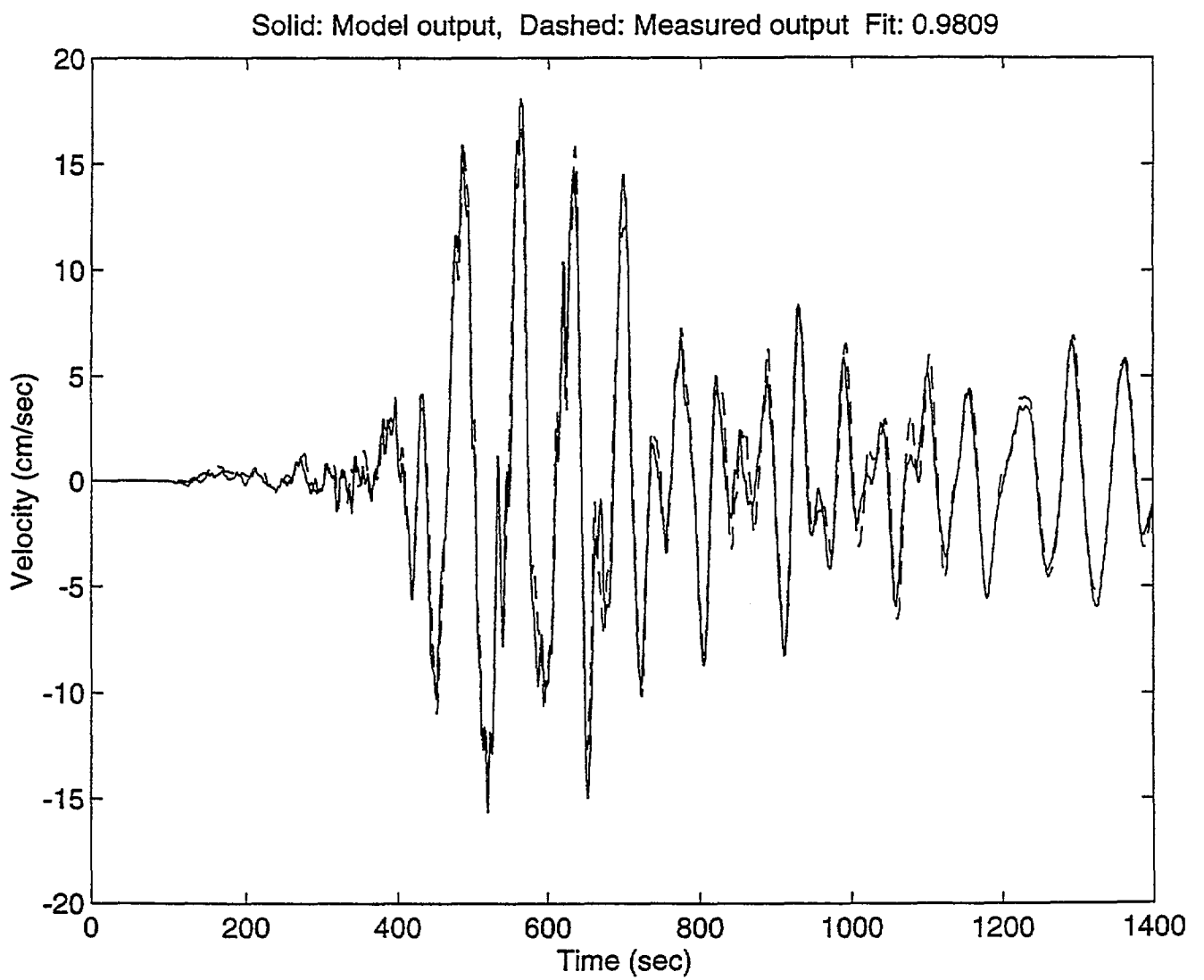
Figure E.50   Modeled versus actual output, Event16, E - W, DHA, 6 to 0 m depth interval.

Solid: Model output, Dashed: Measured output Fit: 0.5604

Figure E.51   Modeled versus actual output, Event16, E - W, DHA, 11 to 6 m depth interval.

Solid: Model output, Dashed: Measured output Fit: 0.3832

Figure E.52   Modeled versus actual output, Event16, E - W, DHA, 17 to 11 m depth interval.

Figure E.53   Modeled versus actual output, Event16, E - W, DHA, 47 to 17 m depth interval.
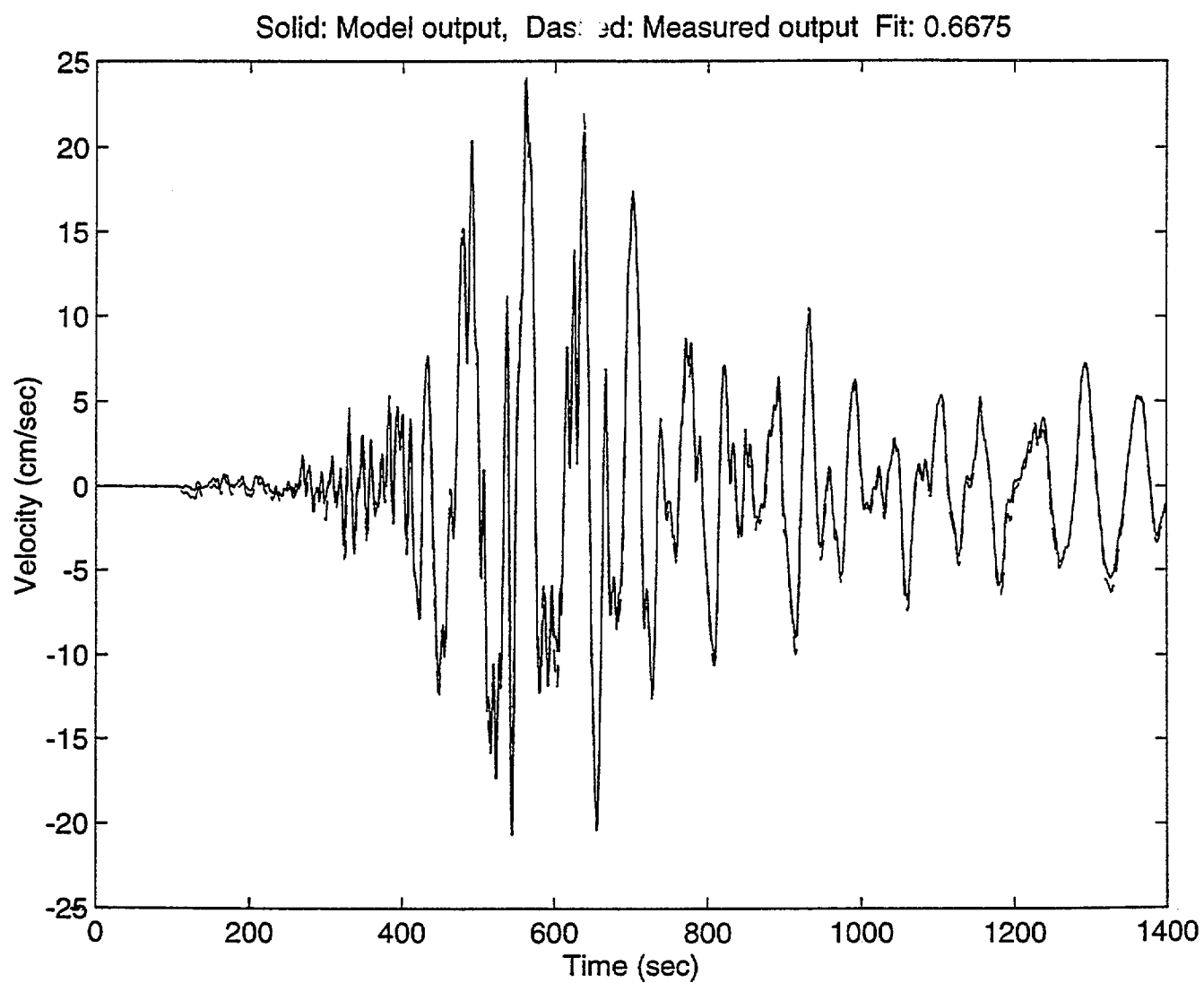
Figure E.54   Modeled versus actual output, Event16, E - W, DHB, 6 to 0 m depth interval.
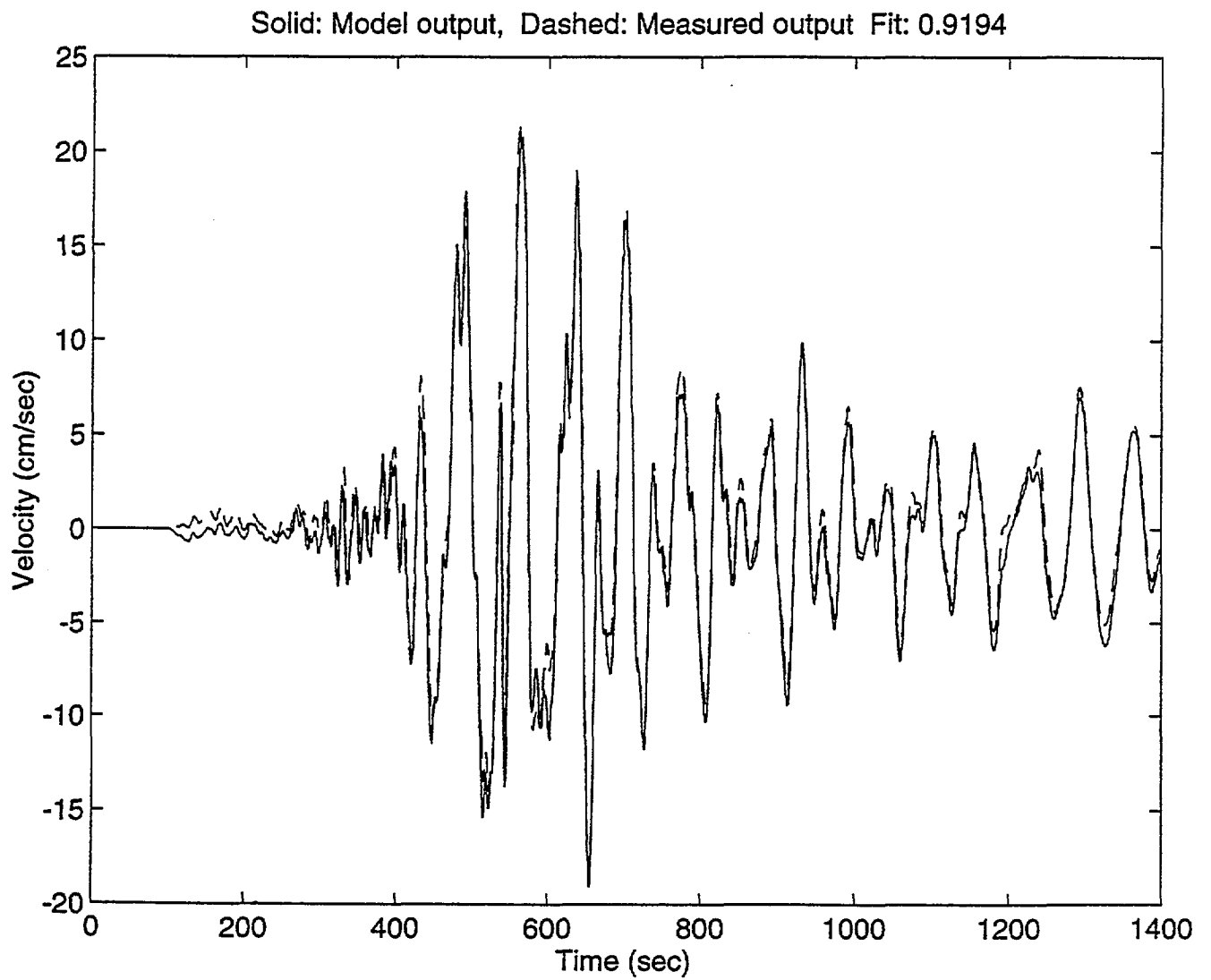
Figure E.55   Modeled versus actual output, Event16, E - W, DHB, 11 to 6 m depth interval.
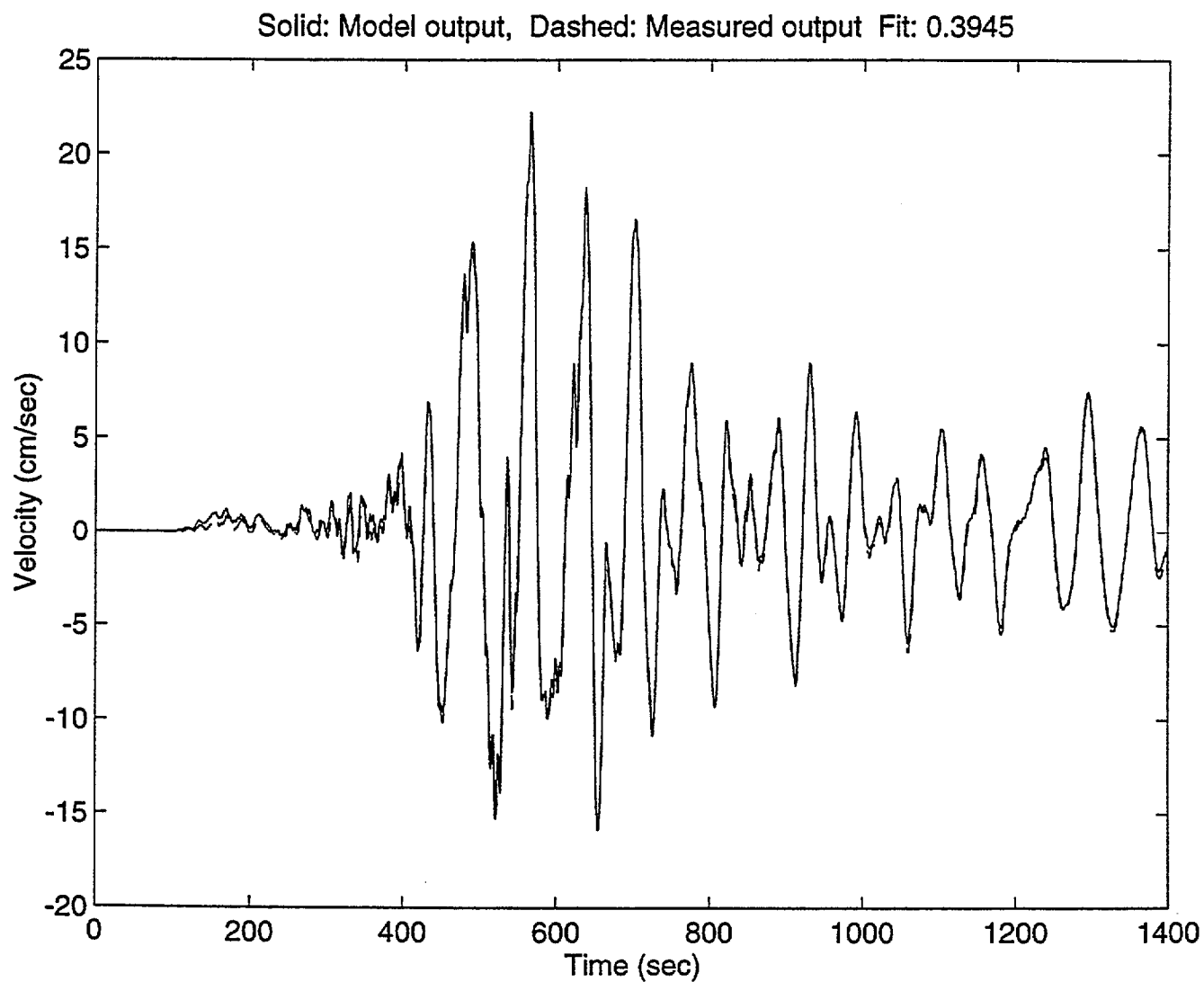
Figure E.56 Modeled versus actual output, Event16, E - W, DHB, 17 to 11 m depth interval.